Characterization of the Upper Arkansas Basin
Chaffee County, Colorado

Colorado School of Mines
Boise State University
Imperial College London

Geophysics Field Camp 2010

June 11, 2010

Abstract

The Upper Arkansas River Valley, Colorado, is the site of extensive hydrothermal activity. It is the northernmost valley of the Rio Grande rift system, and is bounded on the west by the Oligocene age Sawatch Mountains and by the Precambrian age Mosquito mountains in the East. The valley is a half-graben, with its western margin subsiding relative to the Mount Princeton Batholith. Most hydrothermal activity occurs along the Mount Princeton front range fault on the valley's western margin. In the Chalk Creek area, hot springs are associated with the Mount Princeton frontal fault system, but not with the nearby Mount Antero fault system. The relationship between these two fault systems is undetermined.

Extensive fluorite deposits at Brown's Canyon, Hecla Junction, and Poncha Hot Springs on the valley's eastern margin indicate that geothermal sources exist beyond the immediate vicinity of Mount Princeton. The water sources and heating mechanisms for these hydro-geothermal systems is not understood.

The region between Poncha Springs and Green's Creek is a transfer zone connecting the Upper Arkansas River Valley with the San Luis valley in the south, the geology of which is complex.

Between May 14th and June 11th, 2010, the Colorado School of Mines, Boise State University and Imperial College London conducted a joint field session designed to understand the possible sources of potable and geothermal water in the Upper Arkansas River Valley using multiple geophysical methods in four different survey sites.

At Chalk Creek faults are associated with the transfer zone between Mount Princeton and Mount Antero Frontal faults. Self potential and DC resistivity surveys have mapped the circulation of ground water in this area.

At Hecla Junction, self potential, DC resistivity, magnetic and elecrtomagnetic methods map the boundaries to a subterranean resevoir supplying a spring.

Tufa deposits and faults are identified using self potential, DC resistivity and magnetics at Poncha Springs possibly incative of upwelling geothermal water.

At Green Creek, deep seismic, gravity and magnetic methods identify north striking listric fault near the Green's Creek trailhead which may represent extensional faults within the valley.

Information from previous surveys in the Upper Arkansas Valley is also incorporated for interpretation. Posterior to this investigation we now better understand the transition zone. Faults which were previously hypothesized are now crystal clear and possible water presence and upwelling is closer to being determined.

Acknowledgements

The students of the geophysics field camp would like to thank the organizations and individuals who contributed to the success of this field camp. We are grateful for the financial support provided:

Colorado School of Mines
Boise State University
Imperial College, London
SEG Foundation
Rutt Bridges
Global Geophysical
TGS
U.S. Department of Energy

In addition, we greatly appreciate not only the equipment and services that the different instutitions and companies provided, but also the knowledge and time they extended to help make this valuable experience run smoothly and efficiently. This includes:

CGGVeritas
University of Texas (NEES)
Sercel
Ion
Colorado School of Mines
Deer Valley Ranch
Mt. Princeton Hot Springs Resort

Also, we cant thank enough the locals of the Upper Arkansas Valley who provided access to roads and their private properties. Special thanks go to:

Chaffee County
Donald S. Reimer, Chaffee County Development Director
City of Poncha Springs
U.S. Bureau of Land Management
U.S. Forest Service
Becky and Thomas Massey
Dr. Roberta Edwards
Robert Butler
Fred Henderson
Steve Lundgren, Young Life Frontier Ranch

We would also like to express our appreciation to the following companies and personel who provided us with all the equipment and software needed for the surveys. Without the benefit of their knowledge and time, the project would have been impossible to conduct:

Chaffee County Commissioners
Jack Lewis, Administrator, City of Salida
Dr. Terry Young, Dept. of Geophysics, CSM
Rod Kellaway, CGGVeritas
Tom Chatham, Sercel
Robert Kent, NEES, University of Texas
Hans Ecke, Ion
Evan Genaud, Anadarko
Seth Haines, U.S. Geological Survey
Paul Morgan, Colorado Geological Survey
Summer Montgomery, Colog

Staff and faculty from Colorado School of Mines, Imperial College London, and Boise State University were generous enough to offer their time and knowledge to make this project organized and succesful:

Prof. Mike Batzle
Prof. Bob Raynolds
Prof. Helmut Jakubowicz
Prof. Gareth Collins
Prof. Kasper van Wijk
Prof. Lee Liberty
Prof. Andre Revil
Prof. Jeff Andrews-Hanna
Prof. Dave Hale
Prof. Paul Sava
Brian Passerella
Dawn Umpleby
Michelle Szobody

The assistance of the following graduate students and teaching assistants has been greatly appreciated:

Kristen Swaim
Sarah Devriese
Michael Mitchell
Leon Foks
Jeffrey Shoffner
Kyle Richards
Antoine Coyac
Farnoush Forghani-Arani
Andy Lamb
Dylan Mikesell
Thomas Blum
Ahmad Alghamdi
Ahmed Al-Yaqoobi

Finally, all students of Colorado School of Mines, Boise State and Imperial College who participlated in the field camp:

Colorado School of Mines:

Rashed Alghenaim, Abdulla Alkobaisi, Banks Beasley, Jamie Clifton, Catie Cox, Mohammad El-Baharia, Ashley Fish, Andrew Hill, Alex House, Ryan Isherwood, Cameron Keese, Brent Putman, Alex Radelet, Anya Reitz, Saksit Sa-Nguanphon, Dustyn Sale, Megan Sprot and Essau Worthy-Blackwell.

Imperial College London:

Segun Ademonehin, Elizabeth Aquilina, Celal Can Atilgan, Olzhas Berkimbay, Matthew Bolton, Mark Briggs, Ian Drage, Richard Ford, Godwin Geraldo-Delima, Christopher Harris, Dias Kaliyev, Katherine Kho, Christian Lumsden, Ian Mallinson, Dayangku Nurhayati, Chinedu Nwosu, Christine Roumeas, Solomon Soyemi, Dauir Toguzov and Hsin Keui Wang.

Boise State University:

Laura Garchar, Kyle Lindsay, Brian Melander, Mike Morrison and Kat Warner.

Disclaimer

The main objective of this field camp was to introduce the students to many of the geophysical methods that are used in exploration. All the data have been obtained, processed, and interpreted mainly by students from the Colorado School of Mines, Imperial College London, and Boise State University. Therefore, the content of this report should be regarded appropriately. The aforementioned schools do not guarantee the accuracy and validity of the information or the results obtained from this investigation.

Contents

List of Figures

List of Tables

Chapter 1

Introduction

1.1 Background

Since 2005, the Colorado School of Mines has offered a field geophysics course focused on understanding the Upper Arkansas River Valley in Chaffee County, Colorado. Students collect data in the field then return to the Mines campus to process and interpret the data.

The Upper Arkansas River Valley is of particular interest because of water-related issues, such as finding new sources of drinking water and assessing geothermal potential. Fresh water is a scarce resource in the western United States, and 11% of Chaffee County's water already comes from groundwater sources. The population in this area is predicted to increase by 70% by 2030 [2]. Clearly, new sources of groundwater need to be found to support this increased population. Additionally, geothermal activity and resource potential in the Upper Arkansas River Valley are poorly understood. Geothermal is a clean, renewable energy source that is used worldwide to generate electricity; it is currently being used at Mt. Princeton for bathing. The state of Colorado has a target of achieving 30% renewable energy by 2020 [14], and utilizing geothermal energy is one way to reach that goal. Renewable energy also creates jobs, reduces dependence on foreign oil, and reduces greenhouse gas emissions.

A basic groundwater model can be used to help visualize the flow of water in the subsurface. Rain is absorbed by the ground and may be stored in a shallow aquifer, or may sink further down through different layers of earth material until it reaches a depth at which the thermal gradient of the Earth or some other heat source raises its temperature. Once the water is heated, it rises to the surface by convection, typically through some network of fractures, faults, or porous sediments. Usually potable water comes from relatively shallow aquifers, while geothermal water is found at greater depths and is generally unsuitable for drinking because of the total dissolved solids and chemicals it contains. Often, hot springs are the expression of hot water that has traveled to the surface through a fault. Faulting has a big influence on the circulation pathways of groundwater, directing the flow along fractures.

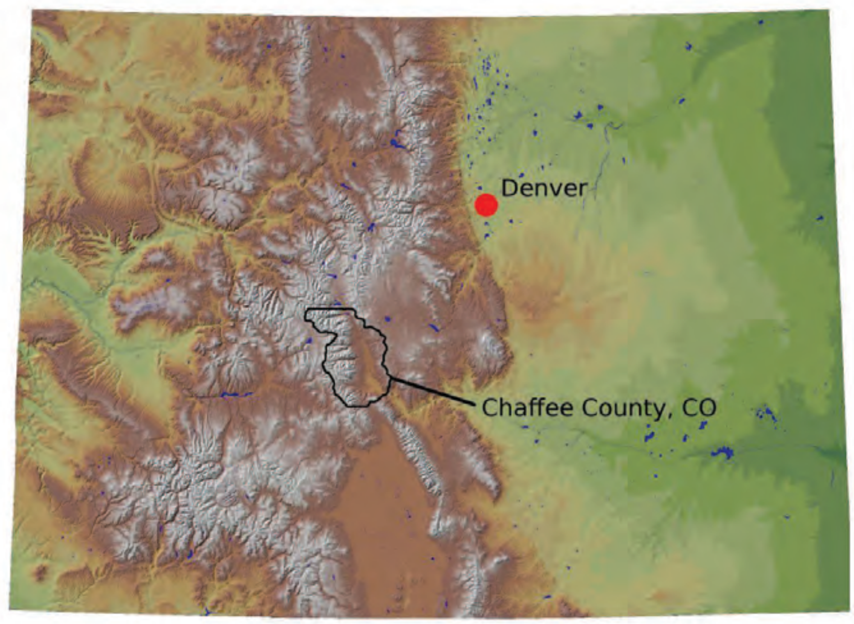

Figure 1.1: *Map of the state of Colorado, showing the location of Chaffee County in relation to Denver.*

Previous years have aimed to characterize the regional surface and subsurface geological structures, identify aquifer geometry, formulate groundwater flow models, examine heat flow, understand local shear systems, and determine ditch leakage. Water resource planning and future water management have been a continued focus. The Upper Arkansas River Valley also presents itself as a promising geothermal prospect, and investigating geothermal featureshas been an important part of research in the area.

This year students from the Colorado School of Mines, Boise State University, and Imperial College London participated in the course. Two weeks were spent in the field at four primary survey areas: Mt. Princeton, Hecla Junction, Green's Creek, and Poncha Springs. Near-surface seismic, deep seismic, direct current (DC) resistivity, self potential (SP), magnetic, gravity, and electromagnetic surveys were conducted from May 16-28. Data reduction, processing, and interpretation were performed over June 1-10. Presentations of the students' research were open to the public and held in Salida on May 27 and also at the Colorado School of Mines campus on June 11.

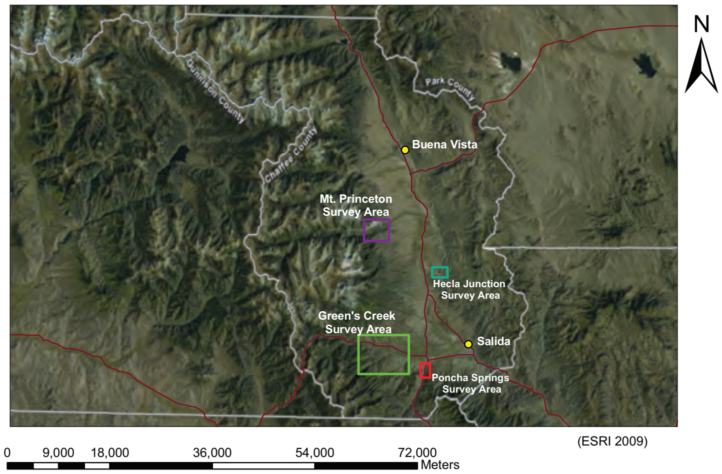

Figure 1.2: *Map of the primary survey areas in the Upper Arkansas River Valley, Chaffee County, Colorado.*

1.2 Objectives

The principal purpose of this investigation is to provide a learning experience. The participating students gain valuable field experience by using a variety of geophysical equipment, while learning the importance of field safety and management strategies. Out of the field, students learn how to manage the collected data, process it into a usable form and interpret the results. The compilation and presentation of the investigations results are strongly emphasized and students are expected to understand and be able to discuss the results. Studies this year build on the work of previous years with special emphasis on understanding the basin geometry, faulting structure and groundwater movement in the Upper Arkansas River Valley.

Chapter 2

Geology

2.1 Introduction

The Upper Arkansas River Valley is the northernmost valley comprising the Rio Grande rift system. The valley extends roughly from Leadville, in the North to the towns of Salida and Poncha Springs in the South (Fig. 2.1).

The asymmetrical valley is bounded on the west by the Sawatch range made up of steep crystalline rocks of Precambrian and Oligocene age, and on the east by the Mosquito Range, made up of gently rolling hills of Precambrian crystalline rock.

Water supplying the hot springs along the valley's western margin are thought to originate in a fault system between the crystalline rock of the Sawatch Range and the valley fill sediments. The most obvious and extensive geothermal activity is associated with the fault system around Mount Princeton at Chalk Creek and Cottonwood Creek. Springs at Hecla Junction, on the valley's eastern margin, produce water with a chemical composition that is similar to those at Chalk Creek and Cottonwood Creek.

The valley's southern edge is bounded by a heavily faulted area of hills that represents a transfer region between an east-dipping basin-bounding fault on the eastern flank of the Sawatch Mountains of the Upper Arkansas Valley, and the west-dipping frontal fault delimiting the eastern edge of the Sangre de Cristo Mountains of the San Luis Valley.

The Upper Arkansas Valley is thought to be underlain by Precambrian crystalline rock overlain by approximately 2,000 meters of poorly consolidated alluvial sediments deposited during the Miocene and late Pliocene epochs. Collectively, these sediments are known as the Dry Union Formation. It is possible that in some areas, the basement rock is also overlain with lava flows and ash-fall material derived from eruptions that occurred in the Mount Princeton area in early Oligocene time. Over much of the valley, particularly on the western side, the Dry Union Formation is mantled by relatively thin (30 m) moraines formed by Pleistocene

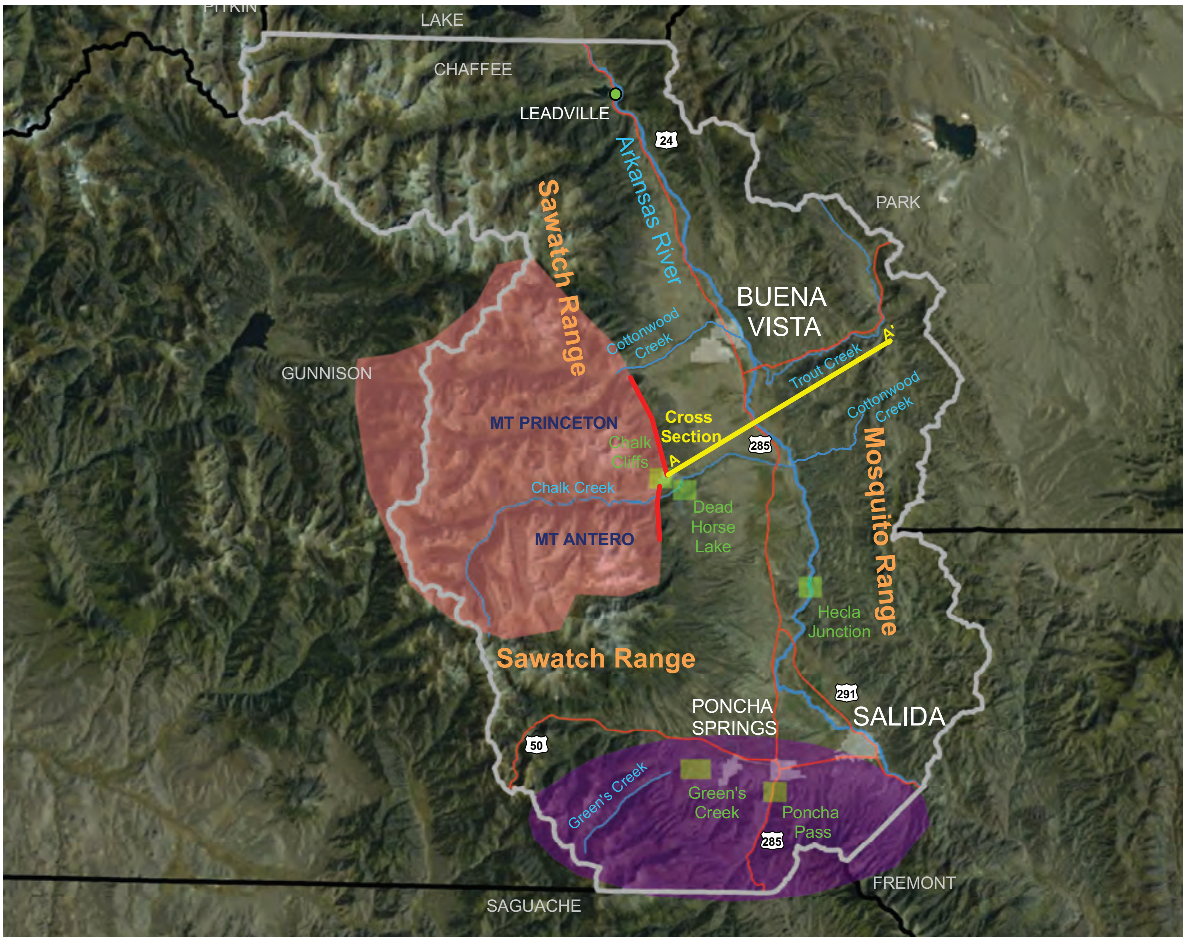

Figure 2.1: *Map of the Upper Arkansas River Valley and its Environs.*

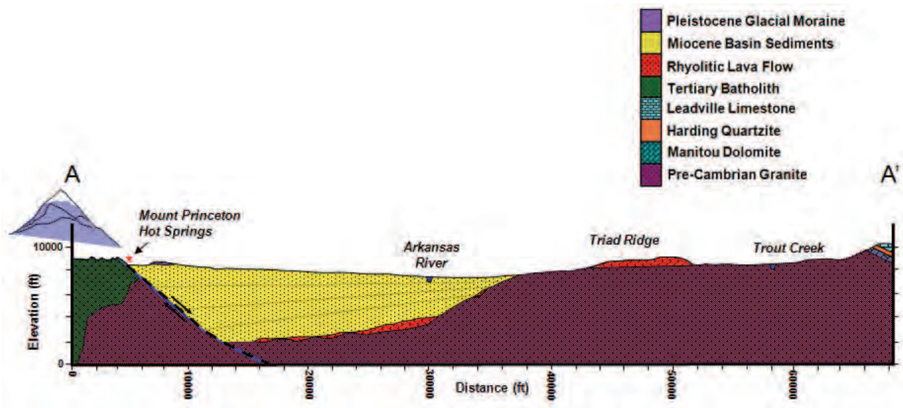

Figure 2.2: *Cross Section of Upper Arkansas River Valley between Mount Princeton Hot Springs and Trout Creek.*

epoch glaciers that developed on the Sawatch Mountains.

2.1.1 The Upper Arkansas River Valley today

The Upper Arkansas Valley is an asymmetric rift valley formed by the subsidence of the valley relative to the Sawatch Range. The valley can be described as a half-graben; on the valley's eastern side, basement rocks of the Mosquito range gently dip into the valley, and glacial till and sediments of the Dry Union Formation lap onto the Mosquito Range's western margin (Fig. 2.2). We posit that the rock horizons of the valley are contiguous with those of the Mosquito Range, and that rock structures beneath the Dry Union Formation are similar to those that are exposed on the flanks of the Mosquito Range: Precambrian crystalline rock, covered by narrow valley fill deposits of lava and volcanic ash (up to 180 m thick) are in turn covered by valley sediments ($\sim$ 2 kilometers thick) of the Dry Union Formation and thin Pleistocene glacial moraines. These subsurface structures end abruptly at the range-front fault bounding the Mt. Princeton batholith (Fig. 2.2).

At Frontier Ranch, north of Chalk Creek, we observe a mylonite sheet covering the granite of the Mt. Princeton batholith, which represents the actual fault interface. Mylonite is characteristic of faults and is typically a few centimeters thick. The mylonite however at Frontier Ranch is several meters thick [33].

The fault system at the base of Mt. Princeton appears to be associated with the Chalk Creek and Cottonwood Creek hot springs. Water (probably meteoric) percolates through this fault system, is heated by the geothermal gradient, and surfaces as hot springs.

2.2 Geologic History

2.2.1 Precambrian, Paleosoic and Mesozoic

Precambrian basement rock is clearly visible throughout the Mosquito Range on the valley's east side. These rocks consist primarily of banded gneiss and hornblende gneiss with dikes of granite, aplite, pegmatitie, and lamphrophere [39]. The gneissic rocks are believed to be the product of highly metamorphosed sediments deposited between 1.73 and 1.43 Ga [39]. At some later time during the Precambrian, these gneissic rocks experienced igneous intrusions along cracks or faults. Most rock records of the subsequent Paleozoic and Mesozoic eras (540 Ma - 66 Ma) are missing. During these eras, however, it is believed that the region experienced at least one orogenic period [33], and several distinct periods of marine deposition [39].

The first period of marine inundation occurred during the early Paleozoic era (540 Ma - 245 Ma), and is evidenced by layers of Ordovician Manitou Dolomite and Mississippian Limestone that can be observed near the intersection of Highway 285 and CR309. At this location, Precambrian basement rock, overlain by quartzite, is clearly visible. Evidence suggests that some 1000 ft (328 m) of sediments were deposited at this time [39].

During the Pennsylvanian period (320 Ma - 286 Ma), an orogeny (mountain building event) formed a range of mountains called the Ancestral Rockies. The Ancestral Rockies have long since eroded away, but the sediments caused by their erosion are still visible as red beds in places in the Mosquito Range. It is estimated that 5000 ft (1640 m) of sediments may once have covered the region now occupied by the Upper Arkansas River Valley [39].

Throughout the Cretaceous period (144 Ma - 66 Ma), Colorado was much lower than it is today and was periodically inundated by an inland seaway that ran from the Gulf of Mexico on to parts of Western Canada [26].

The Laramide orogeny was a series of mountain building events that began during thr late Cretaceous ($\sim$70 Ma), and lasted approximately 35 million years. The exact timing of the Laramide is still debated. It began as a series of upthrusts that lifted parts of Colorado above the inland seaway. Later, the orogeny manifested itself as a series of thrusts centered in northwestern Colorado, but it affected wide swaths of all surrounding states. During the Laramide orogeny, mountain ranges such as the Uinta Range of Utah, the Wind River Range of Wyoming and the Front Range of the Rockies were formed.

2.2.2 The Mt. Princeton batholith

At the end of the Oligocene ($\sim$37 Ma), the Upper Arkansas River Valley region probably consisted of rolling hills with east-west oriented valleys that dipped gently toward Denver. Beneath the hills was relatively flat basement rock and the depression we now call the Upper Arkansas River Valley did not exist [33].

Approximately 36.7 Ma ago the region now occupied by Mt. Princeton and Mt. Antero experienced a series of volcanic eruptions. Two to three kilometers beneath the volcano a magma chamber was emplaced [33]. The Mount Princeton volcano and much of the overlying sediment has eroded away; Mt. Princeton, Mt. Antero and several other peaks are actually remnants of the original magma chamber. At Frontier Ranch the granite of the Mt. Princeton batholith contains large phenocrysts, suggesting that the batholith cooled slowly.

The Mount Princeton eruptions ejected large volumes of ash and lava. Channeled by east-west valleys, lava flowed as far as Castle Rock near Denver. Triad Ridge, near Trout Creek in the Mosquito Mountains, is a remnant of the early lava flows which, in some areas, are thought to have been as deep as 600 ft (180 m) [39]. In the Hecla Junction area, we see basement rock, overlain by a thin (∼2m) layer of reddish mudstone that was top soil when lava poured over it nearly 37 million years ago. In places we can still see the orange and yellow casts of fossilized wood and tree roots.

Topping this ancient soil horizon is a rhyolitic lava flow. The bottom portion (∼1-5 m) of the flow is glassy—evidence that it cooled quickly on contact with the cold valley floor. Further up, the lava becomes broken and columnar, a sign that it cooled slowly. Over ensuing years, the valley's sedimentary rocks eroded away, leaving the harder lava rock behind. Elongated patches of these early lava flows are still visible at Triad Ridge near Trout Creek.

2.2.3 A rift valley

Approximately 25 million years ago, tectonic forces began pulling the area apart [33]. As the crust was stretched in an east-west direction, it thinned slightly, causing it to sink relative to the surrounding terrain. The resulting depression eventually became the floor of the Upper Arkansas River Valley. This stretching was part of a much larger regional phenomenon called the Rio Grande Rift that resulted in numerous rift valleys, including the Upper Arkansas, San Luis, Espanola, and Albuquerque basins. Rifting is still occurring in these areas.

2.2.4 The Dry Union Formation

As the valley subsided, it filled with sediments washed primarily from the Sawatch Mountains. Most of these sediments appear to be fluvial in origin although some layers of airfall volcanic ash are occasionally encountered.

At Droney Gulch near the south end of the valley, the top 79 m of the Dry Union Formation are exposed and have been measured. A thin, pink volcanic ash near the top has been dated to 10.2 Ma [8].

The sediments onlap onto today's Mosquito Mountains, an indication that most sediments were washed from the Sawatch Mountains on the west side of the valley. These sediments consist primarily of poorly consolidated sandstone, pebble beds and mudstone beds that are over 2000 m thick in some parts of the valley. These sediments, known collectively as the Dry Union Formation, may be sufficiently impermeable to act as an aquitard Fig. 2.2.

2.2.5 Pleistocene geologic history

During the Pleistocene epoch (2.5 Ma - 10000 Ya), Earth's climate grew colder and the glaciers formed in the Rocky Mountains. The Upper Arkansas River Valley area experienced many episodes of glacial advance and retreat. Each advance pushed jagged boulders, rocks, sand, and till down the Sawatch Mountains into the valley, forming characteristic ridges called moraines.

Excellent examples of glacial moraines can be found in the area of Chalk Creek, where glaciers pushed material into hills that created a water impoundment area at Dead Horse Lake. Moraines cover much of the northern and western portions of the valley to a depth of 30 m. Poorly graded moraine materials are more porous than the sediments of the Dry Union Formation and the majority of the valley's potable water wells extract water from the relatively shallow layer of glacial material, not from the Dry Union Formation below it [7].

2.2.6 Southern transfer region

The Upper Arkansas River Valley meets the San Luis Valley in the area of Poncha Pass. Like the Upper Arkansas Valley, the San Luis Valley is an asymmetric rift valley with a relatively new mountain range on one side. In the San Luis Valley, however, the relatively young Sangre de Cristo mountains are on the east side of the valley. Thus, faults from these mountains dip to the West rather than to the East, as is the case with the Sawatch Mountains.

The transition between the west-dipping faults of the Sangre de Cristo Range and the east-dipping faults of the Sawatch Range deforms the rocks in the Upper Arkansas Valley's southern terminus.

(Fig. 2.3). Numerous faults in the hills near Poncha Pass are evidence of the complex warping required to accommodate differences between the two valleys' changing geometries.

2.2.7 Chalk Creek hot springs area

Chalk Creek flows between Mount Antero and Mount Princeton. During the Pleistocene, Chalk Creek Canyon was the site of extensive episodes of glacial advance and retreat. Several small moraines can be found near the mouth of Chalk Creek. Of particular interest are three moraines that form the impoundment area of Dead Horse Lake.

The benches on the north and south sides of Chalk Creek are caused by the creeks erosion into the Dry Union Formation. The northern bench abuts Mount Princeton in an area now

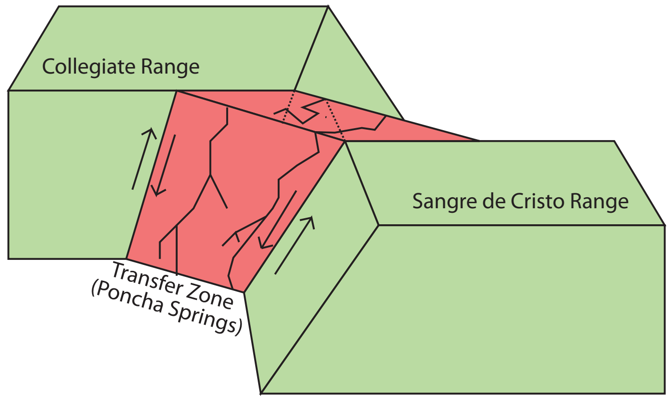

Figure 2.3: *Simplified transfer zone.*

occupied by Frontier Ranch. As noted earlier, this spot also marks the upper extreme of the fault between the Mount Princeton batholith and the Precambrian valley floor basement (located some 2000 m beneath the surface).

On the north side of Chalk Creek Canyon, and west of Frontier Ranch are Chalk Creek's namesake cliffs. The Chalk Cliffs are not actually composed of chalk, but instead are composed of Mount Princeton granite that has been hydrothermally altered by the same hot water that supplies Mount Princetons hot springs. Hot (slightly acidic) water turns feldspars in the granite into kaolinite, a clay mineral, which gives the cliffs their chalky appearance and allows them to weather easily.

On the south side of Chalk Creek, about a half mile from the main-front-range fault is a fault that marks the interface between Mount Antero and the basement rock of the Upper Arkansas River Valley. In this area, there are no hot springs and no chalk cliffs. Analyses of water samples taken from hot springs in the Chalk Creek area indicate high fluorine concentrations [11].

The transition between these two faults is poorly understood and is of particular interest to the 2010 Field Camp. It is possible that the Mount Antero and Mount Princeton faults at Chalk Creek are two separate faults. If so, we would expect to see a sort of transfer region of highly stressed and broken rock in the Dead Horse Lake area between the two faults. A second explanation is that there is a single fault that jogs, or is offset about a half kilometer in this area. Why such an offset might occur is not known. A third explanation is that the Antero and Princeton faults were once contiguous, but that an east-west transverse fault, perpendicular to the original fault, caused the offset.

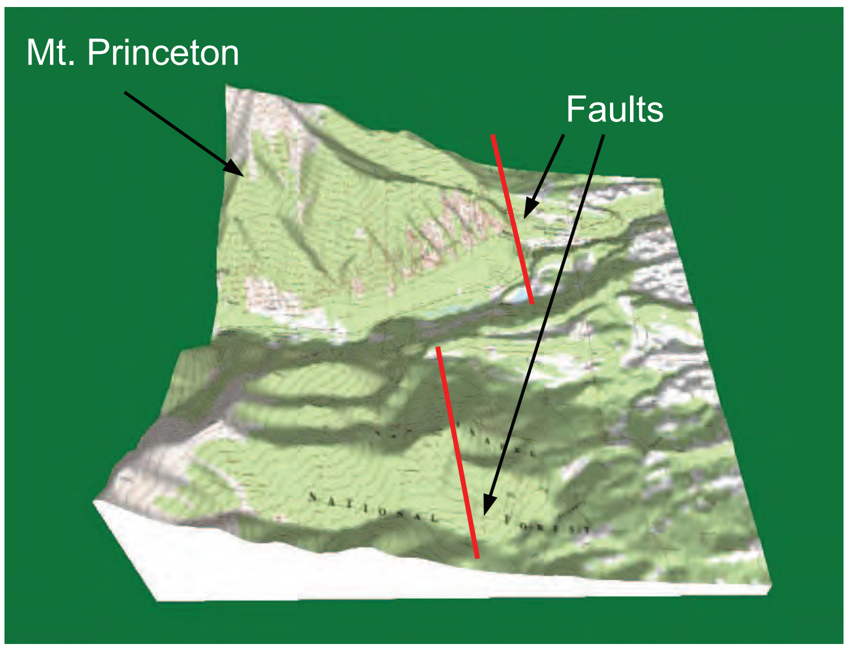

Figure 2.4: *3D topographic map of Mt. Princeton showing fault structure.*

2.2.8 Hecla Junction

At Hecla Junction, we see Precambrian Basement Rock overlain by a relatively thin (∼2 m) layer of ancient soil. Orange-red casts of tree roots can be seen immediately below the rhyolitic lava that flowed through the area at the time of the Mount Princeton eruptions. The base of this lava is glassy, indicating that it cooled quickly; however above about 0.5m, the broken columnar joints indicate that the lava cooled more slowly. At Hecla Junction, these lava flows are about 5 m thick, although evidence at Triad Ridge suggests that the lava may have been much thicker in areas. Above the lava at Hecla Junction are some 33 meters of Dry Union Formation sediments.

Assays of water samples taken from neighboring mines and from nearby Browns Canyon indicate high CaF_2 concentrations. With a 15 ppm concentration of CaF_2, these water sources are nearly saturated. Such a high concentration suggests that water is dissolving fluoride salts at a higher temperature and then depositing them as the water cools. Such formation typically takes place at relatively shallow depth, moderate pressure and temperatures between 50^oC and 200^oC. CaF_2 deposits near the spring are consistent with this theory.

Hecla Junction was once the site of an extensive fluorite mine that exploited the rich CaF_2 deposits associated with faulting around a horst in the area. Such deposits typically are produced at depths below 3000 ft (914 m), and at temperatures between 119^oC and 168^oC [ibid].

The water source at Hecla Junction is unknown. It is possible that it originates as meteoric water in the Mosquito Range. It is also possible that the water originates in the low lying hill immediately east of the spring, but the catchment area of this hill does not seem sufficiently large to explain the annual volume of water flowing from the spring. It has been proposed that nearby water descends and ascends through the faults of the horst structure, where it is heated and saturated with CaF_2. It is also possible that the water originates across the valley in the fault systems of the Sawatch Mountains and is conducted along the valley floor by aquitards formed by the Dry Union Formation. Despite the differences, these explanations require that water be heated at relatively shallow depths, suggesting a near-surface heat source.

2.2.9 Poncha Springs

Poncha Pass is a poorly understood mountainous area that represents a transition region between east-dipping faulting in the west side of the Upper Arkansas River Valley and west-dipping faulting in the east side of the San Luis Valley. Faults in both valleys trend roughly north-south. The cause of this sudden change of faulting character is unclear.

The abandoned Boy Scout camp is located on Precambrian metamorphic hornblende gneiss and banded quartz-feldspar-biotite gneiss intercalated with quartzite and silicicated marble [39]. Calcareous tufa mounds, a flourite mine and hot springs are present near the Boy Scout

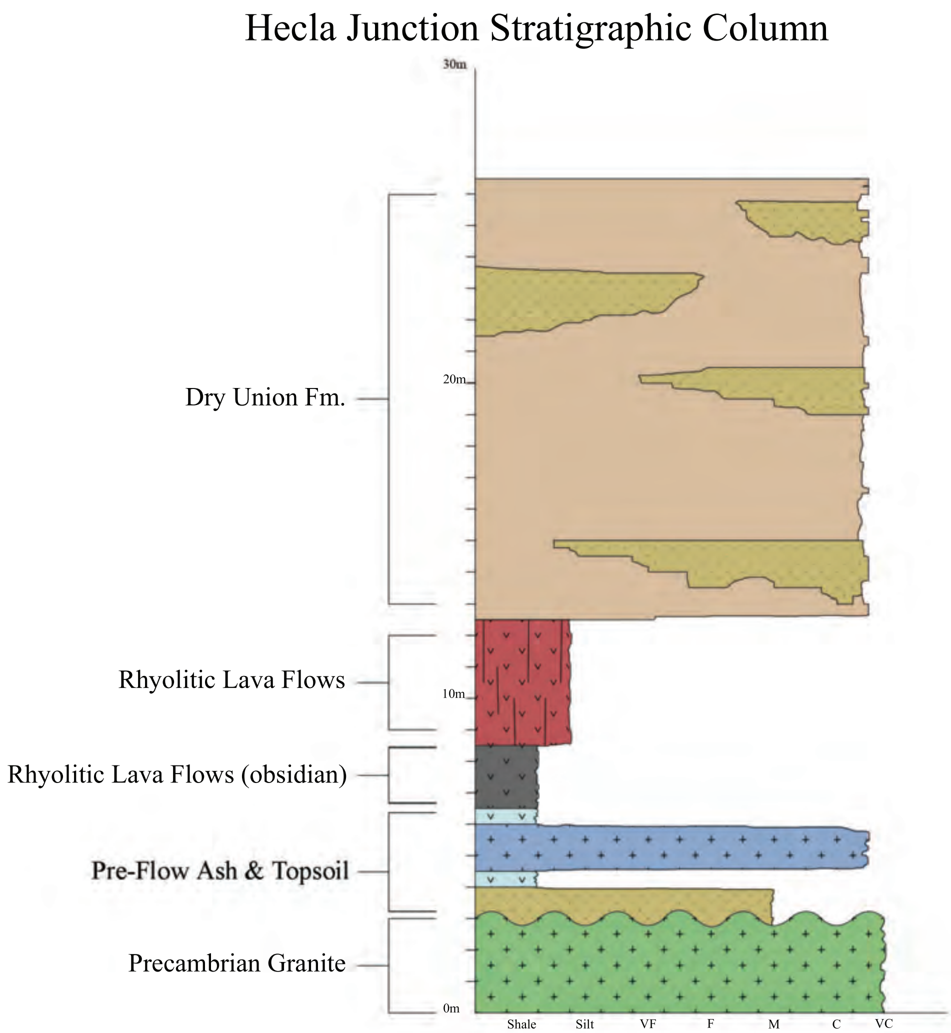

Figure 2.5: *Stratigraphic column obtained at Hecla Junction.*

camp. Several west-east trending faults have been mapped in the southern part of the Upper Arkansas River Valley [34], and it is likely that fault-controlled hot fluid produced the tufa and flourite deposits seen.

2.2.10 Green Creek

Green Creek cuts through Dry Union Formation sediments at the south end of the Upper Arkansas River Valley near the western edge of the transfer region. There is extensive faulting in the area. In particular, two north-west striking faults near the top of Green Creek are thought to be associated with substantial basement rock displacement in the area. These may represent an extension of the range-front-fault of the Sawatch Ranch.

Northwest of these faults is Dry Union Formation sediment. Southwest of these faults is Precambrian basement rock. Such extensive faulting should be detectable using deep seismic and gravity methods. Depending on the composition of the underlying rock, the faults may also be detectable using magnetic methods.

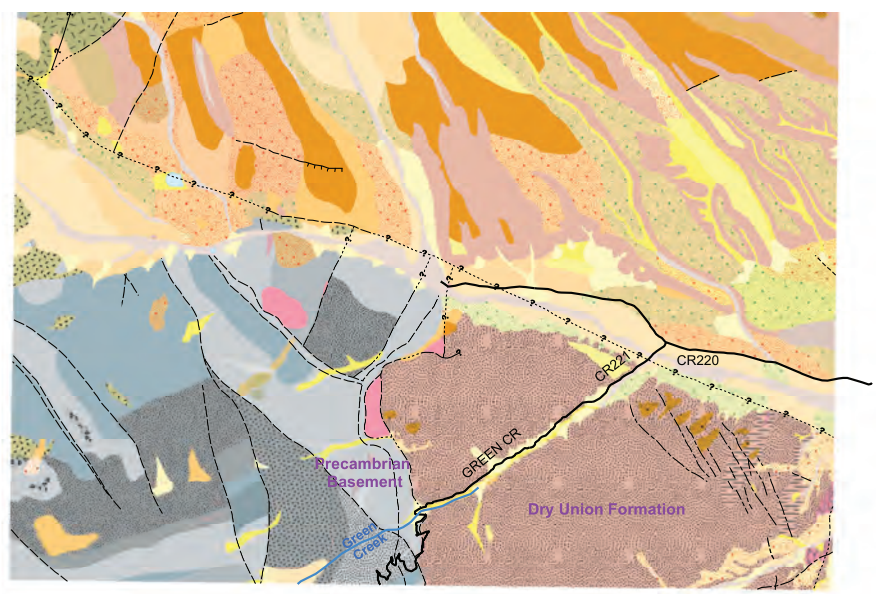

Figure 2.6: *Geologic map of Green Creek.*

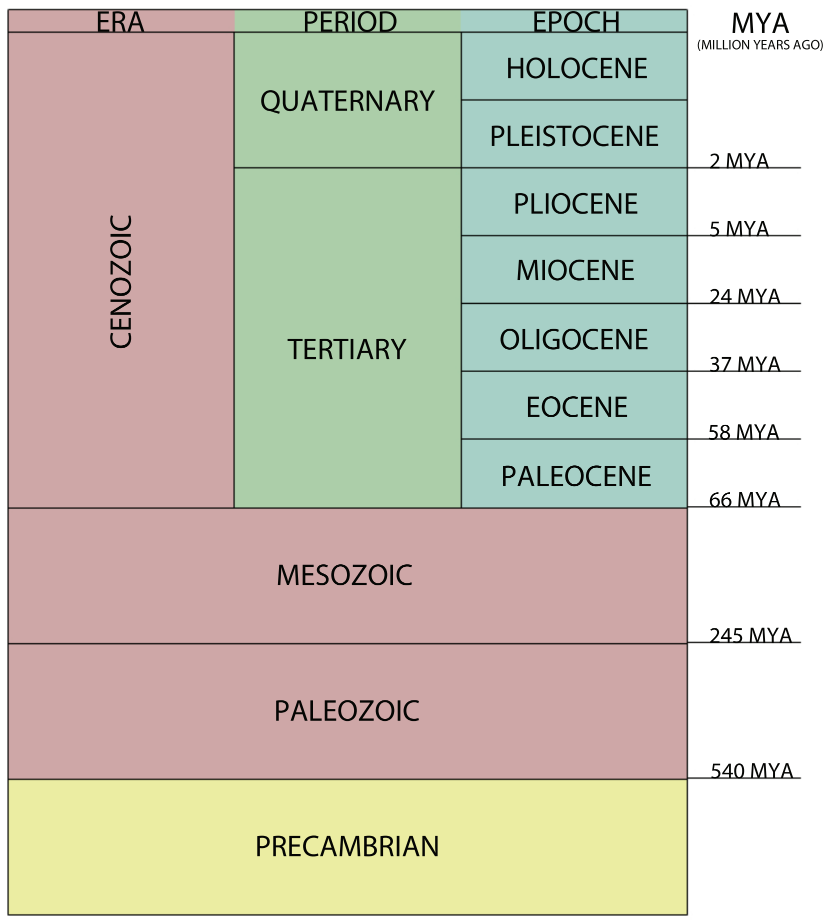

Figure 2.7: *The Geologic Time Scale.*

Chapter 3

Geophysics

Several different and complementary geophysical methods were used in the course of this investigation. The following sections give a brief overview of the geophysical methods that have been used together with a short introduction to the equipment used in each survey. For more detail on the theory behind geophysical surveying please refer to the appendices.

3.1 Seismic reflection methods

Reflection seismic methods can provide fine structural detail. The data are results of sampled and recorded seismic energy as it returns to the surface after traveling through the sub-surface as wave fronts. Changing properties and travel paths as the waves move through different earth layers will change the recorded data. The only energy of interest, in accurately forming the sub-surface image, is p-wave energy that has the simplest possible reflected path to the receiver array. These p-wave reflections can be used to interpret the subsurface geometry of the area.

Noise is incorporated into the data when the p-wave energy is accompanied at the surface by other undesirable energies, generally referred to as noise, and these need to be removed or attenuated to improve the reliability of the final processing results. This includes ground rolls, refraction, air waves and energy that have reflected off more than one interface or surface before being recorded. Corrections were also made for factors that change the nature of the wave-front as it propagates through the subsurface: static corrections due to complex topography and high velocity and unconsolidated weathered layer. Seismic waves lose energy as a result of reflection and refraction and due to geometrical spreading from the original source. Noise also generated by nearby moving vehicles or any other extraneous sources will be eliminated.

The setup used to create and record the seismic waves for reflection surveys includes a source (vibroseis truck) and receivers (geophones), all connected to a central control vehicle.

3.2 Seismic refraction methods

At geological boundaries, when neighbouring rock formations are in contact (possessing different elastic properties), two predominant wave mechanisms occur; reflection and refraction. A refracted wave is one that propagates across the geological boundary and continues to travel in the lower rock layer. Refraction is determined by the angle of incidence of the raypaths that describe the initial compressional wavefront, described by Snell's law.

The refracted and transmitted amplitude depend on the acoustic impedance (velocity multiplied by rock density) of the upper and lower rock layer and the angle of incidence. As the refracted waves propagate along the boundary they continually transmit energy back into the upper layer. Energy returning to the upper layer, represented by the rays that leave the interface at the critical angle, define a plane wavefront known as a head wave.

The refraction seismic method analyzes the acoustic properties of the rock media, just as with reflection seismology. The refracted energies recorded at the surface are processed and then used to interpret the subsurface geometry in the area. In interpreting the results, faulting and other features can be identified.

The equipment involved in a seismic refraction survey is similar to that of a reflection survey except that the source used to generate the seismic waves utilizes some sort of weight drop system such as a sledge hammer or a controled mass.

3.3 Vertical Seismic Profiling

Vertical seismic profiling is a form of seismic reflection survey in which the response of the earth to a source at surface is measured at depth within a borehole or vice versa. It can be run in two configurations: zero-offset and offset. VSP surveys have higher resolution than conventional seismic reflection surveys, but are limited to a much smaller area than conventional surveys and thus a direct comparison of a VSP with a conventional seismic section allows ambiguity to be reduced. Analysis of VSP results also help to build a more accurate velocity model to help constrain the interpretation of larger scale seismic surveys in the area.

The acquisition of VSP involves having receivers, either geophones or hydrophones, at depth down a borehole and having a weight drop source located a defined horizontal distance away at the surface.

3.4 Gravity

Gravity measurements define anomalous densities within the Earth; in most cases, ground-based gravimeters are used to precisely measure variations in the gravity field at different points. Gravity anomalies are computed by subtracting a regional field from the measured field, which result in gravitational anomalies that correlate with source body density variations. Positive gravity anomalies are associated with shallow high density bodies, whereas gravity lows are associated with shallow low density bodies. The gravity method also enables a prediction of the total anomalous mass (ore tonnage) responsible for an anomaly. Gravity and magnetic (discussed below) methods detect only lateral contrasts in density or magnetization, respectively. In contrast, electrical and seismic methods can detect vertical, as well as lateral, contrasts of resistivity and velocity or reflectivity. Gravity measurements are taken using an instrument called a gravitmeter. Measurements are taken in units milliGals.

3.5 Magnetics

The primary goal of the Chaffee County magnetic geophysical investigations was to identify zones that could be water conduits. While magnetic methods in geophysics are more typically used in surveys where there are metallic objects or other objects highly susceptible to magnetization, it can also be useful in determining abrupt changes in subsurface geology because different rocks and layers have different magnetic properties. For this reason, it can identify faults and other subsurface irregularities, especially when cross referenced with other geophysical data.

The magnetic method exploits small variations in magnetic mineralogy. Magnetic rocks contain various combinations of induced and remanent magnetization that perturb the Earth's primary magnetic field. The magnitudes of both induced and remanent magnetization depend on the quantity, composition, crystallographic orientation and size of magnetic-mineral grains. Magnetic anomalies may be related to primary igneous or sedimentary processes that establish the magnetic mineralogy, or they may be related to secondary alteration that either introduces or removes magnetic minerals. Secondary effects in rocks that host ore deposits associated with hydrothermal systems are important and magnetic surveys may outline zones of fossil hydrothermal activity. Because rock alteration can effect a change in bulk density as well as magnetization, magnetic anomalies, when corrected for magnetization direction, sometimes coincide with gravity anomalies. Magnetic methods often are a useful tool for deducing subsurface lithology and structure that may indirectly aid identification of mineralized rock, patterns of effluent flow, and extent of permissive terranes.

The setup and instrumentation used in a magnetic survey includes a base station magnetometer, to measure the daily fluctuation in the Earth's magnetic field which can later be subtracted from the data, and a roving magnetometer to take magnetic susceptibility measurements at the survey stations.

3.6 DC resistivity method

Direct current resistivity methods measure Earth resistivity (the inverse of conductivity) using a direct or low frequency alternating current source. Rocks are electrically conductive as consequences of ionic migration in pore space water and more rarely, electronic conduction through metallic luster minerals. Because metallic luster minerals typically do not provide long continuous circuit paths for conduction in the host rock, bulk-rock resistivities are almost always controlled by water content and dissolved ionic species present. High porosity causes low resistivity in water-saturated rocks.

DC surveys involve planting electrodes at the survey stations, hooking them up to long cables which run to a central computer. The computer then controls which electrodes are injecting current and which are measuring resitivity.

3.7 Self-potential method

The self-potential method is a passive survey, therefore it is relatively simplistic. As fluids travel through a porous rock, because of ion interaction, currents on the order of milliamperes are created. Two electrodes, a base station and a moveable electrode, a voltmeter and a spool of wire can be used to measure the voltage drop produced by the currents. A positive voltage anomaly associated with SP is an indication of upwelling water beneath the surface while downwelling water is observed as a negative anomaly.

3.8 Electromagnetic method

Electromagnetic (EM) methods are used to measure the conductivity and magnetic susceptibility of rocks in the shallow subsurface. These two physical attributes give us insight into how the geology beneath the subsurface is varying. Conductivity typically increases with groundwater saturation. Therefore EM methods were used to monitor subsurface saturation and groundwater location throughout Chaffee County. Changes in the groundwater saturation may be indicators of faulting creating preferential fluid pathways.

EM methods take advantage of the strong relationships between electricity and magnetism. The mathematical representation of these relationships are based on differentials and vector potentials, however the concepts that the math describes are simple in nature. Ultimately EM methods utilize the fact that a change in a magnetic field creates a current (Faraday's Law), and that a change in current creates a magnetic field (Ampere's Law).

EM acquisition falls under two categories: time domain and frequency domain. Time domain surveys are conducted with an instrument such as the EM47 which consists of a large transmitter loop which gives off a primary magnetic field for a period of time then shuts off.

A reciever loop with three components then records the decay curve of the secondary EMF.

3.9 Sources of uncertainty in geophysical surveys

The largest source of uncertainty in any geophysical survey is the positions of the measurements. The absolute position of each measurement in each survey was determined using a combination of the differential global positioning and total distance measurement systems. The high accuracy of DGPS compared to TDM makes position measurements using DGPS preferrable, however tree coverage can prevent the system from detecting the number of satellites needed to make an accurate measurement and in these cases TDM was used.

Chapter 4

Dead Horse Lake

4.1 Seismic refraction survey

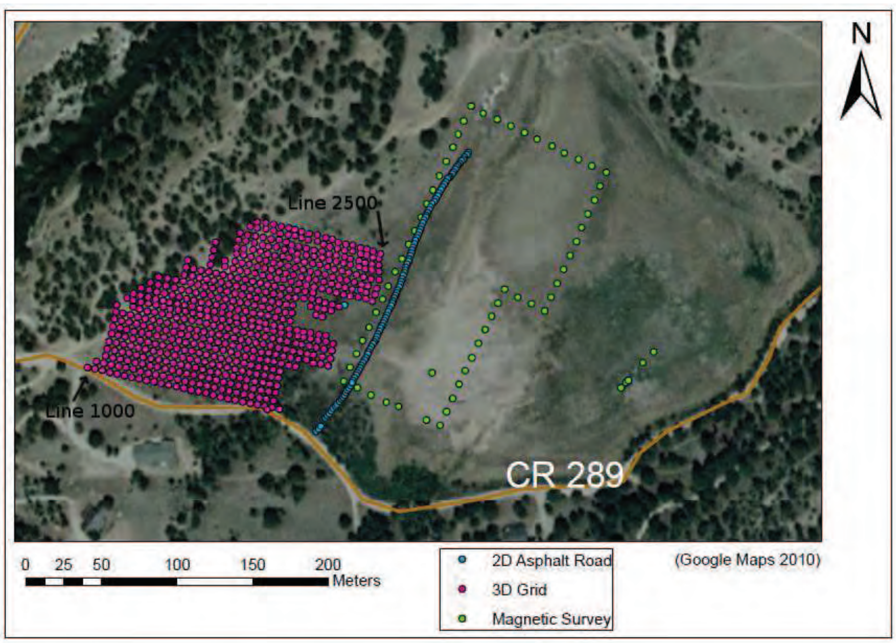

Figure 4.1: *Map of the Dead Horse Lake 3D survey. Sources were placed at the mid-point between two receiver locations.*

A 3D seismic survey was performed at Dead Horse Lake so as to ultimately enable 3D refraction tomography to be performed which would allow a detailed velocity profile of the subsurface to be constructed in conjunction with a map of depth to the bedrock (pre-Cambrian granite), and potentially (from the 2D results), a map of the depth to the top of the weathered granite and to the top of the competent granite. The work performed consisted of forming a preliminary model of depth to bedrock at Dead Horse Lake and calculating the dip of the bedrock, utilizing 2D seismic lines for refraction analysis. This gives an approximate indication of the thickness of the glacial moraine sediments lying on the granite and the topography of the granite. Variations in the depth to bedrock also yield information on large-scale fractures and potential faults. This information is important when analyzing the Dead Horse Lake rock formation in terms of water flow, as the results from this method can be used in conjunction with results from shear-wave seismic, VSP, Gravity and Magnetic methods to map water distribution and assess the permeability of the rocks beneath the surface.

4.1.1 Acquisition

The 3D refraction survey (Fig. 4.1), acquired from May 17th 2010 to May 25th 2010, was composed of 25 receiver lines, spaced 5 m apart, running from west to east, each containing approximately 24 geophones, spaced 5 m apart (lines to the north contained 20 to 24 geophones and lines in the centre of the survey contained 24 to 27). 5 m spacing was chosen to ensure a suitable depth of investigation. The first receiver line was numbered 1000 in the south and ran to 25000 to the north. The geophones numbers ran from 1 in the west to 24 in the east. During one day of acquisition, due to limitations imposed by the availability of equipment, only seven of the twenty-five receiver lines were live. The recording equipment therefore had 184 active channels with a sampling rate of 0.25 s with a listening time of 6 s. The seismic source utilized for the survey was a weight drop truck, shown in Fig. 4.2, which used a 300 lb hammer dropped against a metal plate that was on the ground. The efficiency of the energy transfer from the hammer to the ground depended on the plate contact, which primarily depended on the softness of the ground (which was dependent on thickness of vegetation and the soil saturation) as well as on small-scale topography and local obstacles (boulders, trenches and mounds). The frequencies generated by the weight drop varied from 50-800 Hz, depending on the stiffness of the ground, vegetation cover and the composition of the near surface (refractions are composed of high frequencies due to their shallow depth of penetration). Shots were fired between the receiver lines and the shot lines, spaced 5 m, and ran from line 1500 in the south to 25500 in the north. Shots were generally 1-2 m away from the flag points. Shots at each location were stacked four times to ensure good contact between the hammer, plate and ground. With the source and receiver spacing approximately equal (0.5 m variations are expected due to geophone coupling issues and obstacles) the inline and crossline fold of coverage, on average, is approximately 12 meaning each subsurface location is sampled 12 times per recording.

Figure 4.2: *Weight drop truck.*

4.1.2 Data reduction

For each individual shot, the Geometrics unit records all channels and stores them in an FFID file. The FFID files for each day were then converted to a single segy file using seg2segy. This allowed viewing and processing using the Seismic Unix suite of software (SU). For true 3D refraction processing all shots of a single source location were stacked and then seven picks were made for each shot record. Due to time and humanpower constraints, picks were made only for the near and far shots on lines that had high quality unstacked data. There were only a few shots that showed the direct arrivals clearly, so it was decided to average the two best shots and use 750 m/s as our velocity for the top sediments.

To generate travel-time plots shown in Fig. A.4 (Appendix A), the refracted arrivals and direct arrivals need to be picked from the raw shot records. Example shot records for shots 7503 and 7530 are shown in Fig 4.3. The red boxes indicate the positions of shot 7503 and shot 7530 in Figure 4.4 and the green boxes within these highlight the refractions and the direct arrivals. The refractions are highly visible linear events that occur a significant time before any other events are detected.

Each shot record represents 184 live channels (active geophones) that are split into 7 receiver lines (e.g. channels 1-24 represent line 8000, channels 25-48 represent line 9000). For the entire survey over the two weeks, 25 receiver lines were laid across Dead Horse Lake but only seven lines were live for any one day of acquisition. The initial stage of generating a 2D map of depth to bedrock consisted of selecting the shot records that were generated by a shot at the beginning and end of each shot line (which lay directly between each receiver line) and then picking the first breaks for the receiver lines closest to the shot lines, which are represented by one of the seven receiver lines shown in the shot record. Shots at the beginning and end of the lines were chosen to strictly ensure a 2D profile. This generated the refraction profile shown in Fig. A.4 (Appendix A) by combining the updip and downdip pick profiles. Shot 7503 shows the downdip shot record and shot 7530 shows the updip shot record and the picks were made on the first receiver line in the shot record (line 8000) represented by channels 1 to 30. Fig. 4.4 shows the picks made for the 8000 receiver line and represent shot 7503 and 7530 respectively. The picks shown in each figure are colored red and are highly visible linear events in the shot record.

This process was repeated for the majority of the receiver and shot lines thereby acquiring 2D refraction profiles updip and downdip across the whole of Dead Horse Lake. Several lines were not of sufficient quality to reliably pick the first breaks. Poor shot records were caused by poor contact between the hammer drop plate and the ground so that energy could not be efficiently transferred from hammer to ground, consequently meaning low energy compressional waves were generated. Poor contact was caused by soft ground that was either highly saturated with water or covered by thick vegetation. To counteract soft ground, a minimum of two shots were performed at each shot location, the first generally flattening the ground so as to ensure good contact for the second shot. To counteract noise in the records, a series of filters and processing methods were utilized, which are described in Appendix A. Picking

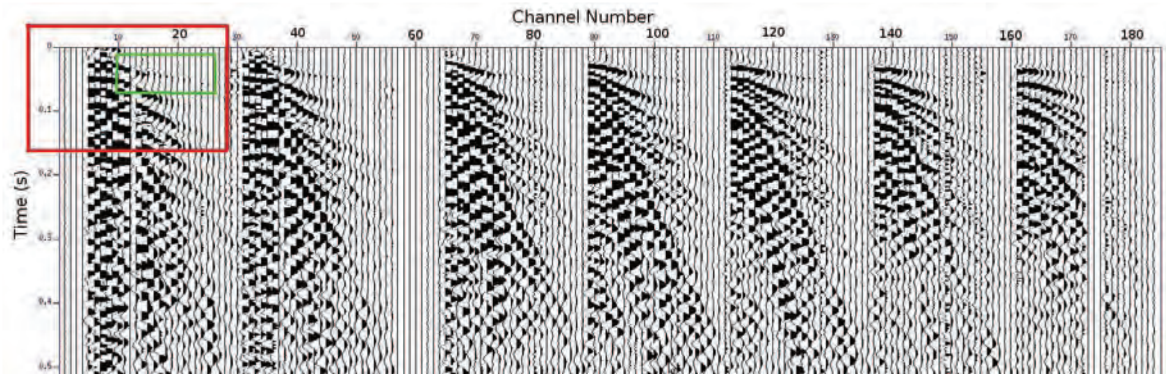

(a) Shot 7503

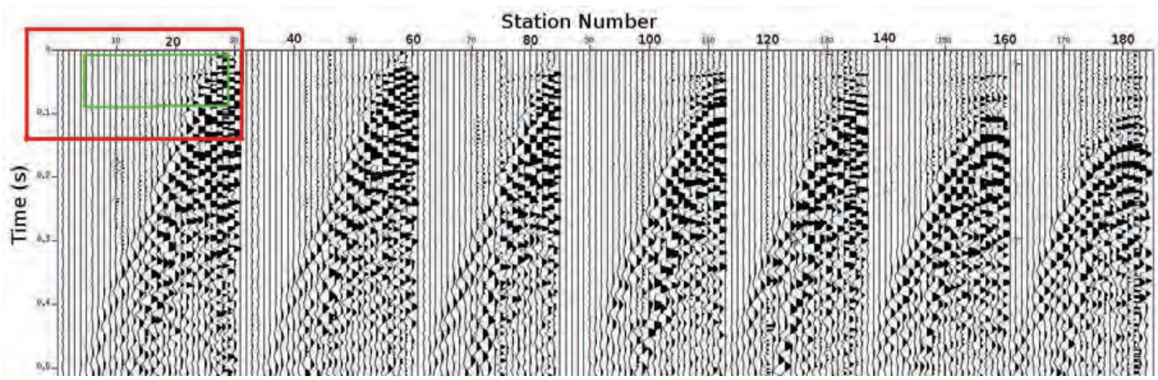

(b) Shot 7530

Figure 4.3: *Shot records for the shot 7503 (left) and 7530 (right). The 7503 shot represents waves that are recorded travelling in an easterly direction and the shot 7530 represents waves travelling in a westerly direction.*

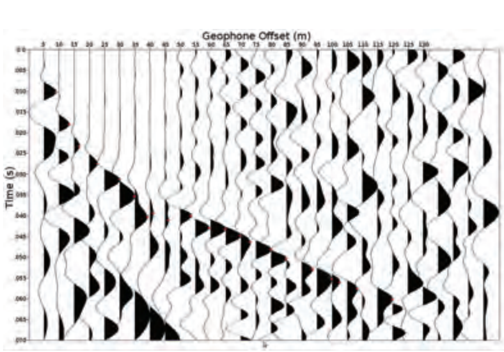

(a) Shot 7503

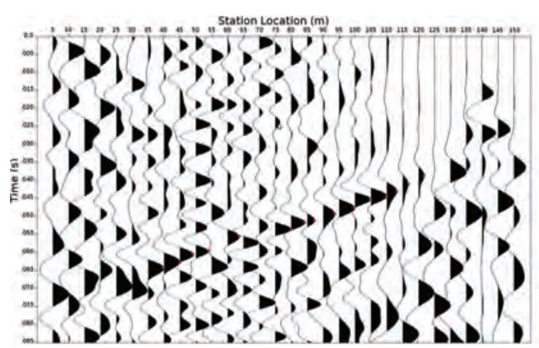

(b) Shot 7530

Figure 4.4: *The shot records 7503 (left) and 7530 (right) for the receiver line 8000 with the picks identified by red dots.*

peaks introduces a systematic error, as the arrival of the refracted waves corresponds to the beginning of the wavelet as opposed to the crest of the peak, but greater accuracy is assured by picking crests. This ultimately means that the arrival of the refracted wave is interpreted as occurring at greater times which does not affect the calculated velocity of the pre-Cambrian granite but means the t_u intercept is greater than the true value which yields greater depths in the calculations (detailed in Appendix A). In total 15 receiver lines were picked with 30 individual refraction profiles.

The refraction events are displayed as peaks, as shown in Fig. 4.4(a) and Fig. 4.4(b), and the pick was made directly on the crest of the peak. A large degree of error is introduced by picking peaks due to the reliability and consistency of picking from trace to trace and across multiple shot records. To assess the reliability and accuracy of picking the peaks, a number of processors picked an individual shot record for one receiver line and the variability of the picks was found, on average, to be $\pm$ 0.003ms. Therefore each individual travel time picked has an associated error of approximately $\pm$0.003ms; this value was later used in error analysis to constraint the precision of the depths to the bedrock. Noise within the shot records introduces uncertainty as it masks the refraction and direct arrival events. Direct arrivals are most susceptible to noise distortion due to the fact they are only detectable on the traces closet to the shot position and the high impact of the hammer drop generates significant ground roll. Electrical cables located close to geophones render these channels unusable and ambient noise sources, including nearby cars and horses also introduce noise that smothers true events. Exacerbating the effect of the noise is the fact that the near-surface is highly variable in terms of its physical properties and its constituent parts which results in appreciable scattering of waves.

Once the first breaks have been picked, travel-time refraction profiles for updip and downdip can be generated. Fig. 4.5 shows the refraction profile for line 8000.

Using the values extracted from the graph (intercept times t_u and t_d; velocities V_1, V_{2d} and V_{2u}) the depth to the bedrock and the dip of the bedrock can be calculated. The detailed theory for calculating these quantities is in Appendix A.

4.1.3 Results & interpretation

Once the dips and depths of the bedrock had been calculated for each receiver line, these quantities were used to construct a 3D map to bedrock, enabling the geometry and topography of the bedrock to be observed over the survey area. To generate the 3D topographic map, an Excel file with updip and downdip depths was created and these depths were then linearly interpolated along the receiver line for points in between these known depths. A Kriging interpolation algorithm was then used to create a grid and created a color shaded contour map using Surfer 8. This was then overlaid onto a map using UTM coordinates which were acquired with both Differential GPS and TDM measurements (Fig. 4.6).

From these results we can see a general 3D trend of the basement rock. The basement is

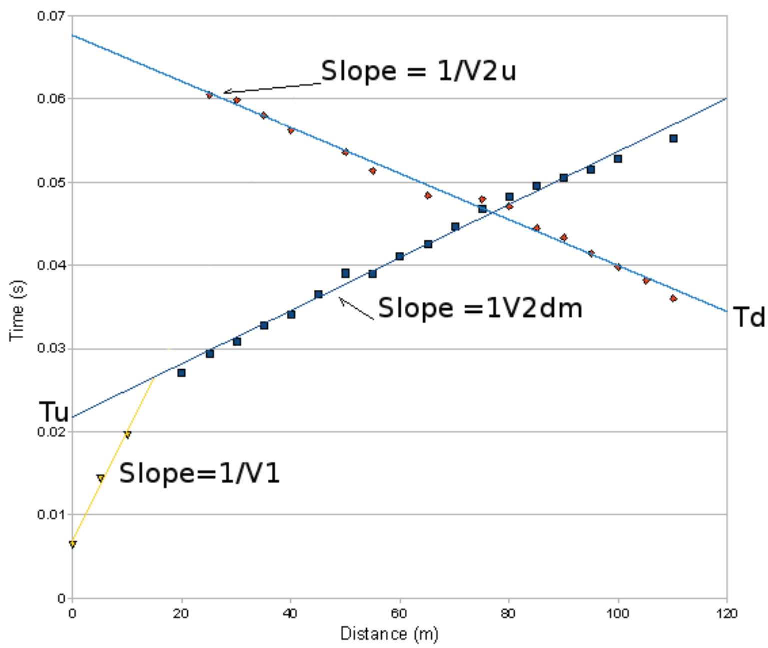

Figure 4.5: *Refraction profile generated by picking the refracted and direct arrivals for the updip and downdip shots along the receiver line 8000. The blue dots represent the arrivals downdip and the red dots represent the arrivals updip. The black lines represent the linear fits made to the refractions and the velocity is equivalent to the inverse of the slope. The intercepts at the beginning and the end of the line are shown by* t_u *and* t_d*.*

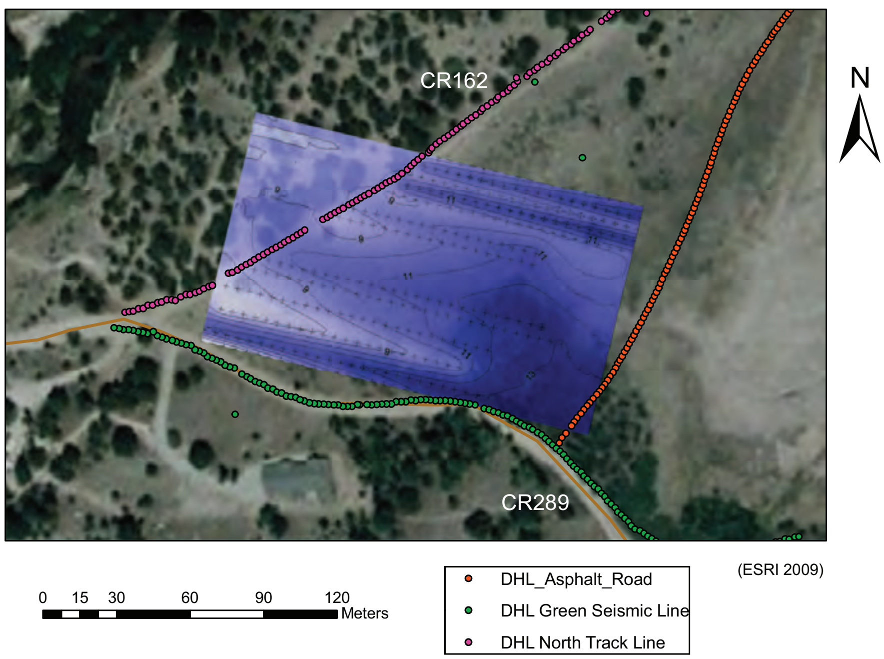

Figure 4.6: *Depth to basement rock from the surface in meters. White denotes shallower basement rock with dark blue representing darker colors. The basement rock appears to be dipping towards the southeast.*

definitely deepening to the southeast. Both the depths and velocities correlate well with other datasets.

Since we are processing a 3D data set as a series of 2D lines we are making some assumptions. We assumed our difficulty in picking breaks on the updip shots was due to soft ground near the lake area. If significant 3D scattering is occurring due to large variations in bedrock geology then this could cause similar effects. If time and people were of no issue we would process this data set as a true 3D refraction survey rather than a series of 2D lines. Although we did use the RAYINVR software to forward model our data sets, no inversions were performed. Refraction surveys are also prone to missing thin layers with small velocity contrasts, although with these survey goals this was not an issue.

4.1.4 Summary & conclusions

The interpretation of the basement rock correlates well with the depth of the basement rock from the migrated shear wave sections. The 2D refraction map displays an overall trend of dipping and deepening towards the southeast which correlates well with the results from shear wave seismic. The average depth to basement to the east is approximately 9 m and the averge depth to basement in the west is approximately 12 m, with an approximate dip of 2 degrees. The weathered granite's velocity was found to be approximately 3300 m/s and the competent granite's velocity is expected to be higher than this, although the two different layers could not be distinguished via refractions. The dip could potentially be related to earlier faulting and regional deformation although futher seismic investigations will be required. There are variations in depth across the bedrock and the surface can therefore be interpreted as being rugose, which suggests a heavily weathered surface. This therefore hints at the possibility of the granite being composed of two dominant parts, a top weathered layer and lower competent layer. The upper weathered layer could be important for local fluid flow in that weathered granite has a greater capacity for fluid storage as well as a greater permeability relative to competent granite ensuring a comparatively efficient flow. With 3D refraction tomography, the two layers of granite may have been resolvable and could potentially have been picked. The possibility of two separate granite layers is supported by the VSP at well MPG-1 which shows a curving reflector which is indicative of a gradational change in the layer's acoustic impedances, which correlates to density and, ultimately, competence.

The lineation apparent in Fig 4.6, running from east to west along the southern edge of the survey area and representing a rise in the pre-Cambrian granite, is potentially indicative of a fault or major fracture. This could be a major control on fluid flow in the area, acting as a conduit for rising hot water or descending cold water. The occurrence of this lineation coincides with a fracture observed in the VSP profile, represented by a diffraction at around 130 m (indicating the position of the fractures base). The occurrence of a major lineation close to well MPG-1 is synonymous with interpretations of the shear-wave line that runs along C209, which display several faults coinciding with the location of the lineation. However, these shear-wave profiles contain a significant number of faults in the granitic bedrock which are not apparent in the 3D profile of the bedrock deduced from refractions. A possible explanation for this is that the throws and heaves of the additional surrounding faults are not as significant as the one generating the lineation which suggests this could be the major controlling fault or fracture in the Dead Horse Lake area. The forward and reverse refraction profiles were only generated for 2D lines, not a 3D grid, so that subtle variations in bedrock depth cannot be detected; if 3D refraction tomography was performed, minor variations in the depth to bedrock could be detected enabling smaller faults and fractures to be mapped. These smaller fractures and faults could be equally as important as the major controlling fracture for the local distribution of water and the total permeability of the surrounding rocks, which is crucial for fluid flow. In conjunction with 3D refraction tomography, deeper penetrating seismic surveys would be useful in determining whether the lineation represents a fault or fracture. This is important because a fracture would be acting just as a conduit for flow (fractures are generally smaller-scale features), whereas a fault (a deeper penetrating horizontal and lateral movement in the rock unit) would be acting as the source of the water from deeper in the subsurface. Determining the depth of penetration of this fault could provide useful information on the local and possibly regional circulatory cycle of water and its movement channels.

The presence of cross-dip means that the major underlying assumption of the analysis (dip in one direction) is compromised so that the recorded refractions, instead of representing head waves travelling in 2D, actually represent head waves travelling in 3D. This means that plotting forward and reverse profiles to calculate time intercepts and inverse gradients is an imprecise method in a 2D sense, and 3D would have been more appropriate. The errors introduced by picking 3D lines two dimensionally cannot be quantified without comparison with results from 3D refraction tomography.

4.2 Vertical seismic profiling

Well MPG-1 was drilled in 2009 at Dead Horse Lake (Fig. 4.7). A vertical seismic profile was acquired here in 2010 to investigate local p-wave and s-wave velocities in the shallow subsurface using a 3-component (3C) geophone. This information was incorporated into the reduction of the 2D near surface seismic survey data acquired over Dead Horse Lake. Data was also acquired at MPG-1 in 2009 using a hydrophone instead of a 3C geophone.

4.2.1 Acquisition

One zero-offset profile and three walkaway profiles were acquired at MPG-1. The seismic wavefield was produced by a hammer striking a metal plate on the ground and was then measured by a 3C geophone at depth in the borehole (Fig. 4.8). Data was acquired in both compressional and directional shear wave modes for each profile.

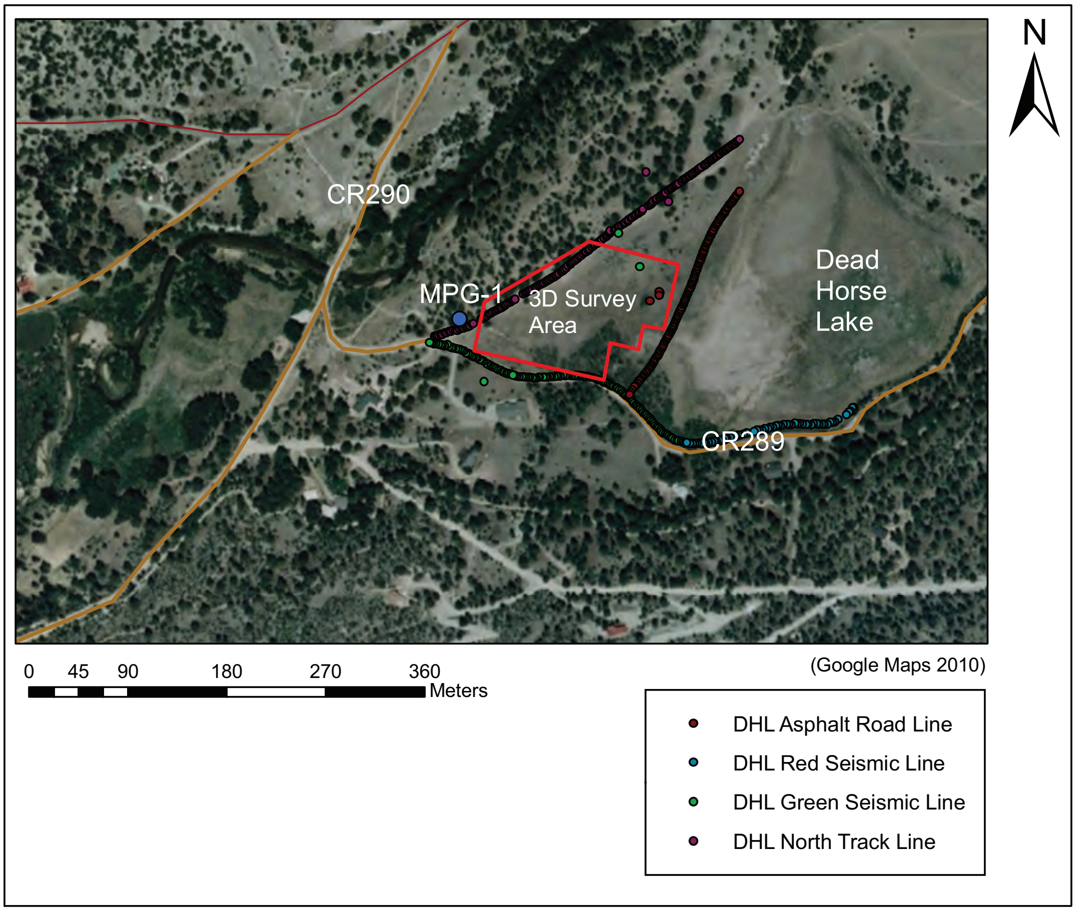

Figure 4.7: *Location map of Dead Horse Lake, Chaffee County*

Figure 4.8: *Vertical seismic profiling equipment.*

In the zero-offset configuration (Fig. 4.9) data, 64 measurements were taken between depths of 85.0 m and 64.5 m. Measurements were taken at every 0.25 m increment within this interval. Shear-wave energy was input from four directions corresponding to the four compass points. Each set of measurements for a source were repeated twice.

For the walkaway profiles (Fig. 4.10), 20 measurements were taken between offsets of 0 m and 20 m with 1 m increments. Data was acquired in NE, N and SE directions. The number of directions in which data was acquired was limited by nearby trees. The depth of the 3C geophone was kept constant at 84 m.

Parameter	Zero offset	Walkaway
Source	Hammer	Hammer
Maximum offset	1m	20m
Depth range	64.5-85m	84m
Source spacing	0m	1m
Receiver spacing	0.25m	0m
Azimuths	N/A	N, NW and SE
Number of measurements	64	20

Table 4.1: *Vertical seismic profile acquisition parameters at well MPG-1.*

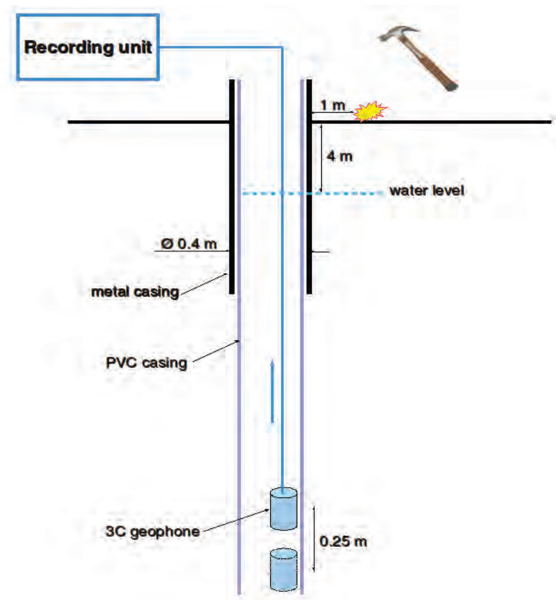

Figure 4.9: *Schematic diagram showing the configuration for zero-offset vertical seismic profiling.*

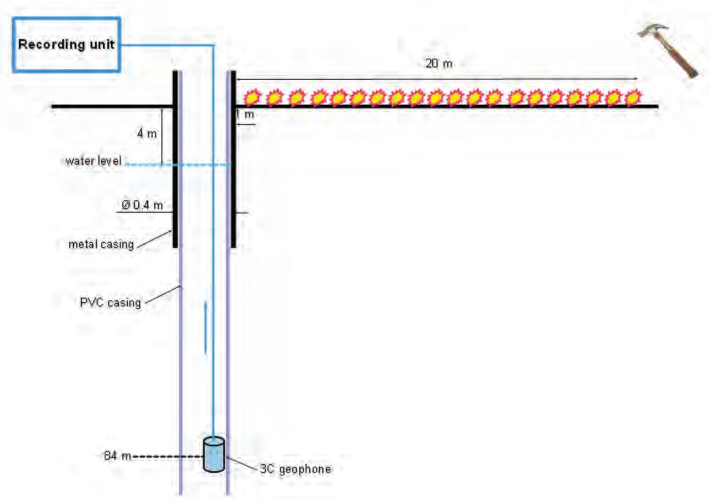

Figure 4.10: *Schematic diagram showing the configuration for walkaway vertical seismic profiling.*

4.2.2 Data Reduction

Observer logs recorded during survey acquisition and VSP records were used to identify and eliminate erroneous traces containing amplitude spikes, artifacts, etc. Traces were sorted into common geophone component VSP records and repeat measurements taken at each depth increment were summed to attenuate random noise. For more detailed information on the processing of the VSP data please refer to Appendix D.

4.2.3 Results & interpretation

Using the processed VSP gathers it was possible to extract subsurface velocities by picking the first dominant amplitude event on each trace which is expected to correspond to the downgoing wave. An example of the downgoing wave picks for a zero-offset primary wave source recorded using the primary wave geophone component is shown in Fig. 4.11. Picking the down going shear-waves was particularly challenging as the direct arrivals were irregularly located on adjacent traces and led to a significant spread of data which is reflected by the low correlation coefficient.

Downgoing wave picks were then plotted in MS Excel and a linear regression was fitted. Table 4.2 displays the calculated velocities of direct arrivals between 70-85 m of depth in the borehole. Difficulties in determining the precise time of the direct arrival has resulted in ambiguity in calculating the gradient of a suitable regression line. Obvious outliers which were inconsistent with the overall trend were removed, increasing the correlation coefficient. However, we still estimate a significant error bar on the calculated velocity values because of the very low correlation that was obtained for both the primary wave and shear wave velocities.

VSP configuration	Geophone component	Velocity (ms^{-1})	Correlation coefficient
Zero offset	V_p	1300	0.48
Zero offset	V_s	600	0.12

Table 4.2: *Direct arrival results from the 2010 Dead Horse Lake VSP survey.*

4.2.4 Summary & conclusions

The velocities obtained from the 2010 VSP survey are significantly lower than that predicted from other geophysical techniques, particularly refraction tomography. Results from Line 4000 on the refraction tomography analysis indicates a primary wave velocity of 3170 m/s at a depth of 6.95 m. At this shallow depth, this velocity is interpreted to be associated with basement granite or possibly a transitional zone of weathered granite.

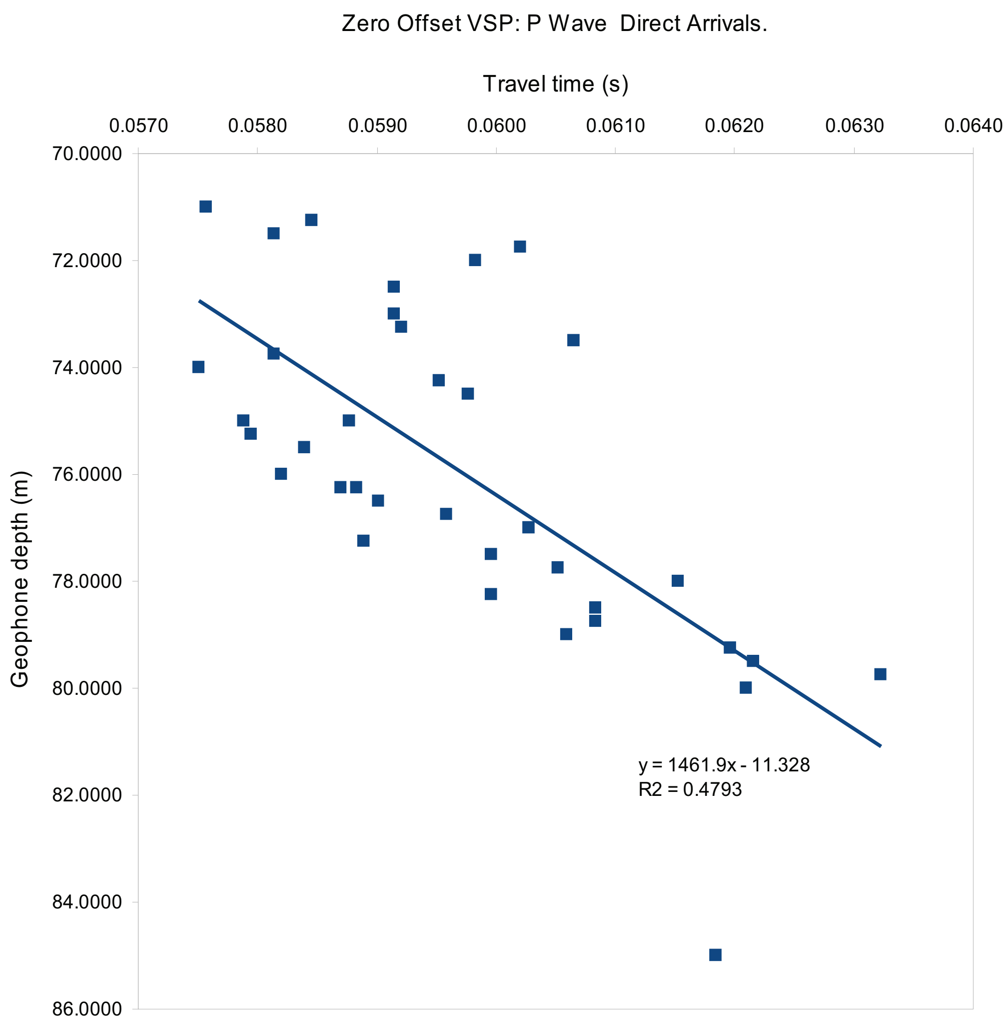

Figure 4.11: *Direct arrivals for a zero offset VSP survey acquired at well MPG-1.*

Extrapolation of velocities from refraction tomography suggest that the velocity at depths around 50-100 m will be in the range of 4000-5000 m/s. At this depth the 2010 VSP survey acquired in borehole MPG-1 indicates velocities of approximately 1300 m/s. Assuming granite velocities obtained from refraction tomography, it is expected that the downgoing wave will arrive at approximately 0.03 s on the VSP display. Fig. 4.11 indicates that the downgoing arrivals occur at approximately 0.06 seconds.

This inconsistency between the velocities and expected arrival times indicates that the VSP survey has not recorded the downgoing wave through the formation. An alternative possibility is that the amplitudes from downgoing waves traveling through the granite are outside the dynamic range of the recording system. The velocity and arrival times are consistent with that of tube waves which travel along the PVC well casing. The borehole environment is thought to have produced poor coupling between geophone and rock which has lead to the inability of the geophone to accurately record particle motion.

As the 2010 VSP survey did not accurately record the downgoing wave field, this year's VSP results are considered inaccurate and have not been used for the processing of the Dead Horse Lake seismic lines. The zero offset 2009 VSP survey was reinterpreted as the hydrophone had accurately recorded the down going p-waves. The recording of direct arrivals by the hydrophone and not by the geophone is thought to be because the hydrophone was not directly coupled to the PVC tubing and consequently was not effected by tube waves. An uninterpreted zero-offset VSP record is shown in Fig. 4.12(a) and an interpreted version is shown in Fig. 4.12(b).

The first 48 m of the VSP is dominated by a 5500 m/s, strong amplitude, direct arrival which is interpreted to represent the steel casing (red line). The diffraction pattern with apex at 48 m depth is associated with seismic energy being scattered off the steel casing base. The steeply dipping, high amplitude direct arrival (blue line) has a velocity of 1500 m/s and is interpreted to represent energy traveling through the water column within the bore hole.

The very low amplitude direct arrival (yellow line) which arrives before the water column arrival is interpreted to have a curved trajectory with a velocity which increases from 2500 m/s at shallow depths to 5000 m/s. This low amplitude event is interpreted to represent the direct arrival from the granite basement and the increase in velocity with depth is interpreted to reflect a transitional zone between a lower velocity weathered layer in the shallow surface and then increased velocity in the unaltered layer. The direct arrival from the steel casing and the associated diffraction pattern have obscured the direct arrival from the basement granite in the upper 48 m. This shadow zone beneath the steel casing has resulted in an accurate velocity profile not being determined through this zone. This is undesirable as the focus area of the Dead Horse Lake shallow surface seismic survey is within this shadow zone depth.

Associated within the unaltered granite basement is a second diffraction pattern which has an apex at 150 m depth. This diffraction is interpreted to represent energy being scattered off a fracture zone which the well has intersected. The interpretation of a fracture is consistent with an increase in drilling rate, as the drill bit passes through less competent material and,

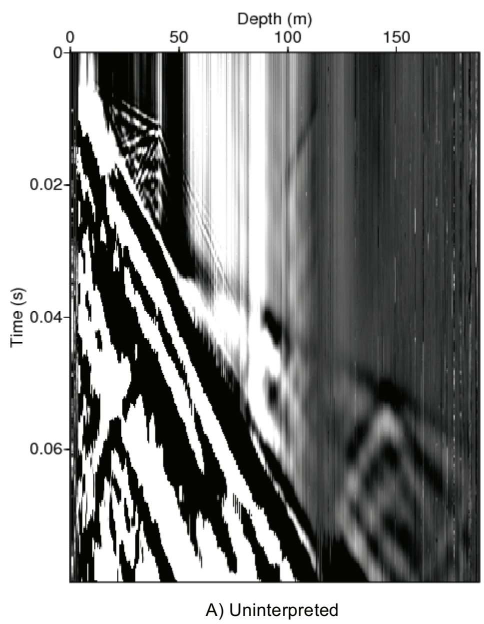

(a) Uninterpreted.

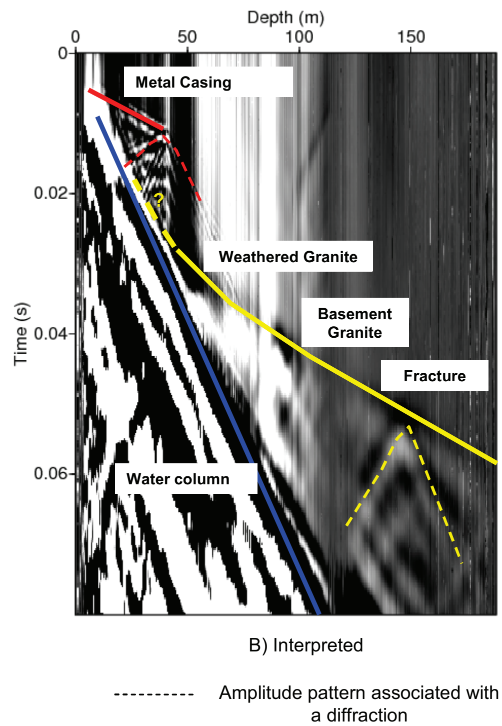

(b) Uninterpreted.

Figure 4.12: *Interpreted and uninterpreted zero-offset VSP record.*

also, an increase in fluid pressure.

In 2010 the water table was measured during the survey to be 4 m. This is unchanged from the water table measured during the 2009 field camp.

4.3 Shear wave seismic survey

Dead Horse Lake is a dry lake bed lying in the transition zone of the offset faults of Mt. Antero and Mt. Princeton. The shallow subsurface is characterized by a geothermal gradient that is high in the western region of the lake, and corresponds to hot water springs at the surface. Variations in water temperature have been observed from well studies with a gradational increase from west to east until the center of the lake is reached. An abrupt change in temperature then occurs with a north-south trending strike through the lake's center; with cold water wells to the east. The change in measured temperatures has been interpreted to be due to an underlying fault system that may be controlling hydrothermal flow which makes Dead Horse Lake ideal for subsurface studies using geophysical methods.

Several geophysical methods were used with the aim of understanding the faulting regime and their influence on hydrothermal flow. These include DC resistivity, gravity, magnetic and seismic methods (VSP, weight drop, and shear-wave seismic). Recent studies using the shear wave seismic method have shown that in the shallow subsurface, an increase in resolution is observed over p-wave seismic records. Understanding the subsurface is vital, as it will provide insight into the nature of temperature compartmentalization in the Dead Horse Lake region.

The depth of investigation at Dead Horse Lake is approximately 80 m over three 2D lines with lateral extents of approximately 250 m. Geophones oriented in the transverse direction took measurements of SH waves, while the source (the Minivib) is also oriented in the transverse direction. The flat surface and isolated location make the area ideal for seismic surveys with the ground providing good geophone coupling.

Shear-wave seismic studies measure energy propagating transversely to the direction of propagation. P-S wave velocity ratios are typically between 2 and 3, although highly fractured or poorly consolidated material can cause this ratio to be higher. The advantage of measuring the shear-wave component is the $(\nu) = f(\lambda)$ relationship, in which the slower velocity for an input source will result in a smaller wavelength. This is especially useful in solving static problems when imaging unconsolidated sediments in land data as the wavelength characteristic of shear waves produces a higher resolution stack than p-waves (see [32] and [31] for stacked data comparisons of P, SV, & SH components). The smaller wavelength of shear-waves also means a greater rate of attenuation, although this is generally not an issue for shallow subsurface studies.

Shear waves can be polarized into vertical (SV) and horizontal (SH) waves (shear-wave splitting), where SV waves are of higher frequency than SH data. The frequency differentiation between vertical and horizontal wave motion reflections may be related with different absorp-

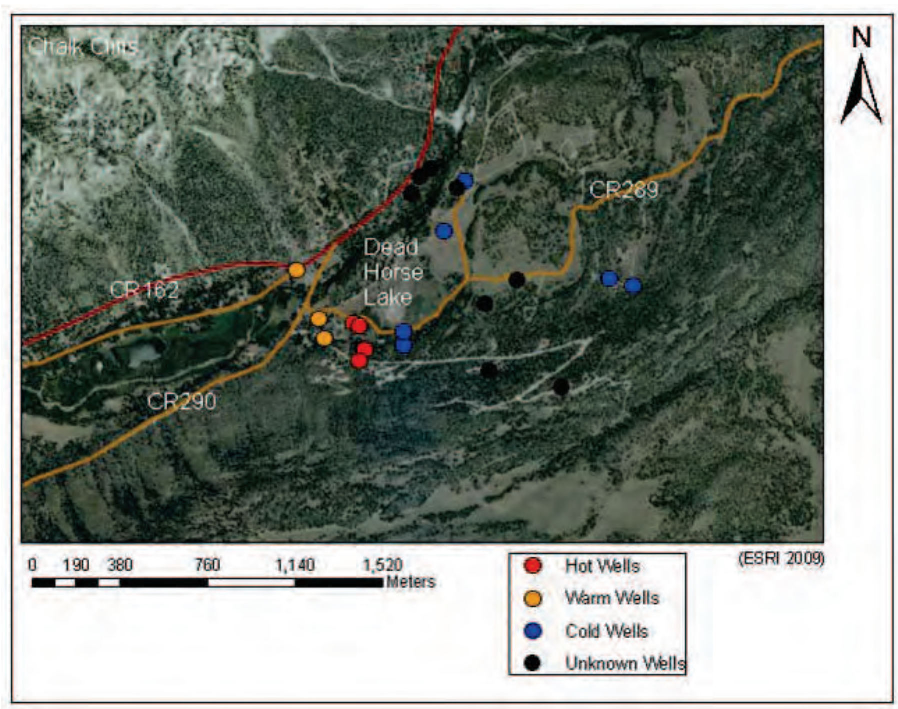

Figure 4.13: *Map of Dead Horse Lake with well locations including the temperature regime.*

tion factors [32]. 9C 3D seismic data have been typically processed with the aim of getting information on vertical cracks, fractures etc. which comes under the general term azimuthal anisotropy [35]. Anisotropy is an encompassing term for the velocity variation with direction (refer to [38] & [21] for an overview) in the subsurface and provides useful information on fracture orientation. The inferred fault from well information in Dead Horse Lake and the seismic study will help to identify the fault direction and may provide explanations for the compartmentalization of hot and cold wells.

One problem that may be encountered when studying the effects of anisotropy at Dead Horse Lake is if there is no recorded reflection of composite (basement) below the altered granite. This may be due to a lack of depth in the investigation or the fact that there is no sharp impedance contrast between the two rock types. The fracture state of the altered granite will produce anisotropic effects that will be useful in characterising the stacks of different components of shear-waves.

Studies using VSP data [2] have shown that velocities through regions saturated with cold water give higher velocities than those saturated with hot water. Thus along the proposed survey lines there is expected to be an increase in velocity in the eastern region of Dead Horse Lake. On the larger, geological scale, another important reason for looking at the subsurface faulting regime is the transition zone. The nature of the zone between the Mt. Princeton and Mt. Antero faults is still unknown with the type of faulting system postulated to be one of shear, tear or ramp configurations. Sediment in the Dead Horse Lake is made up of Pleistocene glacial moraines with varying depths, although they are typically on the scale of 6-15 m.

4.3.1 Acquisition

Three shear wave seismic lines were acquired at Dead Horse Lake, Lines 1 and 3 follow the road paths on the lake's periphery and have a general direction trending E-W. Line 2 trends N-S and lies parallel to the hot-cold well separation which, given the information already known, will provide a profile along the strike of the inferred fault system. Figure 4.2 shows the three lines. Data were acquired using a Minivib source and recorded using 3C geophones in the transverse direction (measuring SH waves).

The recorded data has been reformatted from the original SEG-2 to SEG-Y format, and the record length re-sampled from 1500 ms to 1000 ms. A high-pass, band-pass filter (30Hz) has been applied to reduce the effects of ground roll and the air wave.

4.3.2 Data reduction

A single processing flow, depicted in Fig. 4.15 was developed and used to process the 3 seismic lines. Quality checks are carried out consistently to ensure that no errors were encountered and the ideal result is obtained. The processing flow was carried out using

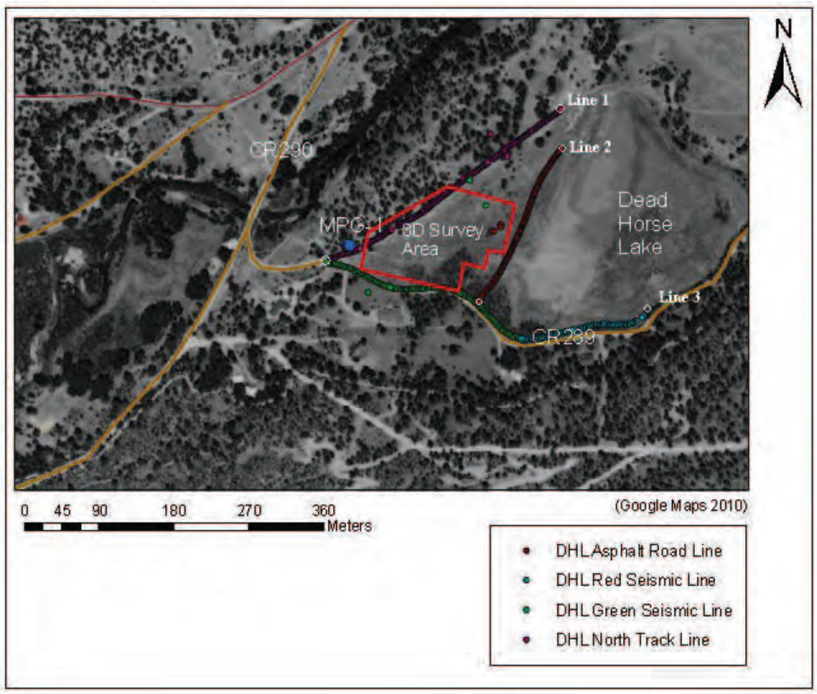

Figure 4.14: *Location Map of Dead Horse Lake. Shear wave seismic were measured along Lines 1-3. Also shown is the line for the 3D weight drop survey and points representing well locations for the VSP survey. The Dead Horse Lake Red Seismic Line is an extension of the Green Seismic Line and together comprises Line 3.*

Measurement direction	transverse (SH)
Source direction	transverse
Survey type	rollover
Source type	minivib
Sweep	7s, 30-300Hz, upsweep
Length of sweep	1400ms
Channels	120
Receiver spacing	2m
Shotpoint interval	4m
Bin size	1m
Geophone frequency	40Hz
Fold	29.75
Receiver type	9C geophones, 40Hz
Recording format	SEG-2
Recording system	Stratorvisor
Sample interval	500ms
Record length	1500ms

Table 4.3: *Acquisition parameters for the shear wave seismic survey taken over Dead Horse Lake.*

Parameter	Line 1	Line 2	Line 3
Acquisition Date	5/24/2010	5/23/2010	5/25/2010
Line orientation	E-W	N-S	E-W
Near offset	26m	26m	26m
Far offset	294m	262m	296m
Flag number convention	1101-1235	1001-1119	3001-3136

Table 4.4: *Line specific acquisition parameters for the shear wave seismic survey taken over Dead Horse Lake.*

ProMAX. The initial processing flow was initiated by defining the geometry according to the true topographical layout of each survey line. This was done in order to allow consistent processing algorithms to be applied to the collected raw data. The geometry was created by locating UTM coordinates using information from GPS surveys (TDM) and observer's logs. The processing flow then continues with converting the raw data from SEG-2 to SEG-Y, then reading this file into ProMAX. After data formatting, vibroseis fundamental ground force (FGF) correlation (see Appendix I for theory) was carried out to ensure the improvement in signal-to-random-noise-ratio for changes in vibrator parameters [17] and input geometry is then applied to the correlated data.

For seismic Lines 2 and 3, phase rotations were applied to the seismic data in order to suppress the p-wave. Two sweeps of opposite initial sweeping direction were applied to the data which created two shot gathers with 180 degree phase difference for the s-wave at each source station, although the p-wave has the same phase in both sweeps. Phase rotation of 180 degrees was then carried out in one of the sweeps so that the shear wave components have the same phase, whereas the primary wave components are out of phase. Stacking the two shot gathers will enhance the S-wave signal and suppress the p-wave. Another quality control that was carried out is trace editing whereby trace muting and shots removal are applied, since bad shots can contribute to erroneous results. Conversely, removing this information also leads to spatial aliasing once filters are applied.

A band-pass filter was used in an attempt to enhance signal, however, amplitudes beyond -40dB do not contribute to useful readings; these signals are mainly of low frequencies within 150 Hz. It was also observed that the decrease in power spectrum indicates a decrease in the amplitude or signal which also implies attenuation (See more in Appendix I). This tells us that the high frequency filter may not be applicable to this data since the main signals are more or less than 150 Hz. To confirm the confinement of the low frequency signals, a number of filter panels and parameters were analysed and applied with the optimal filter found to be 20-30-120-240 Hz.

The next step was to apply an elevation static correction with the aim of correcting for the effect of variations in elevation between source and receivers across the survey lines. The correction depends on the location of respective seismic line which can be referred to the geometry dataset. A brute stack was generated after completing the above processes; this stack aims to provide early observations and interpretations along each survey line and a priori information on how the final stack will look. Constant velocity stack analysis was used to study about the velocity variations of the data. A few panels of different velocities ranging from 200 to 900 m/s were generated to determine the optimal stacking velocity. It was observed that the velocities exceeding 900 m/s did not contribute to any improvement to the data.

In order to establish the most favorable velocities for the Normal Moveout (NMO) of seismic traces, velocities were picked using a combination of semblance and CVA methods at increments of 21 CDP (21 m) for Lines 2 and 3 and 11 CDP (11 m) for Line 1 to create a velocity model. However, the velocity model generated is not used in this project due to migration

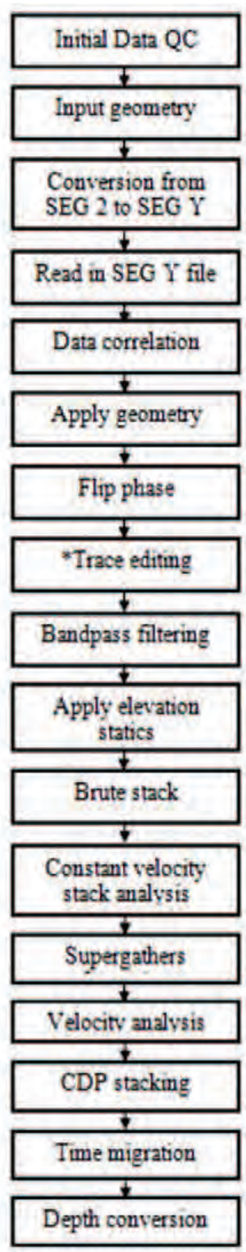

Figure 4.15: *Processing flows for shear-wave seismic Lines 1-3. See Appendix I for detailed steps of the processing flow.*

issues (poorly migrated stacks) and time constraints. Therefore, constant velocities of 200 m/s were used instead for the NMO correction for all seismic lines. CDP stacking is then performed to stack the traces and to boost the signal to noise amplitude ratio. Gazdag phase shift migration and a subsequent depth conversion were applied to the data using a constant interval velocity of 200 m/s.

4.3.3 Results & interpretation

4.3.3.1 Weight drop survey interpretation

In addition to the shear seismic surveys along Lines 1-3, a 2-D weight drop line was acquired on the eastern extremity of Line 3 towards the road intersection of CO289 and CO289A (see Fig. 4.16). The line has not been corrected for statics and has had minimal processing to reduce the effects of noise. To the east of the profile (right of image) a static corrected image will show an uplift of the reflection at 60 ms due to the topography of the surface. The west of the line shows a similar profile to the NE and E sections of Lines 1 and 2 respectively, of the shear-wave seismic survey. The sediments and profile up to 100 ms (maximum depth of investigation of the shear-wave survey) are highly fractured, although caution must be taken when interpreting this line as a static correction could reveal this upper impedance boundary (60 ms) to be a continuous reflector.

4.3.3.2 Interpretation of line 1

In the final stack of Line 1 as shown in Fig. 4.17 and the interpreted section in Fig. 4.18, a 60 degree north-east dipping fault is observed at approximately CDP 2315- 2332. This observation is in agreement with the collected gravity and magnetic data (a prominent magnetic high is observed). The dipping of the fault decreases with depth, however its continuity suggested that this particular fault is deeper than is observed. The presence of this east dipping fault serves as a partition in the mid section of the basin which separates the sediments moving from south-west towards north-east of the line. A series of normal faults are present in this line which characterizes the extensional feature of the transfer zone. The fractured zone also represents a tie with Line 2 to the north which also contains the fractured zone. The main fault towards the center of the section, where there is the separation of cold and hot wells, is also shown in Line 3 and could represent the same fault.

Located at CDP 2400-2405 is yet another 80 degree north-east dipping fault which extends at seismic Line 2. Moreover, complications of data are also monitored at the north-east end of the seismic line which is postulated to be noise or heavily fractured zones. Overlying the granite basement formation in Fig. 4.18 (blue horizon), is postulated to be weathered sediments and glacial moraines and transported alluvial deposits. This suggestion is based on the results from the velocity analysis carried out in the processing section, estimated to be about 200 m/s. Moreover, this observed phenomenon is more astutely explained by Line

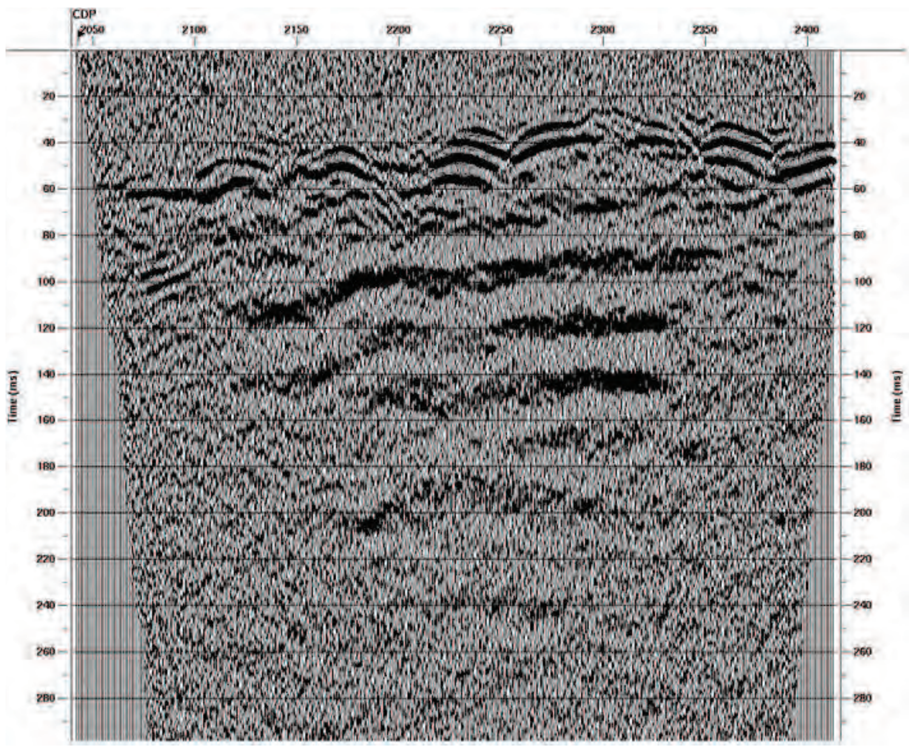

Figure 4.16: *Weight drop seismic performed partly along shear wave seismic Line 3. West is located to the left of the profile, and east to the right. The section remains uncorrected for statics and thus elevations of reflections may be misleading. The east side of the profile has raised topography which will shift up the reflections once corrected. For line location see Fig. 4.14.*

2. The horizon in the seismic section shows a slight dip to the east and the horizon is not interpolated completely, particularly on the far left and right side due to complications of data.

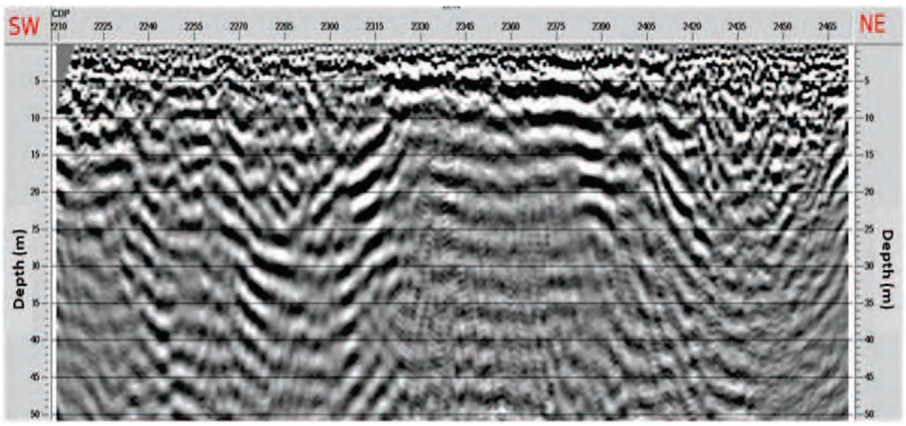

Figure 4.17: *SH wave post-stack time-migrated image for Line 1. The stack was migrated using Gazdag phase shift migration with a constant velocity. The resulting migrated image was depth converted with the final image giving an aspect ratio of the image is 1:2.*

4.3.3.3 Interpretation of the line 2

According to the shot gather depicted in Fig. 4.19, the first main reflection has a velocity around 200 m/s. It is assumed that there are no significant velocity changes in the zone of interest, which is located at upper part of the field. Interpretation was performed on the seismic section which was post-stack migrated with a constant velocity of 200 m/s.

Highlighted in blue in Fig. 4.21 is the non-continuous main reflector, which is proposed to be the Precambrian bed rock, dipping toward the South. This reflector is clearly distinguished due to its strong reflection and homogeneous composition of very dense and crystalline rocks. A series of folds are also observed approximately around CDP 2152 and 2022 where the reflector disappears. Fault networks (marked as red line in Fig. 4.21) are also seen in the Northern part of the seismic data.

4.3.3.4 Interpretation of Line 3

The blue reflector in Fig. 4.23 is suggested to be the top of the Precambrian granite bed rock which is dipping towards east. This is in agreement with the observation in Line 1. In addition, a network of faults is distributed along the interpreted reflector. Located to the west of the line, the granite horizon appears to be discontinuous possibly representing a region in which the rock has been severely eroded. The fault network towards the center of the line

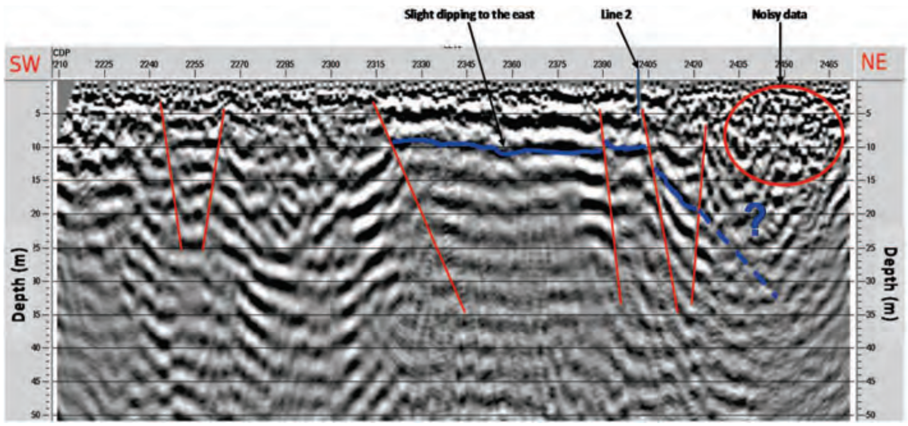

Figure 4.18: *Geological interpretation of Line 1 at DHL. The NE of the line is heavily fractured, see also the N of Line 2 for the fractured zone. There is a prominent fault towards the center of the section which indicates the separation of cold and hot wells.*

could represent a tie with line 1 which explains the hydrothermal segregation in the Dead Horse Lake region.

As mentioned earlier, the main reflector in the seismic section of Line 2 is dipping south which means we expect to observe a deeper layer towards the south. This result agrees well with the observations from the seismic section of Line 1 and 3 where the dipping layer in Line 1 is deeper compared to that in Line 3.

4.3.4 Summary & conclusions

The most obvious observation concluded from the shear-wave seismic is the dipping of the altered granite, mainly to the east and south, which is illustrated in Figs. 4.24 and 4.25. The water table was measured at 4 m in well MPG-1 by VSP and shallows to the east. In addition to that, results show that the altered granite layer deepens to the east. The fractures observed in the shear-wave seismic section illustrated in Figs. 4.24 and 4.25 support the Dead Horse Lake shear zone theory where they separate the hot and cold water locations (Fig. 4.13). Moreover, the major fractures that separate the hot and cold water are not visible in the N-S cross-section (Fig. 4.25) as they cut through the section. In terms of the faulting, the main direction of the normal faults in this survey area is dipping from west to east and the dip is approximately 60 degree. To the east of the cross-section (Fig. 4.24), there is a major normal fault with the start of our interpreted drop-off basement that is observed from the deep seismic section from previous report [1].

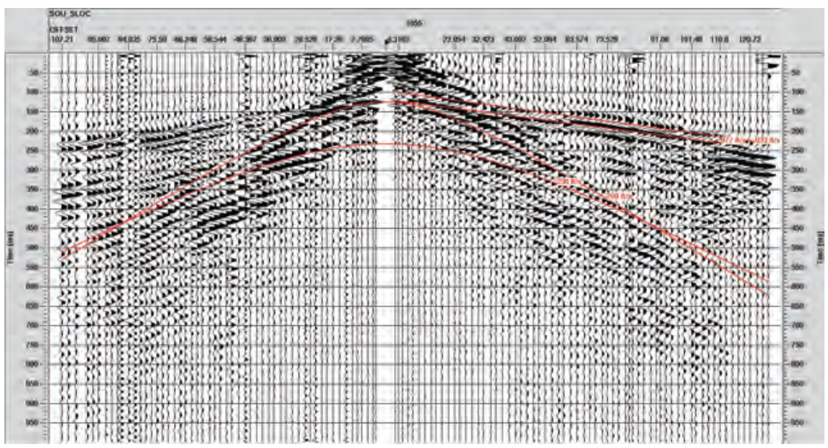

Figure 4.19: *Shot gathers for Line 2. The refraction velocity (flat arrival) is measured to be 900 m/s while the slower reflections are estimated to be between 208 m/s and 236 m/s. The reflected arrivals may be chosen on multiples although the general velocity for both is similar.*

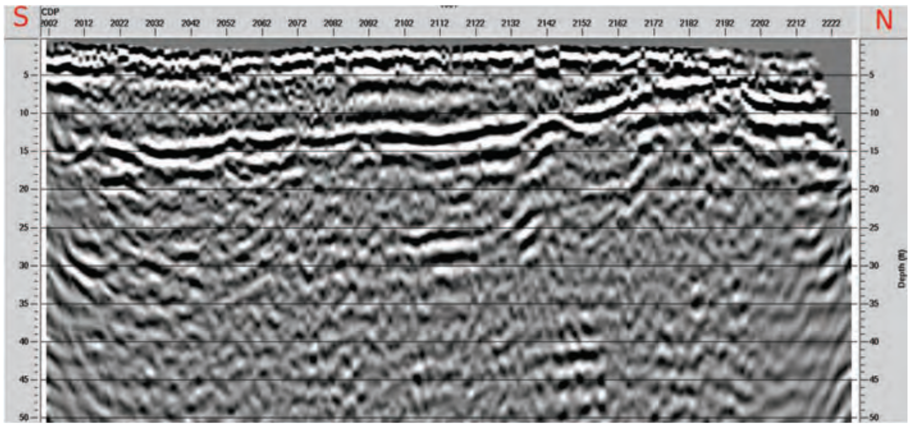

Figure 4.20: *SH wave post-stack time-migrated image for Line 2. The stack was migrated using Gazdag phase shift migration with a constant velocity. The resulting migrated image was depth converted with the final image giving an aspect ratio of the image is 1:2.*

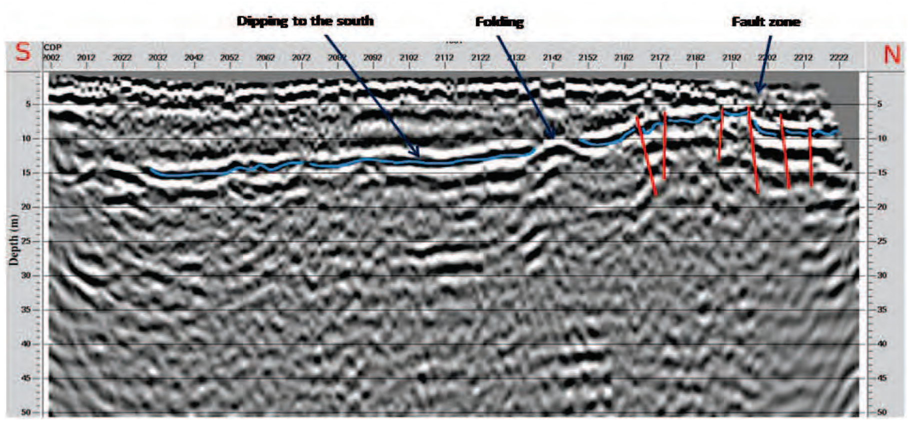

Figure 4.21: *Geological interpretation of Line 2 at DHL. The main fractured region is to the north of the line. The granite reflector is relatively continuous up until this point. See also the NE interpretation of Line 1 for the fractured zone.*

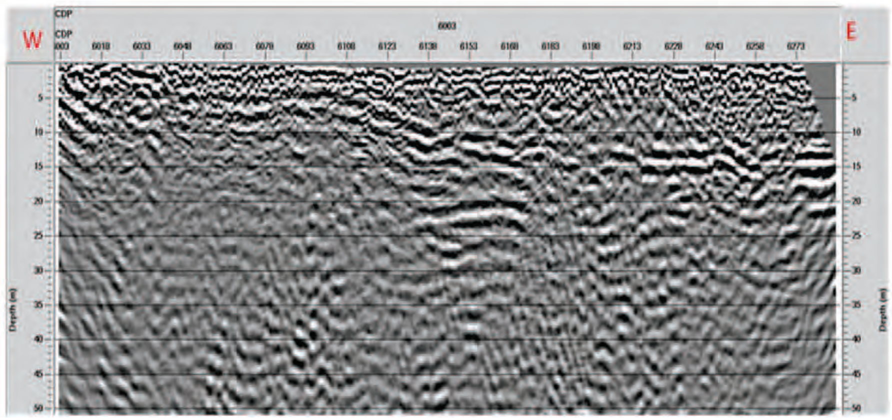

Figure 4.22: *SH wave post-stack time-migrated image for Line 3. The stack was migrated using Gazdag phase shift migration with a constant velocity. The resulting migrated image was depth converted with the final image giving an aspect ratio of the image is 1:2.*

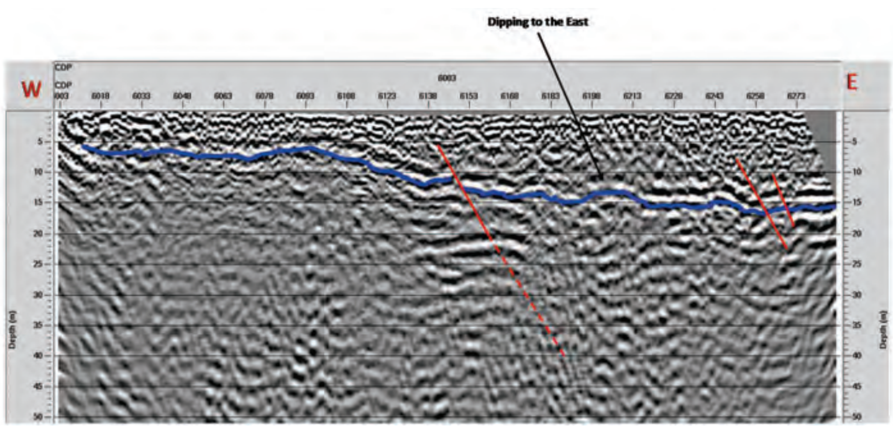

Figure 4.23: *Geological interpretation of Line 3.*

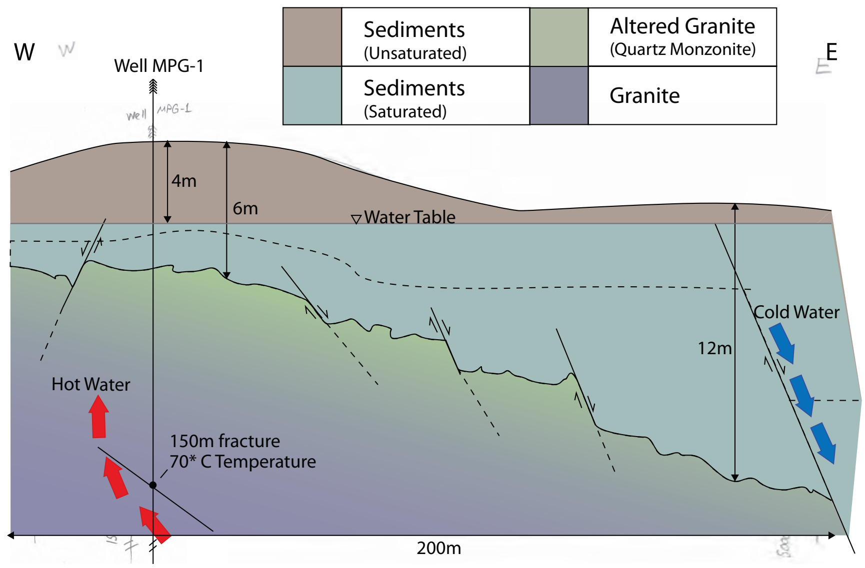

Figure 4.24: *W-E interpreted summary based on results from shear wave seismic, VSP and refraction studies.*

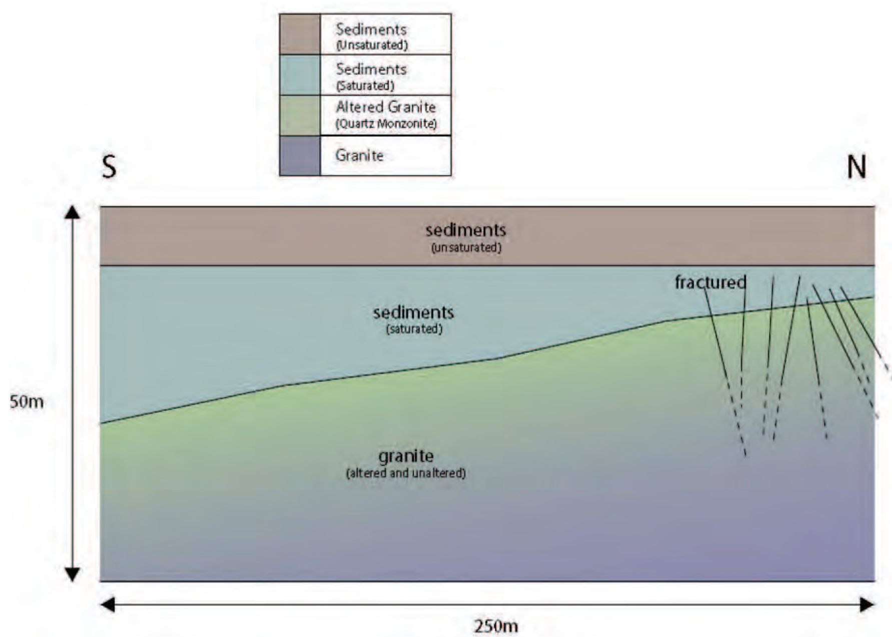

Figure 4.25: *S-N interpreted summary based on results from shear wave seismic, VSP and refraction studies.*

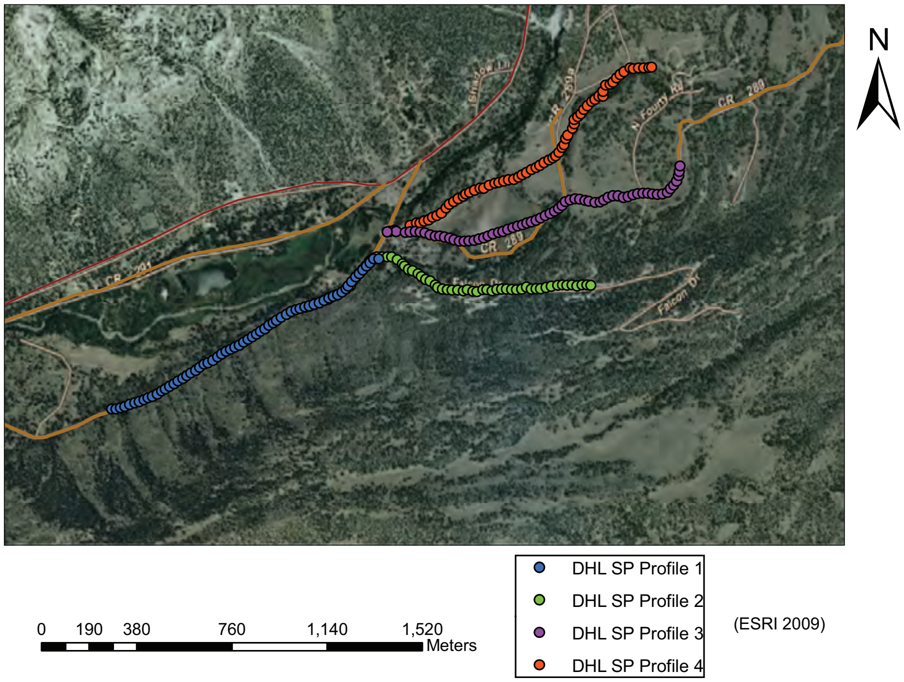

Figure 4.26: *Location of the SP lines in the Dead Horse Lake area.*

4.4 Resistivity & self potential

Due to the close proximity to the Mount Princeton hot springs and the Chalk Cliffs, this area is known to have geothermal water movement. The ABEM and self-potential methods were used to observe locations of water flow as well as the faults used for fluid transport.

4.4.1 Acquisition

Four ABEM Wenner arrays were accompanied by self-potential lines in the Dead Horse Lake area (Fig. F.3.6). Each line had 64 electrodes spaced 20m apart, with the total line spanning 1260 m.

4.4.2 Results & interpretation

In Fig. 4.27 line 1 displays a sharp contrast between conductive sediments and highly resistive quartz monzonite. This discontinuity is caused by the proposed in the fault. There is also noticeable resistive material on the surface. It is know this is glacial moraine caused by a number of ice ages during the Pleistocene.

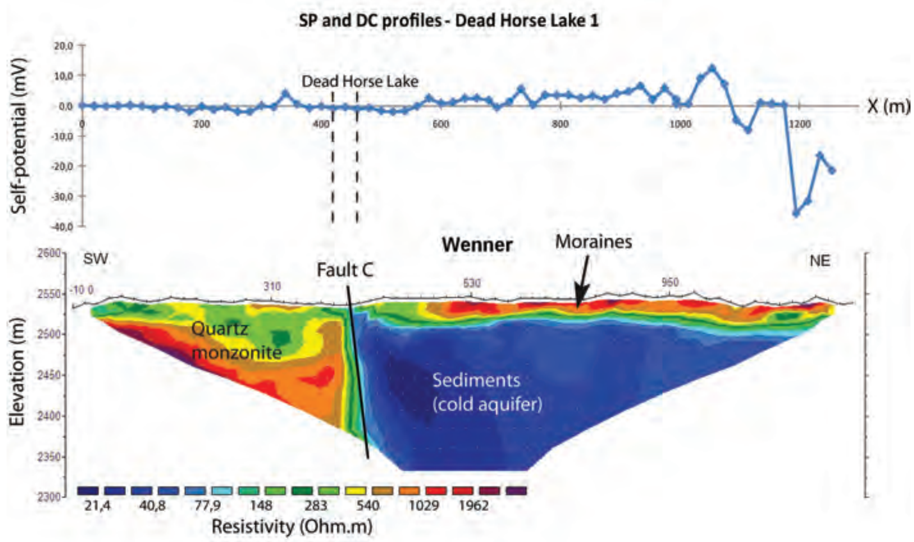

Figure 4.27: *SP and DC resistivity profile acquired along line 1.*

Line 2 runs perpendicular to line 1 and correlates with the data shown in Fig. 4.27. Fig. 4.28 shows that the fault distinguishes between conductive sediments and resistive quartz monzonite.

Line 3 is located north of the fault, which is apparent in Fig. 4.29. In the DC resistivity profile, a layer of less resistive material is buried between two resistive layers can be observed. This conductive layer is the residue of the lake sediment. The self-potential trend downward as the topography implies the water is flowing downhill with topography.

As the northern most line, line 4 begins to exit the Dead Horse Lake area and become mainly composed of the quartz monzonite. There is a large down welling of water at the northeast end of the line; however there is insufficient data to interpret what the cause is (see Fig. 4.30). In the future, another line would give more information.

4.4.3 Summary & conclusions

4.5 Gravity

4.5.1 Acquisition

Dead Horse Lake is located in a known transition zone, although the precise fault location is currently unknown. Gravity can be used to detect large faults by detecting density changes in the rock compositions.

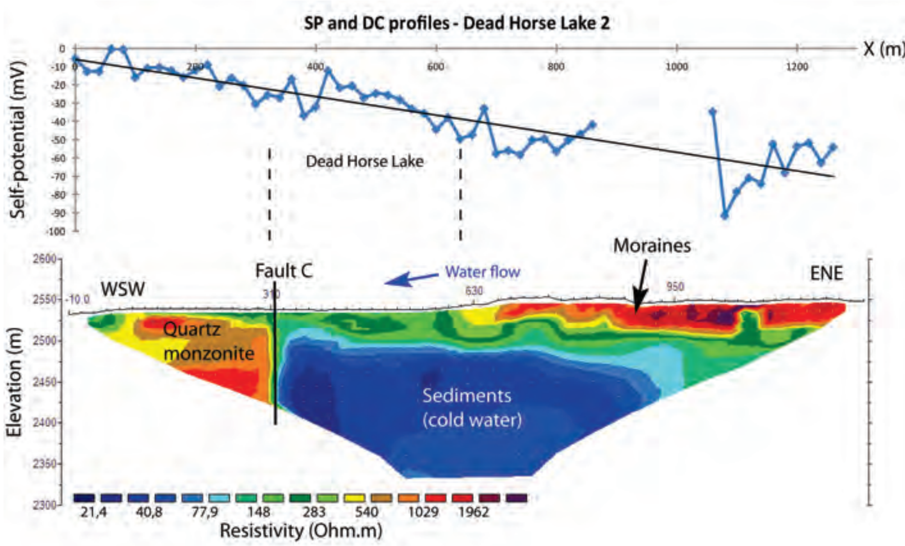

Figure 4.28: *Data from line 2, which shows how the fault distinguishes between conductive sediments and resistive quartz Monzonite.*

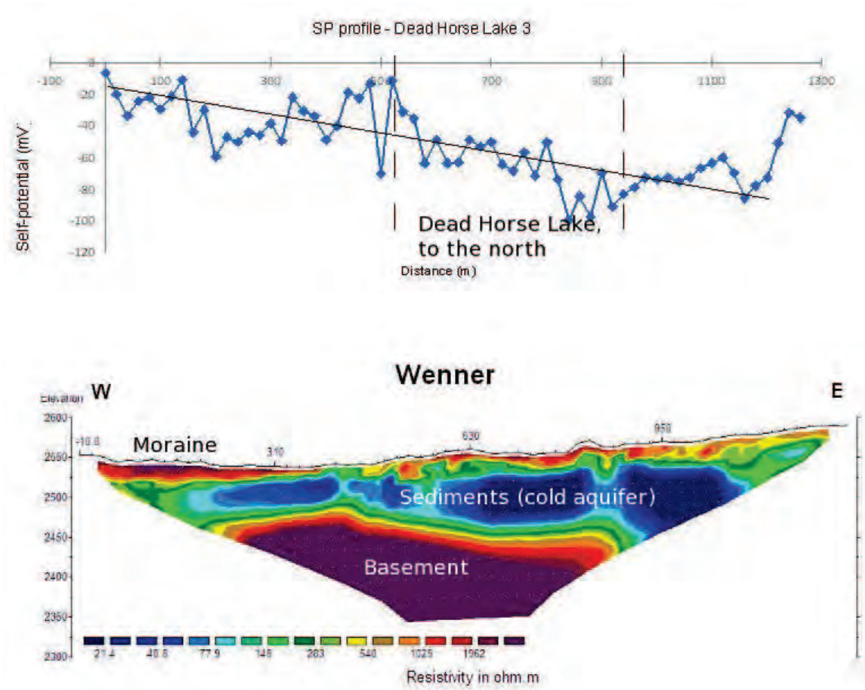

Figure 4.29: *Data acquired on Line 3, located on the North of the fault.*

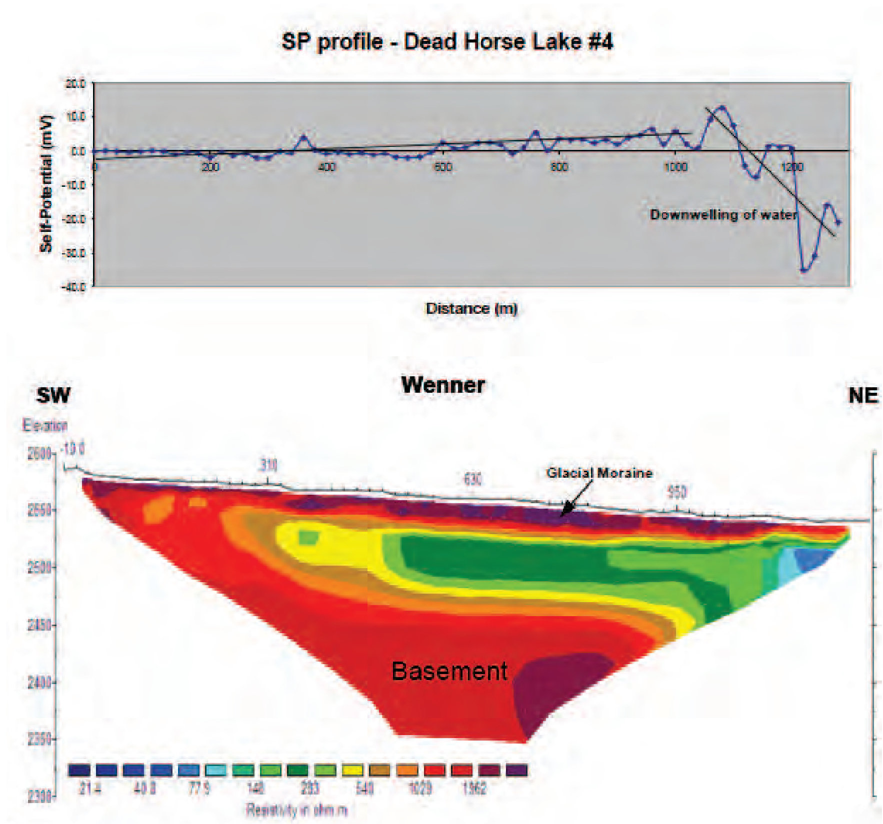

Figure 4.30: *Data acquired from line 4 of the SP survey, showing a down welling of water at the northeast end of the line.*

Operation and transport of the gravimeter required two or three operators. The CG-5 had to be re-leveled at each station before a reading was taken. Two measurements were taken at each station, each one minute apart. Gravity readings, times and standard deviations were recorded by hand in a notebook. As the weather was variable and stormy at times, notes were taken identifying which readings were most likely compromised by wind. In order to be able to later correct the data for instrumental drift, which can be caused by temperature changes and typical use, each new stretch of survey taken was tied to the original station recorded, with an additional reading recorded at the end of the survey.

The instrument used to conduct gravity measurements was the Scintrex CG-5 Autograv gravimeter. The measurement of the gravity field is equivalent to acceleration. The preferred units are mGals. The Scintrex CG-5, used to conduct the gravity surveys in the basin, gives relative gravity readings in mGals. The sensor type is fused quartz with electrostatic nulling. Its resolution is 1 microGal and it has a residual long-term drift of less than 0.02 mGal/day [13].

The Dead Horse Lake survey consisted of several parallel lines with 50 m spacing between lines and stations. The grid was initially surveyed using a handheld GPS and then resurveyed later using a TDM. The grid was not particularly robust because of gravimeter issues on May 25, 2010. For each station along the coarse grid, a handheld GPS was used to navigate to the proposed spot. The instrument was then leveled and took two measurements in a two minute period. A flag was labeled and placed at each measured spot. The grid overlaying Dead Horse Lake can be seen in Fig. 4.31.

4.5.2 Data Reduction

In order to correctly display gravity data, the following steps must be taken:

1. Various corrections of data
2. Static shifting of data so that general trend can be visible.
3. Data is plotted either as a profile or grid.

For a more detailed explanation, please see appendix F.

4.5.3 Results & interpretation

The plot of gravity on a grid (Figure 4.31) at Dead Horse Lake has gravity contours of 0.4 mGal; which are very small compared to observed variations at other sites. Even though there are local maxima and minima present, the variation throughout the surveyed area is minimal. The local minima present on the right edge and in the middle of the relatively high

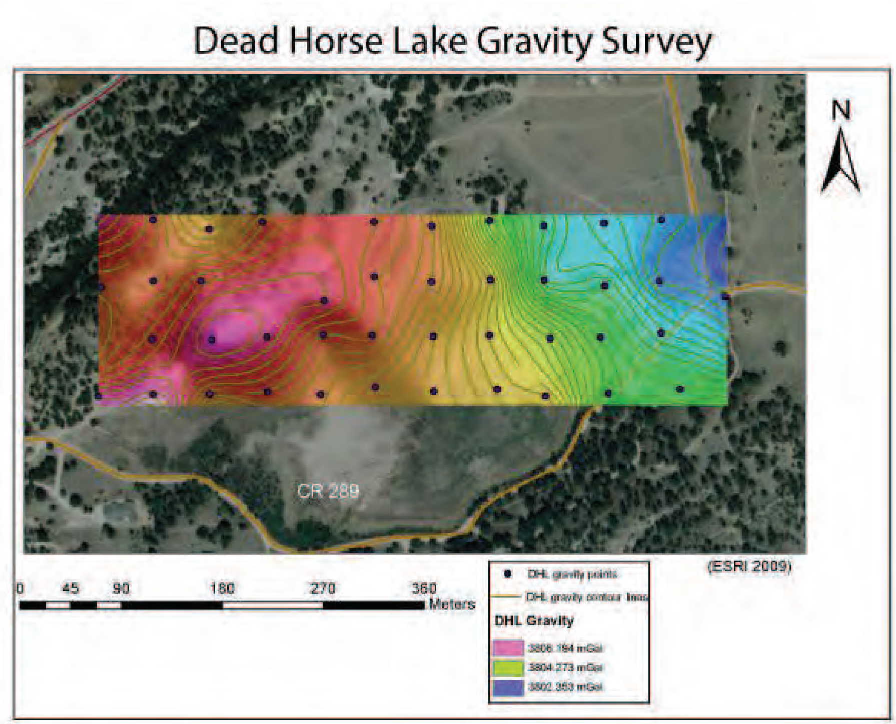

Figure 4.31: *Plot of gravity on grid at Dead Horse Lake superimposed on an aerial photo.*

area near 397520, 4286550 may be attributed to the presence of glacial moraine sediments which are less dense than the other formations in the scene. The general trend from high to low relative gravity values from left to right may indicate thinning sediments and closer basement rock to the right.

4.5.3.1 Noise, Error and Uncertainty

Errors in the data interpreted above may be caused by operator errors during acquisition such as mistakes in recording the data, which was hand-written, errors in leveling the gravimeter, errors in the operation of the TDM collecting the coordinates of the station locations. Factors in nature such as the presence of wind and drastic changes in temperature can also be factors in the data. Errors may also be factored into the processing of the data and the software used for terrain corrections.

As previously mentioned, the forward modeling of gravity data can produce several non-unique geologic models. These models all result in the same or similar gravity signature at the Earth's surface. To reduce uncertainty, the model should be constrained at least by geologic observations and suspected values of the density of the rock. Confining the range of possible density values reduces the variability in the geologic models produced. Forward modeling can also be conducted by taking into consideration magnetics data. Conducting a forward model fitting to both of these datasets reduces the uncertainty and increases the confidence in the model produced.

4.5.4 Conclusions

A broad density variation can be seen in the data due to the coarse nature of the survey locations. The minimal change in gravity response from east to west does not provide much information about the subsurface density variation. A best interpretation from data alone indicate glacial morraines in the east or a general thinning of sediments from west to east.

4.6 Magnetics

4.6.1 Acquisition

Several parameters remained constant for all magnetic surveys. Thirteen surveys total were completed in the four primary Chaffee County investigation sites. The magnetometer used collects continually (every 0.2 s), so grid and line spacing was not a vital factor. At each station, the magnetometer operator was instructed to press a marker button that would take a digital note of the location. This ensured that the data would be correlated to its correct location even in the event that the magnetometer operator changed pace between flags. For each survey, the only parameters entered were the starting line (always set at 0) and the starting mark (always set at 0). The depth of investigation for each survey was relatively shallow, between 10 and 15 m. Unfortunately, depth of investigation is difficult to determine and is not normally calculated. It depends on the strength of the anomaly; a stronger anomaly may still be visible at a depth greater than the suspected depth of investigation.

Two different types of magnetometers were employed for all magnetic surveys: the Geometrics G-858 MagMap 2000 and the Geometrics G-856AX. The G-858, also known as the cesium magnetometer, was used for collecting walking data, and the G-856AX, also known as the proton precession magnetometer, was used for collecting base station data. For more information on how either of these work or technical information, consult the appendix Appendix H.

Four surveys were completed at Dead Horse Lake: three grids and one line. There were human artifacts in the area (such as a large metallic cog, power lines and vehicles) that could contribute to data noise or error, but a note taker walked alongside the individual carrying the magnetometer and recorded any anomalous activities or objects. Use of these notes in correlation with interpretation will likely reduce error. The locations of the grids and lines were chosen because they are assumed to run close (or over) the proposed fault in the area. The spacing at Dead Horse Lake varied between lines. All surveys can be seen on Fig. 4.32.

The first survey, along the 1-D line (part (a) on Fig. 4.32), had 2 m mark spacing between flags. This survey used PVC pipe-stemmed flags. The data for this was collected on May 25, 2010. It followed an asphault cul-de-sac road.

The second survey along the 3-D seismic grid (part (a) of Figure 4.32) was 5 m spacing between flags and 2.5 m spacing between lines, with a general west-east trend. Unfortunately, this survey was not initially set up to accomodate magnetic surveys and therefore used metal-stemmed flags for portions of the grid. These zones were duly noted in walking notes and could have effects on the data.

The third survey along the magnetic grid (part (c) on Fig. 4.32) had 10 m spacing between flags and 5 m spacing between lines, but a portion of the 200 m by 100 m grid was cut off, essentially producing one southerly 100 m by 70 m rectangle and one 100 m by 100 m square combined. This survey used PVC pipe-stemmed flags. The lines trended generally North-South. Some artifacts were noted along the collection walk and will be cross-referenced in the final results.

The final survey was a grid over the entirety of Dead Horse Lake. The lines primarily ran East-West, with 20 m spacing between lines. Marks were used to signify anomalous areas as opposed to periodic placement (such as flags). No base station was used, and instead every hour the magnetometer was tied into a base location where a reading was taken. Because the survey area was so large, the survey itself took several days.

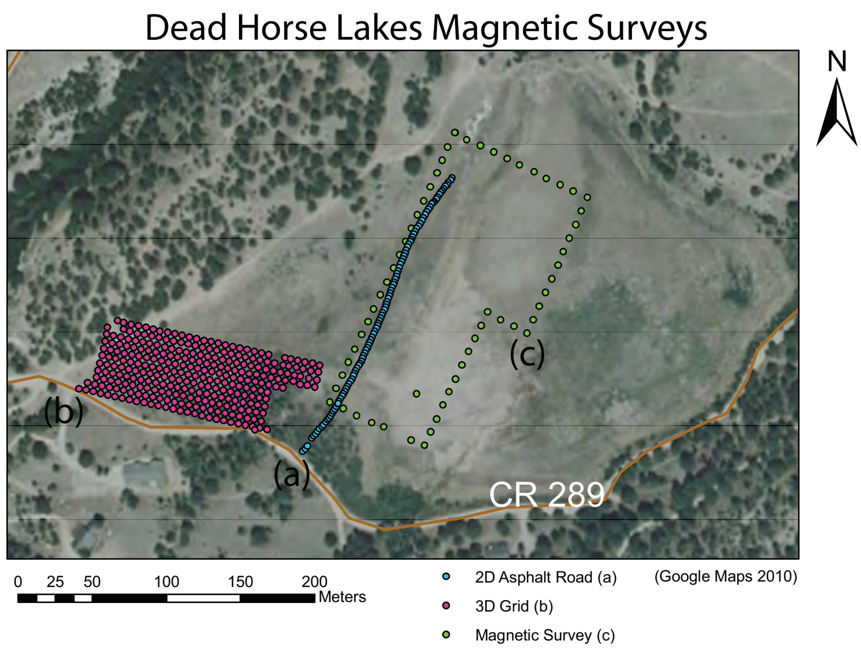

Figure 4.32: *Magnetic surveys conducted at Dead Horse Lake. (a) The 1-D line along the asphault road, 2 m spacing between flags. (b) The 3-D seismic grid, along which only 11 lines were surveyed for magnetic data. 5 m spacing between flags and 2.5 m between lines. The first 6 lines (1-6) go only 130 m (26 stations). Lines 7-11 go 150 m (30 stations). (c) The 3-D magnetics grid, designed specifically for magnetic data collection. The figure pictured here is only an outline of the grid. Inside points were not surveyed, but were laid to have 10 m between lines and 10 m between flags.*

4.6.2 Data Reduction

The basic steps required for magnetic data reduction are as follows:

1. Correct for geometry/diurnal correction.
2. Despike.
3. Apply various filters.
4. Plot and interpret.

This process was used for all magnetic data, including the grid data, which simply followed the same process by breaking down the grids into individual lines.

For a more in-depth look at magnetic data reduction, please consult appendix H.

For the large grid over Dead Horse (not pictured in Figure 4.32), minimal processing was used. The total field and diurnal variations were left in the data. The main processing that took place was geometry correction and despiking.

4.6.3 Results & interpretation

4.6.3.1 Line

The data of the 1-D asphalt road line (seen in Fig. 4.33) was collected from south to north. The profile shows a general upward trend. This profile has a large range of magnetic variation and generally high values. The Dead Horse Lake site likely has more cultural influence that could have affected the data, including the presence of field vehicles and a vibroseis truck. Surface composition may also play a role in producing the maxima and minima observed in the profile. The south end of the line could be influenced by moraine sediments, while lacustrine sediments are likely more prevalent further north.

4.6.3.2 Grid 1

There is a wide range of variation in the magnetic susceptibility values observed along the lines of the top and bottom sensor grids (Fig. 4.34). The high observed at Northing -43, Easting 20 is noted by the observer as a metal fence post. Additional metal was noted near the magnetic high shown in the top left corner of the grid. The dipole anomaly at Northing -33, Easting 55-70 can most likely be attributed to an artifact in the data acquisition.

Little change in vertical gradient is observed over Grid 1 (Fig. 4.35). The dipole anomaly in Fig. 4.34, previously described, also appears in Fig. 4.35, supporting the idea that the anomaly is related to data collection rather than a geological phenomenon.

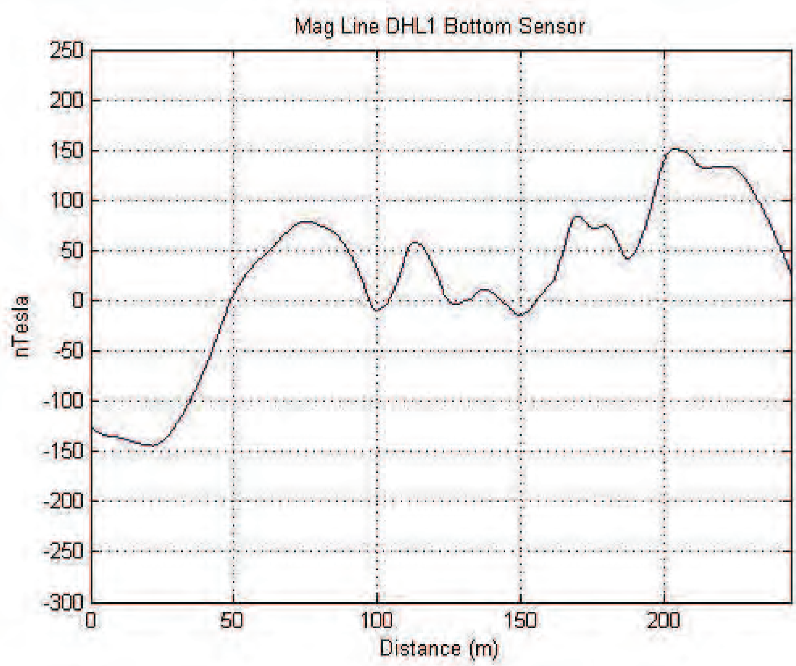

Figure 4.33: *Bottom sensor profile results from the 1-D Dead Horse Lake survey, the location of which can be seen on Figure 4.32. Measured values are relative and not absolute.*

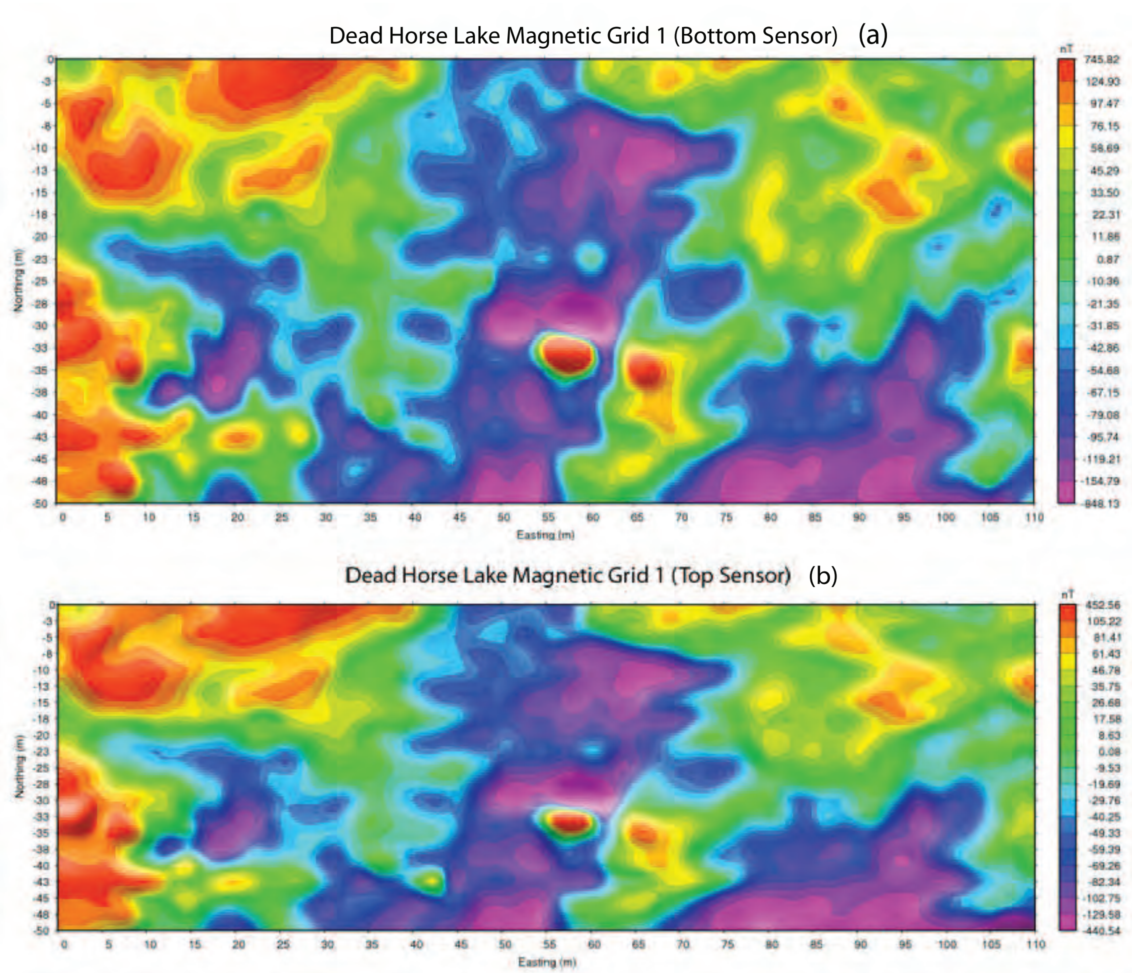

Figure 4.34: *Plot of the (a) bottom sensor and (b) top sensor magnetic data on the Grid 1 at Dead Horse Lake (grid (b) on Fig. 4.32).*

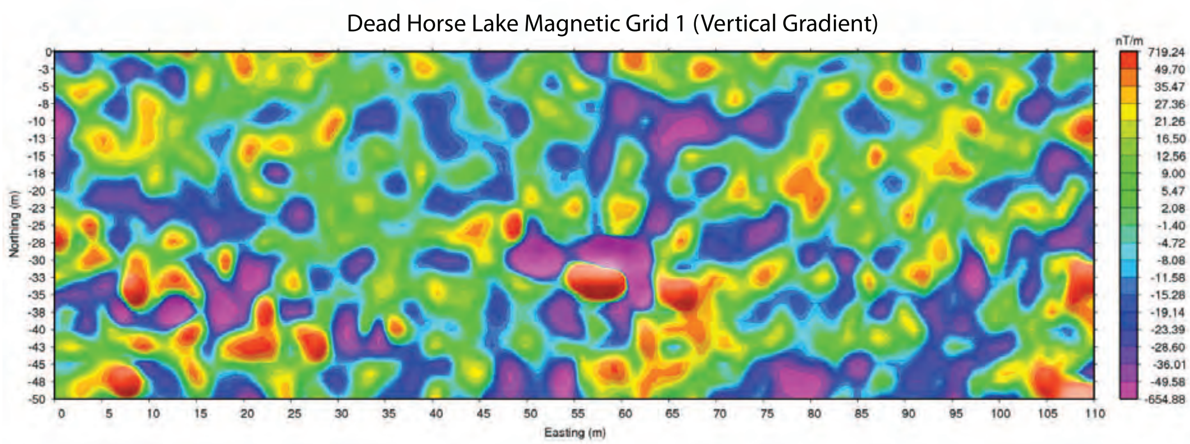

Figure 4.35: *Plot of the vertical gradient of the magnetic data on Grid 1 at Dead Horse Lake (grid (b) on Figure 4.32).*

4.6.3.3 Grid 2

The bottom sensor (Fig. 4.36 (a)) shows a low throughout the centre of the grid which could be related to drainage of the ephemeral Dead Horse Lake. Since the range in the vertical gradient is small (Fig. 4.37), the drainage-related feature in the bottom sensor (Fig. 4.36 (a)) is likely shallow and of small extent.

4.6.3.4 Grid 3

This grid was done over the entirety of the Dead Horse Lake area. It overlaps the other two previously discussed grids. North is approximately toward the top of the image. The highs on the grid represent glacial moraine deposits with nearly two times the susceptibility of the lower organic lake sediments. On the west side of the grid there is an unusual low in the glacial moraine which represents a dip in the bedrock. Also on the west side there is a extremely fast drop in the values of susceptibility which very likely represents a fault, which on Fig. 4.38 is represented by a black line. On the east side there is bumpy magnetic data which seems to correlate to outwash channels out of the glacial moraine. The glacial moraine seems to continue all the way up to the north through the area that was not surveyed. In the middle of the grid there is also a slight low between the organic lake sediments and the glacial moraine which is a flat sandy field.

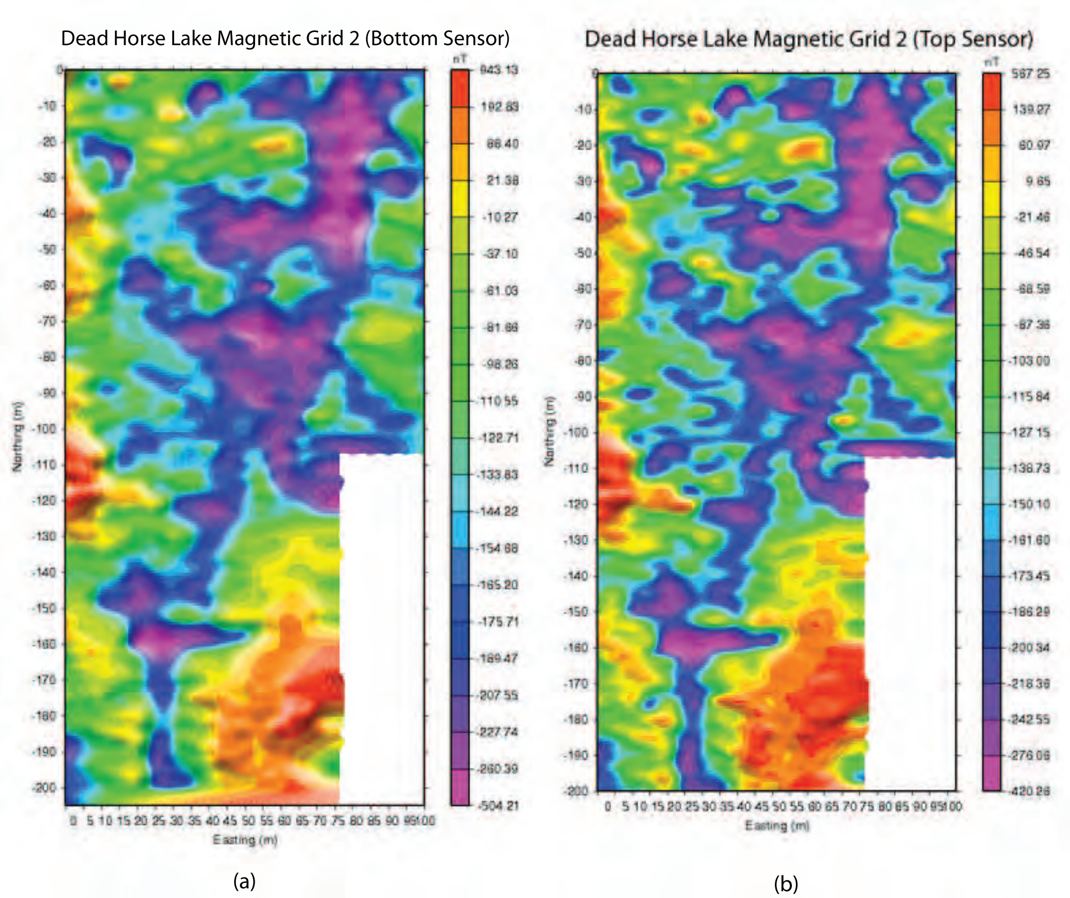

Figure 4.36: *Plot of the (a) bottom sensor and (b) top sensor magnetic data on the Grid 2 at Dead Horse Lake (grid (c) on Fig. 4.32).*

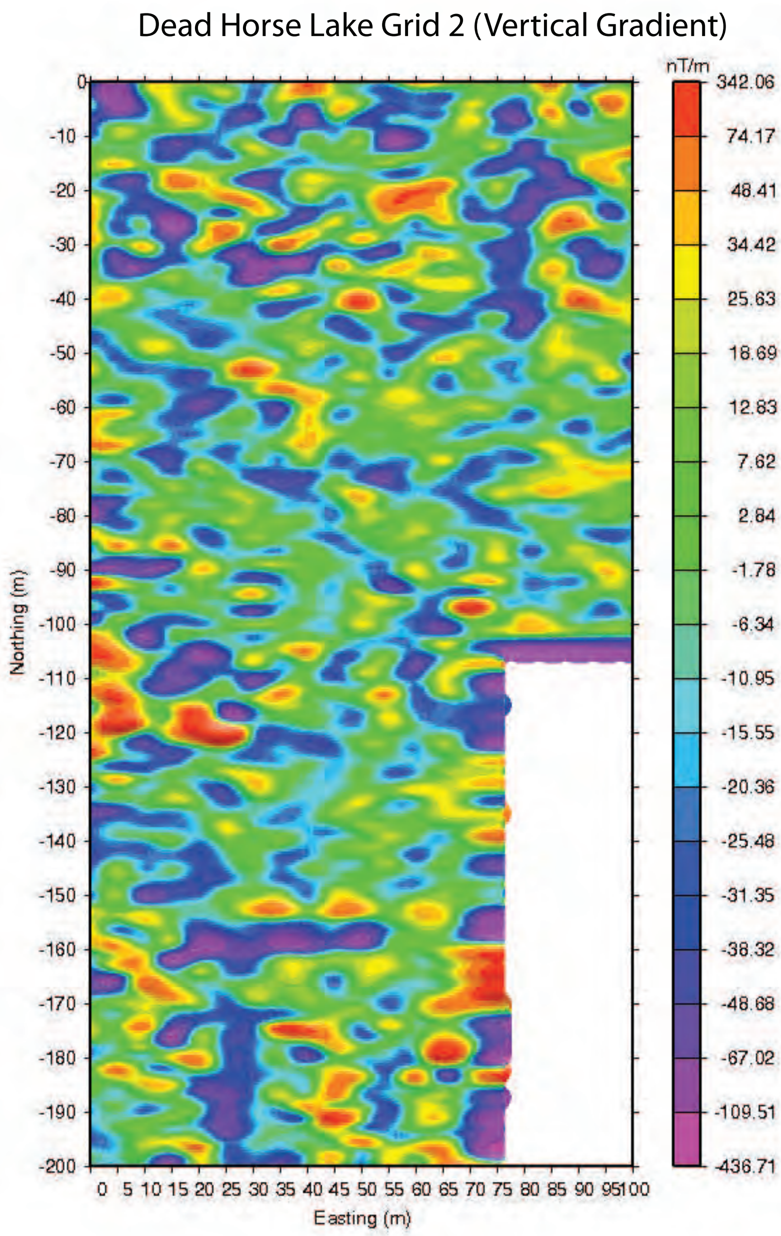

Figure 4.37: *Plot of the vertical gradient of the magnetic data on Grid 2 at Dead Horse Lake (grid (c) on Fig. 4.32).*

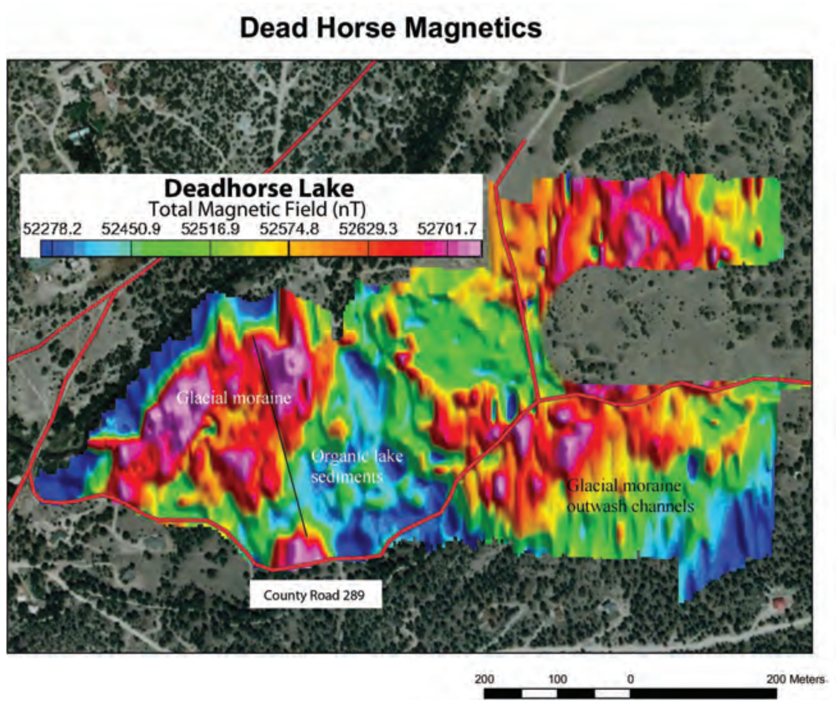

Figure 4.38: *Large magnetic survey done of the entirety of the Dead Horse Lake area. Data is not diurnally corrected so some of the data is slightly off. Over the course of the day the magnetic fluctuated around 10 nT. The point of interest is the fault, over which a black line has been superimposed. This corresponds to seismic data collected from the area.*

4.6.3.5 Noise, Error and Uncertainty

Magnetic surveys are extremely sensitive to cultural artifacts. Most noise is the direct result of human objects (such as garbage) that contains metal. The best way to avoid interference with data is to take note of all artifacts visible on the ground and note them later in the interpretation. The other primary source of noise is diurnal variations in the Earth's total field. A base station is used to remove this post data collection.

The primary source of error in magnetic data is human error. When walking, if sensors are not oriented properly (if the user does not hold the sensors directly above one another), or if a user jars the device during data collection, the result may be erroneous data.

Because magnetic data is relative differences in magnetic susceptibility between rocks, it can be difficult to determine any precise information about the subsurface. All results should be correlated with another geophysical method in order to ensure the highest quality interpretation.

4.7 Electromagnetics

4.7.1 Methodology and Acquisition

The EM equipment consists of two loops, a transmitter loop and a receiver loop (Fig. 4.39). A varying current is sent through the transmitter loop in order to induce a primary magnetic field into the ground. At this point, the ground then tries to resist this change in primary magnetic field. The ground resists change by creating a secondary magnetic field in the opposite direction. The strength of this secondary magnetic field is affected by the conductivity of the ground. This secondary magnetic field goes through the receiver loop and induces a current in the receiver to be measured. For further explanation please see Appendix E.

When an EM survey is conducted, two types of data are collected: quadrature and in-phase. Quadrature is calculated by examining the the decay of the secondary current loop. The quadrature is measured in milliSiemens/meter. In-phase is calculated as the ratio of the phase difference between the primary and secondary magnetic fields. In-phase is measured in parts per thousand(ppt). Changes in magnetic susceptibility indicate the presence of metallic objects [24]. When analyzing ground water saturation, note that metallic objects may also create an anomaly in the conductivity. These false positives can be removed by taking the magnetic susceptibility into account as well as taking observations of any metallic objects found in the survey

There are two different approaches to EM acquisition methods: Frequency Domain EM (FDEM) and Transient or Time Domain EM (TDEM). Both of these methods were applied throughout Chaffee County, though FDEM was used more extensively. The theory and useful applications of each approach is described in detail below and further described by Fig. 4.40 .

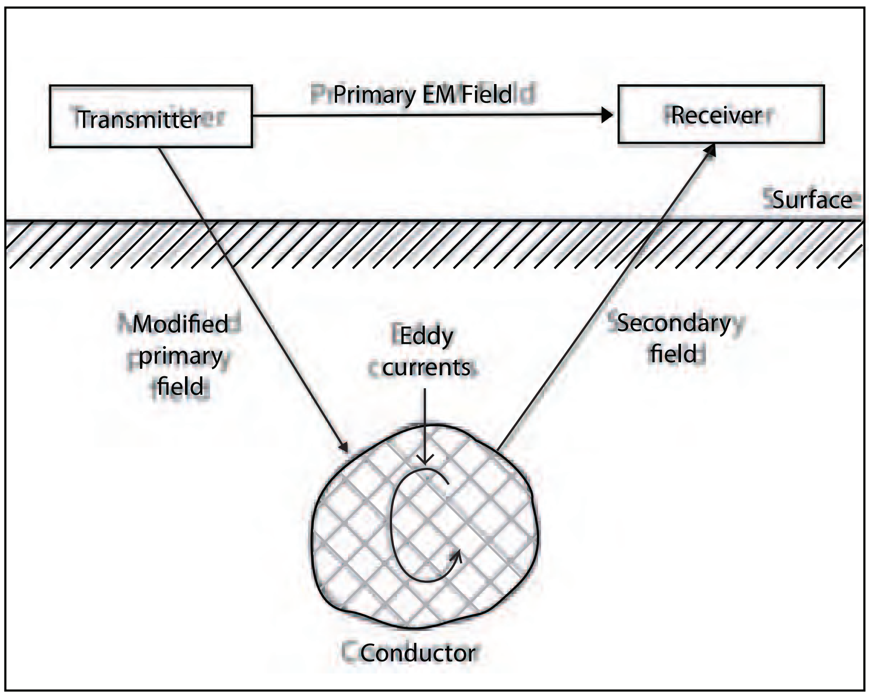

Figure 4.39: *A schematic diagram to explain the principle behind acquisition of Electromagnetic data. Figure taken from Joanna Morgan course notes, Imperial College.*

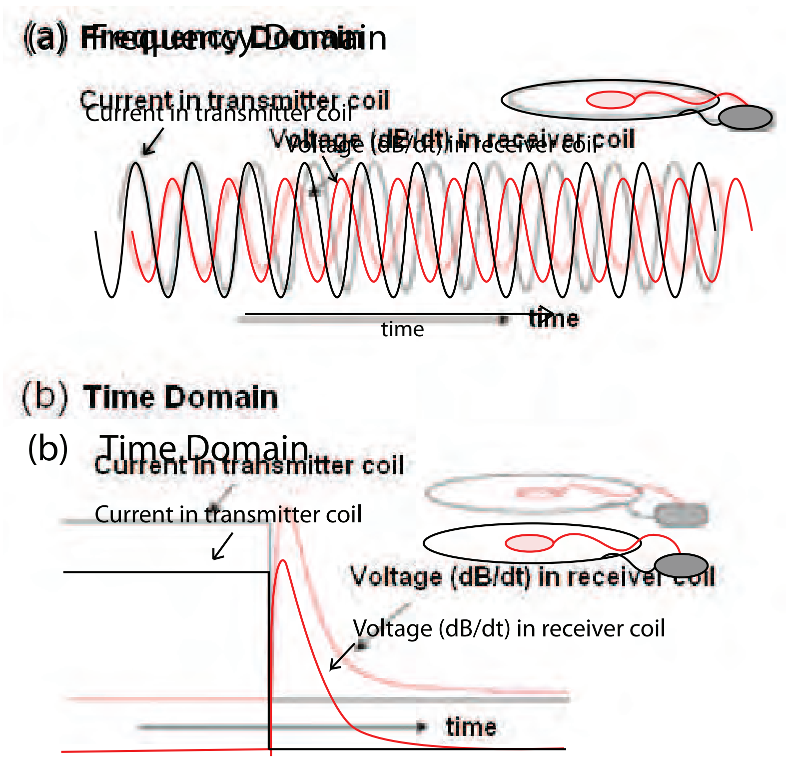

Figure 4.40: *A schematic diagram illustrating the basic differences between Frequency Domain EM (a), and Time Domain EM (b). Figure taken from Joanna Morgan course notes, Imperial College.*

In FDEM, a transmitter coil with a primary current running through it induces a magnetic field that penetrates the ground. This primary current varies sinusoidally. Because of this sinusoidal variance, the resulting magnetic field varies as well. This change in magnetic field then induces a secondary current in the subsurface, the characteristics of which are determined by the rock properties. The secondary current in the rocks then induces a secondary magnetic field, which is measured by the receiving coil in the EM instrument. Because FDEM is transmitting and receiving simultaneously, the primary magnetic field must be removed from the measurements of the magnetic field.

In TDEM the primary current running through the transmitter coil is shut off rapidly rather than varying as a sinusoid like FDEM. This results in an exponential decay in the secondary current. The rate of decay is mainly governed by the conductivity of the subsurface. The more conductive the subsurface is, the slower the secondary current decays.

FDEM data was collected at three different sites in Chaffee County using the Geonics EM31 instrument: Hecla Junction, Dead Horse Lake, and Poncha Springs (at the abandoned boyscout camp). In addition, TDEM was collected using the EM47 instrument at Hecla Junction.

The survey areas were prospected using the Geonics EM31, a frequency domain EM instrument (Fig. 4.41). The EM31 provides rapid estimates of near surface conductivity, penetrating to an average depth of 6 m [27]. The device consists of a 4 m long boom with source and receiver coils at opposing ends (3.66 m separation), aligned vertically co-planar to one another. It is held horizontally at waist height oriented either perpendicular or parallel to the survey line depending on the survey parameters. The user walks at a comfortable, consistent pace ensuring the device remains in the same orientation and parallel to the ground. The instrument measures continuously (sampling at 80 msecs intervals) along each survey line and data is stored in a handheld computer where it can be later downloaded from.

The Dead Horse Lake area is a site of heavy investigation. A series of geothermal wells have been drilled in the vicinity, some that have discovered hot water while others have only found cooler waters. This illustrates the complexity that exists in this region, and the need for a better understanding of the near-surface geology. The EM survey has the potential to differentiate changes in near surface water saturations and temperatures—both can be used to infer the permeability, and potential fluid pathways in the bedrock.

The EM31 survey was conducted on the magnetic survey grid at Dead Horse Lake (MAP-DHL MAG GRID). The grid was 200 m by 100 m, although a 25 m by 100 m rectangle in the south-east corner was not surveyed due to access problems. Flags were placed at 5 m intervals in both the inline and crossline directions. As data is continuously recorded, the inline spacing of the stations is not important other than to mark at a consistent increment the distance along the survey line. Crossline spacing is more important as design must ensure the full subsurface volume is sampled by the instrument. The EM31 has a investigation radius of 3 m ([27]), hence a 5 m survey line spacing was chosen to sufficiently sample the subsurface.

Figure 4.41: *Photograph of EM31 fully assembled and operational.*

4.7.2 Data Reduction

Data is continuously recorded during acquisition of a single survey line, hence the raw data is measured in time not distance. In order to determine the true distance of the measurements along the line, a marker is digitized in the data series at each incremented station location. This marker is accurately added by the instrument user during acquisition. With the known marker increments for each survey location, the continuous data series can be correctly calibrated to the line length. This was achieved using software which allowed the user to interactively stretch and squeeze the data so that it fitted to the true survey parameters. An image of the final re-distributed data is shown in Fig. 4.42.

During acquisition the device which added the markers to the dataset was not always triggered by the instrument user. In some of the worst cases, five or more marker positions were missing along a single survey line. This issue was resolved by firstly correcting the lines with the all of the markers present, and then trend matching the conductivity measurements where markers were missing on nearby lines. This clearly introduced uncertainty based on the individual users' interpretation, experience and therefore bias.

The redistributed data was then exported as a text file containing the ordered spatial coordinates, along with the quadrature and in-phase measurements. In order to view the spatial variation in conductivity over the survey area the data was gridded to create a 2D contoured surface of both the quadrature and in-phase components. This was achieved using a minimum curvature gridding algorithm. Minimum curvature contouring creates the smoothest possible surface which fits the data, however can have limitations when applied on line acquired data [15].

To fit a smooth surface to the raw data, the algorithm re-grids the data uniformly over the survey area. The spacing of the uniform grid is dictated by the initial sampling intervals unique to each survey. To sufficiently avoid spatial aliasing, the uniform grid spacing should be approximately one quarter the sample interval [15]. Finer re-gridding would take excessive time to compute, and is not necessary for this dataset.

Clear linear trends or corrugations exist on the contoured surfaces which do not correspond to geological features. Instead these are an acquisition footprint known as heading errors, typical of gridding of line acquired EM and magnetic data. It is possible to remove this noise using advanced processing methods, however due to the fairly broad anomalies present in the data, the existence of these heading errors does not mask any finer geological detail. To partly suppress the corrugations, the grid spacing was coarsened. This step is acceptable in the case where anomalies are low frequency, such as we see in these results.

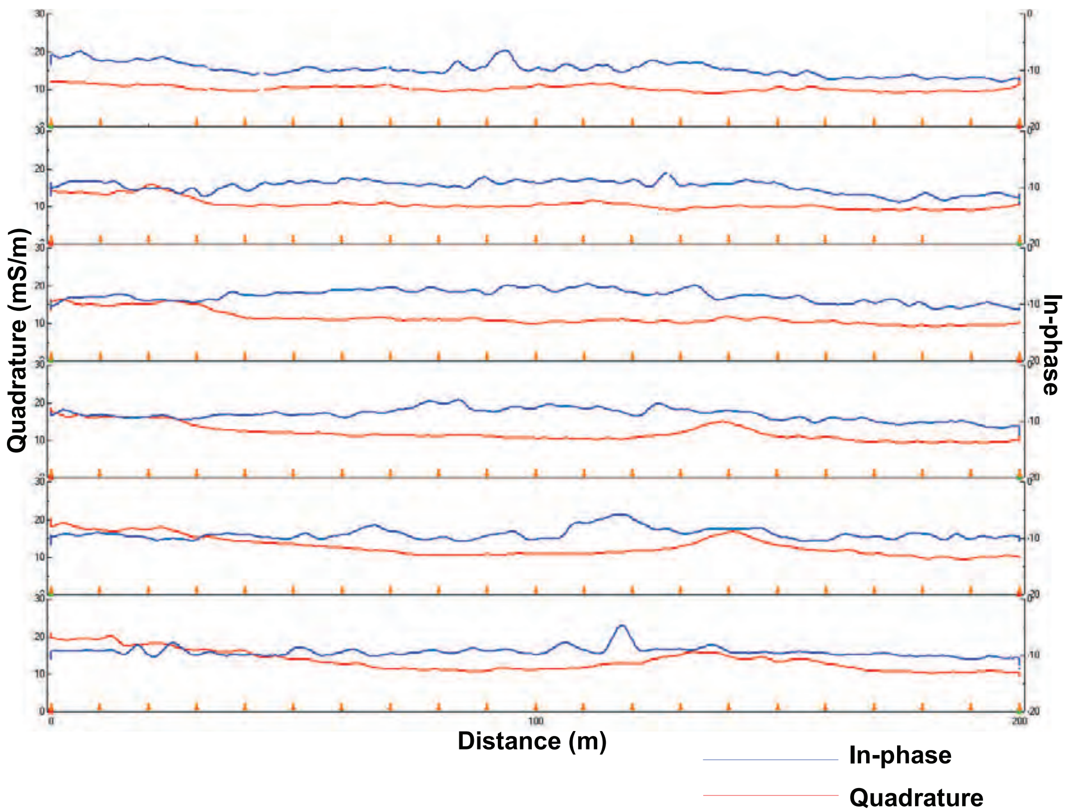

Figure 4.42: *Pre-processing of the EM31 data from the Dead Horse Lake survey. The data in this figure has been corrected to the survey parameters. For clarity only six survey lines are shown although in all 21 lines were collected. The line separation is five meters. The green and red dots illustrate the start and end of each 200m line respectively. The markers added by the user during acquisition at each station location are shown by the orange arrows. For the Dead Horse survey, markers were added every 10m. In the top line we see that one marker is missing from the data due to triggering problems during acquisition.*

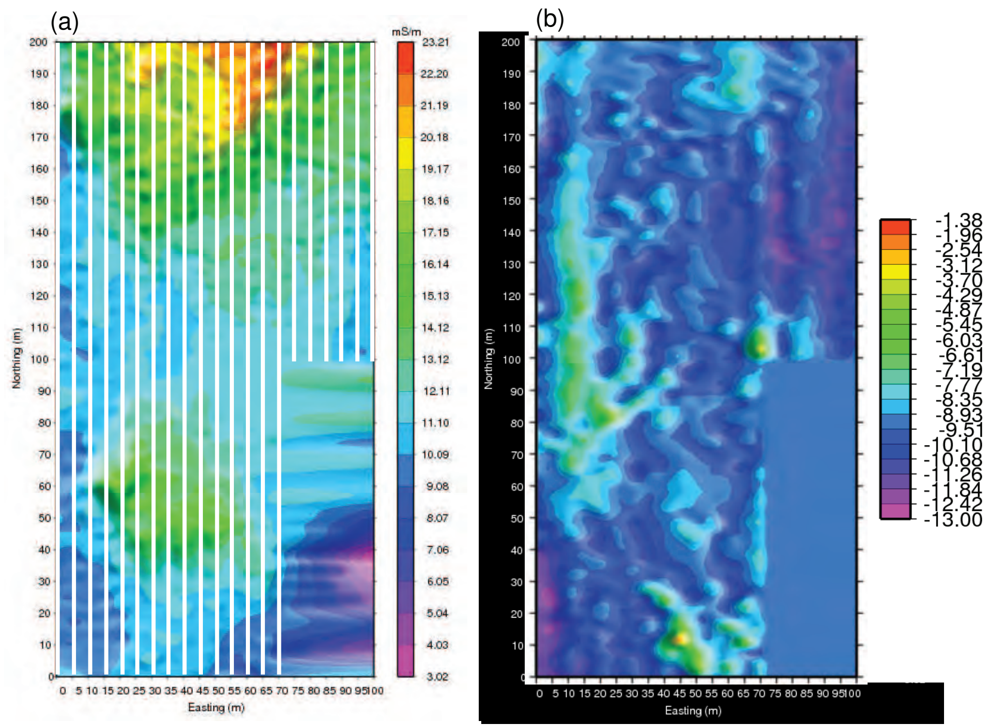

Figure 4.43: *Contoured quadrature (a), and in-phase (b) acquired at Dead Horse Lake. Survey lines are shown by the white lines on the quadrature display. These data points were contoured using a minimum curvature gridding algorithm.*

4.7.3 Results & interpretation

4.7.4 Dead Horse Lake

The quadrature data at Dead Horse Lake shows two clear anomalous regions of high conductivity (refer to Fig. 4.43). The one of most interest is that at the North of the grid where conductivity reaches a maximum value of 23.2 mS/m. The anomaly is constrained by North-East to South-West trending lineation which could potential be related to geological structure. However this region of the grid also corresponds to the edge of Dead Horse lake, hence higher conductivities may be indicative of water saturated lake sediments.

The smaller anomaly to the south of the grid is more likely due to environmental noise. The observer logs highlight a series of metallic objects in the southern region of the grid. This can therefore be discounted from geological interpretation. It can be commented that generally the conductivities at Dead Horse Lake are low, with a small range in values.

The in-phase response at Dead Horse Lake is poor due to the relatively low conductivity values in the grid area. The anomalies which exist in the in-phase data at Dead Horse lake are not as spatially consistent nor extensive as in quadrature. There is a subtle similarity in the Northern part of the grid, where the diagonal lineation clearly seen in the quadrature component can be partially detected. More noticeable are the small circular anomalies that appear to be positioned randomly on the grid. These features are most certainly related to buried or exposed metallic objects. A close correlation between observer reports of potential noise sources at station location and these anomalies exist. In-phase data is an excellent indicator of buried metallic objects [24].

4.7.5 Summary & conclusions

Conductivity of the near surface material at Dead Horse Lake was general low, suggesting mainly dry basin sediments. The main region of interest on this grid is to the north, where conductivities greatly increase. The region of the grid corresponds closely to a region where the Lake had recently drained. Although the ground conditions appeared relatively similar to the rest of the survey area, water saturations a few metres below the surface are still clearly high. The sharp linear feature which exists potentially could indicate geological structure, as it is also evident in the magnetic data.

4.8 Well logging

Once a borehole or a well has been drilled, well logging is performed in order to develop a detailed picture of the geologic formations penetrated by the well. There are two types of logging: geological and geophysical. Geological logging involves taking samples from the well and studying them. Geophysical logs employ tools that take measurements within the well which can be used to interpret the geological formations. For the purposes of the study, geophysical methods were employed at well Mount Princeton Geothermal 1 (MPG-1) located at Dead Horse Lake in Chaffee County. An induction log and a temperature log were recorded, and a gamma ray log was attempted but was not successful. This report will introduce the three logging methods used, explain the quantities measured by each method, and will incorporate the results into the interpretation of the subsurface.

The subject well, MPG1, is 600 ft deep, and is cased with 6 inch steel casing and 4 inch PVC piping. The top of the well is cased using steel casing and runs from 16 in above ground level to 140ft deep. The PVC piping runs from 20 ft to the bottom of the hole at 600ft. The well, in UTM coordinates, is located at 38S 43.234', 106N 10.764', at an elevation of 8345 ft.

4.8.1 Acquisition

All well logging was conducted at the MPG-1 well. Only a temperature log was recorded. Induction and gamma ray logs were attempted but were deemed unsuccessful. Temperature log data were used from two previous logs recorded 8 and 28 of May, 2009 in conjunction with the temperature data recorded 4 June 2010, for interpretation purposes.

The temperature logging tool was provided by Colog, a local Colorado logging company. The logging measurement interval was 0.1 ft and the starting position of the log is located at the top of casing, 16 inches above ground level. The depth was measured using a calibrated sheave wheel counter attached to the logging cable winch reel within the logging truck. The logging tool and depth counter were attached to a laptop which recorded the depth and temperature measurements in MS Log, a log recording software package used by Colog. While recording, the temperature tool got caught on the PVC piping around 25 ft deep. This did not affect the data. When the line went slack, it was indicative of the tool reaching the bottom of the hole. The accuracy of the temperature tool is $\pm 0.5^{o}$C and the accuracy of the depth counter is ± 0.5 ft.

The temperature plots provide valuable information about the Mt. Princeton geothermal anomaly and are used in conjunction with other geophysical surveys conducted in the area for the purpose of a joint interpretation of the geothermal anomaly and geologic structure of the Dead Horse Lake area.

4.8.2 Data reduction

In order to determine the geothermal potential of the Dead Horse Lake area at well MPG-1, temperature logs and the induction logs were processed using PowerBench, a well log processing software. All acquired well logs were loaded into PowerBench as an LAS format and were plotted and compared to one another as well as to the well's drilling report. In addition, the acquired logs were compared to previously recorded temperature logs and a VSP log recorded in 2009. If there were significant errors or if the trends of the logs did not agree with one another or the drilling report, the logs were rendered unsuitable for interpretation purposes and completely unusable.

The geothermal gradient of well MPG-1 was calculated in an Excel spreadsheet. A linear trend line was fitted to the acquired data according to distinct visible trends within the temperature data.

4.8.3 Results & interpretation

4.8.3.1 Temperature log: Geothermal gradient

From the drilling date to present, the geothermal gradient has remained fairly constant within the borehole of well MPG-1. The completion date of well MPG-1 was 13 May 2009. A temperature log was run down hole once before completion on 8 May 2009, and twice after completion on 28 May 2009 and a year later on 4 June 2010. Data from the 2009 temperature logs were obtained from the Mt. Princeton Geothermal 500 foot Temperature Gradient Study conducted 15 August 2009 by Fred Henderson, Paul Morgan, and Harry Olson. The geothermal gradient and trends of all three temperature logs are nearly identical. For quality control purposes, all three temperature logs were used in determining the geothermal gradient of well MPG-1. In a sense, the temperature data were stacked in order to increase the signal to noise ratio. Please see Fig. 4.44. Accordingly, the geothermal gradient was determined by taking an average of all three temperature logs and fitting a trendline to the average using excel.

Within the temperature data, there are three distinct inflection points that indicate a change in geothermal gradient. The first inflectaion point is located at 20 ft from the surface. 20 ft deep is approximately the location of the water table within the well. The water table is indicated in figure 1. The second and third inflection points are located at 230 ft and 470 ft from the surface. According to the drilling report for the well, and in accordance with the VSP data and seismic data for the Dead Horse Lake area, at 470 ft deep there is a highly fractured zone, also indicated in Fig. 4.44.

From 0-20 ft, the temperature gradient is quite steep and behaves as a power function. For the purposes of determining a geothermal gradient, the data were assumed to be linear. Towards the surface of the borehole, from 0-20 ft, the temperature gradient is 2820^{o}C/km (86^{o}C/ 100 ft). This extremely high gradient is mostly likely caused by near surface effects from the atmosphere and sun, and the fact that there is dry air from the top of the hole to 20ft deep within the borehole. This temperature gradient is not representative of the geothermal system at hand. From 20 ft deep and beyond, the temperature logs were recorded in a fluid filled borehole. From 20-230 ft the temperature gradient is linear: 407^{o}C/km (12^{o}C/ 100ft). At 230ft, there is a distinct change in the geothermal gradient; it becomes less steep and averages to about 216^{o}C/km (6.6^{o}C/ 100ft). At 470ft, the geothermal gradient flattens out into an

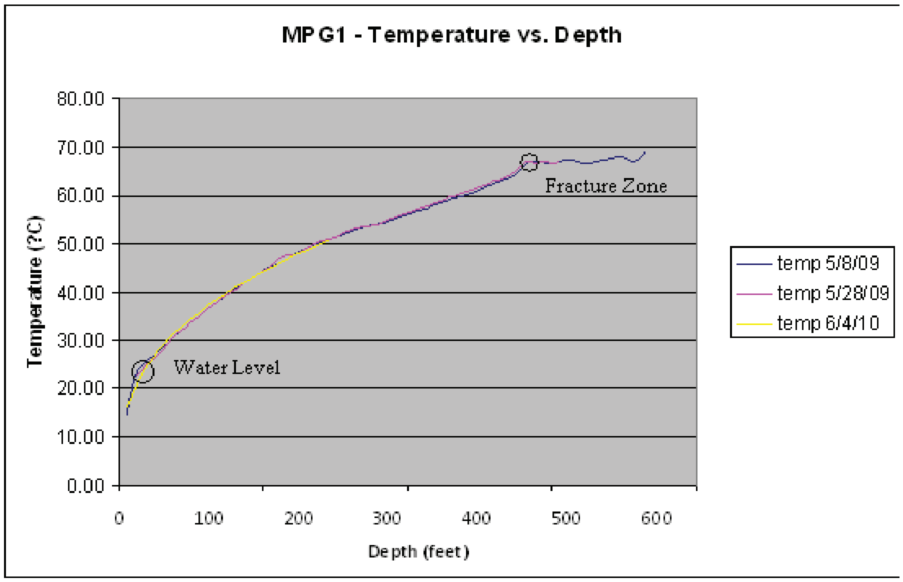

Figure 4.44: *MPG1: Temperature vs. depth profile. Data sets include temperature data from 5/8/09, 5/28/09, and 6/4/10.*

isotherm zone with a gradient of a mere 30^{o}C/km (0.9^{o}C/ 100ft). The isotherm most likely is produced by convection of the fluids between the annulus and the outside of the PVC casing. As an average, assuming that the temperature gradient is linear throughout the entire borehole, the geothermal gradient is 250^{o}C/km (7.6^{o}C/ 100ft).

4.8.3.2 Temperature log: Heat flow

Unfortunately, the available heat flow (in units of power) was unable to be directly calculated, as the thermal conductivity of the formation is unknown. It was not possible to directly measure this quantity within the MPG1 borehole, as the well is cased to the bottom of the borehole. According to the drilling report, there is steel casing from the top of the hole to 140ft and PVC pipe from 20 ft deep to the bottom of the hole, which is at 600 ft. With this in mind, any measured quantity is the result of fluid convection throughout the borehole casing and not true formation parameters.

However, it is possible to determine thermal conductivity from an integration of information from the 2009 MPG1 VSP profile, the well's drilling report, geologic observations, and published thermal conductivity charts. From the drilling report and geologic observations, there is glacial till to about 30 ft deep. As determined from the VSP profile, the drilling report, and geologic observations, there is granite from Mt. Princeton batholith to the bottom of the hole. The granite is highly fractured and weathered at depth. With this in mind, the granite is more likely to be characterized by a lower thermal conductivity value. From published thermal conductivity charts, granite would have a thermal conductivity ranging between 1.8 W/(m)(^{o}C)to 5.8 W/(m)(^{o}C). Given that the granite is weathered, the thermal conductivity is assumed to be on the lower end of the spectrum, around 1.8 W/(m)(^{o}C) to 3 W/(m)(^{o}C).

Assuming that the thermal gradient of the granite within the borehole is approximately between the range of 1.8 W/(m)(^{o}C) and 3.0 W/(m)(^{o}C), and assuming that the measured borehole fluid temperature is representative of the formation temperature, the MPG1 well has the potential for heat flow at an average rate of 0.6 W/m/m. As a simple comparison, in areas of normal temperature gradient (non-geothermal locations) the heat flux ranges between 0.04 to 0.08 W/(m)(^{o}C) [18].

4.8.3.3 Induction Log: Conductivity

The induction log recorded 4 June 2010, is determined to be erroneous and unusable for interpretation purposes. There are several reasons as to why this is the case.

Firstly, concerning fluids in a borehole, as temperature increases the mobility of ions increases and thus increases the conductivity of the fluid. Appropriately, the induction tool response should show an increasing conductivity reading traveling down hole because of the increase in mobility of ions in the fluid. This is not the case, however. As temperature increases down hole, the conductivity readings from the induction tool decrease, which is opposite to what is expected. Please refer to Fig. 4.45.

Secondly, the induction log will not work in steel casing; it will short out and produce erroneous readings. What is peculiar about the induction data collected 4 June 2010 is that the data shows no effect of the steel casing within MPG1 borehole. The vertical seismic profile (VSP) data shows that there is steel casing from the surface to a depth of 140 ft (as determined from a VSP reflection whose velocity is approximately 5000m/s, which is the velocity of steel). In addition to the VSP evidence, steel casing is visible at the top of the borehole. There is plenty of evidence for steel casing, but no trend in the induction data. This fact induces a fairly large amount of skepticism in the reliability of the induction log data set. Please see Fig. 4.45.

4.8.3.4 Gamma Ray Log: Formation Evaluation

It was the intention of the well logging company, Colog, to record a gamma ray log in well MGP1. However, upon lowering the tool into the borehole, the gamma ray tool's electrical circuitry was fried from the heat within the borehole at depth. The tool was rated up to 50^{o}C. The temperature at depth, as interpolated from the temperature log recorded on 6/4/2010, and as recorded from both temperature logs in 2009, the temperature at the bottom of the borehole exceeds 50^{o}C. In fact, the temperature at the bottom of the borehole reached 70^{o}C. Consequently, the data recorded by the gamma ray tool is incomprehensible and unusable.

4.8.4 Summary & conclusions

In agreement with VSP data, seismic data, geologic observations, and previous logs, the temperature log acquired 4 June 2010 is indicative of a geothermal anomaly. The water table is located at 20ft deep and a fractured zone at 470 ft deep. The average geothermal gradient is 250^{o}C/km (7.6^{o}C/ 100ft), with a gradient of 407^{o}C/km (12^{o}C/ 100 ft) towards the top of the hole and a gradient of 216^{o}C/km (6.6^{o}C/ 100 ft) towards the bottom of the hole. There is an isothermal zone from 470 ft to the bottom of the hole, which is in accordance with a fracture zone at 470 ft.

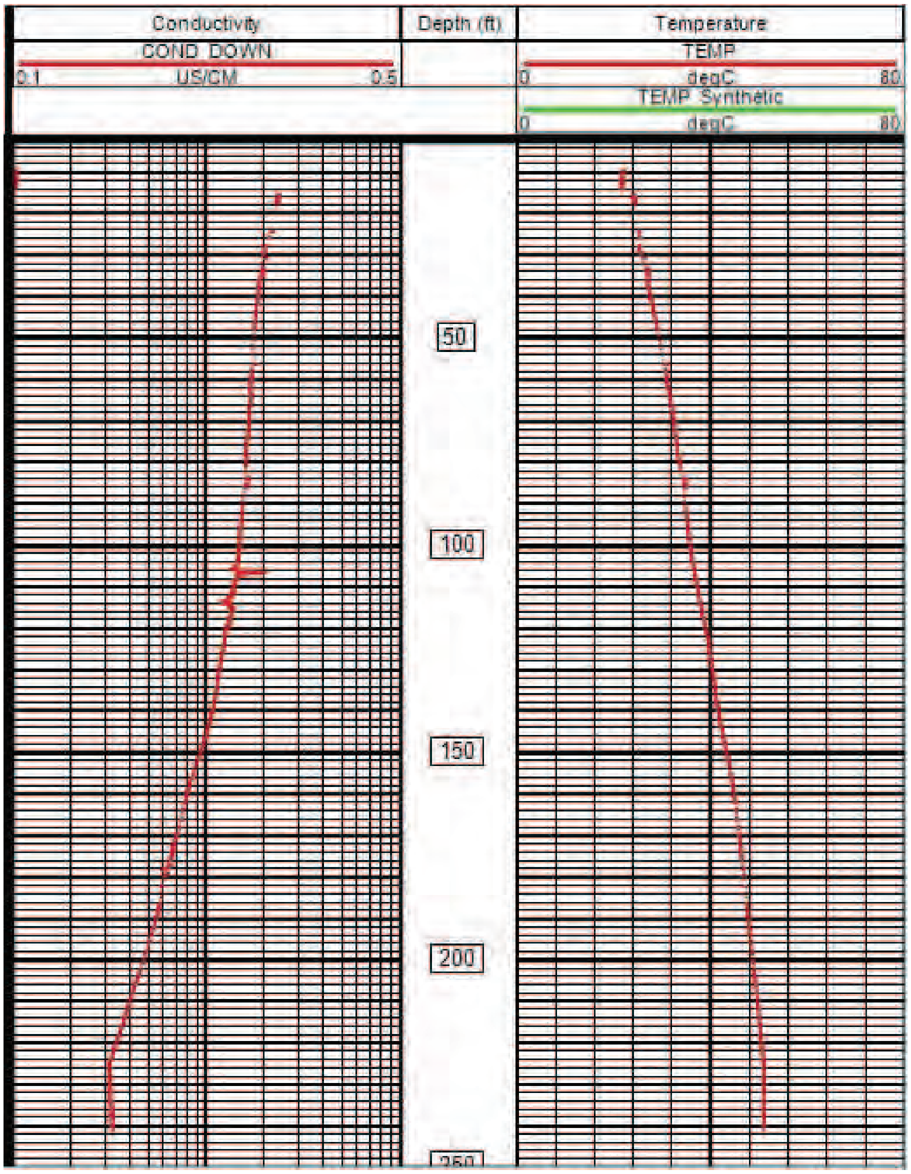

Figure 4.45: *MPG1 - Induction and Temperature Log data from 4 June 2010. The induction log is on the left, depth in the center, and temperature log on the right.*

Chapter 5

Hecla Junction

Hecla Junction is a zone with anomalous warm springs, and therefore a mystery when compared to hot springs on the west side of the Upper Arkansas Valley. It is also a region with exposed geologic features such as lava flows and Precambrian basement. The goal of the geophysical surveys was to characterize the depth of sediment before reaching bedrock as well as characterize the flow of water in the area. Four different types of surveys were performed: DC resistivity, self potential, frequency domain electromagnetics and magnetics. DC resistivity and self potential can describe water location and flow direction, while magnetics and electromagnetics can possibly identify previous channels (due to the mineralization) and bedrock location.

5.1 Resistivity & self potential

5.1.1 Acquisition

The DC resistivity and SP surveys were carried out in a few areas, one of those being the Hecla Junction site. Figure 5.1 shows the location of the 3 DC survey lines at Hecla Junction. The electrode spacing on these lines was 10 m. The data for these surveys was collected on May 24th and 25th, 2010.

5.1.2 Data reduction

In order to produce interpretable sections the data must be inverted using various methods and adjusted for topography.

For more information on this process, consult the Appendix B.

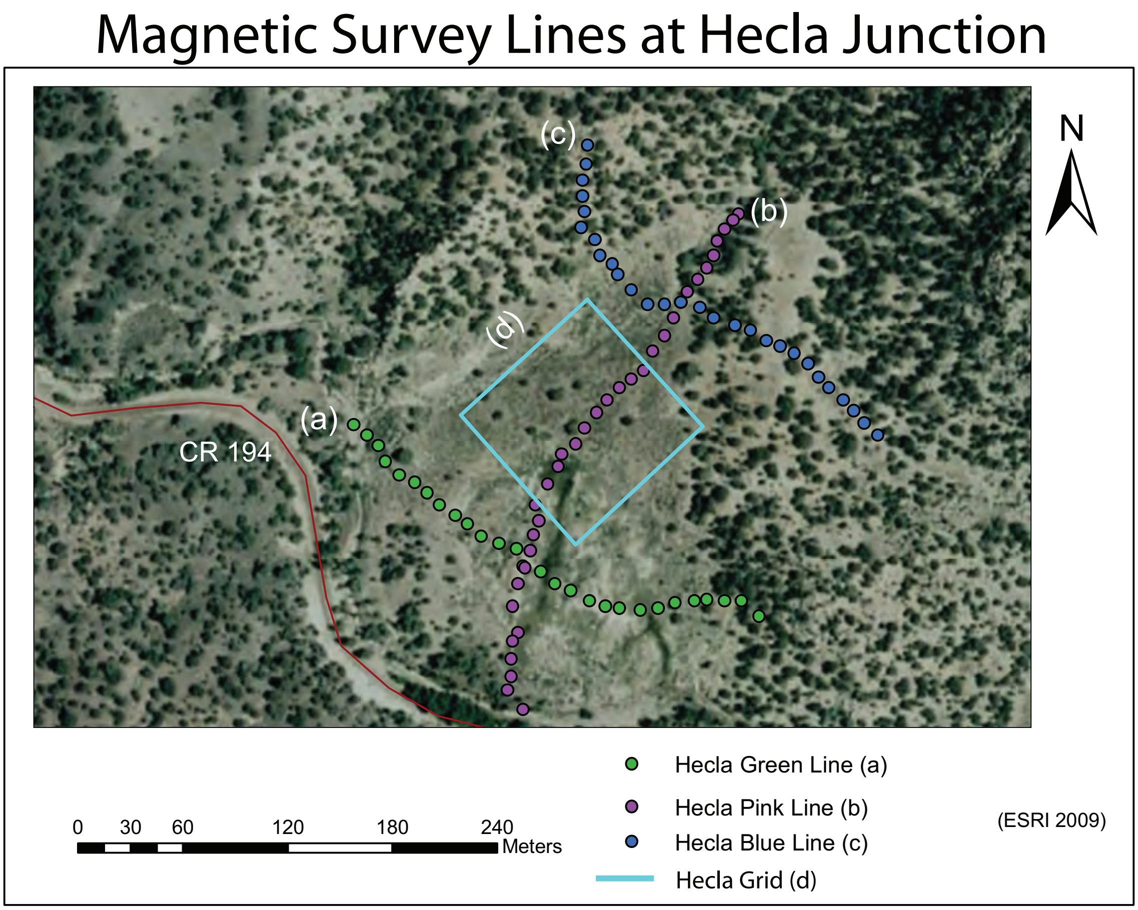

Figure 5.1: *Map of geophysical surveys taken at the Hecla Junction site. (a) The green flag line. (b) The pink flag line. (c) The blue flag line. (d) The grid.*

5.1.3 Results & interpretation

5.1.3.1 Pink Line

Figure 5.2 contains the SP profile and the two inverted resistivity sections taken over the pink line in Figure 5.1. These resistivity sections were made by splicing together two shifted, overlapping surveys of the same type. The blue areas (Figure 5.2 b and c) correspond to zones of saturated sediment, which places the bottom of the saturated sediment at 20 m to 30 m deep. The self-potential profile (Figure 5.2 a) demonstrates a general positive trend downhill, which is expected from a water table flowing downhill. The indicated local positive self-potential anomaly (Figure 5.2 a) on the southern most end occurs near springs found on the surface, and the positive self-potential anomaly directly under the word 'upwelling' (Figure 5.2 a) also occurs next to a spring.

5.1.3.2 Blue Line

Figure 5.3 contains the SP profile and the two inverted resistivity sections taken over the blue line (Figure 5.1). Again, the blue areas (Figure 5.3 b and c) correspond to zones of saturated sediment. The SP profile (Figure 5.3 a) shows a sizable negative anomaly over this saturated zone, which generally indicates that groundwater is flowing downward at that location. This is expected, as the pink line's SP data (Figure 5.2 a) shows that the groundwater is indeed flowing downhill, towards the south.

5.1.3.3 Green Line

Figure 5.4 contains the SP profile and the two inverted sections taken over the green line (Figure 5.1). The inversion images are slightly smaller than the previous inversion files, as some data points were lost. Blue areas (Figure 5.4 b and c) correspond to saturated zones. In the Wenner image (Figure 5.4 c), there is a relatively conductive body that extends as a lobe from the larger saturated zone. Because there is no self-potential anomaly over this lobe feature, there is no water currently flowing through this zone. Therefore, this lobe feature could be the remains of a former groundwater flow path. It could also represent a wet, but unsaturated zone that results from surface water percolating downward. This interpretation is based on the presence of a spring directly uphill from the green line (Fig. 5.4).The positive self-potential spikes on the eastern half of the blue line (Figure 5.4 a) indicate areas of upwelling groundwater. This is expected, as there were springs on the ground surface near those positive self-potential anomalies.

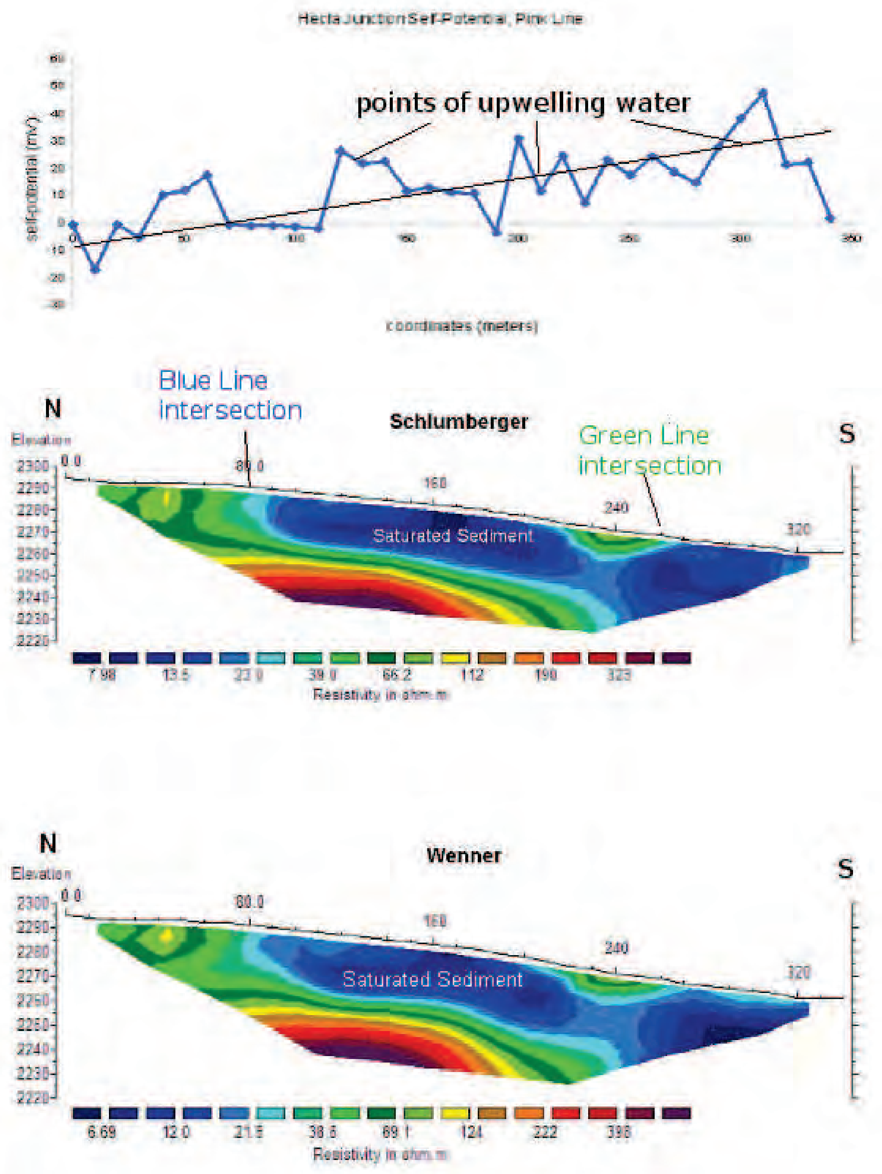

Figure 5.2: *The electrical surveys over the pink line: (a) the self-potential profile, (b) the Schlumberger resistivity inversion, and (c) the Wenner resistivity inversion. Schlumberger inversion parameters: 2 iterations, absolute error = 5.5%, vertical exaggeration = 1. Wenner inversion parameters: 2 iterations, absolute error = 3.5%, vertical exaggeration =1.*

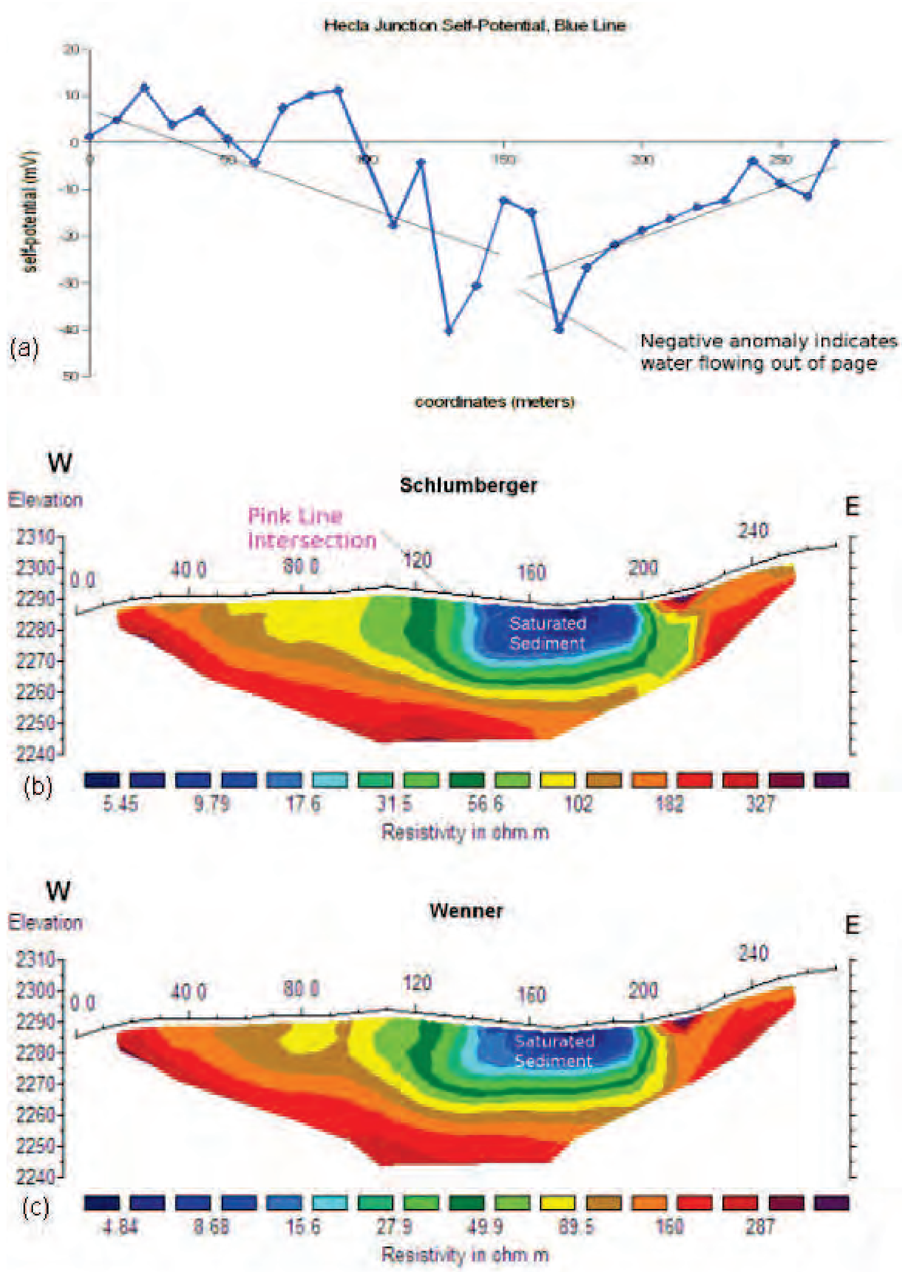

Figure 5.3: *The electrical surveys over the blue line: (a) the self-potential profile, (b) the Schlumberger resistivity inversion, and (c) the Wenner resistivity inversion. Schlumberger inversion parameters: 2 iterations, absolute error = 5.1%, vertical exaggeration = 1. Wenner inversion parameters: 2 iterations, absolute error = 5.9%, vertical exaggeration = 1*

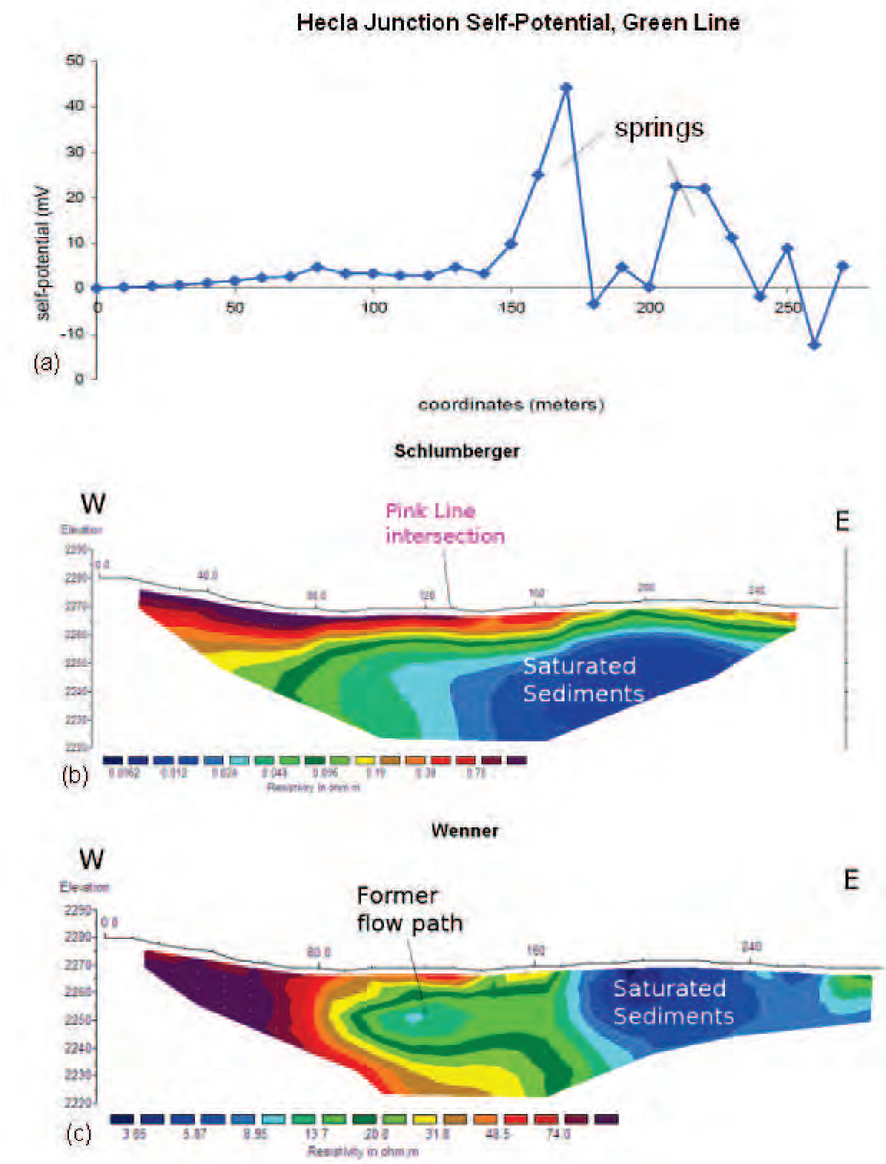

Figure 5.4: *The electrical surveys over the green line: (a) the self-potential profile, (b) the Schlumberger resistivity inversion, and (c) the Wenner resistivity inversion. Schlumberger inversion parameters: 2 iterations, absolute error = 22.5%, vertical exaggeration = 1. Wenner inversion parameters: 2 iterations, absolute error = 11.3%, vertical exaggeration = 1*

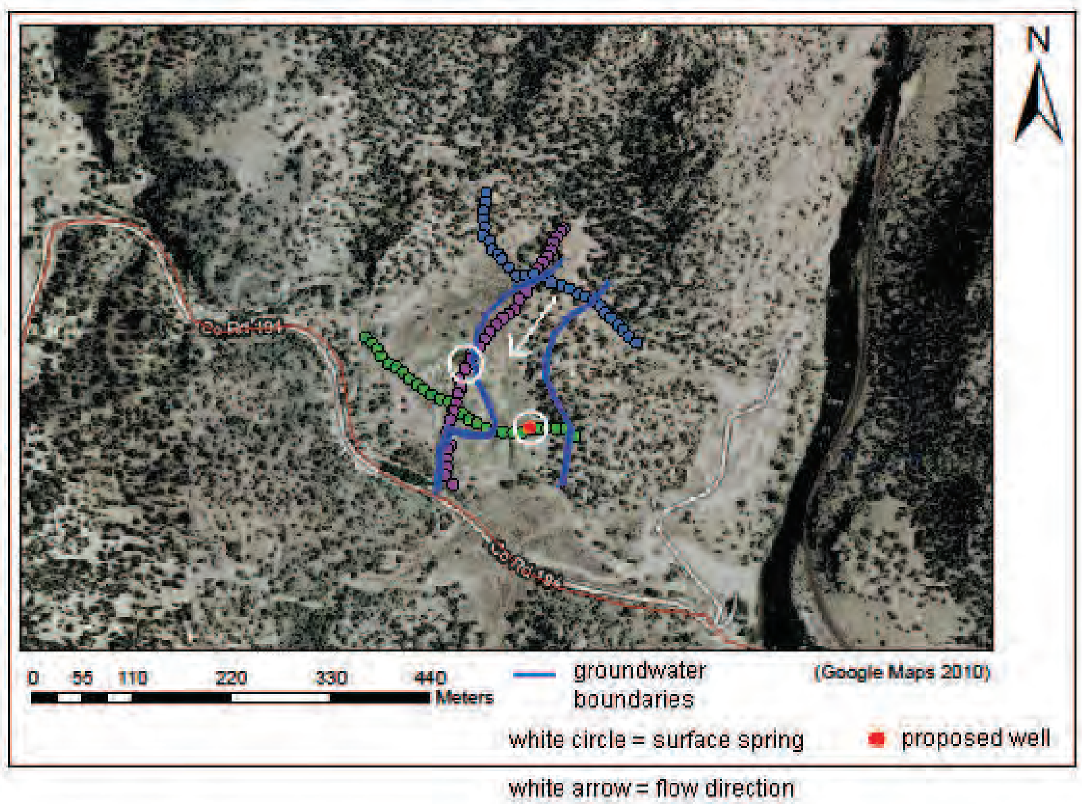

Figure 5.5: *This figure shows a map of the proposed boundaries of the subsurface saturated sediment at depth and the groundwater flow direction, along with the location of surface springs and a proposed well location. These subsurface boundaries were derived from the resistivity profiles in Figures 5.2, 5.3 and 5.4.*

5.1.4 Summary & conclusions

By combining the data from these previous plots, a diagram of the groundwater flow was made (Figure 5.5). The two large springs in the survey area occur on or very near the proposed boundaries of the subsurface saturated zones. Included in this figure is the location of a proposed water well. This location was chosen because the saturated zone beneath it appears to be the deepest aquifer according to the resistivity sections, and because it is near a spring, where the natural water pressure could be taken advantage of.

5.2 Magnetics

5.2.1 Acquisition

For the parameters and information that remained constant for all magnetic surveys, see Section 4.6.1.

Four magnetic surveys were conducted at Hecla Junction: three lines and one grid. All surveys can be seen on Figure 5.1. PVC pipe flags were used to ensure no magnetic anomalies. The area was isolated and relatively free of human influence, but observers walked along with the magnetometer users and recorded notes to ensure quality data.

The grid spacing was 10 m by 5 m (and was 100 m^2, total), and each of the lines had 10 m spacing (two of which were 270 m long, one of which was 340 m long). Two lines, the blue and green lines (both 270 m long), ran parallel to each other, and one, the pink line (340 m long), ran perpendicular through the center of each. On Figure 5.1, these are denoted as (a) the green line, (b) the pink line and (c) the blue line. The lines ran across evaporated mineral deposits indicative of hot springs. These locations were chosen to possibly identify faults that could act as spring conduits. Unfortunately, the grid was not properly surveyed and therefore the precise location of it is unknown. In Figure 5.1, (d) is an approximated location from available survey data.

The grid data was collected on May 23, 2010. The three lines (labelled the pink, green and blue lines, based on the color of flags used for each) were surveyed on May 24, 2010.

5.2.2 Data reduction

For information on magnetic reduction, see Section 4.6.2.

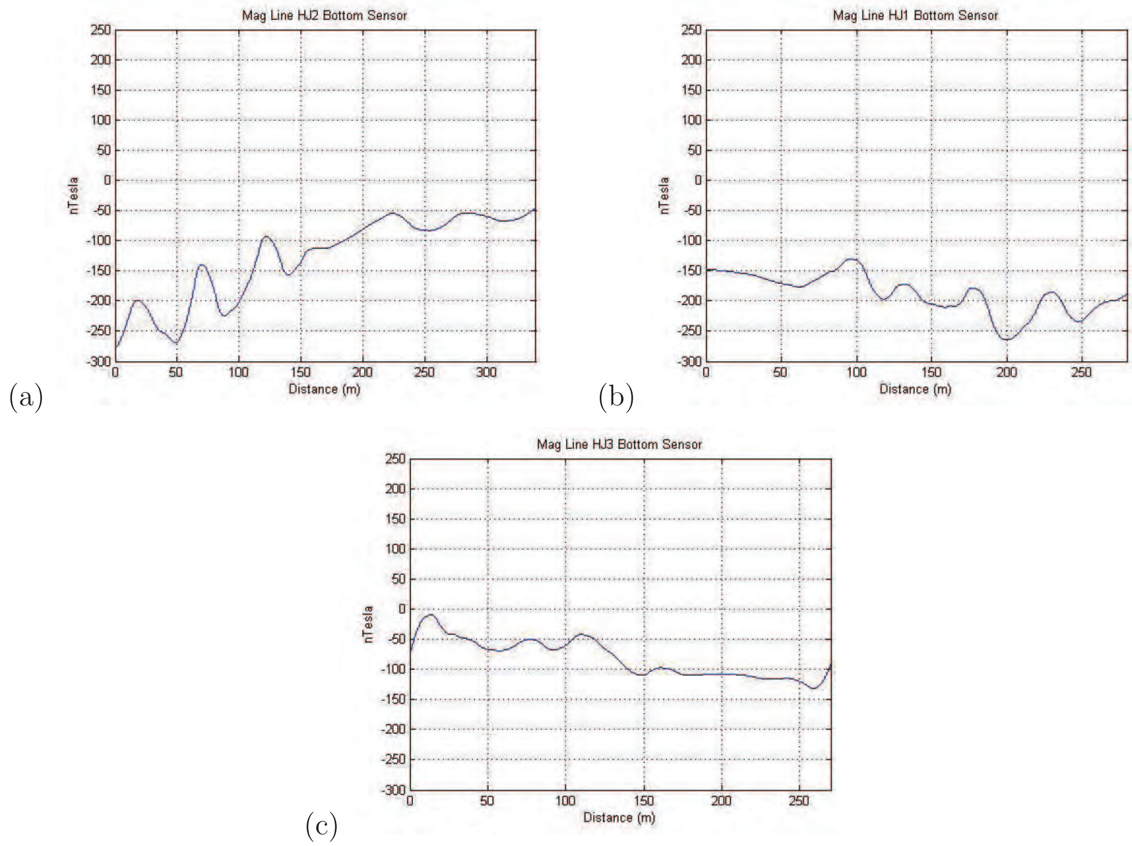

Figure 5.6: *Magnetic 1D lines collected at Hecla Junction: (a) Pink line (b) Green line (c) Blue line.*

5.2.3 Results & interpretation

5.2.3.1 Pink Line

In (a) of Figure 5.6, acquired from (b) of Figure 5.1, the data was collected along the line from South to North. A general trend of increasing magnetic susceptibility can be seen from south to north. Observer's notes indicate the presence of interference from an electromagnetic survey being conducted nearby. The low near 140 m possibly corresponds to the presence of a spring.

5.2.3.2 Green Line

In (b) of Figure 5.6, acquired from (a) of Figure 5.1, data was collected from east to west. Several dipolar anomalies are visible in the data. The observed magnetic field is negative. The

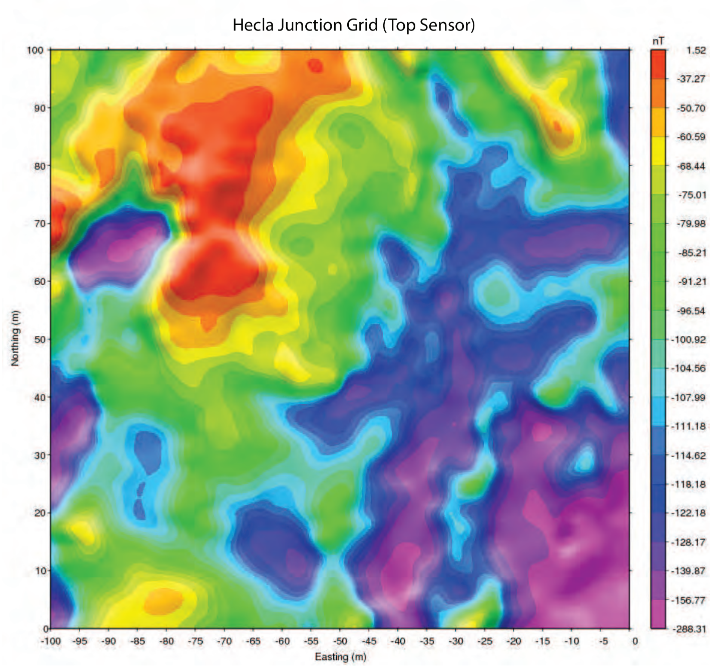

Figure 5.7: *Plot of the top sensor of the magnetic data on the grid at Hecla Junction.*

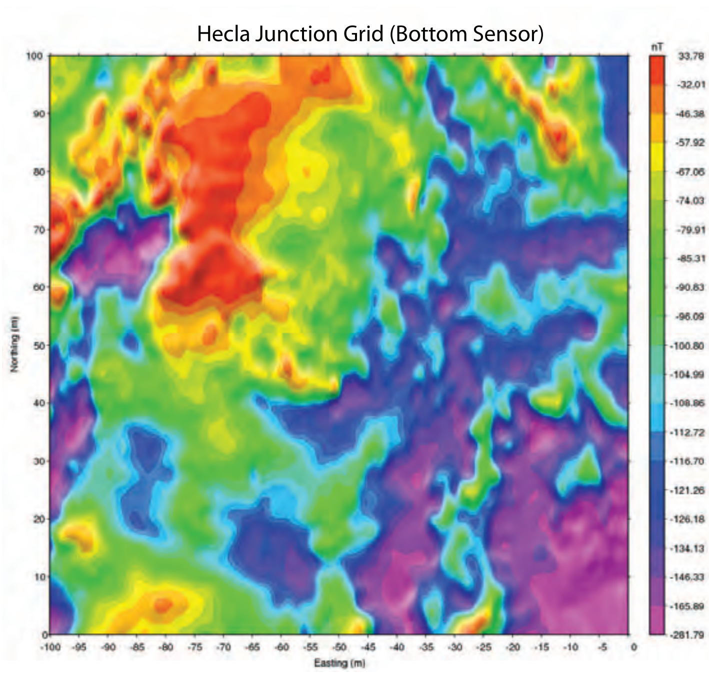

Figure 5.8: *Plot of the bottom sensor of the magnetic data on the grid at Hecla Junction.*

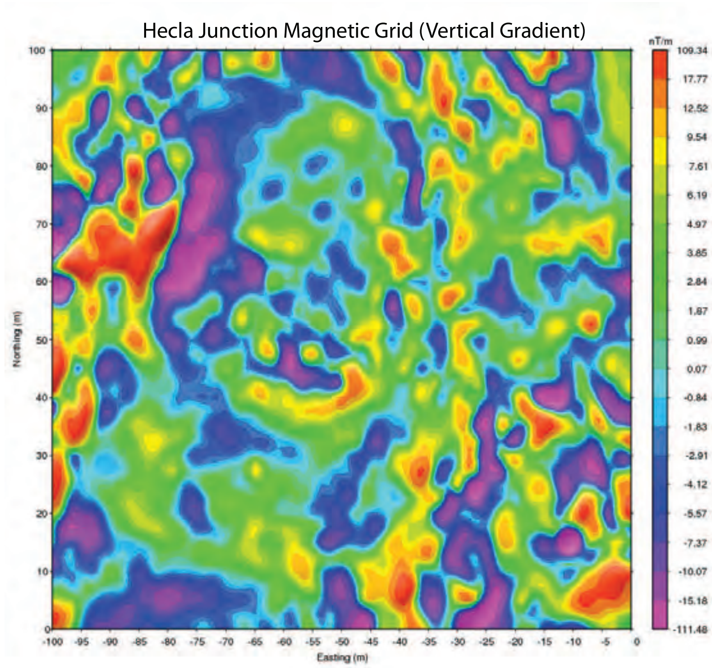

Figure 5.9: *Plot of the vertical gradient of the magnetic data on the grid at Hecla Junction.*

changes in observed magnetic susceptibility could be due to differences in surface composition, the effect of rugged terrain on data acquisition, or the presence of water at or near the surface.

5.2.3.3 Blue Line

In (c) of Figure 5.6, acquired from (c) of Figure 5.1, the data was collected roughly parallel to that of the Pink Line ((a) of Figure 5.6). Some similarities between the two can be observed, such as the limited range of magnetic variation and the subtle trend in decreasing value from east to west. This line was also located on rough terrain, which could have affected the accuracy of the data collection.

5.2.3.4 Grid

The magnetic data plotted in Figure 5.8 and Figure 5.7 are composed of a compilation of lines in a grid spaced 2.5 m apart with stations along the lines spaced 5m apart. The low area near Northing 50, Easting -35 possibly corresponds to the location of a spring, while the area of high observed magnetic susceptibility corresponds to a topographic low.

The vertical gradient (Figure 5.9) is a measure of the difference between the values recorded by the bottom sensor (Figure 5.8) and the top sensor (Figure 5.7). A large difference between the two indicates a smaller localized target anomaly which is easily sensed by the bottom sensor, but not as strongly by the top. The large dipolar change seen near Northing 65, Easting -80 may possibly indicate that the large positive anomaly in Figure 5.8, previously described, is a relatively localized, possibly small feature. Conversely, the low in Figure 5.8 does not display a large gradient, so the low may be relatively large and deep.

5.2.3.5 Noise, error and uncertainty

Magnetic surveys are extremely sensitive to cultural artifacts. Most noise is the direct result of human objects (such as garbage) that contains metal. The best way to avoid interference with data is to take note of all artifacts visible on the ground and note them later in the interpretation. The other primary source of noise is diurnal variations in the Earth's total field, which can be eliminated by using a base station.

The primary source of error in magnetic data is human error. When walking, if sensors are not oriented properly or if a user jars the device during data collection the result may be erroneous data.

Because magnetic data shows relative differences in magnetic susceptibility between rocks, it can be difficult to determine any precise information about the subsurface. All results should be correlated with other geophysical methods in order to ensure the highest quality interpretation.

5.3 Electromagnetics

5.3.1 Acquisition

The EM31 survey was completed on the 100 m by 100 m Hecla Junction grid (Figure 5.1). Flag spacing here was five meters in both spatial directions. Due to this grid being smaller than at Dead Horse Lake, a higher resolution survey was designed. Line spacing was reduced to 2.5 m, giving a total of 41 survey lines of 100 m length. Ground conditions at Hecla Junction caused issues in acquisition. The highly water saturated nature of the soil meant that straight line survey acquisition was not possible throughout the entire survey area.

In addition, two EM47 surveys were completed along the green and pink DC resistivity lines (Figure 5.1). The orientation of the transmitter coil to the receiver coil was directly to the north, however where this was not possible it was noted in the observer logs. The receiver coil was centered on the flag location at each station. The source-receiver coil seperation was maintained at 10 meters for all data points. This separation gave a maximum depth of penetration of 7.7 m (depth$\approx$seperation/1.3, [36]). This is not a significant improvement on the depth penetration of EM31.

5.3.2 Data reduction

Data reduction on the Hecla Junction EM31 data was identical to that outlined in Section 4.7.2. Attempts were made to process the EM47 TDEM data in MATLAB. However, calculations showed that the acquisition method applied only gave a depth penetration of approximately 7.7 m - little improvement on the EM31. Hence further processing to determine depth to bedrock were not continued.

5.3.3 Results & interpretation

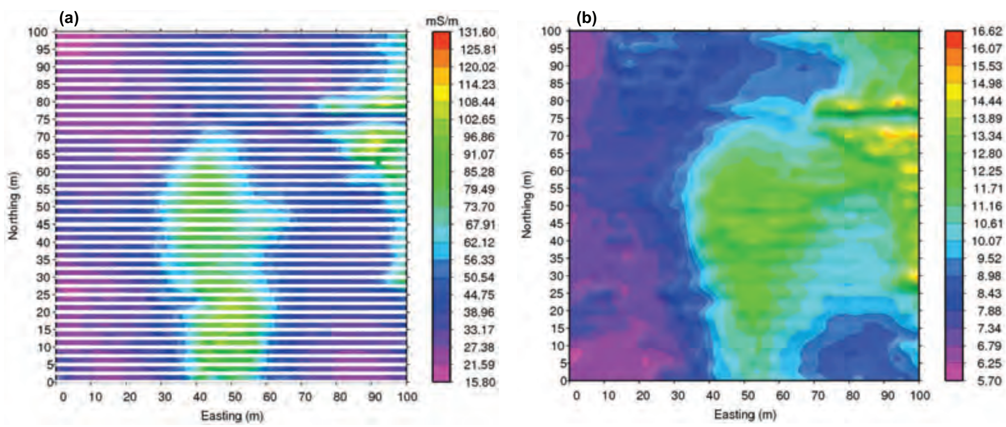

Figure 5.10: *Contoured quadrature (a), and in-phase (b) acquired at Hecla Junction. Survey lines are illustrated by white lines on the quadrature display. A minimum curvature gridding algorithm was applied to the data.*

The contoured Hecla Junction EM31 quadrature data (Fig. **??** (a)) indicates there are two regions of higher conductivity compared to the background average of approximately 30 mS/m. The general conductivity at Hecla Junction is therefore considerably higher than at Dead Horse Lake. The most significant anomaly is found centrally exhibiting a vertical north - south trend from the southern edge of the grid to 75 m further north. It has an average width of 10 m. Conductivity values reach a maximum value of approximately 110 mS/m. The in-phase data (Fig. **??** (b)) has a much stronger response at this location, hence this anomaly is also clearly present in the data.

The second anomaly is present at the eastern edge, and has similar conductivity values to the larger anomaly. This may suggest the source of the anomaly is from a similar cause, i.e. water saturated soil. The in-phase data shows a similar strong response, but with a larger spatial extent. Within this anomaly there is a survey line that is not consistent with the neighboring lines (line at 75 m). This is an erroneous line, as such a feature is not geologically reasonable.

5.3.4 Summary & conclusions

The contoured quadrature and in-phase data at Hecla Junction is dominated by a highly conductive region centrally located towards the south of the survey area. When this surface is overlain on the satellite image (MAP:SAT IMAGE), it becomes apparent this coincides with a topographic low, characterized by highly water saturated ground conditions. At Hecla Junction a reasonable conclusion is the high conductivity regions correspond to where the soils are highly water saturated. This high water saturation is due to the existence of a natural spring in the survey area which is constantly replenishing the near surface with meteoric water.

Chapter 6

Poncha Springs

Poncha Springs is located in a transition zone between the Upper Arkansas Valley and the San Luis Valley. As a result, the geology is relatively mysterious and highly fractured. There are known faults in the area, as well as hydrothermal activity (as evidenced by the flourite mine in the area). The goal of the geophysical investigations conducted here was to identify the precise location of such faults, characterize water flow in the area and attempt to understand the local geology.

6.1 Magnetics

6.1.1 Acquisition

For the parameters and information that remained constant for all magnetics surveys, see Section 4.6.1.

Two single-line surveys were conducted at Poncha Springs. The first line ran parallel to the DC Resistivity line in the area, and was thought to cross the suspected faults in the area. This line ran roughly north-south, had a mark spacing of 5 m and a length of 370 m.

The second line ran across the tufa mounds (mounds of precipitated minerals indicative of water flow) behind the abandoned Boy Scout camp in the area. It lay approximately west-east, had 10 m mark spacing and was 260 m long.

The map of these two lines can be seen in Fig. 6.1.

6.1.2 Data Reduction

For information on magnetic reduction, please see Section 4.6.2.

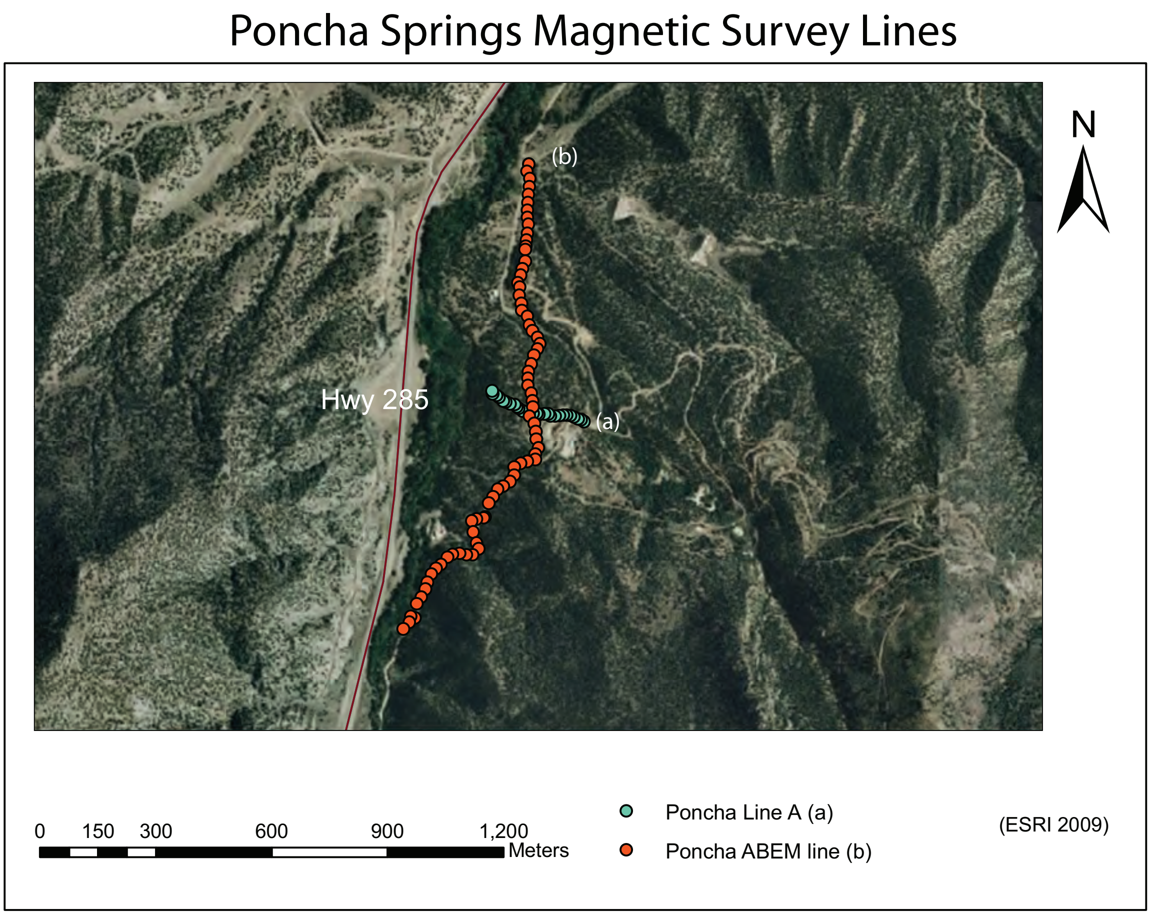

Figure 6.1: *Map of the locations of magnetic surveys taken at the Poncha Springs site. (a) The A Line, otherwise known as the line that crossed the tufa mounds (line 1). (b) The line that ran parallel to the ABEM data (line 2). Note that the collected data did not actually extend as far as the line depicts here, but the orientation and location is accurate.*

6.1.3 Results & interpretation

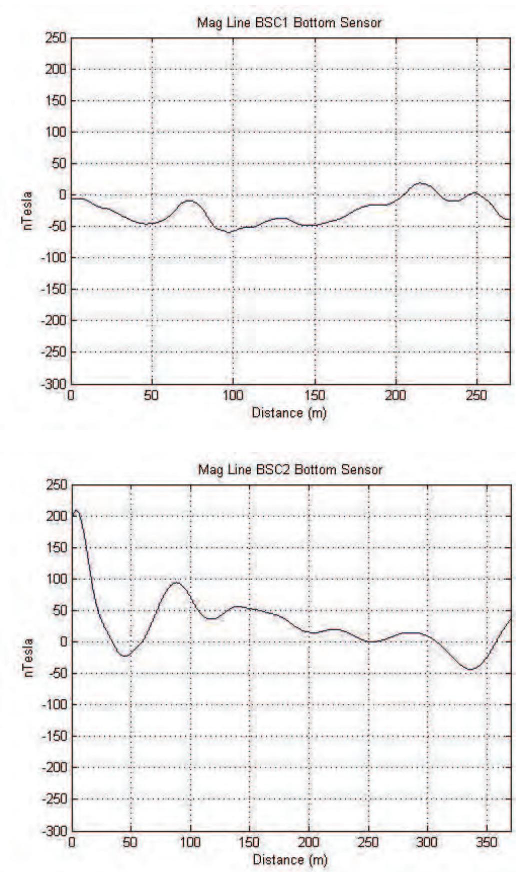

(a)

(b)

Figure 6.2: *Magnetic 1-D lines collected from Poncha Springs. (a) Line 1. (b) Line 2.*

6.1.3.1 Line 1

The magnetic profile in (a) of Fig. 6.2 displays the data taken on line A (Fig. 6.1) from east to west. The fluctuations in the observed magnetic susceptibility are relatively small on this line. Variations along the line could be due to differences in ground composition such as differing amounts of soil over basement rock.

6.1.3.2 Line 2

The magnetic profile pictured in (b) of Fig. 6.2 was collected along the ABEM line from south to north for 370 m. A general trend of high magnetic susceptibility can be seen from South to North. There are local minima near 40 m and 335 m, and local maxima near 0 m, 80 m, and 370 m. The subtle local variations visible around 280m correspond to field notes which indicated the presence of small metal objects near the survey line, and therefore may not be the result of geology. The large dipolar anomaly at the beginning of the line could help confirm the location of a fault, one of many which were observed at the surface in the area.

6.1.3.3 Noise, error and uncertainty

Magnetic surveys are extremely sensitive to cultural artifacts. Most noise is the direct result of human objects (such as garbage) that contains metal. The best way to avoid interference with data is to take note of all artifacts visible on the ground and note them later in the interpretation. The other primary source of noise is diurnal variations in the Earth's total field, which can be eliminated by using a base station.

The primary source of error in magnetic data is human error. When walking, if sensors are not oriented properly or if a user jars the device during data collection the result may be erroneous data.

Because magnetic data shows relative differences in magnetic susceptibility between rocks, it can be difficult to determine any precise information about the subsurface. All results should be correlated with other geophysical methods in order to ensure the highest quality interpretation.

6.2 Electromagnetics

6.2.1 Acquisition

A series of 2D lines were designed at the Boy Scout Camp at Poncha Springs to determine the near surface structure and how it relates to the known hot springs in the area. Numerous mineral deposits related to former hot springs were also discovered at the camp. Although the EM31 depth penetration is limited in comparison to complimentary methods such as magnetics, the single EM survey along line A could highlight near surface saturation effects which may help in the interpretation of other datasets in the area.

Line A was oriented east-west, and flags were placed at ten meter separation ((a) on Fig. 5.1). Data was collected along the line continuously, with marks being placed in the time series every 10 meters. Due to the step gradient between flags A25 and A27, it was unsafe to operate the EM31 hence data was recorded up to and including station A25 giving a line length of 240 m.

6.2.2 Data Reduction

For information on electromagnetic data reduction, please see Section 4.7.2.

6.2.3 Results & interpretation

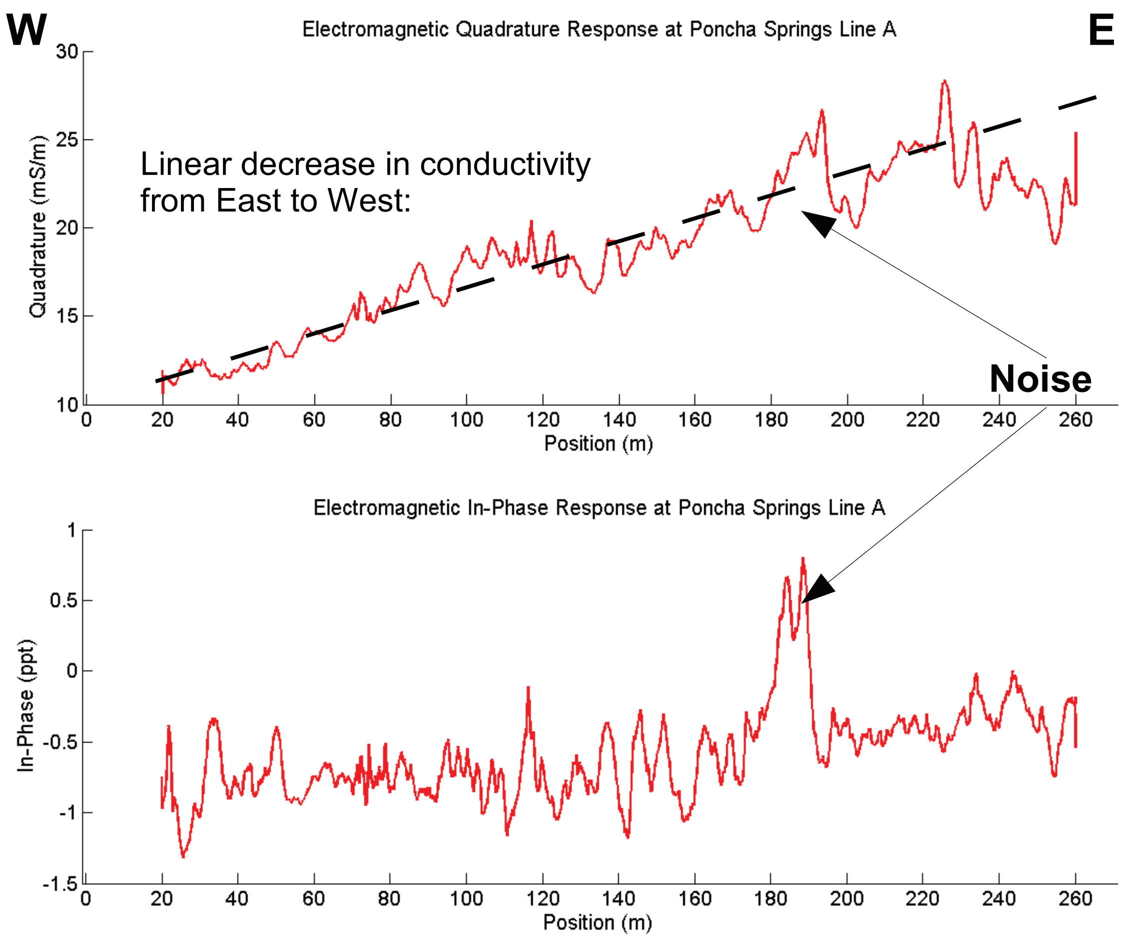

Figure 6.3: *Plot of quadrature (top) and in-phase (bottom) measurements acquired along Line A at Poncha Springs - Abandoned Scout Camp. The axis is formatted for comparison with resistivity data where flag A27 is assigned as the origin.*

Two surveys were conducted along the Line A 2D transect at Poncha Springs. For this summary of results, the data for the forward survey will be used as it appears less noisy with a lower variance in data values than the reverse survey. The data in Fig. 6.3 shows a general trend of decreasing conductivity from east to west (downhill). Within this background trend, there are some interesting sharp increases and decreases in conductivity. These include a region of increased conductivity at a distance of 180-200 m along the line. This anomaly correlates with a sharp anomaly in the in-phase component, so can be discounted as noise. It is typical that for EM31 data, sharp changes in conductivity do not represent geological or groundwater saturation changes. Instead they are distortions in the data due changes in the orientation/height of the device caused by steep terrain or obstacles along the line. Again metallic, or any type of conductive object may be a cause.

6.2.4 Conclusions and summary

EM data quantity at Poncha Springs was relatively limited. Only one survey line was acquired - line A which ran east to west through the abandonned scout camp. The general trend of decreasing conductivity in a westerly direction may be indicative of sediments thinning, i.e. the bedrock is becoming shallower as the line goes downhill. This is a more likely explanation of the results than any water saturation effects as unlike the other two survey areas, no evidence of water sources were present along the line.

6.3 Resistivity & self potential

6.3.1 Acquisition

Three DC resistivity and two self-potential surveys were conducted at Poncha Pass. The SuperSting surveyed parallel lines, Line A and Line B, running west to east and the ABEM surveyed one line titled Poncha ABEM in the north to south direction (Fig. 6.4). A Wenner array was performed for each line, as well as a Schlumberger Sounding for Lines A and B. Self-potential was taken along Line A and Poncha ABEM.

Line A was 280 m long, with 10 m spacing between each electrode. The line was placed near a previous Boy Scout camp where water from hot springs was channeled.

Line B is offset from Line A by 110 m, and is 280 m long with 10 m electrode spacing.

The ABEM has 20 m electrode spacing, and spans over 1560 m running north to south. There is hot water upwelling to the surface located to the east of Poncha ABEM.

6.3.2 Data reduction

In order to produce interpretable sections, the data must be inverted using various methods and adjusted for topography.

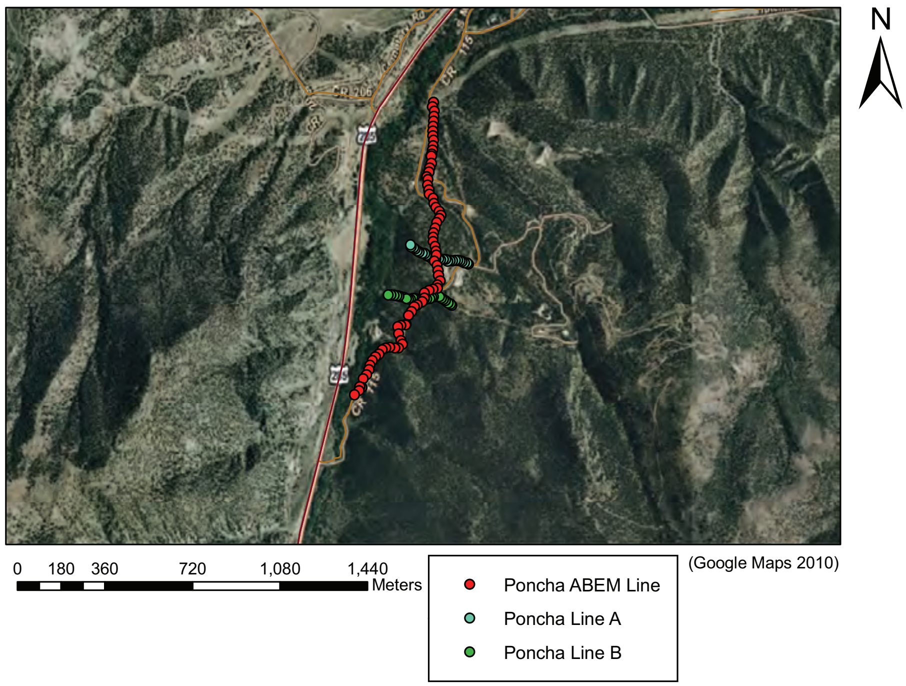

Figure 6.4: *Poncha ABEM survey, Line A, and Line B plotted on an aerial view of Poncha Pass.*

For more information on this process, consult Appendix B.

6.3.3 Results & interpretation

6.3.3.1 Line A

Fig. 6.5 displays the results of the self-potential line, Schlumberger sounding and Wenner array from the Poncha Pass line A.

Since Line A crossed a road, the drainage ditch can be recognized in the Schlumberger and Wenner arrays. Near 100 m, a noticeable change in resistivity occurs over a short distance. This is typical behavior of a fault in DC resistivity. Correlating the DC resistivity surveys to the self-potential line, the water travels laterally and upward until it intersects the fault, where it flows downhill towards the stream.

6.3.3.2 Line B

The Wenner and Schlumberger arrays for Line B, located in Fig. 6.6, show a similar trend of more conductive rock towards the east and more resistive rock to the west. The most

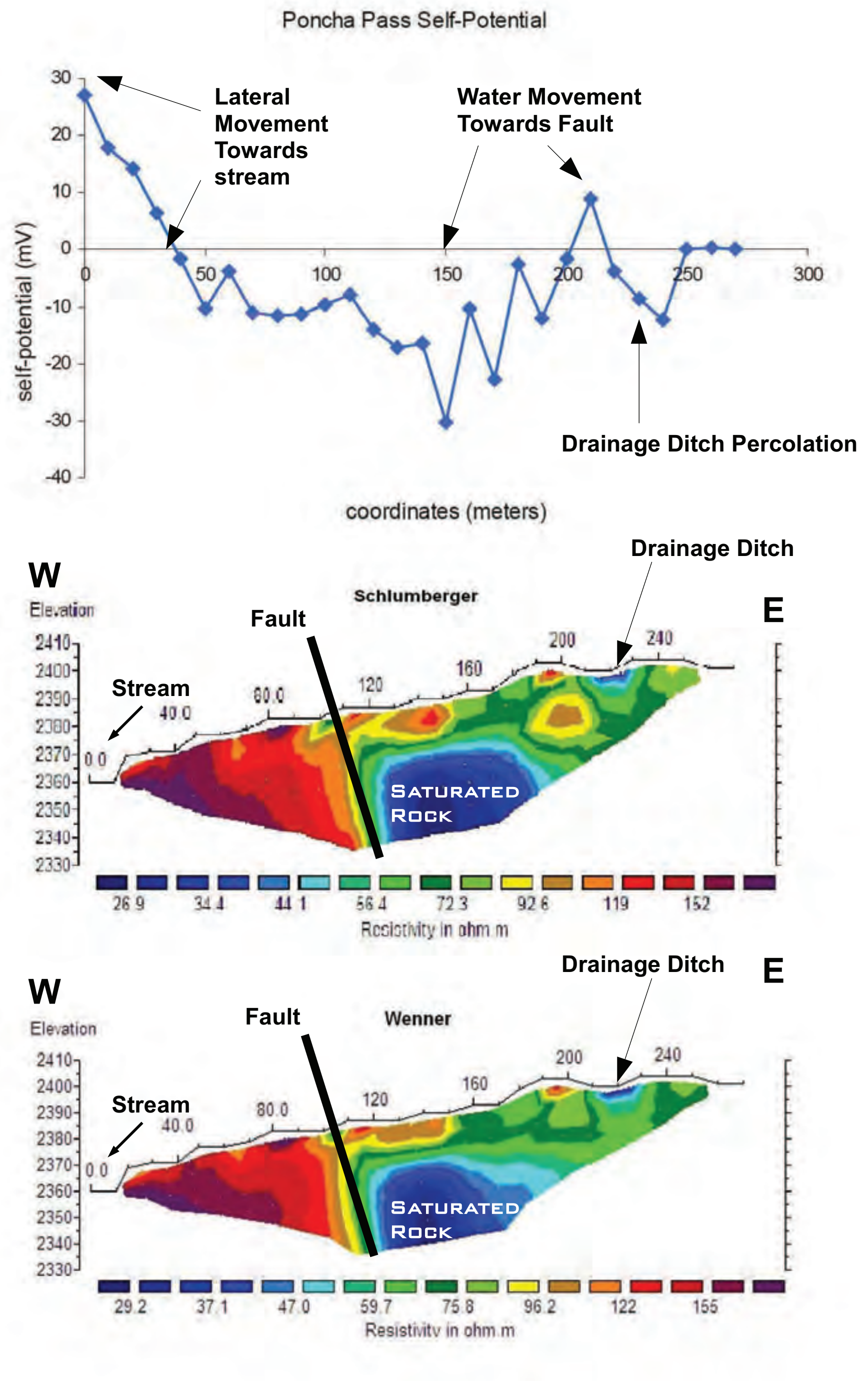

Figure 6.5: *Results of the Wenner and Schlumberger arrays done by the SuperSting, and the results of the SP survey done on the same line (line A).*

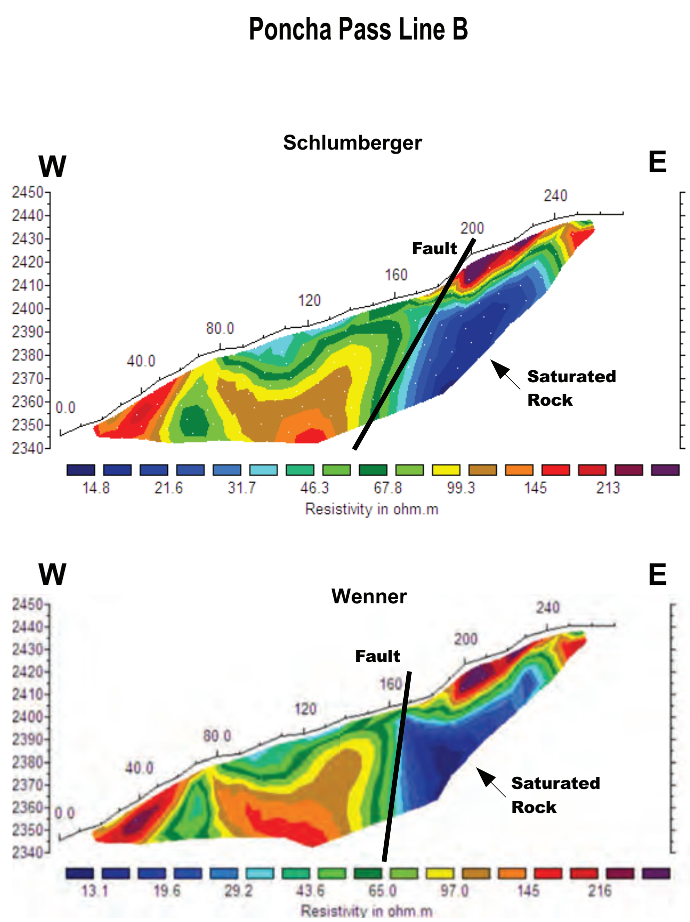

Figure 6.6: *Results of the Schlumberger and Wenner arrays executed on Line B by the SuperSting.*

apparent difference between Line A and Line B is the orientation of the fault. Both lines show a near vertical fault, however in line A, the fault is dipping towards the west and the fault is observed to be dipping east in Line B.

6.3.3.3 ABEM Line

In Fig. 6.7, the results of the Wenner array and self-potential profile for Poncha ABEM are shown. These correlate with Line A and Line B as well as the known geological setting.

A fault zone is seen near 860 m, which separates saturated rock with more resistive rock. Corresponding to the location of the hot springs, the self-potential profile displays an upwelling of water near 400 m that continues until 800 m.

Since two of the three lines were preformed parallel to the main faulting zone, a proper interpretation must continue to be vague. The area is heavily faulted, which acts as a pathway for the upwelling water. Once the water reaches the surface, it flows downhill with gravity as a driving force. This is unlike the pattern observed at Mount Princeton.

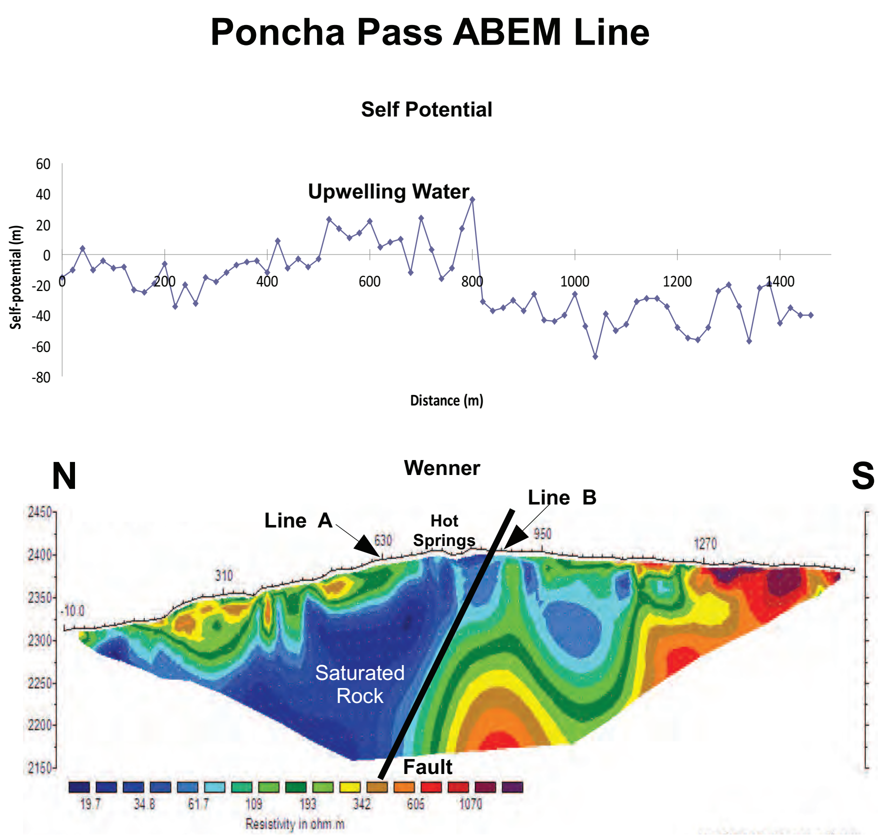

Figure 6.7: *Results of the Wenner array and self-potential profile for Poncha ABEM.*

Chapter 7

Chalk Cliffs

The Chalk Cliffs were identified by previous investigations as a site for further study. Resistivity and self-potential studies have previously found that the subsurface of the Chalk Cliffs contains upwelling water.

7.1 Resistivity & self potential

7.1.1 Acquisition

Three lines were acquired at the Chalk Cliffs; their positions are indicated in Fig. 7.1. The lines were designated CC1, CC2 and MP1. Measurements were taken at 20 m intervals along each line. The CC1 and CC2 lines were positioned so that they crossed the proposed shear zone fault, indicated by the dashed line on Fig. 7.1.

7.1.2 Data reduction

Please refer to the Appendix for detail on specifics of processing the raw data.

7.1.3 Results & interpretation

CC1 DC resistivity and SP profiles, shown in Fig. 7.2 clearly show the shear zone fault proposed in Fig. 7.1.

According to the DC resistivity pseudosection as seen in Fig. 7.2, there is a fault dipping to the south that correlates well with the placement of the proposed shear fault zone. The SP trend indicates that water is flowing downhill towards the south.

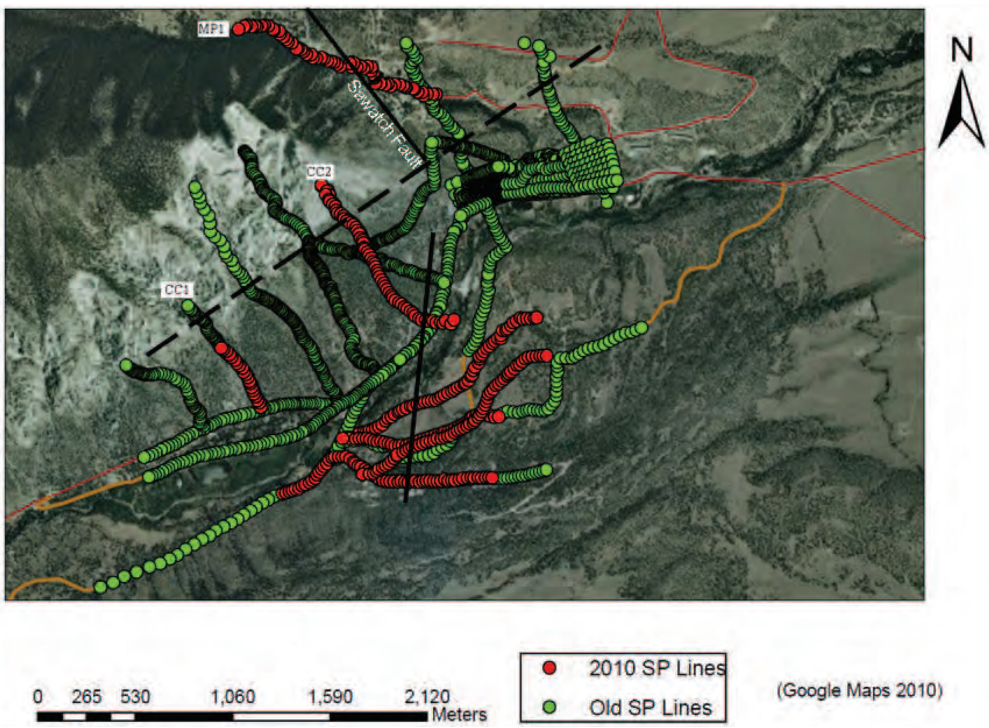

Figure 7.1: *A map showing past and present DC and SP lines. The area of interest is the Chalk Cliffs area, which is along the northern portion of this map. DC and SP profiles were acquired along the same lines. Three profiles were conducted, they are labeled in red as CC1, CC2, and MP1. Two known and one proposed fault are indicated on the map.*

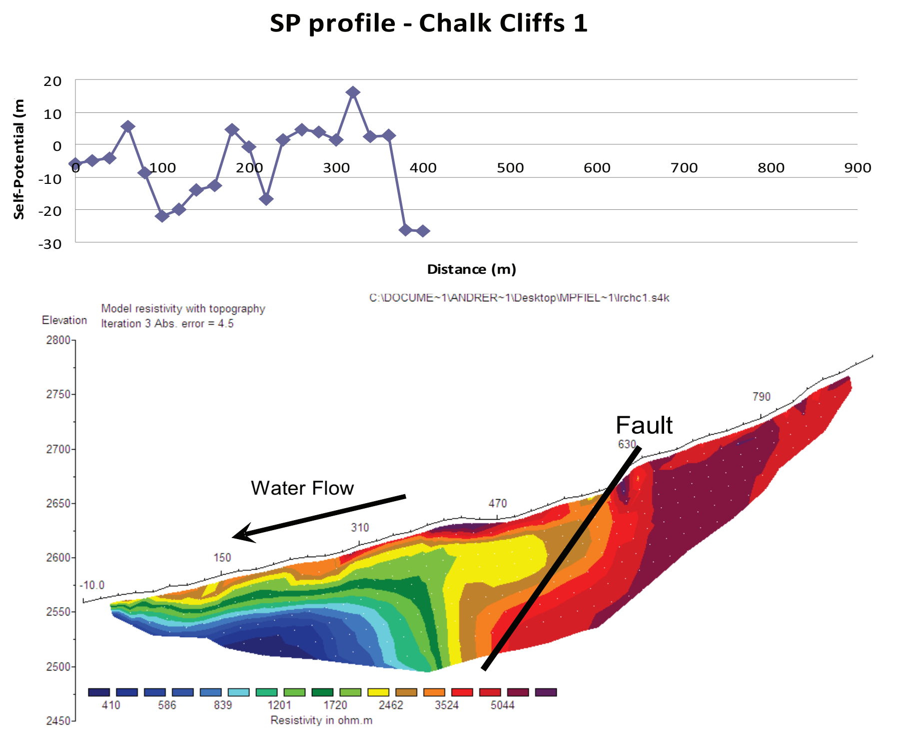

Figure 7.2: *SP and DC resistivity profiles taken along line CC1. The SP profile is displayed on top and DC resistivity on the bottom. North is to the right of the diagram. Length and height are measured in meters.*

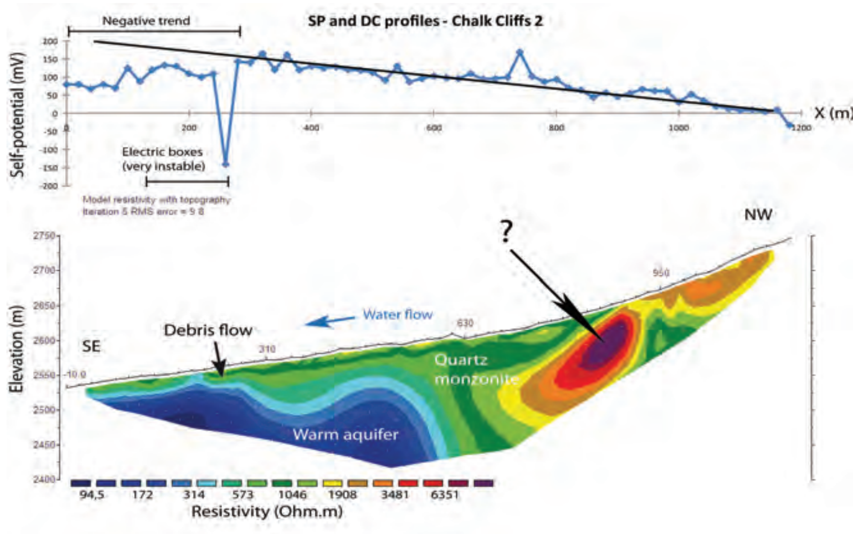

Figure 7.3: *SP and DC resistivity profiles taken along line CC2. The SP profile is displayed on top and DC resistivity on the bottom. North is to the right of the section. Length and height are measured in meters.*

CC2 DC resistivity and SP profiles, shown in Fig. 7.3, clearly show the proposed shear zone fault. The SP and DC profiles for line CC1 are in agreement with those generated for line CC2.

According to the DC resistivity pseudosection as seen in Fig. 7.3, there is a warm aquifer represented by the blue and altered granite (Quartz Monzonite) represented by the green and yellow. There is nothing in the DC resistivity section that represents a fault. In accordance with surface observations, there is a distinct portion of the DC resistivity pseudosection that is indicative of a debris flow and is labeled in Fig. 7.3. In the SP data, there is an overall negative trend as we move uphill. Such an SP trend is indicative of water flowing downhill in the DC resistivity pseudosection. There is a rather large spike in the SP data, but is mostly likely an erroneous data point. There is no correlation between the SP data and the DC resistivity data around this anomalous spike.

There is a profound, highly resistive body located around x=900 m as is seen in the SP data as a negative anomaly. Most likely this resistive body is a highly weathered patch of Quartz Monzonite and evidence of geothermal activity in the area.

In accordance with observed geology, Line MP1 distinctively shows the Sawatch Fault in the DC Resistivity pseudosection. Please refer to Fig. 7.4.

In accordance with known geology, the position of the fault in the DC resistivity pseudosection is in agreement with the position of the Sawatch fault. Unfortunately, the SP data is rather

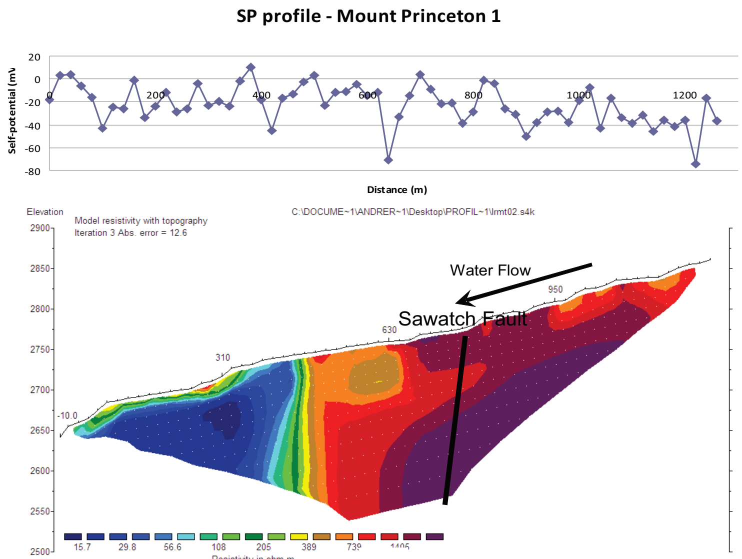

Figure 7.4: *SP and DC resistivity profiles taken along line MP1. The SP profile is on the top of the figure and DC resistivity is on the bottom. North is the top of the diagram.*

noisy. However, there is an apparent positive trend in the SP data traveling downhill. Such a positive trend in the SP data is indicative of water flowing downhill.

7.1.4 Summary & conclusions

Combining both DC Resistivity and SP methods provides a great deal of information about the structure of the subsurface, the flow path of geothermal water, and the extent of the geothermal anomaly in the Chalk Cliffs area. The Sawatch Fault is visible in the Mt. Princeton section. Within the two Chalk Creek profiles there is evidence of faults within the transfer fault zone in the granite of Mt. Princeton batholith. The DC resistivity profiles show evidence of altered granite, or quartz Monzonite, which is evidence of geothermal activity in the area. In conjunction with the evidence of groundwater movement in the SP profiles, the DC resistivity profiles clearly demonstrate that there is a high degree of geothermal activity in the area.

Chapter 8

Green Creek

8.1 Magnetics

8.1.1 Acquisition

Three single-line surveys were conducted at Green Creek. A major consideration during acquistion and processing was that all the flags marking the data collection points were metal-stemmed, which produces magnetic anomalies that will need to be filtered. Additionally, there were numerous artifacts and sources of noise (such as pipes, cans, power lines, houses, wires) randomly spaced along the sides of the survey points that could lead to noisy data. The terrain was rugid at points and lead lead to an irregular spacing of data collection points, reducing the reduancy and density of coverage of the survey (interpolation of data points during processing can resolve this issue).

Each line at Green Creek was spaced 30m between flags. Two lines followed the acquistion path of the Deep Seismic surveys. These lines were labelled as the 1000, 2000 and 3000 lines. The survey locations can be seen on Fig. 8.1.

The 1000 line had 144 stations, with 30m spacing, and went from station 1100 to station 1244. The survey was done three times, due to poor base station data for the first two tries. The first two unusable datasets were collected on May 18 and May 19, the final dataset collected on May 21, 2010.

The 2000 line had 70 stations, starting at station 2120 and continuing to 2050 with 30m spacing between stations. This survey, like the 1000 line, was performed three times due to poor base station data. The first two unusable datasets were collected on May 18 and May 19, the final dataset collected on May 21, 2010.

The 3000 line was acquired only once on May 22, 2010. However, due to time constraints and the fact that there would be no gravity to correlate it to, the line was not processed or interpreted.

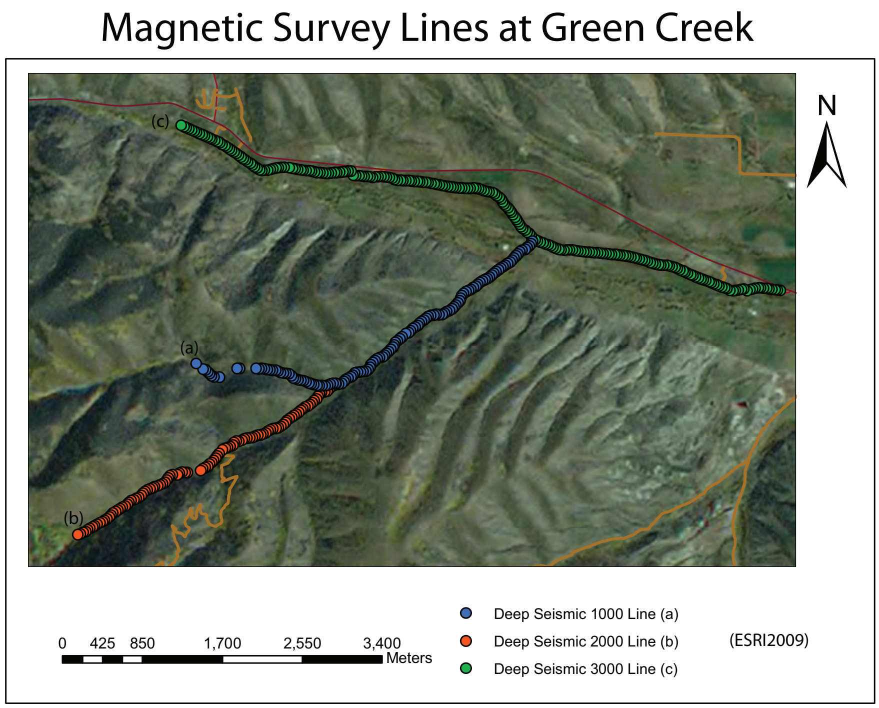

Figure 8.1: *Magnetics completed around the Green Creek area. All three lines were 30m spacing between stations. The blue line (a) is known as the 1000 line, the red line (b) the 2000 line, and the blue (c) line the 3000 line. This convention for naming has little significance other than to distinguish the three lines from one another; the surveys conducted at each were virutally identical. The 3000 line did not run the entirety of the marked stations, and instead only went as far as the paved road.*

8.1.2 Data reduction

8.1.3 Results & interpretation

8.1.3.1 1000 Line

In (a) of Fig. 8.2, the data was taken from west to east along a very long line. The line is extremely noisy when compared with the other sites. However, there are still some very noticeable trends. Firstly, the extremely large increase on the east side is likely to represent a fault due to the order of magnitude change in the measured magnetic field. The east side also contains a lot of metallic objects such as metal fences and cattle guards which could have

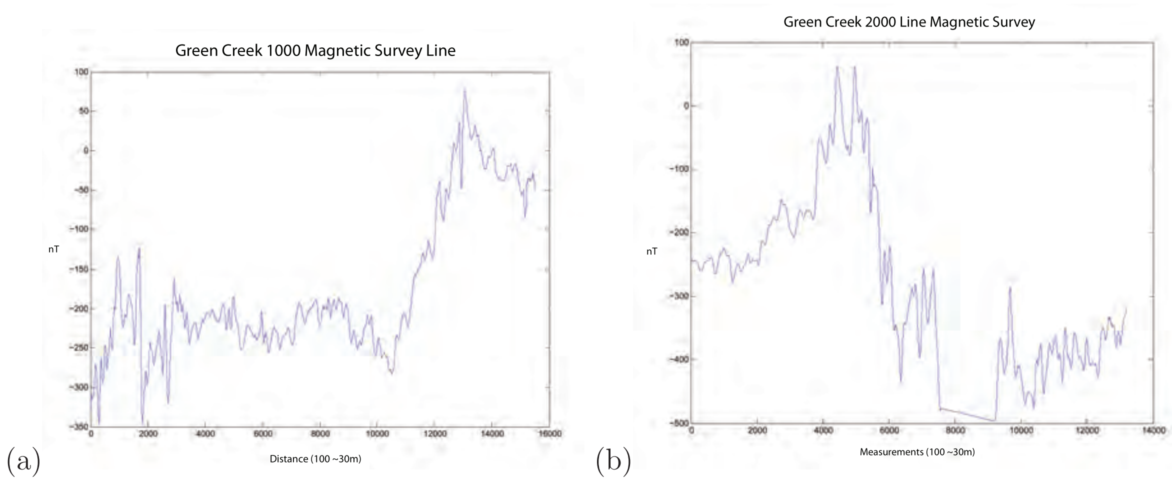

Figure 8.2: *Magnetic 1-D lines collected from Green Creek. (a) The 1000 line. (b) The 2000 line. Reference locations can be seen at Figure 8.1.*

contributed to the high frequency noise. The middle of the data is fairly smooth with the differences most likely coming from rugid terrain and some metallic objects. The west side of the plot is very noisy and is difficult to discern any definite trends.

8.1.3.2 2000 Line

In (b) of Fig. 8.2, the data was despiked because of the large amount of noise. The spikes in the data may be attributed to the proximity of the survey line to large outcrops of highly magnetic rock. The interpretation of the profile from measurement 7500 to 9200 is highly obscured due to this anomaly. The drastic increase in observed magnetic susceptibility near measurement 4000 - 5000 can either be interpreted as a fault structure or possibly some sort of intrusion of magnetic igneous rock. The east side of the line tended to be closer to metallic artifacts, which made the data less smooth.

8.1.3.3 Noise, Error and Uncertainty

Magnetic surveys are extremely sensitive to external noise. Most noise is the direct result of human objects (such as garbage) that contains metal. The best way to avoid interference with data is to take note of all unmoveable artifacts visible on the ground and note them later in the interpretation so they can be dealt with in processing. The other primary source of noise is diurnal variations in the Earth's total field which can be eliminated via the base station measurement of magnetic field during processing.

The primary source of error in magnetic data is human error. When walking, if sensors are not oriented properly (if the user does not hold the sensors directly above one another), or if a user jars the device during data collection, the result may be erroneous data.

Because magnetic data provides information on relative differences in magnetic susceptibility of different rocks, it can be difficult to determine the absolute values of susceptibility for subsurface rock formations. All results should be correlated with another geophysical method in order to ensure the highest quality interpretation. However, rapid changes in relative differences are indicative of faults and fractures.

8.2 Gravity

Green Creek is located in a known transition zone, though the precise fault location is currently unknown. Gravity can be easily used to detect large faults such as this.

8.2.1 Acquisition

Operation and transport of the gravimeter required two or three operators. The CG-5 had to be re-leveled at each station before a reading was taken. Two measurements were taken at each station, each one minute apart and then averaged. Gravity readings, times and standard deviations were recorded by hand in a notebook. As the weather was variable and stormy at times, notes were taken identifying which readings were most likely compromised by wind or rain. In order to be able to later correct the data for instrumental drift, which can be caused by temperature changes and extended periods use, each new stretch of survey taken was tied to the original station recorded with an additional reading recorded at the end of the survey.

The instrument used to conduct gravity measurements was the Scintrex CG-5 Autograv gravimeter. The measurement of the gravity field is based on measuring the acceleration of a fused quartz elastic system. The Scintrex CG-5, used to conduct the gravity surveys in the basin, gives relative gravity readings in mGals. The sensor type is a fused quartz using electrostatic nulling with a resolution of 1 microGal and it has a residual long-term drift of less than 0.02 mGal/day [13].

Gravity surveys conducted along Green Creek occurred from May 17th to May 24th, 2010. The survey line was 7.9 km with station spacing of 30m, and a can be seen in Fig. 8.3.

8.2.2 Data Reduction

In order to correctly display gravity data, the following steps must be taken:

1. Various corrections of data

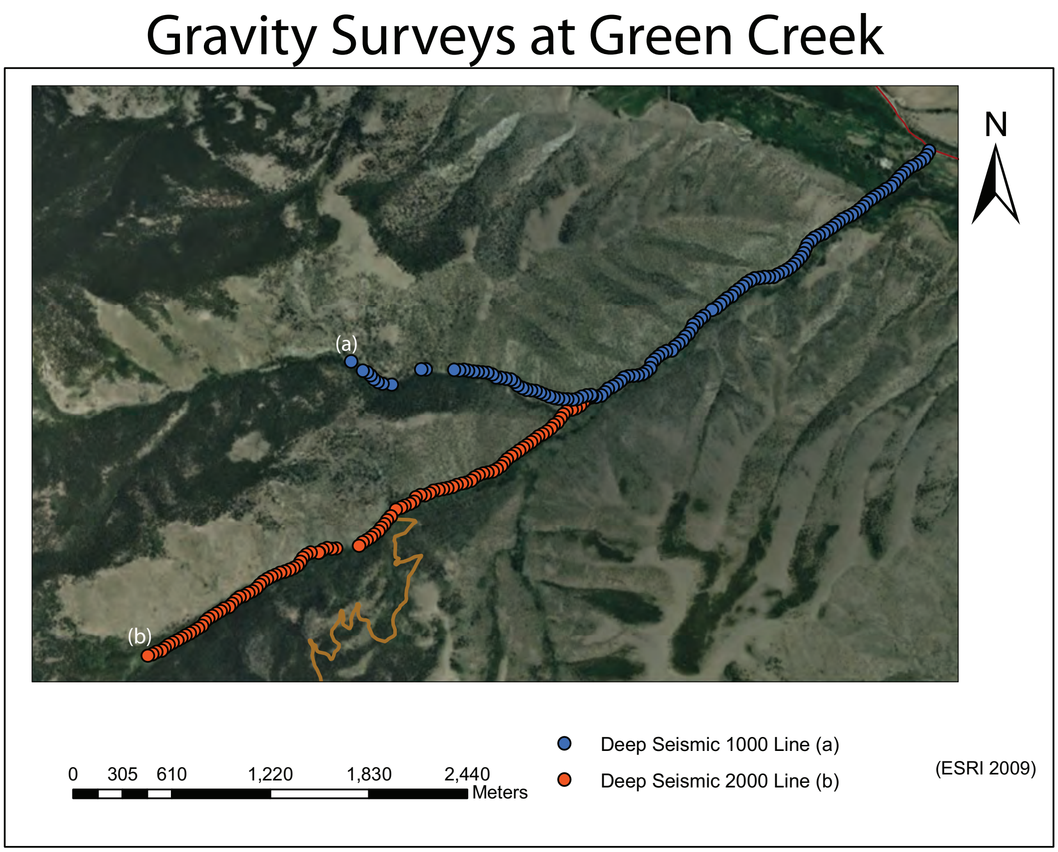

Figure 8.3: *1000 and 2000 lines at Green Creek on which gravity data was collected.*

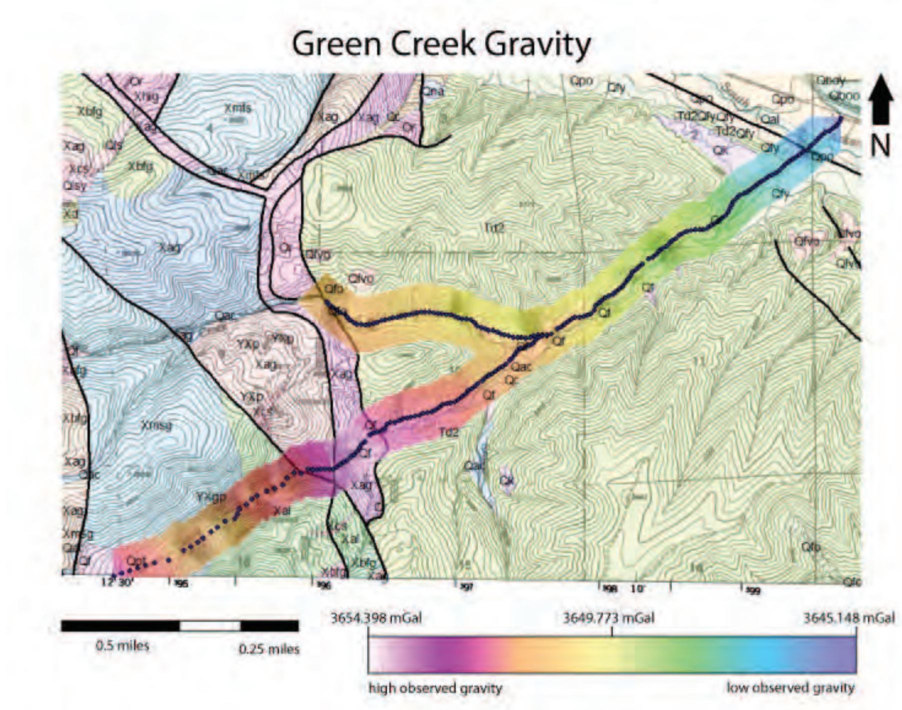

Figure 8.4: *Plot of gravity data on the deep seismic line, overlain on a geologic, topographic map.*

2. Static shifting of data so that general trend can be visible.
3. Data is plotted either as a profile or grid.

For a more detailed explanation, please see the Appendix F.

8.2.3 Results & interpretation

The plot of gravity lines in Fig. 8.4 taken at the Green Creek site is extensive and contains a wide range of variation. The expected general trend of lower gravity, less dense material, towards the centre of the basin is observed. The marked increase in the observed gravity near 12'30" 396, the purple high on the line, is suspected to be due to fault structuring.

8.3 Deep seismic survey

8.3.1 Acquisition

Data was acquired over two lines at Green Creek using two vibroseis trucks in tandem for near and far offsets. Line 2000 was acquired along a 6870m stretch of CR221 and line 3000 along a 5730 m stretch of CR220, shown in Fig. 8.5. The vibroseis truck maintained a separation of ∼2.1km during the survey corresponding to 70 channels, where each channel consisted of 6 geophones with a 5 m separation (Fig. 8.6). Table 8.1 describes the acquisition parameters for each line. Sweep lengths of 5 and 10 seconds were tested for data quality before surveying began. The seismic wavefield was sampled at 2 ms giving a f_N of 250Hz. An antialias filter was applied in the field to remove high frequency noise. The survey was desiged in such a way that the reciever arrays acted as spatial antialias filters to eliminate horizontally travelling waves (considered noise).

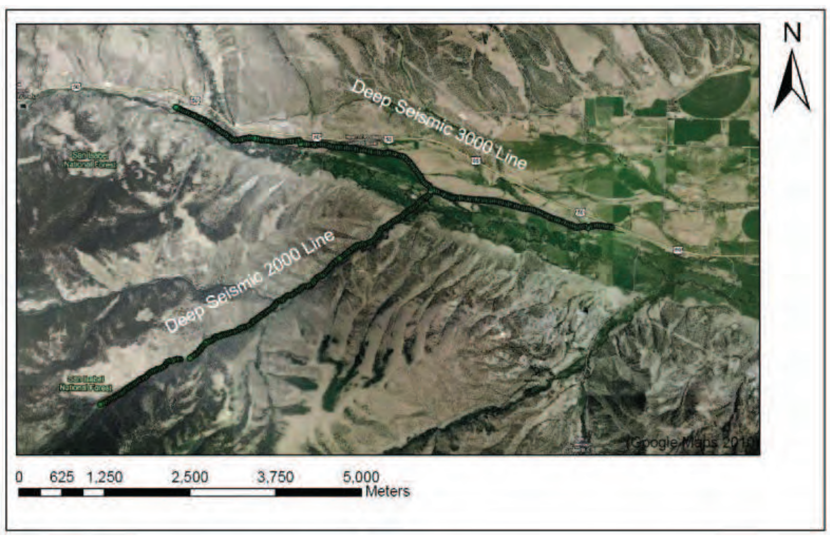

Figure 8.5: *Survey configuration for line 2000 along CR221.*

During acquisition on line 3000 a small number of shot points were omitted due to environmental considerations. Nearby residences prevented shots 3014-3016, 3036-3038, 3043-3045, 3081-3083 and 3092-3094. The presence of a winery prevented shots 3149 to 3151. Omissions also occurred on line 2000 at shots 1100-1106 and 1141-1144 due to nearby residences.

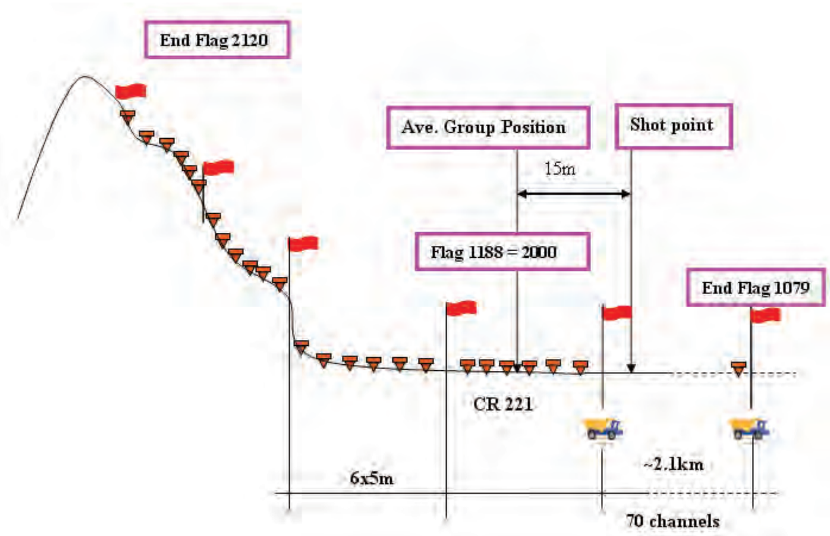

Figure 8.6: *Acquisition diagram for line 2000 along CR221.*

8.3.2 Data reduction

The acquired seismic data was processed at ION GX Technologies using the software package ProMAX. The non-uniformity of the topography as well as inconsistencies resulting from the acquisition phase is corrected during processing. The deliverable of the processing sequence is a meaningful and interpretable image of the subsurface.

Fig. 8.7 is an outline of the processing sequence that was carried out on both seismic lines. The processing parameters were kept constant for both lines being processed with minor exceptions. These differences will be pointed out throughout the discussion.

8.3.3 Results & interpretation

8.3.3.1 Line 2000

As expected from the observed geological outcrops, the seismic section of the line 2000 which extends along the county road 221 has a dipping event. It is dipping with an angle about 45 degrees to the North East and has been interpreted as a fault starting nearly at 950 meters from the start of the line. As shown in the interpreted section in Fig. 8.9, there are 4 main geological features: a major fault, the Dry Union formation, a displaced basement and the Precambrian basement. All these features have been interpreted based on strong reflections

Source type	vibroseis	vibroseis
Source array	double offset range	double offset range
Shotpoint separation	70 channels (2.1 km)	70 channels (2.1 km)
Shotpoint interval	30 m	30 m
Receiver	geophone	geophone
Group interval	30 m	30 m
Number of geophones per group	6	6
Near offset	15 m	15 m
Far offset	2.1 km - 4.2 km	2.1 km - 4.2 km
Recording system	Sercel	Sercel
Data format	SEGD	SEGD
Sample interval	2 ms	2 ms
Sample frequency	500 Hz	500 Hz
Record length	5000 ms	5000 ms
Sweep	5-80 Hz	5-80 Hz
Line length	6.87 km	5.73 km
Shooting direction	NE-SW	E-W
Number of shots	2080	2190
Maximum fold	150	150
First and last shotpoint	1100 - 2120	3001 - 3220
Receiver geometry	Linear	Linear

Table 8.1: *Survey acquisition parameters for line 2000 and 3000 at Green Creek.*

of continuous events. The fault, depicted in red, most likely extends to about 2 seconds. Everything below the fault in purple is believed to be a Precambrian basement. The top section is interpreted as Dry Union formation ending at 0.8 seconds deep and shown in yellow. The last section, in blue, is more likely to be a displaced basement. The uninterpreted seismic section is shown in Fig. 8.8 for reference.

8.3.3.2 Line 3000

Based on the best processed section so far, certain features are observed on the seismic section of the line 3000 that extends along County Road 220. As indicated on the section (Fig. 8.11) in red, the main fault runs from west to east starting at about 900 m from the west end of the line. The fault is dipping with an angle of about 60 degrees to the east, and extends to about 1600 ms. Three main formations are also identified, namely, the Dry Union formation, the displaced basement, and the Precambrian Basement. These three formation boundaries are interpreted based on the high reflectivity of continuous events on the seismic section, in addition to the observed geological outcrops in the survey area. The Dry Union formation is believed to extend down to about 800 s. The Precambrian Basement is seen at a TWT of

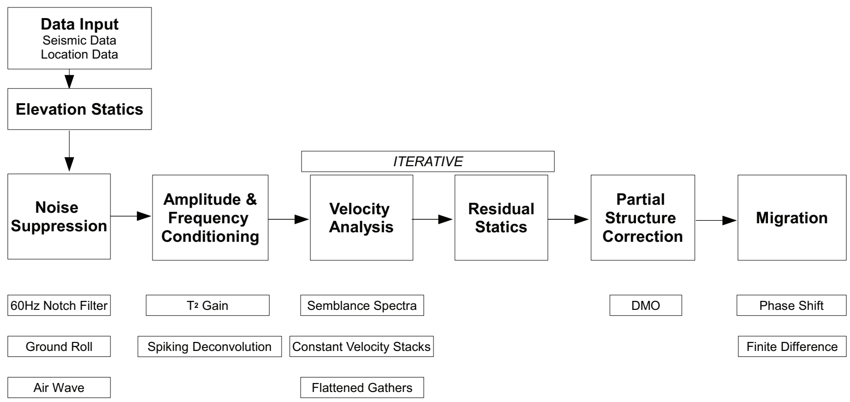

Figure 8.7: *Processing sequence flowchart.*

about 2000 ms. The uninterpreted section is shown in Fig. 8.10 for reference. Better estimates can be obtained by integrating the gravity and magnetic survey results together with the seismic survey results.

Finally, shown in Fig. 8.12 is the intersection of the two seismic lines. The listric fault observed on the line 2000 is seen on the seismic line 3000 as a continuous reflector. This is interpreted as the boundary between the Precambrian Basement and the Displaced Basement formations. It should be noted that for interpretation, the seismic lines were flipped with respect to the ones discussed in the processing sequence in order to correspond to the natural orientation. This facilitated the interpretation of our results.

8.3.3.3 Analysis of errors

Most geophysical problems have non-unique solutions. This implies that a geophysical problem can lead to diverse solutions. The solution to the geophysical investigation in this project is expected to have semblance to the geological interpretation of the region under study.

The difficulties in the integration of the geometries were corrected since data from the GPS and TDM were employed in the survey. Static corrections were applied to the data to adjust for the irregularity in the topography of the region. The effect of the near surface time delays owing to differences in elevations at each shot and receiver location was removed via static corrections.

Noise removal was applied to reduce errors. The automatic gain control (AGC) was applied to the data so that noise can be reduced. Noise removal involved the use of 60Hz notch filter to remove electrical interference. True Amplitude Recovery (TAR) approximately recovers amplitudes that are lost due to wavefront spreading in the earth (spherical divergence). Air

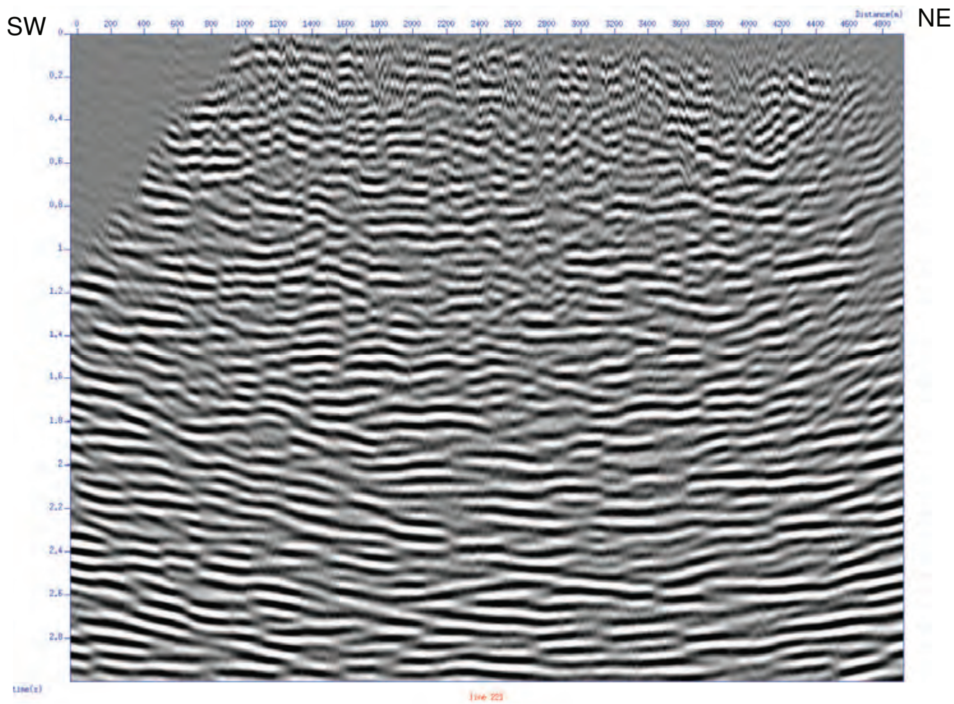

Figure 8.8: *The uninterpreted migrated section of the seismic line 2000.*

blast Attenuation searched for anomalous amplitudes based on a constant velocity and applied an inverse amplitude scalar based on surrounding traces. Surface Wave Noise Attenuation (SWNA) transformed the data from the T-X data to the F-X domain where adjacent traces were searched for a specified velocity and frequency to attenuate - a frequency dependant trace mix was performed based on parameterization. Time windows were converted to the frequency domain where frequency panels were examined for anomalous amplitudes. Amplitudes above a given threshold value were then normalized (ION GX Technology, 2010).

There were uncertainties in the course of picking velocities. In the processing part, velocities were manually picked by the team to the best of their knowledge. The picked velocities were smoothed to attain a velocity profile which was applied in later processing. Mute picking also contributed to the errors since it was done manually.

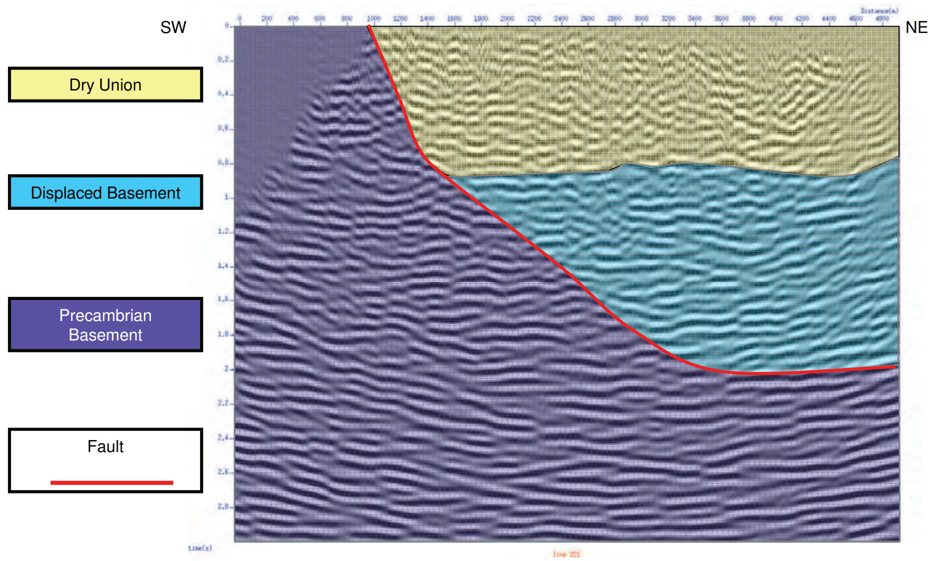

Figure 8.9: *The interpreted migrated section of the seismic line 2000.*

8.3.4 Summary & conclusions

The deep seismic technique was used to image the subsurface geology at a greater depth than any other known geophysical method. The results from our investigation complement existing geological models as well as previous results obtained from seismic surveys done in the Upper Arkansas Valley.

During processing of the deep seismic data, several corrections were applied to the raw data. Noise was minimized so that the true reflectivity from the Earth's subsurface was not obscured. Owing to local heterogeneity and geological complexity within the transfer zone, simplifying assumptions about the rock formations physical properties and elastic behaviour were made which were inherent to the majority of the processing steps so that usable images were generated for interpretation purposes.

Listric faults were mapped in the region. As expected from the observed geological outcrops, the seismic section of the line 2000 which extends along County Road 221 has a dipping event. It is dipping with an angle about 45 degrees to North East and has been interpreted as a

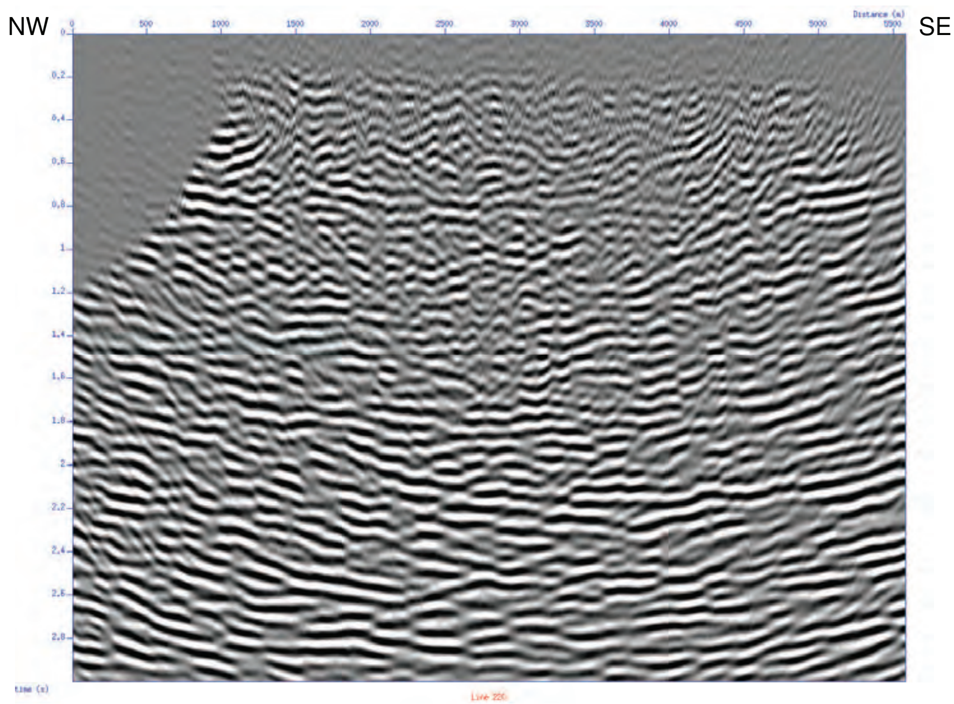

Figure 8.10: *The uninterpreted migrated section of the seismic line 3000.*

fault starting nearly at 900 m from the beginning of the line.

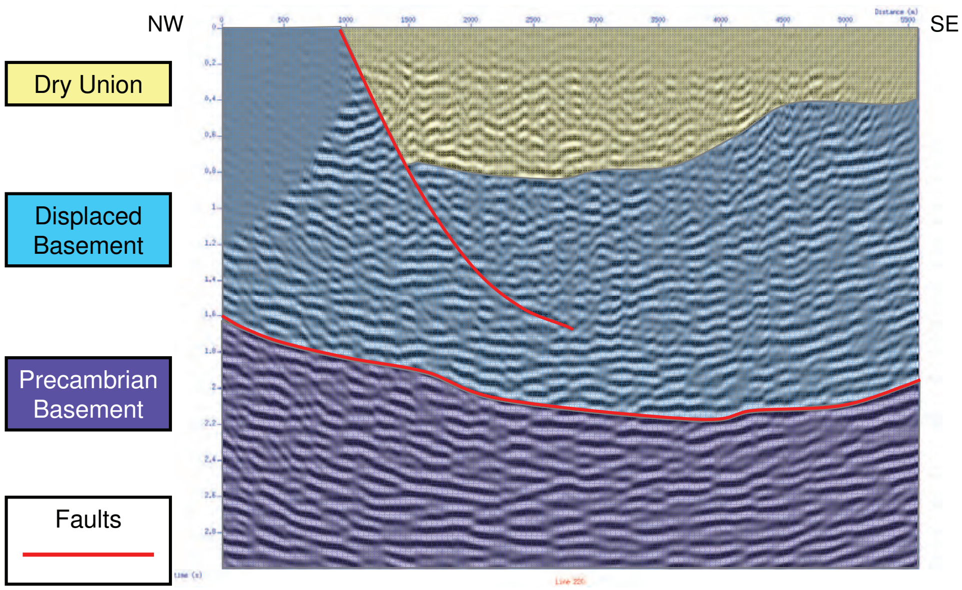

Figure 8.11: *The interpreted migrated section of the seismic line 3000.*

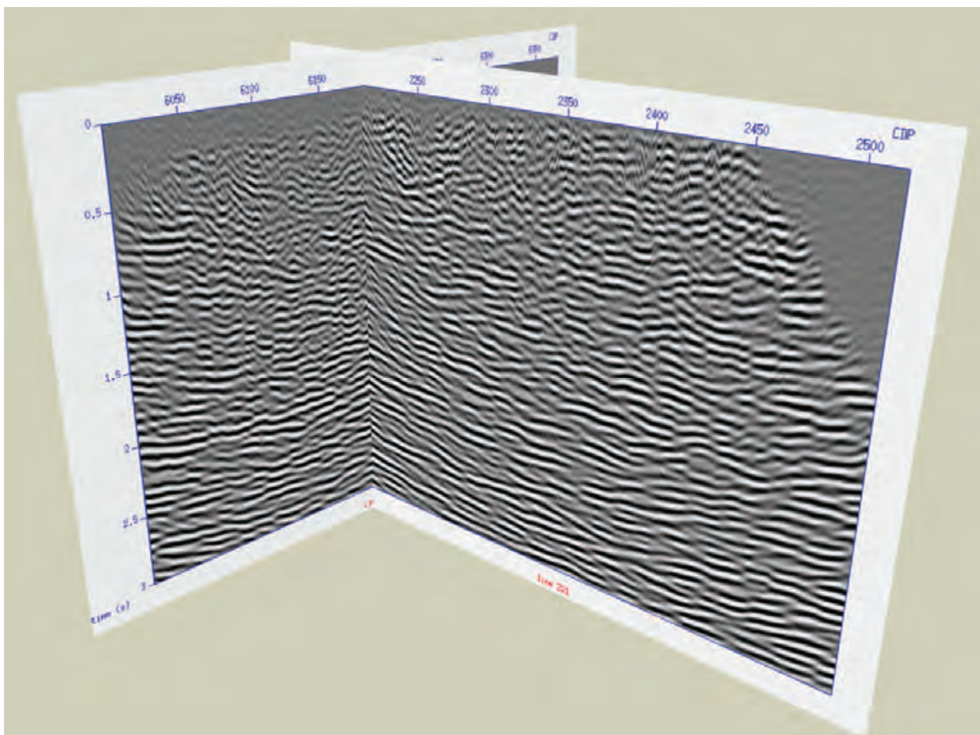

Figure 8.12: *A 3D image of the intersection of the seismic lines 2000 and 3000.*

Chapter 9

Synopsis

9.1 Dead Horse Lake

9.1.1 Background

The Dead Horse Lake area and surrounding region is a transition zone between two major north-south trending faults along the Collegiate range. These faults are offset from one another, but have the same characteristics. Hot and cold springs are present in the area, but the mechanisms that control the spatial distributions of hydrothermal fluid pathways are poorly understood. Dead Horse Lake was an ideal place to analyze and hypothesize on the overall structure of the transition zone, and potentially suggest sites to drill for hot or cold water.

In order to characterize the subsurface, a variety of geophysical methods were used, including seismic, self potential, DC resistivity, refraction tomography, well logging, vertical seismic profiling, magnetics, gravity and electromagnetics.

9.1.2 Data interpretation

By combining all the results from each of the individual survey methods, a cross section through Dead Horse Lake has been generated, shown by Fig. 9.3, and a final interpretation of the major faults in the region has also been constructed, shown by Fig. 9.4.

From the VSP direct arrival the top basement interface is not a sharp change in rock properties; rather it exists as a gradational transitional zone of weathered granite overlying less altered granite with velocity increasing with depth. Determining the thickness of sediments overlying the basement and mapping depth to basement can not be determined from the VSP because of the shadow zone that exists due to the diffraction off the edge of the steel casing. Mapping of the basement proved effective using 2D refraction tomography which showed that the overall trend of basement deepening towards the south east. The basement surface is faulted with a lineation in the depth map indicating that the south western side of the basement has been uplifted relative to the north east. The trend of this fracture is offset slightly from well MPG-1. However, assuming that the fracture possesses dip, the fracture observed on the VSP record could correspond to this fracture plane. The significance of this is that there exists at Dead Horse Lake fractures which extend up through the unaltered granite through to the weathered layer indicating that there exist potential fluid pathways that are continuous through the granite. The increased drill bit rotation through this fault indicates the presence of poorly consolidated material which is likely to have high permeability acting as an effect conduit to fluid flow.

The 2010 Dead Horse Lake joint interpretation has improved the spatial mapping and understanding of a significant bounding fault to the east of the study area, shown in Fig. 9.3 and Fig. 9.44. This east bounding fault had initially been identified on the 2008 Deep Seismic Line which was interpreted as an extensional fault with basement down thrown to the east. This region of accommodation space had subsequently in filled with younger sediment. The change from shallow basement in the west to increased thickness to the east has resulted in a decrease in gravity. This rapid decrease in the magnitude of the gravitational field to the east across the fault plane correlates with a lineation in the magnetic field, Fig. 9.2. The large spatial coverage which magnetic and gravity surveying provides across the study area has enabled the fault trace to be mapped with a north-west to south-east orientation, corresponding to the orientation of the major Sawatch fault forming the western boundary to the Arkansas rift valley. Smaller faults which have the same extensional framework as the bounding fault have also been imaged by the shear wave survey and are consistent with the faults identified

The SP/DC resistivity profile across the bounding fault shows no positive SP deflection suggesting that there is no upwelling or migration across the fault at the depths of investigation which SP allow. However, because of the shallow depth of investigation it is unknown whether this still hold for deeper depths where there may be cross fault migration and fluid flowing through fractures in the basement on the others side of the fault. On the far eastern side of the SP profile there is an order of magnitude deflection in SP suggesting that there is fluid movement downwards. It is unknown whether this is connecting to a deep regional circulatory system or whether it is feeding a more localized aquifer within the sediments. Water from the surface could be migrating downwards along the fault plane into the sediments; however, this is unlikely due to the fact there is no negative deflection in the SP response.

An alternative interpretation of the regional circulatory system of water, completely independent of the SP results concerning fluid migration, is based on the existence of deep fractures and faults identified from the 2008 deep seismic line, the shear wave seismic line, VSP results and DC resistivity results. The east bounding fault juxtaposing the permeable sediments to the east and impermeable pre-Cambrian granite to the west has an undefined throw thus the total extent of it's depth of penetration is unknown. From the shear wave seismic, the bounding fault is observable at relatively shallow depths, approximately 20 m, but a number of unattenuated multiples and reverberations obscure the underlying granitic layers thus the bounding faults depth cannot be reliably defined. The deep seismic line acquired in 2008 also displays the bounding fault but low quality reflections and geological complexity obscure the depth of penetration. However, the downthrown bedrock to the east has generated accommodation space possessing a minimum thickness of approximately 200 m which suggests significant downthrow of the hanging wall side of the fault. Thus shallow interpretations of the bounding fault can be extrapolated downwards to greater depths (¿200 m), albeit with low confidence. This fault could therefore be intersecting deeper water migration which represents the lateral movement of water within a greater regional circulatory system. From the temperature logs from well MPG-1, the temperature of the rock formation at 200 m is approximately 70 degrees (with a temperature gradient of 0.33 degrees per m) which suggests that laterally migrating water beyond 200 m could be heated to high temperatures. From the VSP and hammer drop seismic profiles, a significant fracture was identified at approximately 130 m possessing a shallow angle of dip towards the east, shown in Fig. 9.1. The shear wave seismic at Dead Horse Lake shows that signal at depths greater than 130 m are more susceptible to attenuation, absorption and scattering (therefore loss of high frequencies and resolution) so that subtle fractures at depth are unidentifiable. However, this high permeability fracture may penetrate to greater depths towards the bounding fault with a potential connection of the two at an unknown subsurface location. Therefore, this fracture could be acting as a significant conduit for hot water flow essentially tapping into the circulatory water system and allowing hot water migration towards the surface. The shallowness of the fracture detected in the shear wave seismic profiles suggests that its termination point may be outside the proximity of our survey area. Therefore, the hydrothermal fluid pathway could be allowing water to reach the surface as a hot water seep to the west of Dead Horse Lake region.

EM 31 data, only measures to 6 m depth. The anomaly seen on the EM data directly corresponds to an area of recently drained lake fill. The near-surface sediments are therefore still water saturated, hence are conductive. To acquire more useful EM data in this region, the EM47 time domain instrument should be used. This can penetrate to greater depths, and also benefits from only measuring the decay secondary EM field. This method could potentially resolve the basement rock.

9.2 Hecla Junction

9.2.1 Background

The surveying goal for Hecla Junction was to understand the purpose of the anomalous warm water springs in the area. The area was of geologic interest due to its exposed basement rock and volcanics.

DC, self potential, electromagnetic and magnetic surveys were performed at Hecla Junction.

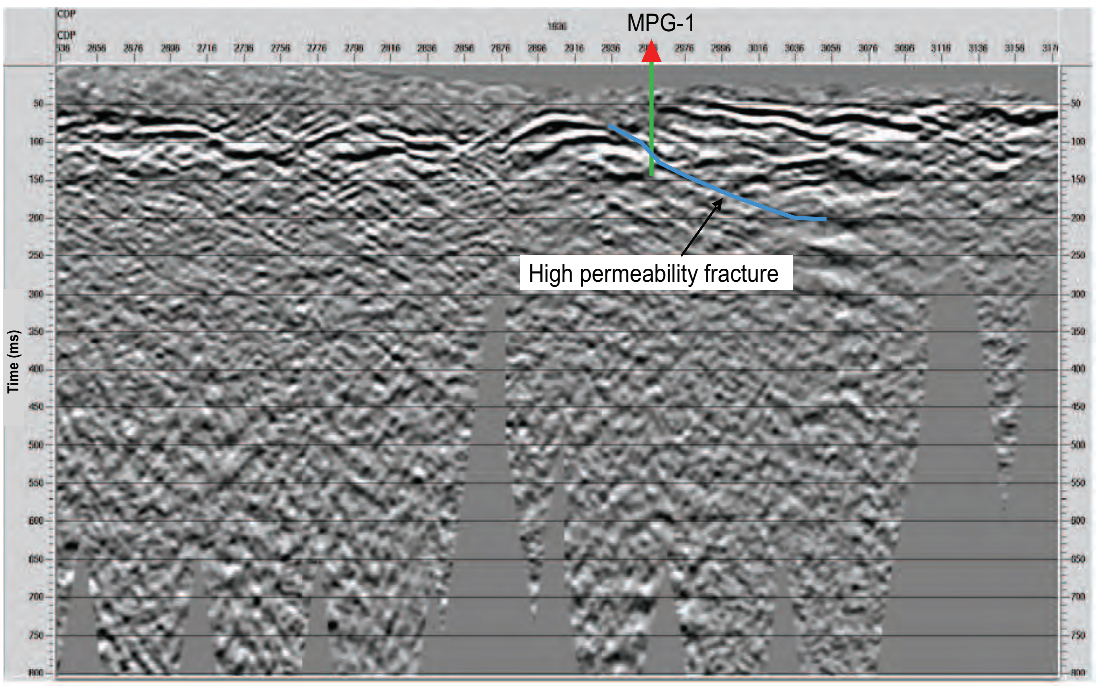

Figure 9.1: *Cross-section showing the stack from the hammer seismic survey showing the high permeability fracture through well MPG-1.*

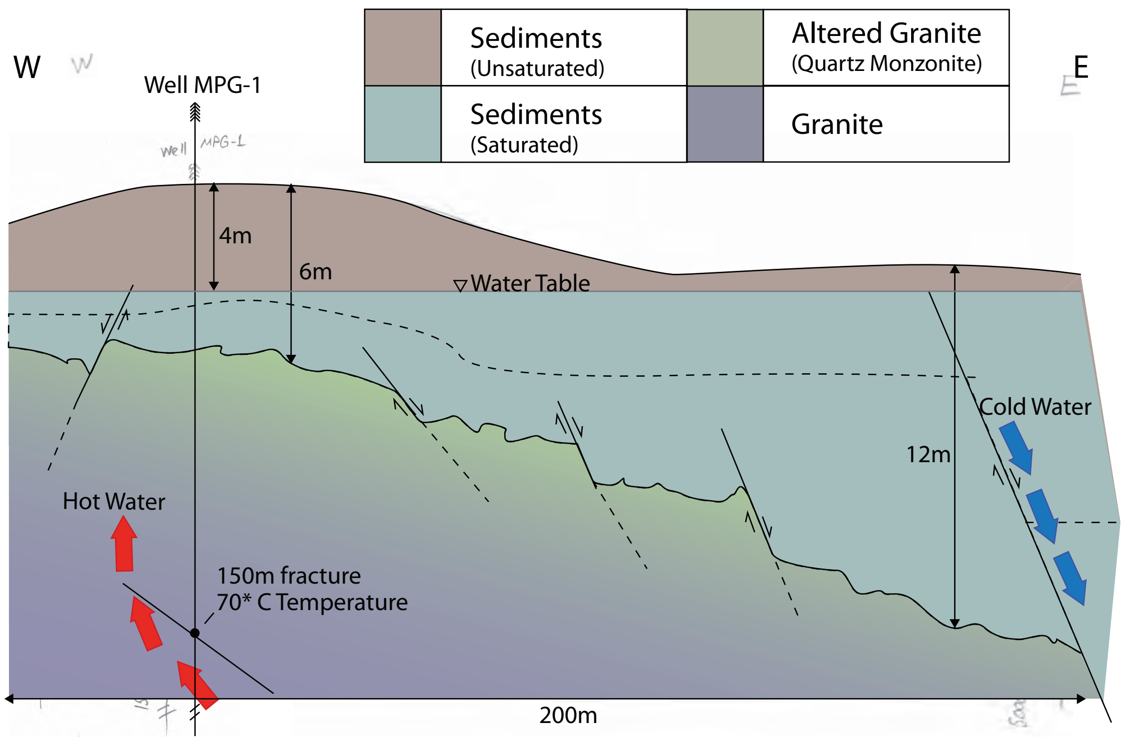

Figure 9.2: *Regional scale magnetic survey of Dead Horse Lake and surrounding regions. Points along lines 1-3 of the shear-wave seismic line have been superimposed with interpreted faults from each respective section.*

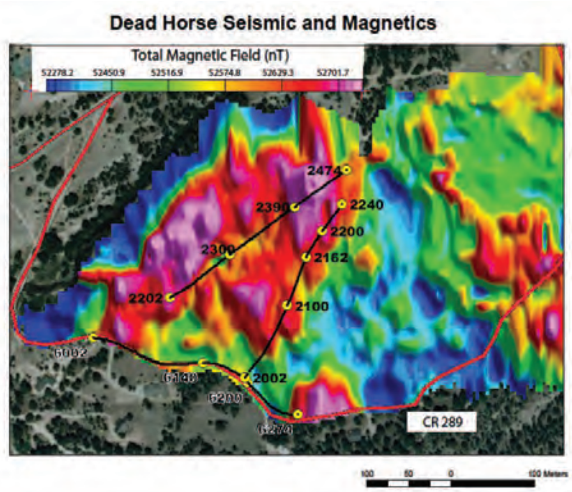

Figure 9.3: *Representative W-E cross-section of Dead Horse Lake.*

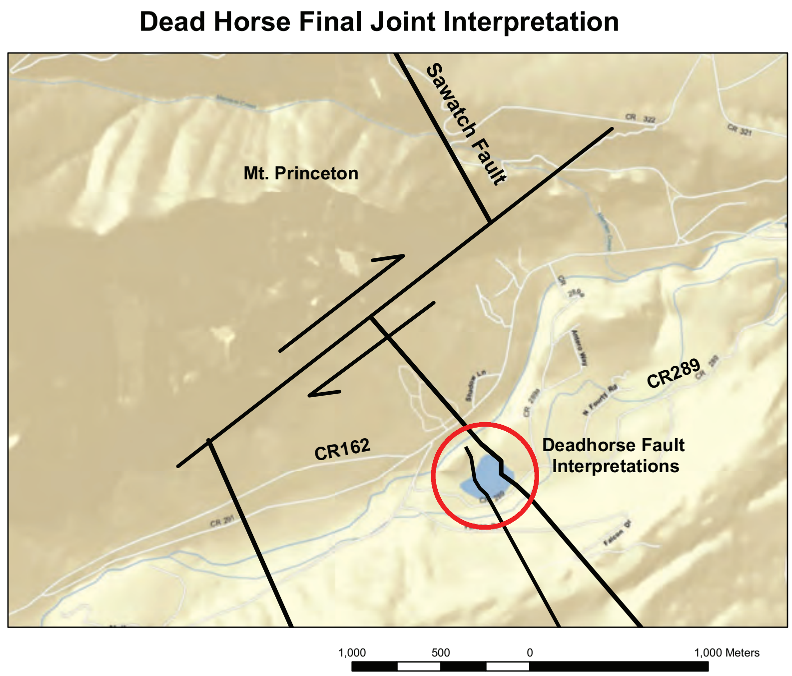

Figure 9.4: *Integrated interpretation of the Dead Horse Lake region.*

Fig. 9.5 shows the location of the 3 survey lines at Hecla Junction and one grid. The spacing on the lines was 10 m, and the spacing on the grid was 10 by 5 m.

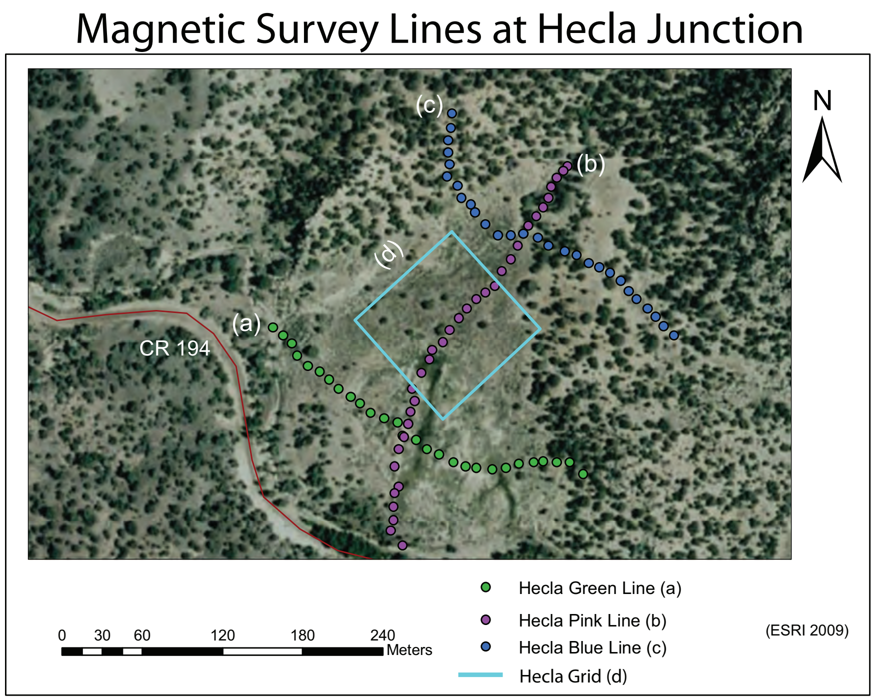

Figure 9.5: *Location of the surveys at Hecla Junction.*

Using DC, self potential and electromagnetics, water presence and flow direction was confirmed. Magnetic surveys were able to characterize the nature of the bedrock beneath surface sediments.

9.2.2 Data Interpretation

Fig. 9.6 contains the SP profile and the two inverted resistivity sections taken over the pink line in Fig. 9.5. These resistivity sections were made by splicing together two shifted, overlapping surveys of the same type. The blue areas (Fig. 9.6 b and c) correspond to zones of saturated sediment, which places the bottom of the saturated sediment at 20 m to 30 m deep. The self-potential profile (Fig. 9.6 a) demonstrates a general positive trend downhill, which is expected from a water table flowing downhill. The indicated local positive self-potential anomaly (Fig. 9.6 a) on the southern most end occurs near springs found on the surface, and the positive self-potential anomaly directly under the word 'upwelling' (Fig. 9.6 a) also occurs next to a spring.

Figure 9.7 contains the SP profile and the two inverted resistivity sections taken over the

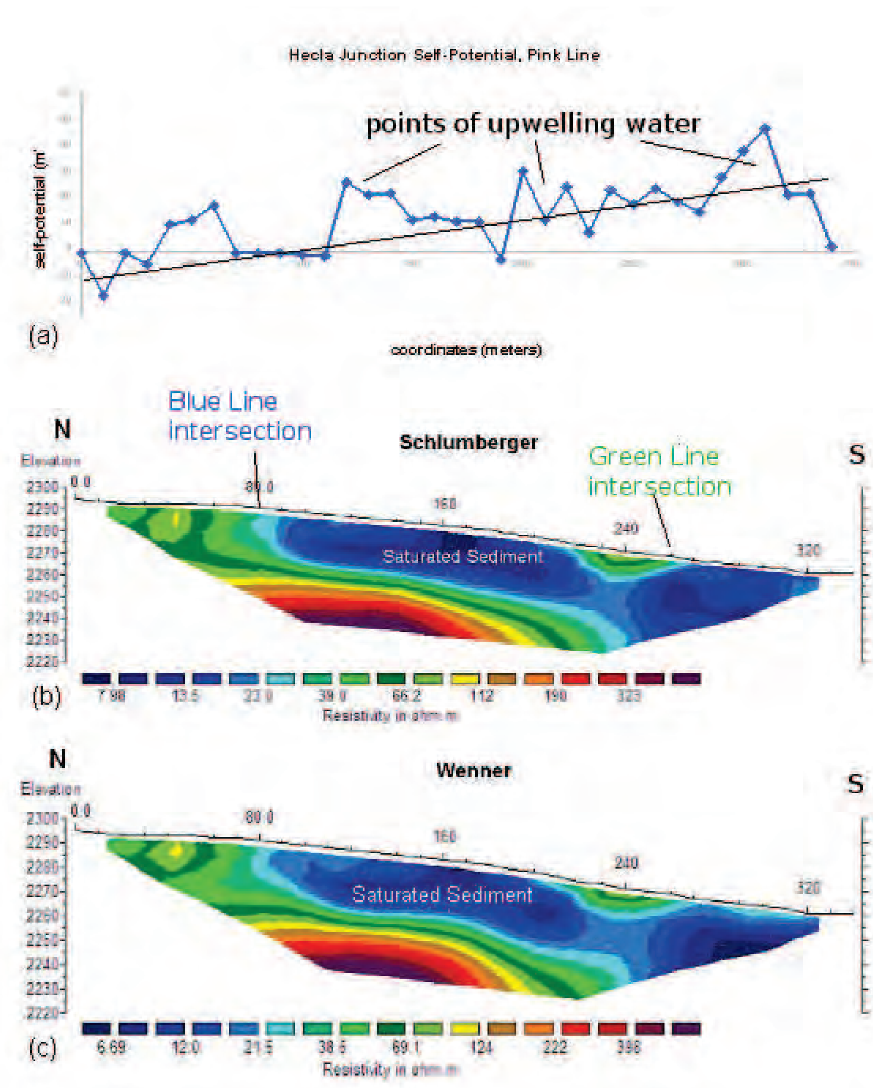

Figure 9.6: *The electrical surveys over the pink line: (a) the self-potential profile, (b) the Schlumberger resistivity inversion, and (c) the Wenner resistivity inversion. Schlumberger inversion parameters: 2 iterations, absolute error = 5.5%, vertical exaggeration = 1. Wenner inversion parameters: 2 iterations, absolute error=3.5%, vertical exaggeration = 1.*

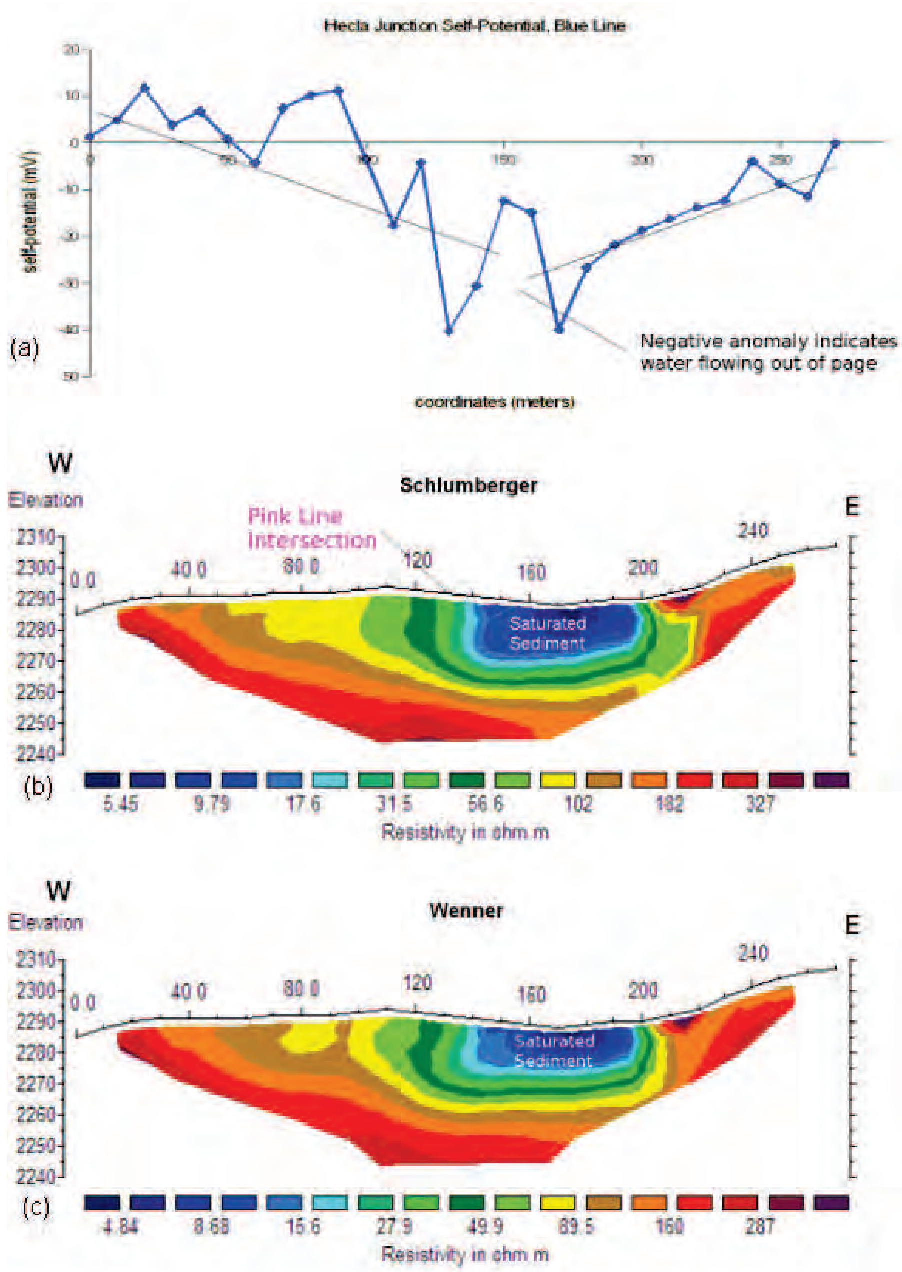

Figure 9.7: *The electrical surveys over the blue line: (a) the self-potential profile, (b) the Schlumberger resistivity inversion, and (c) the Wenner resistivity inversion. Schlumberger inversion parameters: 2 iterations, absolute error = 5.1%, vertical exaggeration = 1. Wenner inversion parameters: 2 iterations, absolute error = 5.9%, vertical exaggeration = 1.*

Blue Line (Figure 9.5). Blue areas (Figure 9.7 b and c) correspond to zones of saturated sediment. The SP profile (Figure 9.7 a) shows a sizable negative anomaly over this saturated zone, which generally indicates that groundwater is flowing downward at that location. This is expected, as the Pink Line's SP data (Figure 9.6 a) shows that the groundwater is indeed flowing downhill, towards the south.

Figure 9.8 contains the SP profile and the two inverted sections taken over the green line (Figure 9.5). The inversion images are slightly smaller than the previous inversion files, as some of the data points were lost. Again, the blue areas (Figure 9.8 b and c) correspond to saturated zones. In the Wenner image (Figure 9.8 c), there is a relatively conductive body that extends as a lobe from the larger saturated zone. Because there is no self-potential anomaly over this lobe feature, there is no water currently flowing through this zone. Therefore, this lobe feature could be the remains of a former groundwater flow path. It could also represent a wet, but unsaturated zone that results from surface water percolating downward. This interpretation is based on the presence of a spring directly uphill from the green line (see Figure 5). The electromagnetic (EM) survey showed a high conductive anomaly where the surface expression of the spring was located. The positive self-potential spikes on the eastern half of the blue line (Figure 9.8 a) indicate areas of upwelling groundwater. This is expected, as there were springs on the ground surface near those positive self-potential anomalies.

By combining the data from these previous plots, a diagram of the groundwater flow was made (Figure 9.9). The two large springs in the survey area occur within, or very near the proposed boundaries of the subsurface saturated zones. Included in this figure is the location of a proposed water well. This location was chosen because the saturated zone beneath it appears to be the deepest aquifer according to the resistivity sections, and because it is near a spring, where the natural water pressure could be taken advantage of.

The magnetic surveys conducted at this site mainly indicated the dipping of the Precambrian basement, which has higher magnetic susceptibility than the surrounding sediments. The bed appears to dip to the southeast, given that the higher magnetic susceptibilities were found in the northwest region of the magnetic grid (see Figure 9.9). This reinforces the flow direction determined by the DC and SP surveys.

9.3 Green Creek

9.3.1 Background

The seismic data was integrated with magnetic and gravity data as shown on Figures 9.11 and 9.12. This joint interpretation was carried out in order to restrict the number of plausible geophysical models. Two common features were observed on the gravity and seismic data models, namely the faulting and layered formations.

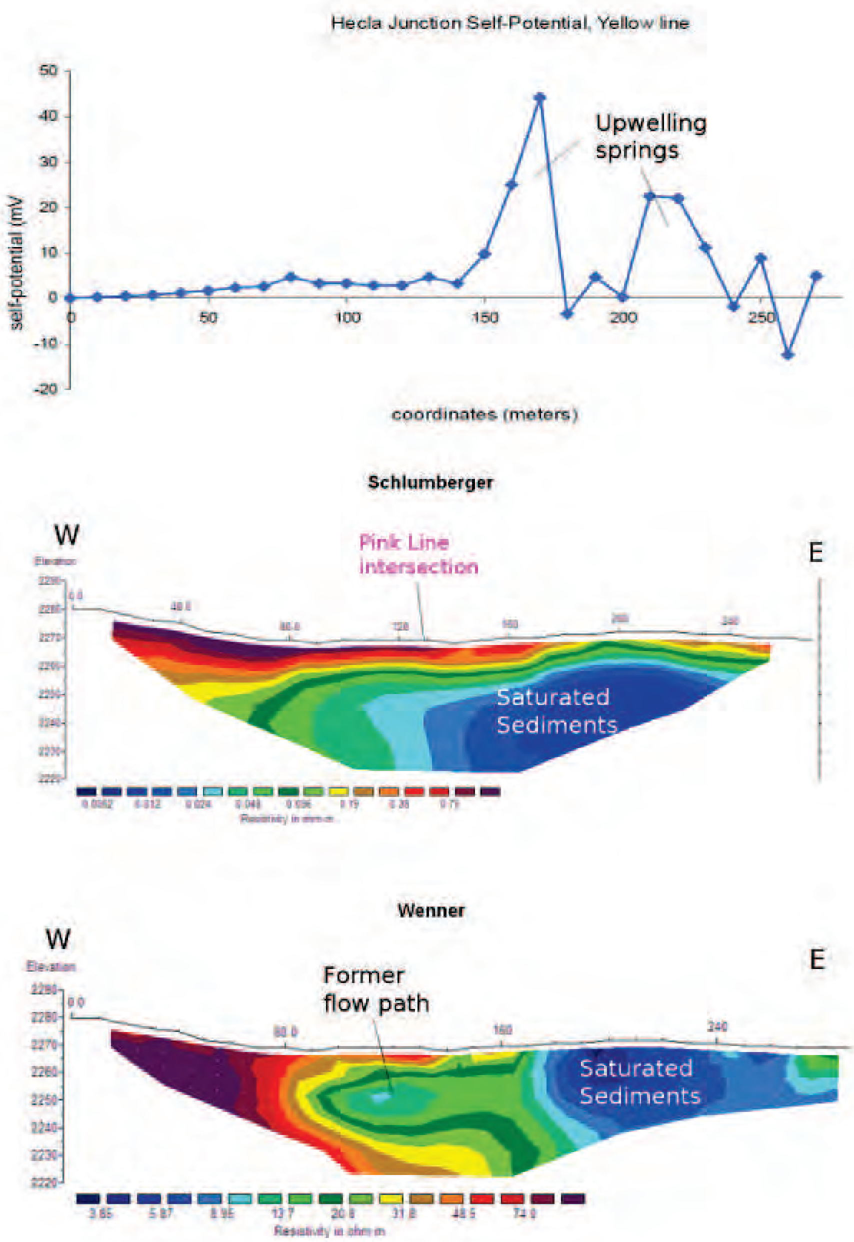

Figure 9.8: *The electrical surveys over the green line: (a) the self-potential profile, (b) the Schlumberger resistivity inversion, and (c) the Wenner resistivity inversion. Schlumberger inversion parameters: 2 iterations, absolute error = 22.5%, vertical exaggeration = 1. Wenner inversion parameters: 2 iterations, absolute error = 11.3%, vertical exaggeration = 1.*

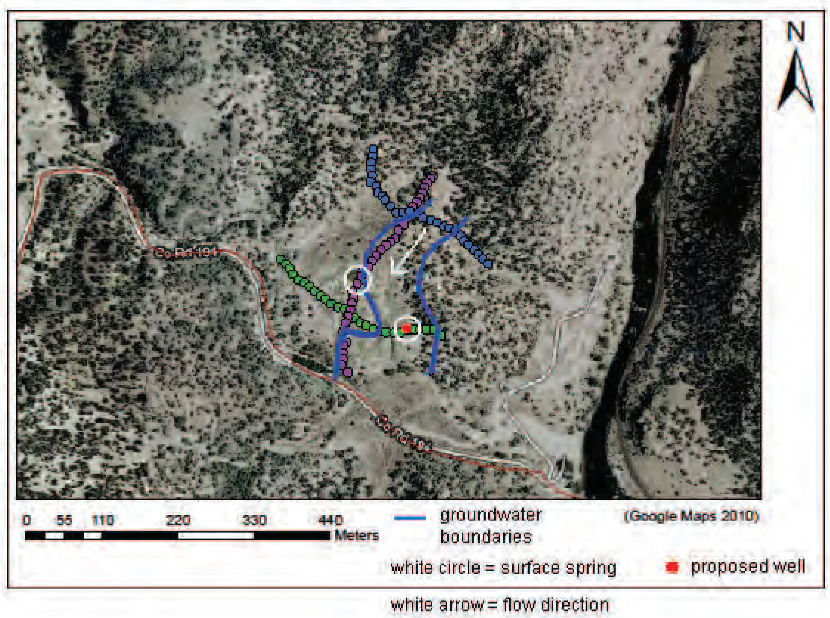

Figure 9.9: *A map of the proposed boundaries of the subsurface saturated sediment at depth and the groundwater flow direction, along with the location of surface springs and a proposed well location.*

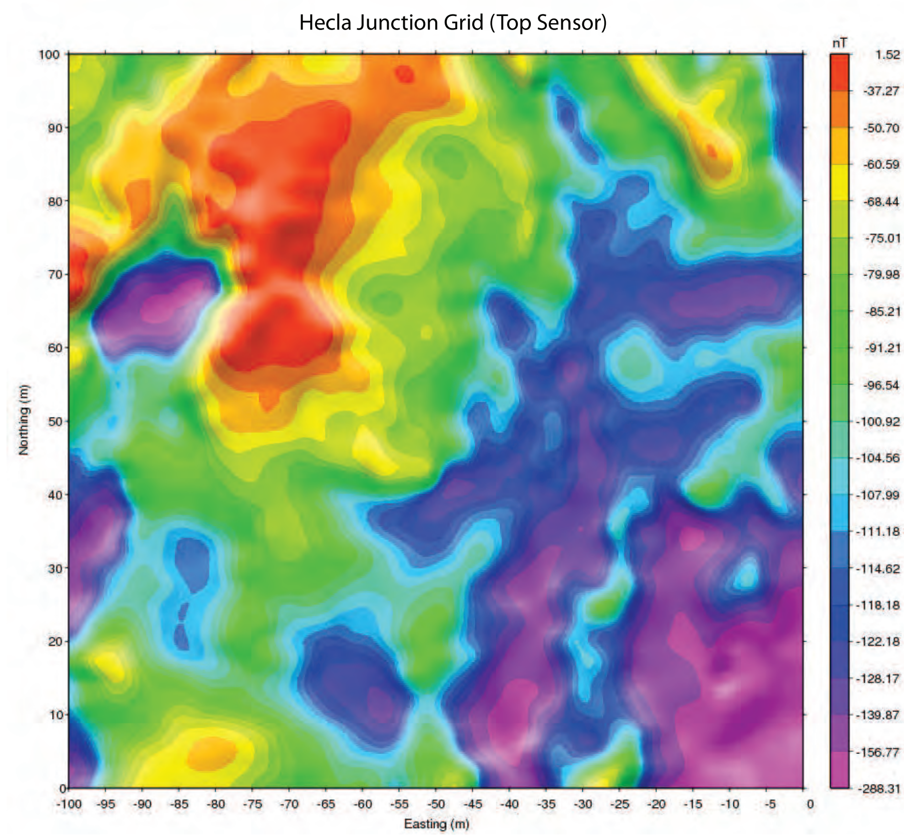

Figure 9.10: *Magnetic data from the top sensor at the Hecla Junction grid. Note the high zone in the northwest.*

9.3.2 Data Interpretation

The listric fault interpreted on the deep seismic line 2000 corresponds well to the observed the gravity trend. The gravity model was designed using the expected densities for the basement and Dry Union formation. The decreasing gravity values towards the NE of the line fit a gently-sloping fault. The glacial till deposits extending to the shallow SW area are not visible on the seismic section due to inaccessibility for the seismic trucks.

Our magnetic data contains many spikes, especially on the first half of the line to the SW. A plausible reason for this is the presence of volcanic boulders that were observed along the line in this same region.

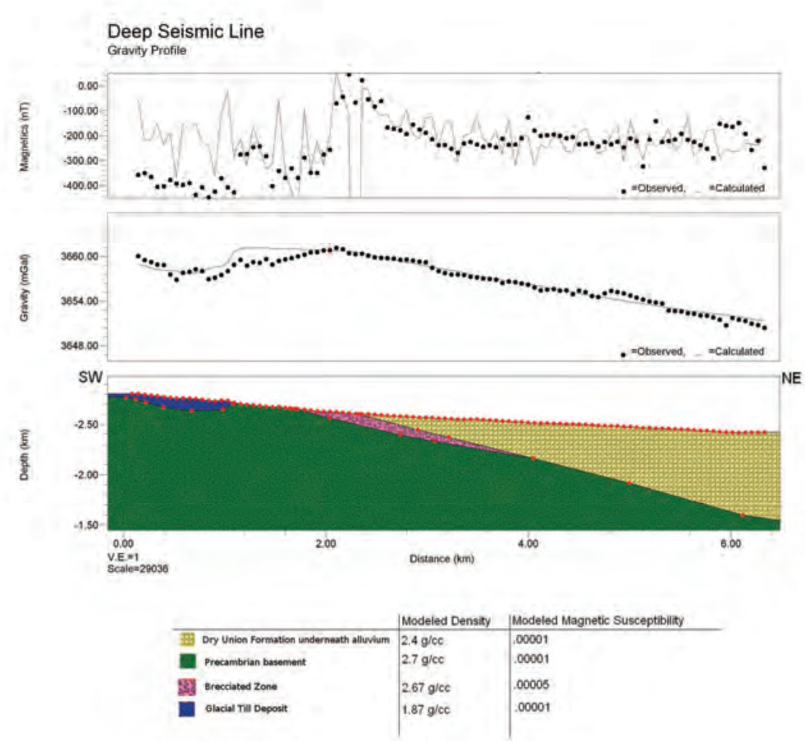

Figure 9.11: *Green Creek line gravity model, generated based on the measured gravity and magnetic data.*

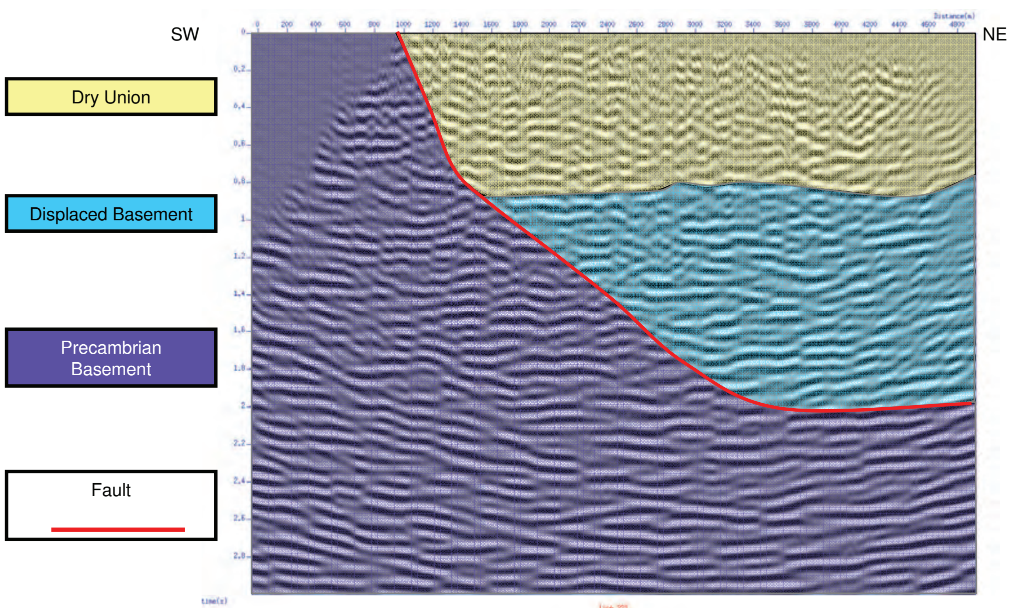

Figure 9.12: *Interpreted seismic profile of data obtained from Green Creek.*

9.4 Poncha Springs

9.4.1 Background

Five geophysical surveys were conducted at Poncha Springs: Supersting (DC Resistivity), ABEM (DC Resistivity), SP, EM, and Magnetics. The DC Resistivity and EM methods measure resistivity in the subsurface, and were used at this location to identify regions of fluid-saturated rock. SP, which shows the directional movement of fluids was used to characterize water flow. Magnetics were used to measure the magnetic susceptibility of the subsurface in order to help classify rock types. By using the aforementioned surveys together we hope to better understand the locations of faults, water saturated rock, and the movement of water in the subsurface.

As previously mentioned in the Geology section, Poncha Pass represents the transition zone between faults. They follow the same north-south trend but dip in opposite directions and are located on opposite sides of the valleys they bound. One theory is that the faults are connected beneath Poncha Pass in a horizontal structure, in which case we should see shallow-dipping faulting directly north and south of Poncha Pass. The faulting mechanisms and structure are poorly understood, but are especially interesting because these faults likely control the flow of water seen at the surface as hot springs and evidenced by tufa deposits, shown in Figure 9.13. Understanding the faulting would help us understand geothermal reservoir characteristics, and allow for better informed decisions about using this water in Salida.

9.4.2 Data Interpretation

Data has been collected by the 2009 field camp at Poncha Pass, but is not particularly meaningful because of the lack of survey data and unclear processing results. This year we used the same survey techniques in different locations, which can be seen in Figure 9.14 and hope to achieve more meaningful results.

Along Line A in (a) of Figure 9.15, we see an increase in conductivity to the east indicated by the EM Quadrature profile and Supersting pseudo-section. A large lateral contrast in resistivity around 100m on the Supersting pseudo-section corresponds to a steep decrease in SP measurements. This anomaly can be interpreted as a fault. SP supports this interpretation by showing water movement toward the interpreted fault. The Magnetics profile does not indicate a lithology change over the interpreted fault, and the minimal variations are interpreted to convey differing amounts of soil cover.

Along the ABEM line in (b) of Figure 9.15, the ABEM pseudo-section shows a large contrast in resistivity between 630m and 950m. SP measurements show upwelling water between 500m and 800m, then a sharp drop just after 800m. These observations, as well as a corresponding large dipolar anomaly in the magnetic data, suggest the presence of a fault. This interpretation is supported by the presence of hot springs on the surface.

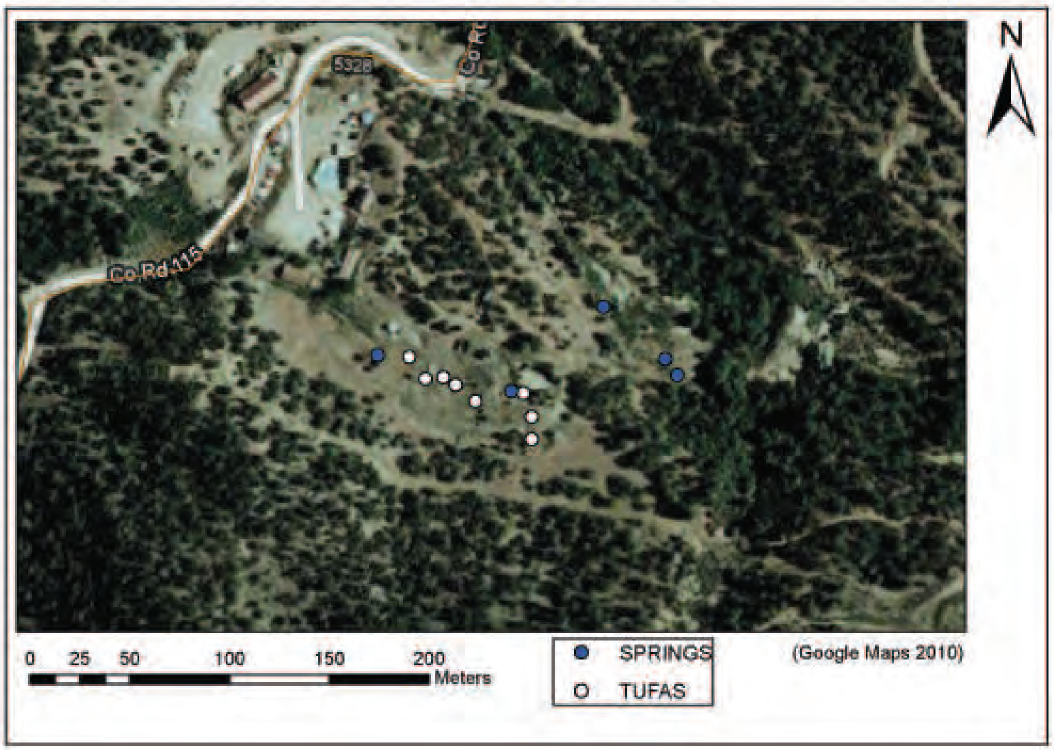

Figure 9.13: *Map showing the locations of springs and tufa deposits just south of the Boy Scout Camp at Poncha Pass. These features are likely controlled by the faults and are formed as water flows up the faults to the surface. The presence of tufa deposits indicates hot water, since this type of deposit is formed by the precipitation of silica from solution. This process requires water of significantly high temperature.*

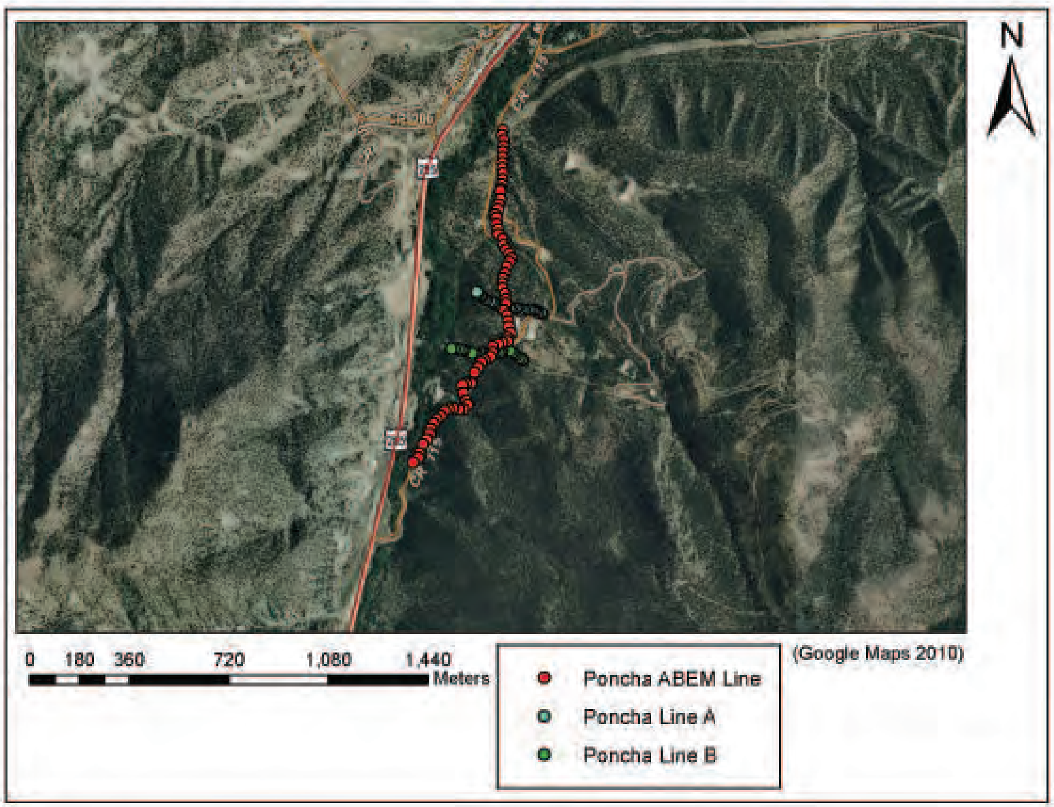

Figure 9.14: *Map showing the locations of the five geophysical surveys conducted at Poncha Pass. Along the ABEM line we collected ABEM, SP, and Magnetic data. Along Poncha Line A we collected Magnetics, Supersting, SP. and EM data. Along Poncha Line B we collected Supersting.*

Along Line B in (c) of Figure 9.15, Supersting pseudo-profiles show a large contrast in resistivity between 160m and 180m. This contrast is interpreted as a west-dipping fault.

All of the data collected at Poncha Pass supports the presence of faulting, possibly one fault that intersects the survey lines at an angle.

If one fault is inferred, the differing angles shown in the pseudo-profiles could be accounted for by a complicated viewing geometry, or apparent dip effects. This fault appears to trend roughly north-south. Another observation is that large areas of low resistivity in all the pseudo-profiles occur on the east and north sides. This inferred fault may control this change from low resistivity to higher resistivity. The observed low resistivity could be caused by water saturation, in which case the inferred fault would affect the movement of groundwater.

Another possibility is that the faults inferred at each survey line are not related or connected. This is entirely possible, as the Poncha Pass area is known to be heavily and complexly faulted.

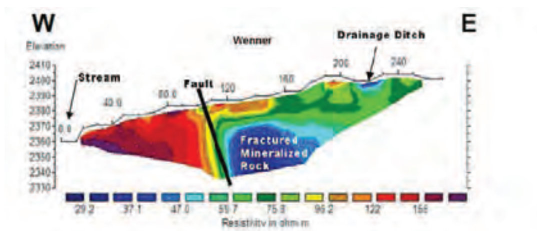

(a)

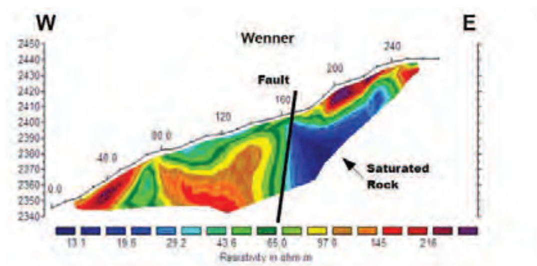

(b)

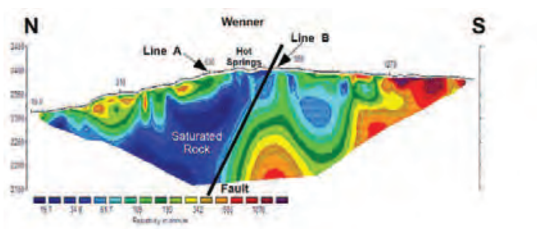

(c)

Figure 9.15: *Pseudo-sections of DC survey lines at Poncha Pass, shown for clarity. (a) Poncha Line A (Supersting), (b), Poncha Line B (Supersting), and (c) the Poncha ABEM Line (ABEM). The presence of a fault is inferred in each case.*

Chapter 10

Summary & conclusions

10.1 Summary

In addition the fieldwork carried out by the class of 2010, this report builds on the corporate knowledge of the Upper Arkansas Valley built up by successive field camps over the years 2005-2009. These previous studies have shared the objective of aiming to characterize both groundwater and geothermal water within the basin with a view to evaluating its potential for use by the citizens of Chaffee County.

Although specific details of the objectives and approach have varied over the years, a number of common themes prevail. The objective to locate and characterize subsurface water sinks, sources, reservoirs and conduits has been pursued through examination of surface geology, deep seismic exploration and near surface geophysical methods. In each of these areas the work of each subsequent year has added to the understanding derived from previous studies, and by drawing the results the current and previous years' results together it is possible to build a global interpretation of the Upper Arkansas Valley.

10.2 Conclusions

Chapter 11

Recommendations

11.1 Poncha Pass

Future groups doing field work at Poncha Pass could perform more targeted SP surveys, make a more detailed geologic map, integrate possible borehole information, collect shallow temperature data for a temperature profile, or collect water samples for geochemical analysis at the hot springs. These steps would shed more light into the heat flow of the area, and nature and path of the groundwater. A denser sampling of resistivity surveys would help determine the faulting structure in better detail. Satellite remote sensing could be used to both image mineralized deposits as well as monitor snow melt rates in the area. This will give an indication of surface temperatures.

11.2 Hecla Junction

Longer, more dense resistivity surveys would allow for more quality data and greater depth analysis. Additionally, a full self-potential grid (as opposed to three lines) would be useful in determining ground water flow patterns. Electromagnetic and magnetic surveys could be used to plan these resistivity and self-potential grids by characterizing the geologic surface under the topsoil. Finally, geochemical surveys of the active springs would assist in studying the water temperature and quality.

11.3 Green Creek

In order to find the strike of the fault, an additional line should be surveyed that parallels the 221 line. The 220 line would need to be extended in order to meet up with this new line. Finally, because the data was very noisy and poorly obtained, magnetic data should be recollected along both the 220 and 221 lines. This would give more credence to the obtained seismic and gravity data.

11.4 Dead Horse Lake

Extension of the microgravity survey at Dead Horse Lake northwards across Chalk Creek and over the transfer zone between the offset Sawatch Fault.

An east-west 2D hammer seismic line along CR162 to intercept the north-south striking Sawatch fault.

The PVC tube within the borehole MPG-1 should be removed and replaced with a cemented 2 inch PVC to facilitate a 3 component VSP survey. For further VSP planning in shallow geothermal wells the existing casing design needs to be considered and a hydrophone should be used where casing has not been cemented to well bore wall.

Reprocessing of all near-surface seismic data using velocity model derived from SASW (spectral analysis of surface waves).

3D refraction tomography should supersede the 2D refraction calculations performed to generate a highly resolved and more reliable topographic depth map to bedrock in conjunction with a high density spread of bedrock velocity measurements; potentially useful for the reprocessing of shear wave and compressional wave seismic data.

Extension of the SP and DC resistivity line to the east as an attempt to capture the location of a potential upwelling hot spring derived from the fracture.

11.5 Chalk Cliffs

The data collected at Chalk Cliffs could be used to estimate where hot or cold water wells can be developed. However, to better characterize the geothermal system in the region, more self-potential surveys should be conducted. Mt. Princeton Hot Springs Resort would be a good target for self-potential surveys due to its active springs. Additionally, the resistivity surveys conducted in the area should be repeated to ensure quality data. Unfortunately, due to the two-week time limitations, this step was not plausible.

Appendix A

Seismic refraction studies

A.1 Theory

As previously discussed, a weight-drop seismic vehicle was used as a high-energy seismic source which generated compressional waves (the direction of particle motion is parallel to the direction of prorogation) that propagated through the subsurface and subsequently interacted with geological boundaries, which represent rock type transitions (which possess different densities). At the boundaries, two predominant wave mechanisms occur; reflection and refraction. A refracted wave is one that propgates across the geological boundary and continues to travel in the lower rock layer. Refraction is determined by the angle of incidence of the raypaths that describe the initial compressional wavefront, described by Snell's law [40]:

$$\frac{sin\theta_1}{sin\theta_2} = \frac{V_2}{V_1} \tag{A.1}$$

The refracted and transmitted amplitude depend on the acoustic impedance (velocity multiplied by rock density) of the upper and lower rock layer and the angle of incidence. For the refraction experiment at Deadhorse lake, refractions that propagate along the geological boundary are of primary interest. The raypaths intersecting the boundary have to form the critical angle with the horizontal plane for this to occur. The critical angle is determined by the velocities of the upper layer and lower layer [25], described by:

$$\sin i_c = \frac{V_1}{V_2} \tag{A.2}$$

As the refracted waves propagate along the boundary they continually transmit energy back into the upper layer, shown in Fig. A.1. Energy returning to the upper layer, represented by the rays that leave the interface at the critical angle in Fig. A.1, define a plane wavefront known as a head wave. For 2D refraction analysis, it is the headwaves originating from the boundary between the glacial morraine and the pre-Cambrian granite that are of primary interest.

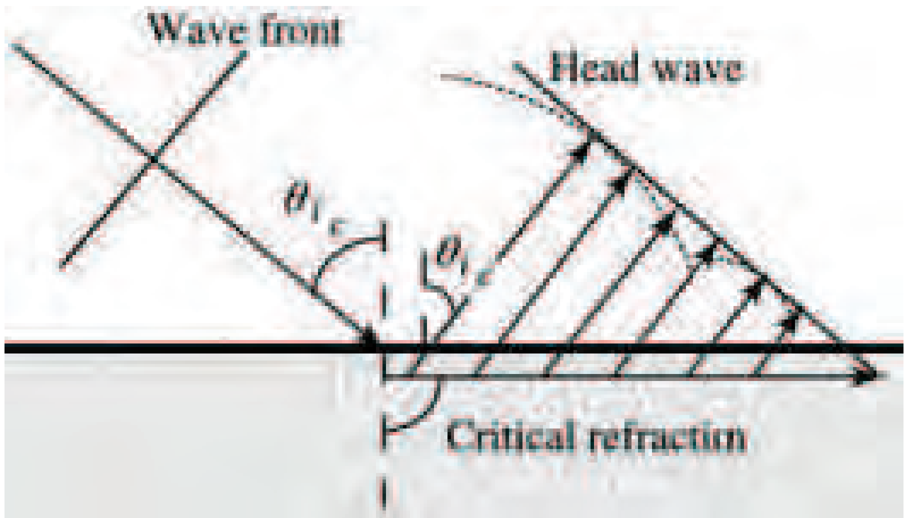

Figure A.1: *A wave that hits an interface at the wave's critical angle is refracted parallel to the interface. Energy transmitted from the refracted wave back into the upper layer produces a plane wavefront that commonly is referred to as a head wave.*

The experimental arrangement and the arrival of the headwaves at the receiver locations are shown in Fig. A.2 and these arrivals, combined with the direct arrival and reflections from the boundary combine to form a travel-time graph shown in Fig. A.3. This simple model assumes horizontal layers. The direct arrival is the first mode to be detected at the receivers as it travels horizontally directly from the source to the receivers. At the critical distance, the distance at which the refracted wave is first detected (half the source-receiver distance corresponds to the distance from the source at which the critical angle requirement for head waves is satisfied), the refracted wave arrives before the direct arrival as the headwaves propagate through a higher velocity medium. Both the direct arrival and refracted head wave display linear moveout so that linear regression can be used to describe the traveltime behavior of the waves. Linear regression yields the gradients of the best-fit-lines which can be inverted to give the velocity of the upper (glacial morraine) and lower layer (pre-Cambrian granite), where the direct arrival gives the upper velocity and the refracted wave gives the velocity of the lower layer. The intercept time, calculated from the linear fit for the refracted wave, can be used to calculate the thickness of the upper layer thus the depth to the lower layer.

At Dead Horse Lake the pre-Cambrian granite does not form a flat, horizontal layer, which has been indicated by previous studies in the area. For a dipping layer, a refraction profile

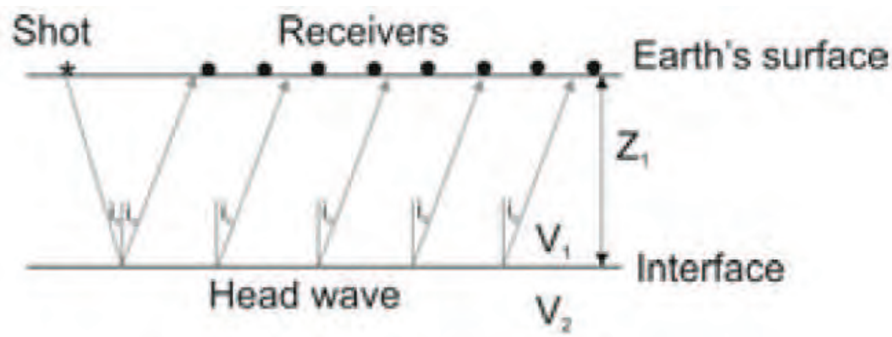

Figure A.2: *Basic illustration of the experiential arrangement at Deadhorse lake indicating the arrival of the head wave at the receivers.*

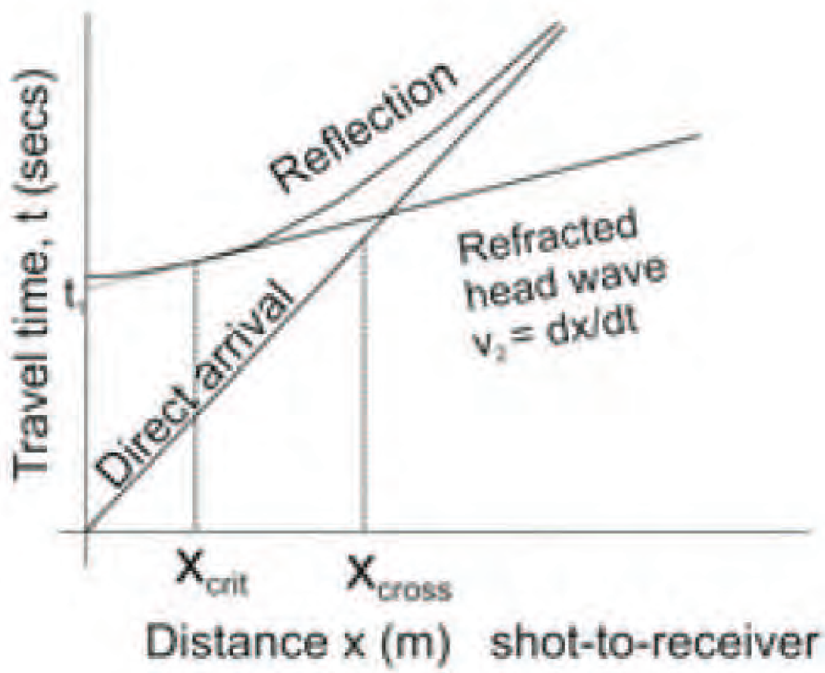

Figure A.3: *The travel-time graph for the direct arrival, reflected and refracted wave. The gradients of the lines can be inverted to yield velocities of the layers.*

has to be constructed by shooting up and down dip thereby forming two travel-time graphs that can be combined to generate an up and down dip profile. This achieved by acquiring head waves from a shot fired at the down-dip end and then acquiring head waves with the shot at the downdip end. The reason for this is that refractions traveling updip arrive earlier than expected consequently meaning the apparent velocity is greater than the true medium velocity, and vice-versa for headwaves traveling downdip. To get the true velocity requires an average of the two velocities calculated from the inverted gradients. Shooting up-dip also gives a different intercept time to down dip shooting which enables the depths to be valuated to the downdip and updip end of the profile. Therefore the general condition $V_{2u} > V_{2d}$ and $t_u > t_d$ apply to all updip and downdip refraction profiles. Fig. A.4 shows an example refraction profile for a dipping layer.

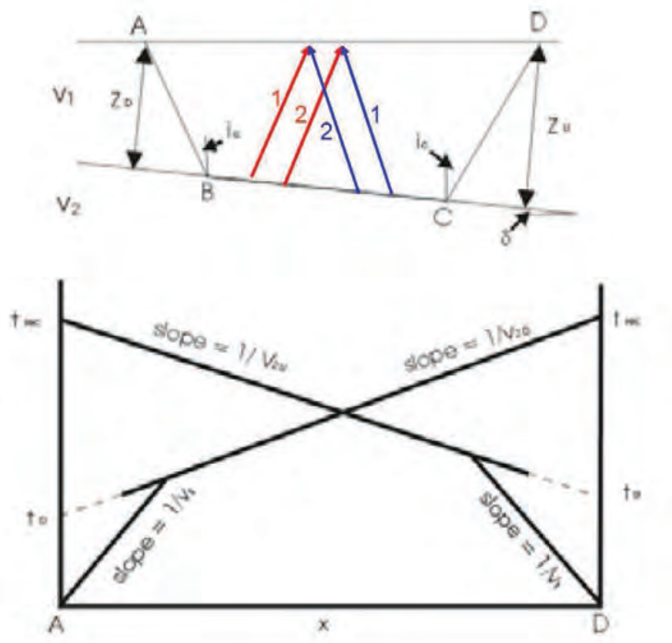

Figure A.4: *The top diagram shows the dipping interface with the critical angle (i_c), dip angle (δ) and the depths (Z_u and Z_d) labelled. The bottom diagram shows the refraction profile generated by downdip and updip shots.*

As the refracted wave arrives earlier updip than down dip, the intercept times, indicated by the dashed lines in Fig. A.4 and marked t_u and t_d, are different and these can be used to calculate the depths to bedrock, given by eq. A.3 and eq. A.4:

$$Z_u = \frac{t_u V_1}{2cosi_c} \tag{A.3}$$

$$Z_d = \frac{t_d V_1}{2cosi_c} \tag{A.4}$$

From the calculated updip and downdip velocities, the critical angle and dip angle can be calculated, described by eq. A.5 and eq. A.6:

$$i_c = \frac{1}{2}[sin^{-1}(\frac{V_1}{V_{2D}}) + sin^{-1}(\frac{V_1}{V_{2U}})] \tag{A.5}$$

$$\delta = \frac{1}{2}[sin^{-1}(\frac{V_1}{V_{2D}}) - sin^{-1}(\frac{V_1}{V_{2U}})] \tag{A.6}$$

A.2 Error analysis

As previously discussed, the error associated with each pick was taken to be 0.003ms. This error propagates through to the graphs utilized for linear regression so that the calculated gradient, hence the velocity, possesses an associated error. The velocities and times were then used to calculate depths thus an error for the depths could be consequently calculated using eq. A.7:

$$dZ = Z((\frac{dt}{t})^2 + (\frac{di_c}{i_c})^2 + (\frac{dV_1}{dV_2})^2)^{\frac{1}{2}} \tag{A.7}$$

Where V represents the velocity (down or updip), i_c represents the critical angle and t represents the intercept time (down or updip). The error in the critical angle, which is calculated from the velocities is given by eq. A.8:

$$di_c = i_c(1 - (\frac{V_1}{V_2})^{-\frac{1}{2}}(\frac{dV_1}{dV_2}) \tag{A.8}$$

Where V_1 represents the velocity of the glacial morraine and V_2 represents the velocity of the granite.

A.3 Results

The table in Fig. A.5 lists the calculated velocity for the bedrock with its associated error along with dip, the critical angle and the depths to the top and bottom of the dipping layer with the associated errors. The depth values were used to generate the 2D map of depth to bedrock shown in the main report.

A.4 Unix codes for picking first breaks

Before the data can be picked, the raw field data has to be converted from .seg to .segy then from .segy to .su so that the data is in the appropriate form for the picker. The following codes are required for the conversion, which must be performed within the folder containing the raw field data.

Convert seg to segy:

```
~/seg2segy/seg2segy 2217 717
```

The 2217 corresponds to the first FFID number in the file and 717 corresponds to the number of FFID files there are within the folder.

Converting segy to su occurs in two steps; the first code: segy to su:

```
segyread tape=2217.sgy | segyclean| surange
```

2217.sgy corresponds to the segy file containing the field data in segy form.

After the software has completed the conversion, the following command is then used:

```
segyread tape=2217.sgy | segyclean> 2217.su
```

Once the data is converted to .su, the shot records can then be anlaysed and picked. To view the shot record for a particular shot, the following code is used:

```
suwind < 2217.su key=fldr min=1014 max=1014 | suxwigb perc=98
```

2217.su corresponds to the .su file created previously containing all the field data and 1014 corresponds to the FFID of a particular shot (recorded in the observer sheet). Suxwigb corresponds to a wiggle display, suximage can also be used to observed it as an apparent image. Perc=98 corresponds to the gain applied to each of the traces.

The picker is activated by the following code:

```
suwind < 2217.su key=fldr min=1014 max=1014 | suwind key=tracf min=66 max=88
| sufilter amps=0,1,1,0 f=5,50,100,200| suop op=norm | suxpicker f2=0 d2=5
```

2217.su corresponds to the main file. 1014 corresponds to the FFID. Min=66 max=88 correspond to the minimum and maximum channel number allowing you to isolate particular receiver lines for picking. Sufilter corresponds to a filter to remove low and high frequency noise; refractions are generally high frequency due to a low depth of penetration (at DHL) thereby the maximum cutoff frequency should be relatively high (a Butterworth filter is used to circumvent Gibbs phenomenon). Amps=0,1,1,0 define the amplitude of the passband and f=5,50,100,200 define the cutoff frequencies. Suop op=norm is a function that normalizes the trace amplitude thereby bringing out the refracted wave at higher trace numbers where it is weaker. Suxpicker loads the actual picker and f2=0 d2=5 makes the plot start at 0m and then causes it to increment in 5m steps, converting trace number to distance. — suop op=neg — can also be used to invert the traces converting a peak to a trough and vice-versa which in some cases brings out the refraction pattern making it easier to pick.

A.5 RAYINVR codes for forward modelling

Rayinvr is a programme that calculates how to best update the velocity model to improve the fit between calculated and observed travel times. For a detailed description of RAYINVR codes, details on forward modeling and details on inversion refer to: http://terra.rice.edu/department/faculty/zel

The input for the RAYINVR programme consists of v.in (velocity model input file), txt.in (picked travel times with uncertainties) and r.in (control file e.g. plotting parameters and assignment of phases) files.

The files will first be shown and then explained. The r.in file reads as follows:

```
&pltpar            isep=0, itx=1, idata=1,
imod=1, iray=2, ibnd=0, isum=3,
xwndow=292., ywndow=175.,
ircol=1, itcol=1,iroute=4,iplot=1,vred=0,
istep=0, idata=1, irays=0, itx=1,
iroute=2, isum=1,
&end
&axepar          xmax=115., xmm=265.,
zmax=40.,  zmm=60.,
tmin=0.0,tmax=100.,  tmm=60.,
albht=3.5, orig=15., sep=10.,
&end
&trapar            imodf=1, ibsmth=1, i2pt=1,
ishot=2,2,
xshot=0.,115.,
ray=1.1,2.3,
nsmax=15,
nray=100,
space=1.,
```

```
aamin=0.25, aamax=75.,
&end
&invpar           invr=0,
ivray=1,1,1,
&end
&amppar          iamp=0, isect=0,
&end
```

The txt.in file reads as follows:

```
0.000       1.000     0.000         0
5.0000    14.354     0.500         1
10.000    19.637     0.500         1
20.000    27.057     0.500         1
25.000    29.412     0.500         1
30.000    30.895     0.500         1
35.000    32.825     0.500         1
40.000    34.152     0.500         1
45.000    36.534     0.500         1
50.000    39.056     0.500         1
55.000    39.050     0.500         1
60.000    41.126     0.500         1
65.000    42.529     0.550         1
70.000    44.638     0.600         1
75.000    46.748     0.650         1
80.000    48.264     0.700         1
85.000    49.585     0.750         1
90.000    50.608     0.800         1
95.000    51.494     0.850         1
100.00    52.774     0.900         1
110.00    55.290     0.100         1
115.00     -1.000     0.100         0
25.000    60.536     0.500         1
30.000    59.867     0.500         1
35.000    58.005     0.500         1
40.000    56.262     0.500         1
50.000    53.575     0.500         1
55.000    51.391     0.500         1
65.000    48.341     0.650         1
75.000    47.941     0.700         1
80.000    47.099     0.750         1
85.000    44.446     0.800         1
90.000    43.322     0.850         1
```

```
95.000    41.417     0.900          1
100.00    39.853     0.950          1
105.00    38.168     0.100          1
110.00    36.001     0.105          1
0.0000      0.000     0.000         -1
```

The v.in file reads as follows:

```
A). 1     0.00 115.00
       0    0.00     0.00
                 0         0
B). 1     0.00 115.00
       0    0.75     0.75
                 0         0
C). 1     0.00 115.00
       0    0.75     0.75
                 0         0
D).  2     0.00 115.00
        0    8.47 13.090
                  0         0
E).   2  115.00
        0    3.349
                    0
F).   2  115.00
        0      4.00
                    0
```

The r.in file details the plotting parameters and the types of waves that are to be traced through the model. The green labels relate to how to display and save information from the model. Itx=1 means that a text file, labeled txt.out is generated in the active folder that rayinvr is being run from. Isum=1 displays statistical information about the reliability and accuracy of the forward modeling. Specifically, it displays chi-squared value that indicates the accuracy of the fit. A value of 1 indicates a perfect; all the calculated times macth the observed times to within their level of uncertainity. This can be used to guide iterations of the model, although over-fitting is a potential disadvantage thus the model chosen should be as simple as possible to generate low values of chi-squared.

The values highlighted in red in each of the text files indicate the length of the line. For the refraction survey at Dead Horse Lake the average receiver line was 115m, starting from 0m. Therefore these red values correspond to the total length of the refraction lines and have to be changed in all three files. The blue lines in r.in correspond to the type of rays being traced through the model. 1.1 means that direct arrivals are being traced through layer 1 and 2.3 means that head waves are being traced through layer 3. Therefore the first number corresponds to the layer number and the second corresponds to the ray type; 1=direct arrival, 2=turning wave, 3=head wave. For refraction only direct and refracted arrivals are necessary. Over the distance of the survey, turning waves are unlikely to contribute significantly to the observed refractions.

The txt.in file is derived from the picking programme previously discussed. The v.in specifics the properties of the model in terms of layer thicknesses, layer lengths, layer velocities and velocity gradients. The v.in is composed of the following parts:

A). Line 1: Specifies the receiver line length, running from 0.00 to 115m. The 1 at the beginning specifics the layer number, which is 1. Line 1 is the same for all sections of the v.in file. Line 2 and Line 3: disregard for the purposes of simple model building.

B). Line 2: The velocity at the beginning (left value) and end of the line (right value) for the top of layer 1. For this particular line the velocity is 0.750kms-1 at the beginning and end of the line.

C). Line 2: The velocity at the beginning (left value) and end of the line (right value) for the bottom of layer 1. There is no vertical velocity gradient as the sediments form a relatively thin layer with a minimal compaction differential between the top and the bottom thus generating no corresponding velocity gradient.

D). Line 2: Beginning of the second layer. The 8.47 and 13.090 correspond to depth in meters for the beginning and end of the line.

E). and F). Line 2: The same as sections B). and C).

For forward modeling the only file that is required to be varied between iterations is the v.in file. Depending on the simplicity of the model and the chi-squared value, the depths to the second layer as well as layer velocities can be altered to achieve a better fit.

A.6 Results from RAYINVR

Six receiver lines had their forward and reverse refraction profiles forward modeled by rayinvr as a step in error analysis. The depths and velocities calculated directly from manual calculations were entered into the models and the chi-squared value was calculated. The chi-squared value varied from 0.97 to 0.93 therefore indicating reliable fits.

Line	Shot	V (ms^{-1})	dV (ms^{-1})	Dip (deg)	i_c (deg)	Z_u (m)	d(Z_u) (m)	Z_d (m)	d(Z_d) (m)
1000	1501	2828.04	52.09	2.08	13.30	13.87	1.39	6.17	1.20
	1525	3857.37	71.62						
	V_a (ms^{-1})	3342.71	61.50						
2000	2501	3072.03	172.45	1.12	13.01	13.09	1.36	11.16	1.31
	2525	3641.12	138.53						
	V_a (ms^{-1})	3356.57	155.30						
4000	4502	2877.24	51.79	1.61	13.50	8.36	0.45	6.12	1.05
	4222	3642.38	65.56						
	V_a (ms^{-1})	3000.00	58.63						
6000	6501	2749.56	49.48	1.90	13.93	11.59	1.32	6.95	1.22
	6524	3600.15	64.80						
	V_a (ms^{-1})	3174.86	56.91						
8000	7503	3127.62	56.30	0.88	13.00	13.09	1.36	8.47	1.25
	7530	3571.21	64.28						
	V_a (ms^{-1})	3349.41	60.29						
9000	8504	3309.92	59.58	0.49	12.61	13.07	1.36	9.61	1.27
	8528	3571.21	64.28						
	V_a (ms^{-1})	3440.56	61.85						
10000	9506	3337.74	183.58	-0.12	13.11	11.03	1.33	8.17	1.22
	9526	3275.83	180.17						
	V_a (ms^{-1})	3500.00	182.12						
12000	12509	2986.60	164.26	0.23	14.31	11.61	1.33	8.13	1.24
	12526	3082.01	169.51						
	V_a (ms^{-1})	3034.30	166.87						
13000	12509	2886.29	158.75	1.67	13.39	11.56	1.32	8.87	1.26
	12526	3689.94	202.95						
	V_a (ms^{-1})	3288.12	180.83						
17000	16513	3099.80	55.80	1.33	12.68	10.40	1.29	8.86	1.25
	16534	3810.76	68.59						
	V_a (ms^{-1})	3455.28	62.76						
18000	17514	3098.81	55.78	1.16	12.85	13.08	1.36	11.54	1.32
	17534	3702.61	66.65						
	V_a (ms^{-1})	3400.71	51.72						
19000	18514	3012.92	54.23	1.16	13.25	10.50	1.23	8.48	1.20
	18534	3581.69	64.47						
	V_a (ms^{-1})	3297.31	59.34						
20000	19514	2521.33	45.38	2.17	15.13	12.43	1.35	10.88	1.31
	19534	3343.26	60.18						
	V_a (ms^{-1})	2932.29	53.21						
21000	20515	2851.52	51.33	1.26	13.99	11.21	1.31	8.12	1.24
	20534	3405.29	61.30						
	V_a (ms^{-1})	3128.41	56.32						
24000	23517	2998.48	53.97	0.14	14.35	13.16	1.37	9.68	1.28
	23535	3055.54	55.00						
	V_a (ms^{-1})	3027.01	54.46						

Figure A.5: *Table of depths, velocities and dips of Dead Horse Lake basement.*

Appendix B

DC Resistivity and Self-Potential

B.1 Introduction & Theory

Resistivity is an intrinsic property of a rock that describes the rock's resistance to flowing current. The electrical property correlates to porosity, mineral and fluid content, water saturation, and temperature, causing the DC resistivity method to be useful for characterizing groundwater bodies. DC resistivity surveys are typically accompanied by self-potential surveys. A self-potential survey measures the amperage of the naturally occurring current produced by subsurface water movement. The method allows groundwater's flow patterns to be tracked. Groundwater movement is largely influenced by faulting, since the faults and fractures act as pathways for fluids. In Chaffee County, the electrical surveys were performed to image and locate the faults in addition to discovering areas of low resistance and upward moving water.

B.1.1 DC (Direct Current) Resistivity

Electrical surveys aim to non-intrusively observe the electrical properties of the subsurface by measuring the voltage drop between two stations. The DC resistivity survey injects a known current into the ground, measures the potential difference between two electrodes, and determines the apparent resistivity using Ohm's Law, equation B.1 where I is current, V is voltage, and R is resistance.

$$I = \frac{V}{R} \tag{B.1}$$

$$R = \rho \frac{l}{A} \tag{B.2}$$

Apparent resistivity, equation (where R is resistivity, ρ is static resistivity. l is length and A is cross-sectional area), applies the geometric factor of the equipment and electrode spacing to resistivity. Resistivity is measured in Ohm m, and is the inverse of conductivity, σ. High water saturation and temperature cause rocks to become more conductive, thus giving a lower resistivity measurement.

The electrical resistivity methods used in Chaffee County include the Wenner and Schlumberger array. Both methods inject current through electrodes labeled A and B, and measure the subsurface resistivity with electrodes labeled M and N, which are positioned in between electrode A and electrode B. The survey's design includes laying multi-core cables along the site in a line as straight as topography allows. The cables have multiple electrical take-outs at equal spacing that allow for electrodes to be attached. A computer unit attached to a battery automates the selection of electrodes being used for each measurement of current and voltage.

B.1.1.1 Wenner Array

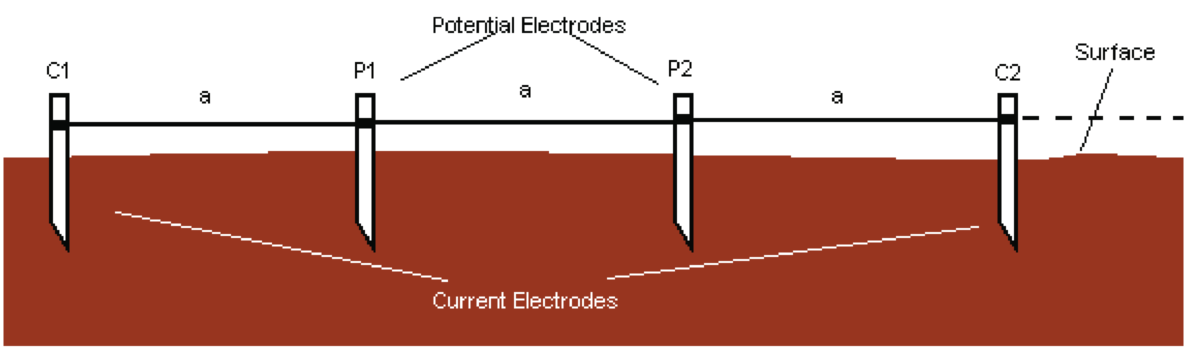

Figure B.1: *Wenner Array: The electrodes of the Wenner array are equally spaced. All spacings are increased automatically in successive measurements by the selection of different electrodes by the computer unit.*

For a Wenner array, the electrodes are equally spaced at a distance a (see Figure B.1 for the configuration). The array is designed to observe vertical variations such as faults and folding, and is less sensitive to horizontal changes. The Wenner array has a small geometric factor, $2\pi a$, and the largest signal strength. Combined with the array's simplistic design, the Wenner is widely used in the field.

B.1.1.2 Schlumberger Array

The Schlumberger array is more sensitive to lateral variations (see Figure B.2 for configuration). The Schlumberger array is similar to the Wenner array in that they both have a nested electrode configuration. However, the spacing is different; the Wenner array has 2 potential

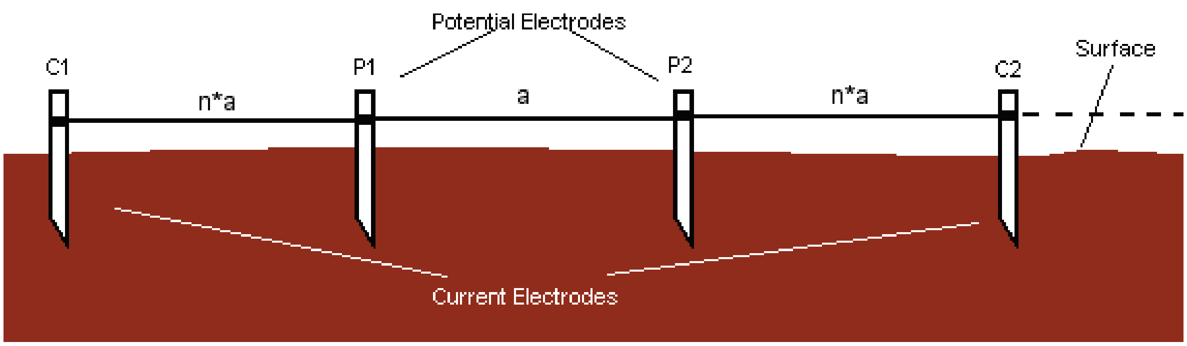

Figure B.2: *Schlumberger Array: Only the outer electrodes are moved during a survey. Lateral changes are resolved better with the Schlumberger array*

(electrodes M & N) electrodes with a spacing of a, which are both spaced a distance of a from the current (electrodes A and B) electrodes. The Schlumberger array has the same potential electrodes with a spacing of a, but they are placed some distance $n * a$ away from the current electrodes, where n is an integer that depends on the size and depth of the target. The geometric factor, K, for the Schlumberger array includes the distance between the injecting electrode and the middle, as well as the distance between electrode M and electrode N (equation B.3), where c is half the distance between electrode A and electrode B and d is the distance between electrode M and electrode N.

$$K = [\pi fracc^2 d][1 - \frac{d^2}{4c^2}] \tag{B.3}$$

B.1.2 Self-Potential (SP) Theory

The self-potential method is a passive survey and therefore is relatively simplistic. As fluids travel through a porous rock, because of ion interaction, currents on the order of milliamperes are created. Two electrodes, a base station and a rover electrode, a voltmeter and a spool of wire can be used to measure the voltage drop produced by the currents. The base electrode is buried in an area where no anomalies are present. It is then connected to the voltmeter and other electrode by the spool of wire (see Figure B.3 for this setup) [29].

B.2 Equipment

The instruments used in the DC (direct current) resistivity surveys were the ABEM Terrameter SAS (4000) Lund Imaging System (ABEM), and the AGI SuperSting R8 IP (SuperSting). The SP (self-potential) method employs a different kind of electrode and cable. This section

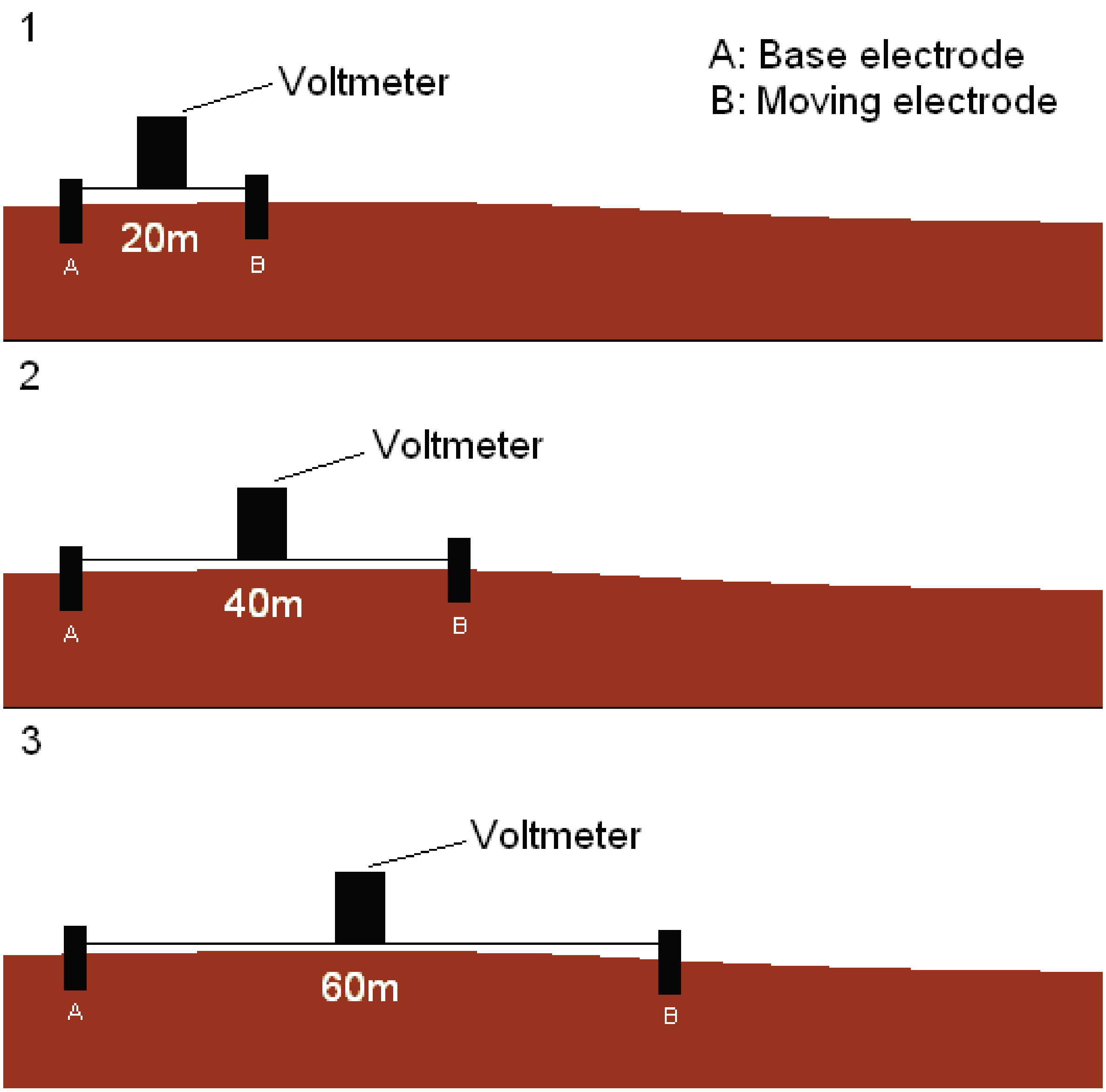

Figure B.3: *Setup for the SP survey, with a base/reference electrode with a roving electrode and a voltmeter.*

will explain the benefits of each system and how each instrument was used to acquire data in the field.

B.2.1 ABEM

The ABEM instrument supports arbitrary cable arrangement and electrode arrays, including the Wenner, Schlumberger and dipole-dipole arrays. The array refers to how the electrodes and cables are set up during the survey in order to conduct a 1D (Schlumberger array) or a 2D (Wenner array) survey, etc. This instrument has automated roll-along capability for 2D and 3D surveys (the roll-along technique allows for a measuring a bigger electrode grid), and has the option to measure IP (induced polarization). The ABEM has high resolution at shallow depths, and the output from the instrument is presented in an easily interpretable form [5]. Figure B.4 shows a picture of the ABEM instrument that was used.

Figure B.4: *Picture of the ABEM Terrameter SAS (4000) instrument used to perform DC resistivity surveys in the field [29].*

The acquisition process involved laying the cables along the profile to be survey with pre-determined electrode spacing. The electrodes are hammered into the ground, and then the following field parameters were entered into the ABEM:

- Current: 100Ma
- Frequency: 60Hz
- Electrodes: 64
- Time for collection: 0.6s
- Electrode arrays: Wenner

The instrument has a built-in automatic roll-along switch which records the different electrode array resistivity without having to move the electrodes manually. The ABEM is then set to record the data.

B.2.2 SuperSting

The SuperSting has 8 channel simultaneous measuring capability, which cuts field time dramatically. This instrument provides high accuracy and low noise levels, and has automated roll-along capability. The SuperSting electrode arrays the SuperSting supports include the Wenner array, the Schlumberger array and dipole-dipole array, and also has the option to measure IP (induced polarization) [6]. Figure B.6 shows a picture of the SuperSting instrument.

The acquisition process involved laying the cable along the profile to be surveyed with predetermined electrode spacing. The electrodes are hammered into the ground, and then entering the following field parameters into the SuperSting:

- Current: 1250Ma
- Frequency: 60Hz
- Electrodes: 28
- Electrode arrays: Wenner and Schlumberger

The instrument has a built-in automatic roll-along switch which records the different electrode array resistivity without having to move the location of the electrodes manually, and the instrument measures resistivity in the 3 different directions (x, y and z). The SuperSting tests the electrodes, and if the resistivity is too high on any of them, then the electrodes can either be moved or have salt water poured on them to increase their conductivity [6].

Figure B.5: *Picture of the SuperSting R8 IP instrument used in the field to perform DC resistivity surveys [5].*

B.2.3 SP

The SP (self-potential) employs rolls of wire, 2 lead electrodes and a voltmeter. The acquisition process involves laying the cable along the profile to be surveyed, with a "reference" electrode at the start of the line. At predetermined spacing (the same as the electrode spacing of the ABEM) the field operator digs a small hole and places the lead electrode into the hole. The voltmeter is plugged into the wire roll, and attached to the electrode. The reading on the voltmeter is then recorded by the operator. Figure B.6 shows some of the students working with the SP instruments during a survey.

Figure B.6: *Picture of some of the students operating the SP instruments during a SP and ABEM survey in the field. The yellow voltmeter is plugged into the wire via the roller, and is attached to the lead electrode that is placed on the ground.*

B.3 Data Reduction

B.3.1 Inversion Problem

The objective is to develop a model of the subsurface whose geophysical response most directly resembles that of the observed data. To attain this objective, the acquired DC resistivity data were inverted using the RES2DINV inversion software package. The inversion software operates on the principles of least squares Gauss-Newton and quasi-Newton optimization methods and is designed to create apparent resistivity(ohm m) pseudosections of the subsurface using the acquired data from 2D DC resistivity sounding lines.

For the majority of the pseudosections, the data were inverted using the non-linear least squares Gauss-Newton optimization method, emphasizing model smoothness. The optimization method aims to minimize the difference between the calculated model and the observed data. This difference is called the RMS error and is displayed for every pseudo section produced. The software conducts 5 iterations to produce the best fit model; each iteration reduces the RMS error and increases the similarity between the developed model response and the acquired data. An optimal RMS value lies between 10% and 3% error. A RMS error above 10% implies that the apparent resistivity model could be too ambiguous and not representative of subsurface. A RMS error below 3% implies that the apparent resistivity model could be too precise and could contain subsurface structures that are not present in reality.

For pseudosections that are expected to have sharp boundaries between high and low apparent resistivity, a normal inversion approach is not sufficient. It is necessary to conduct a robust or blocky inversion, implementing the quasi-Newton inversion method. The robust inversion reinforces the resistivity contrast, rather than smoothing the contrast boundary (Revil).

During the inversion process, all erroneous data points were removed from the data set. Bad data points are defined as being much larger or smaller in amplitude than their respective neighboring data points. Such points will adversely affect the resulting model and thus need to be removed from the data set entirely.

For all inversions, the associated 2D sounding line topography relief was incorporated. It is essential to include a topographical relief profile when inverting data, as the topography will change the geometry of the resulting apparent resistivity pseudosections.

B.3.2 Assumptions

When inverting, it is necessary to be aware of the associated assumptions taken, and take heed when interpreting the final results.

The inverse problem, most importantly, is a non-unique problem.

Secondly, when inverting the acquired data, it is assumed that all of the data are a correct representation of the measured subsurface property. This is not always the case, however. With DC resistivity acquisition, a number of situations can occur that could result in anomalous, erroneous datum points: Electrode cables could be connected in reverse; electrodes might not be connected to the cables correctly; the electrodes might not have sufficient ground contact due to gravely, or unusually dry ground conditions; or, electrodes could be shorted out due to unusually high water saturation of the ground (Revil).

B.3.3 Sources of Error

In DC resistivity, sources of error include the polarization of the electrodes, contact resistance (between the electrodes and the ground), and proximity to conductors, such as buried pipes and chain link fences [12]. In SP surveys sources of error include the electrode polarization and contaminants in the soil.

Appendix C

Deep Seismic

C.1 Processing

C.1.0.1 Recording

The deliverables of the seismic survey were a data tape, notes taken by the observers during acquisition and a set of location points. Prior to processing, the tape containing the raw seismic data was converted to SEG-D format.

C.1.0.2 Configuration

Reflection processing aims to provide an image of the true reflector geometry. Consequently, applying the correct geometry to the acquired data is a crucial first step in the processing sequence. Locations of each survey point were obtained during acquisition using two different methods - namely, the total distance measurement (TDM) and the Differential Global Positioning System (DGPS) methods - and these were meshed seamlessly to give the required input for ProMAX. Linear interpolation was used for missing data points. This assigns a geographical position, that is, latitude and longitude, to each survey point.

The observers' notes were used to focus on shots which required amendments. Erroneous records included those resulting from falsely-triggered shots and those having different offsets to the planned acquisition survey parameters. Void records were eliminated and the appropriate skids were applied as necessary. This ensures that the processing sequence is applied to good quality shots and that consistency is maintained throughout.

The seismic lines were acquired on non-uniform topography, therefore necessitating the application of elevation statics to the sources and receivers in order to correct for their elevations. The elevation static correction is subtracted from the two-way travel time (TWT) of the trace belonging to the source-receiver pair and is given by:

$$t_D = t_R + t_S = ((E_S - Z_S - E_D) + (E_R - Z_R - E_D))/V_r \tag{C.1}$$

where $t = staticcorrection$, $E = elevation$, $Z = depth$, $V_r = replacementvelocity$ and R refers to the receiver, S refers to the source and D refers to the datum.

This type of correction assumes that statics are pure time shifts, which implies that the rays travel vertically within the weathering layer. In our case this assumption is valid since the near-surface is poorly consolidated and, therefore, a large velocity contrast is present between it and the underlying strata.

Elevation statics were applied iteratively to compute and eliminate the effect of different source and receiver elevations. A common datum of 2600 m was chosen for the source and receivers using a replacement velocity of 2450m/s for the weathering layer. This value was selected using knowledge of the area from previous surveys.

C.1.0.3 Noise suppression

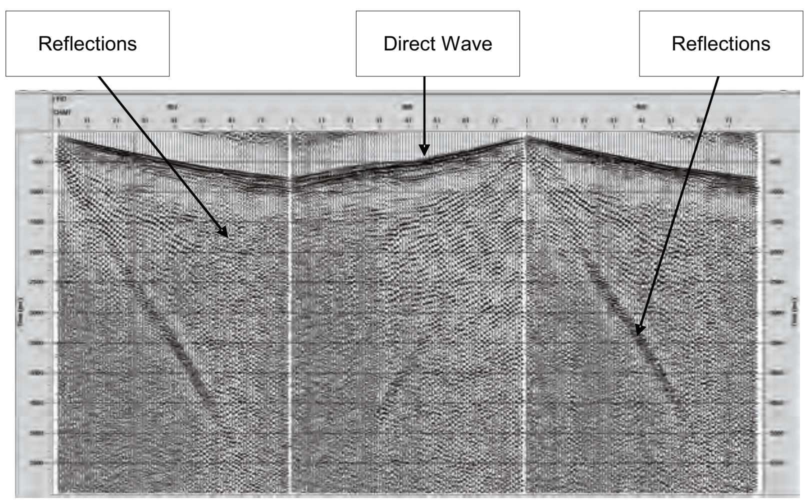

Figure C.1: *A selection of shot records for line 3000 showing ground roll, airwave, refraction and direct arrivals prior to muting and filtering.*

Fig. C.1 above depicts selected records for line 2000. Determining the apparent velocity of different types of noise aids the identification of its origin. The appropriate filters can then be designed to remove or reduce it considerably. Noise suppression techniques were applied to selected shot records and the appropriate parameters were determined. Refraction muting, ground roll removal and air wave removal all improved data quality. Muting was also found helpful in testing the validity of the survey geometry which had been applied to the data.

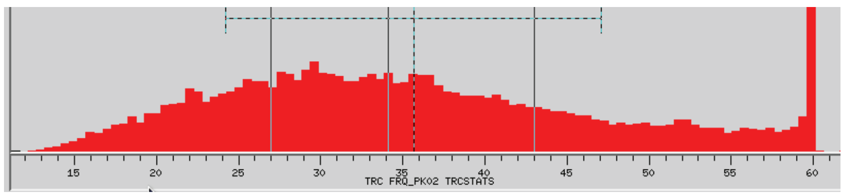

Figure C.2: *The frequency spectrum of the data shows a spike at 60Hz.*

Another source of noise in the dataset resulted from interference of the main power supply in the US. Fig. C.2 shows the frequency spectrum of the data and a spike is visible at 60 Hz. This was remedied through the use of a notch filter which removed data having this frequency.

C.1.0.4 Frequency conditioning

Low frequency noise was present in the dataset and, at depth; the high frequencies did not represent useful information. This was overcome by using bandpass filtering in the frequency domain. An Ormsby filter having parameters 6-12-40-60 Hz was applied to remove these unwanted frequency components. The choice of parameters was based on the frequency range where signal was expected. The geophones used in acquisition operate at 12Hz and, therefore, no signal was expected below this frequency. The upperbound of the filter was selected by taking the sweep frequency into consideration. Tapering was used in order to have gentle slopes and avoid Gibbs' effect.

C.1.0.5 True amplitude recovery

In seismic data, the relative impedance changes across boundaries are reflected in the wave amplitudes. True amplitude recovery seeks to regain the actual amplitudes by removing the effects of spherical divergence and attenuation. Spherical divergence is proportional to $\frac{1}{v^{2t}}$ where v is the velocity and t is the two way time (TWT). A t^2 gain was applied to every sample by multiplying each trace by t^2 where t is the two-way time (TWT). Trace equalization was also performed. This compensates for coupling effects through scaling to boost weaker shots and receivers.

C.1.0.6 Deconvolution and common depth point (CDP) sorting

Following pre-processing, the data quality was significantly improved. With the correct geometry in place, midpoints and bins were assigned to the shot-ordered data. An initial stack was compiled using brute velocities derived from the processing of the lines acquired during the 2009 Field Camp. The velocity information at this stage was therefore limited and corresponded to a different area. Nonetheless, this stack was meaningful and provided a reasonably good start for velocity analysis.

Spiking deconvolution was used to reverse the convolution process. The spiking filter is a special type of shaping filter which aims to compress the wavelet and make it as close as possible to a spike. This process is also referred to as whitening since it attempts to achieve a flat spectrum. Deconvolution removes ringing and thus improves the temporal resolution. Autocorrelation can be used to complement the choice of the gap and operator length.

C.1.0.7 Velocity analysis

Velocity analysis is the crucial next step in the processing sequence and determines the quality of the final product to a great extent. However, it should be kept in mind that such an analysis is not without its limitations. Its accuracy and resolution are determined by factors such as the spread length, stacking fold, S/N ratio, muting, velocity sampling, true departures from hyperbolic moveout and the bandwidth of the data; amongst others. Velocity analysis is employed in an iterative manner with velocities being revised a number of times in order to obtain the most suitable velocity field.

Velocity estimation uses data which is recorded at non-zero offsets. Assuming horizontal layers of constant velocities, waves reflected off the surface are expected to lie on hyperbolae. The normal moveout (NMO) velocities for the different layers are estimated using these hyperbolae. Semblance spectra, NMO corrected gathers and constant velocity stacks were used together as a guide in defining an initial velocity function for each set of selected CDPs to maximally flatten the gathers. At each iterative step, velocities were picked every 15 CDPs down to about 3000 ms. The picked velocities for line 3000 are illustrated in Figs. C.3 and C.4 which are the first and final velocity iterations respectively. Velocities in the range of $2000ms^{-1}$ to $6000ms^{-1}$ were observed to flatten the reflections in the section. (The reader should note that the velocity iterations were run simultaneously with the residual statics iterations which are described below. A mute was also applied to avoid NMO stretching resulting from this process.

C.1.0.8 Residual statics

Residual statics persist in the traces and degrade the quality of the stack having a detrimental effect on subsequent processing and displays. Anomalies due to statics distort the apparent

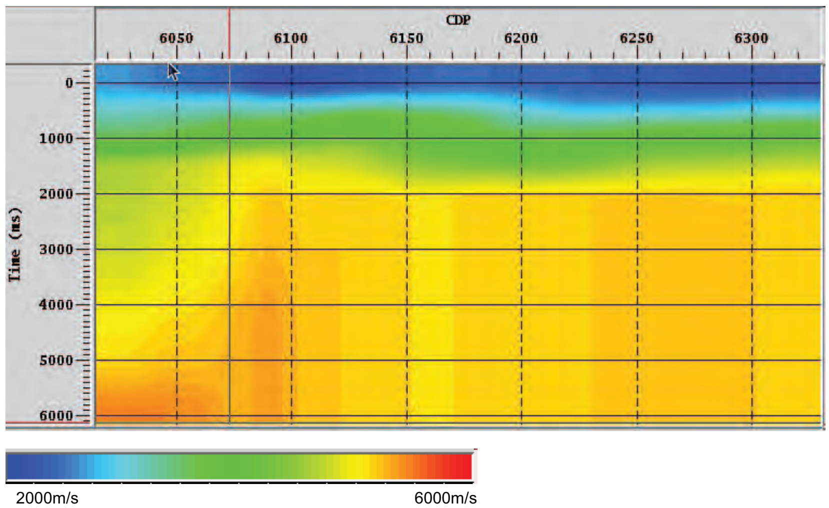

Figure C.3: *The velocities obtained in the first iteration of velocity analysis for the line 3000.*

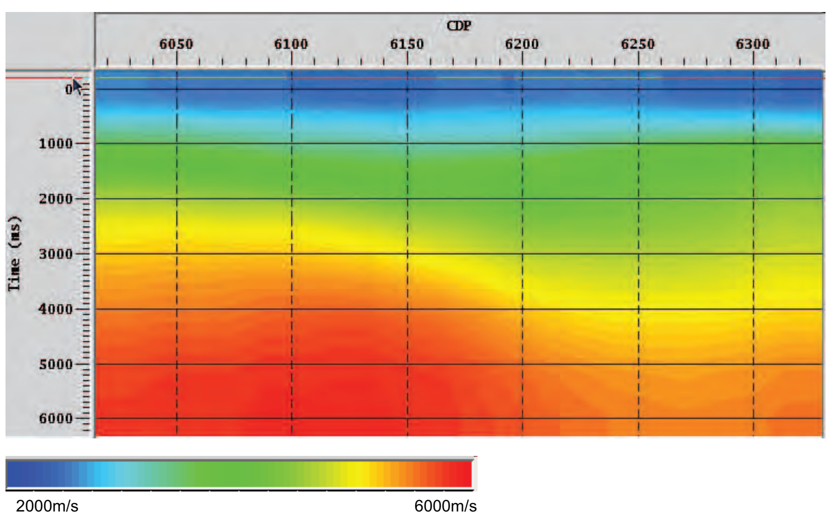

Figure C.4: *The smoothened velocity picks after the final iteration of velocity analysis for the line 3000.*

structure and stratigraphy in seismic sections thus giving rise to poor wavelet form in CMP stacks. Residual statics also affect the apparent velocity and, if not addressed, introduce errors in the velocity analysis process (Wiggins et al, 1976).

Static corrections were calculated using the NMO-corrected data. A surface consistent model was used which involves applying the same shot static (alternately, receiver static) at a particular location, regardless of the receiver locations (alternately, shot locations). The relative time shifts are then determined using cross correlations of the data. This method is susceptible to incorrect interpretation of cross correlation peaks, for example, cycle-skipping. This occurrence is minimized through the use of weighted least-squares inversion. Together with velocity analysis, the residual statics process is also an iterative one. At each step of the iteration, the prestack data, the best statics estimate and the stacking velocities are supplied as input to the algorithm. The static corrections and NMO are applied and the data is stacked and correlated. The surface consistent equations are then solved and the new static corrections are output. At the end of the second iteration, the statics were fairly well behaved and the variation was deemed sufficiently negligible for our purposes.

C.1.0.9 Partial structure correction

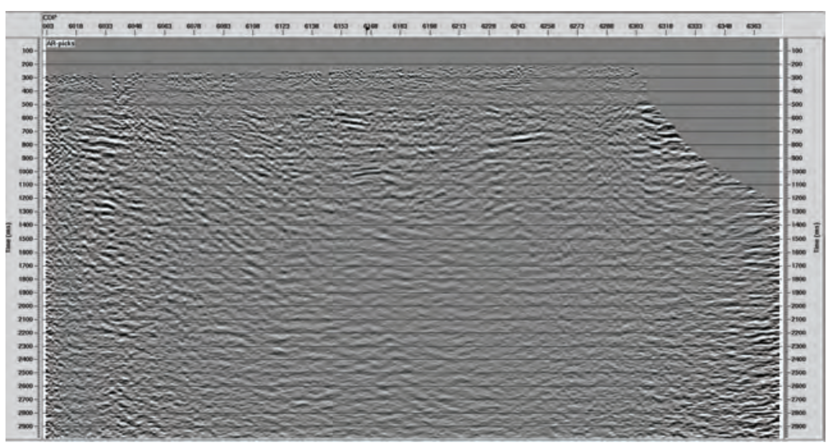

Figure C.5: *The stack for line 3000 following the application of normal move-out (NMO) and dip move-out (DMO).*

Dipping surfaces were expected to be present in the area which was surveyed. This would imply that the apparent velocities defined thus far do not correspond to the true velocities. Dip move-out (DMO) was applied to correct for any dipping reflectors by a 'partial migration' scheme. This was preceded and succeeded by NMO and a mute was also used to eliminate any stretching caused by NMO. Following this, another stack was obtained for each line. This provided a crude but meaningful image of the subsurface. The stack for the seismic line 3000 is displayed in Fig. C.5.

C.1.0.10 Comparison of CDP gathers

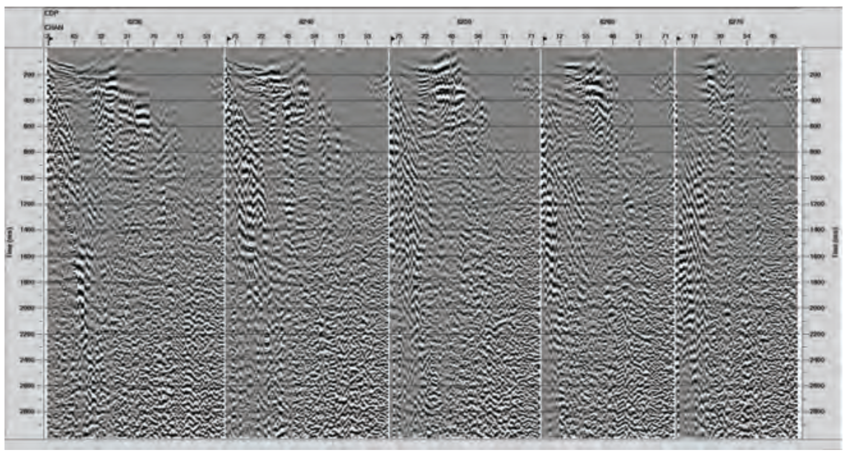

Figure C.6: *A selection of CDP gathers with true amplitude recovery, trace equalisation and elevation statics applied.*

The following figures (Figs. C.6 to C.9) illustrate the improvements throughout the processing sequence described up to this point for the line 3000. The same CDP gathers are shown throughout for straightforward comparison. Fig. C.6 depicts gathers which have been corrected for amplitude variations and for elevation. In Fig. C.7 the noise identified in the analysis is suppressed. Fig. C.8 shows the deconvolved data and has a less 'ringy' appearance when compared to the previous figures. The final figure, Fig. C.9, shows the same gathers with DMO applied.

C.1.0.11 Imaging

In migration reflection events are shifted to their true geological position using the zero-offset section (after DMO) and the smoothened, scaled migration velocities. The data was post-stack migrated in the time domain using two wave equation methods, namely, finite difference and phase shift.

Finite difference time (or depth) migration - developed by Claerbout in 1976 - involves finite differencing in time (respectively space) and uses a one-way wave equation. The accuracy of the solution (for example, 15 degrees) is dependent of the order of the expansion assumed in the approximation.

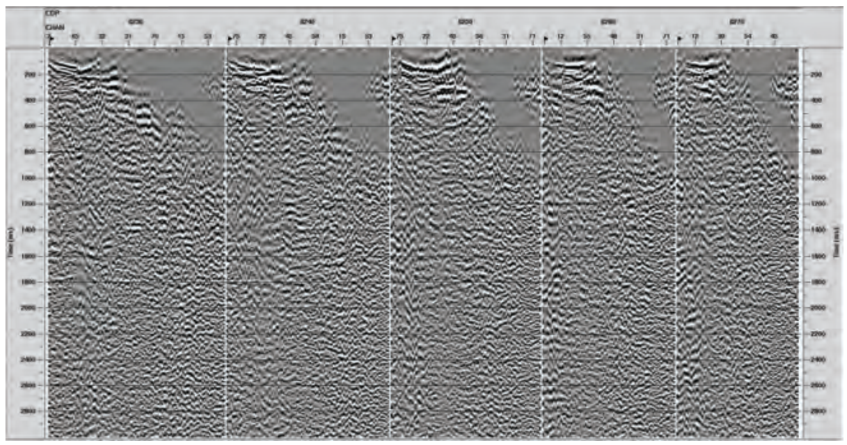

Figure C.7: *Same selection of CDP gathers as shown in Fig. C.6 after noise suppression techniques for the airwave and ground roll were applied.*

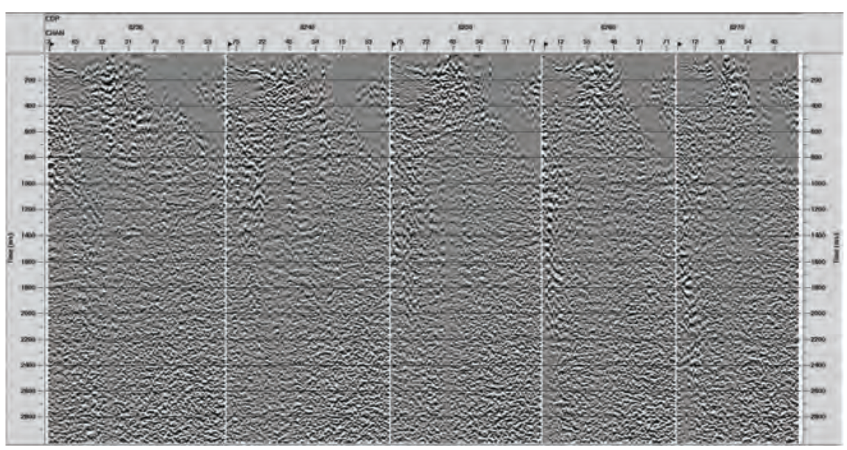

Figure C.8: *Same selection of CDP gathers as shown in Fig. C.6 following deconvolution.*

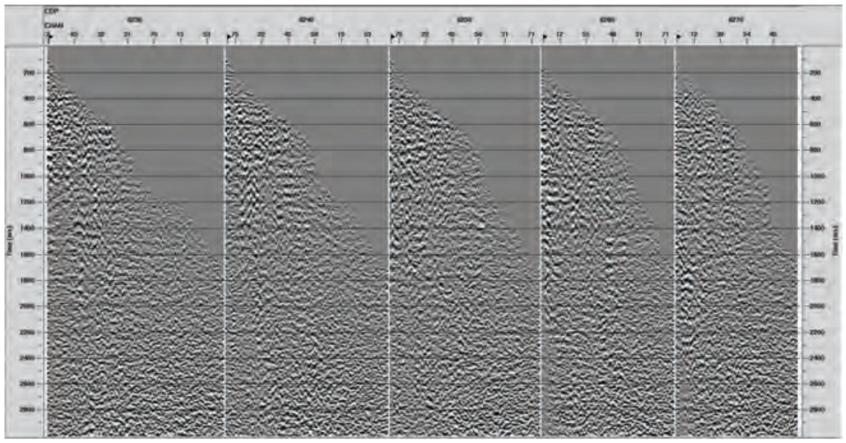

Figure C.9: *Same subset of CDP gathers as in Fig. C.6 with DMO and a mute applied.*

Phase shift migration was developed by Gazdag in 1978. This method involves a 2-D Fourier Transform of the dataset. It makes use of exploding reflectors whereby pulses emanate from a geologic reflector at depth and travel at half the velocity of the medium towards the receiver. The transformed data is downward continued in the FK domain and solved for $t = 0$. The results are approximate solutions to the wave equation and are therefore inexact.

After testing these two migration methods, the finite difference scheme was selected for line 3000 and the phase shift scheme was chosen for line 2000. The enhanced migrated sections include whitening and further deconvolution which helped to compress residual reverberations and short period multiples in the data. The final migrated sections can be seen in Figs. C.10 and C.11.

Time constraints prevented us from testing further options for better results. For future reprocessing of this data, prestack migration would be a good recommendation to follow in order to obtain a better image of the sections.

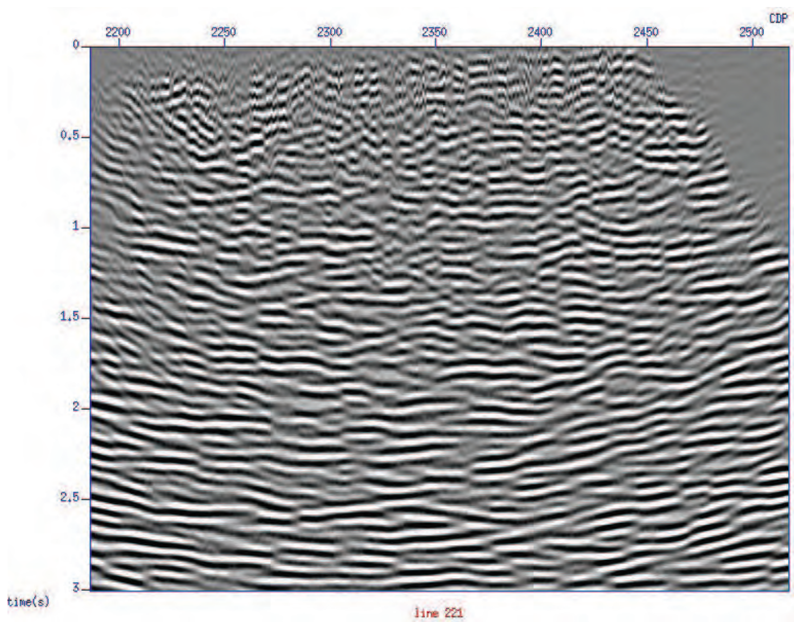

Figure C.10: *Enhanced image obtained for line 2000 using phase shift migration.*

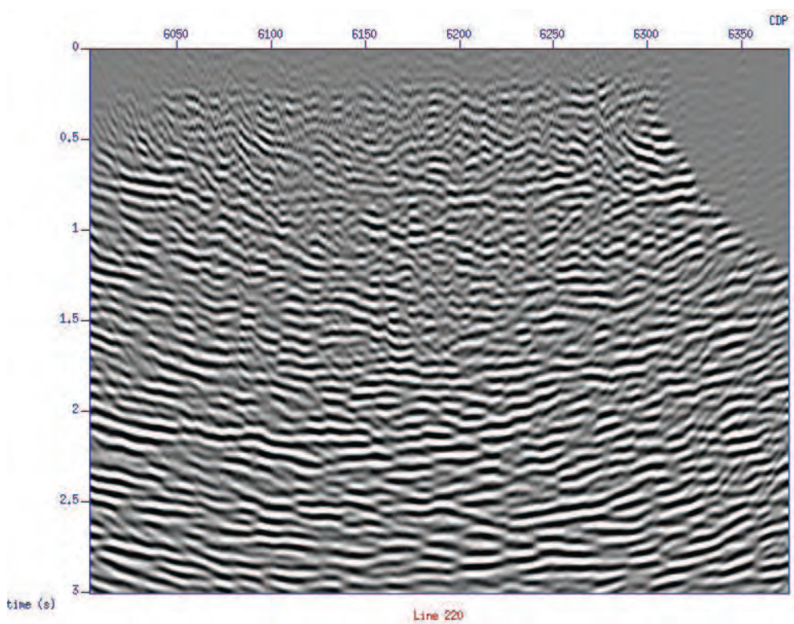

Figure C.11: *Enhanced image obtained for line 3000 using finite difference migration.*

Appendix D

Vertical seismic profiling

D.1 Well MPG-1 summary

Well Mount Princeton Geothermal 1 (MPG-1) is located on the south western edge of Dead Horse Lake. The well was completed on the 13th of May 2009 with parameters shown in Table D.1 and casing design shown in Fig. D.1. The purpose of the well is to measure the geothermal gradient in this area. MPG-1 was part of a larger drilling programme which included the drilling of 6 geothermal exploration wells within the Mt Princeton area [22].

Location	$38^o43.234'$, $106^o10.764'$
Well head elevation	2543m
Depth	190m

Table D.1: *Well MPG-1 design parameters.*

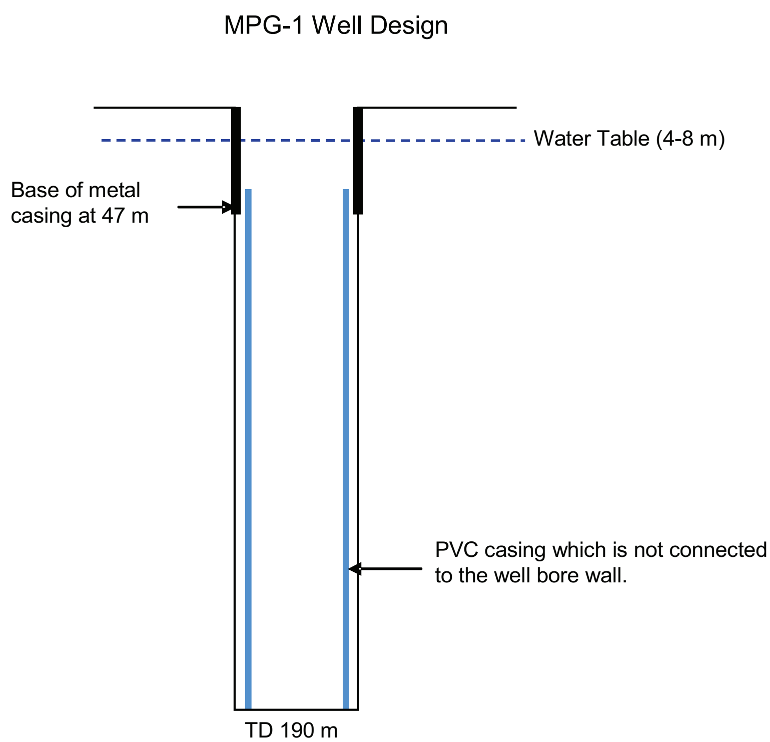

Figure D.1: *Casing design for well MPG-1 showing the position of metal and PVC casing.*

Appendix **E**

Electromagnetics Appendix

E.1 Theory

In both frequency domain electromagnetics(FDEM) and time domain electromagnetics(TDEM) there are typically two loops: one transmitter loop and one receiver loop.

We control the current, voltage, and frequency of this primary loop. By controlling this loop, we also govern the responding magnetic field running through the loop. The relationship used for this controlling of the magnetic field is known as Ampere's circuital law:

$$\nabla \times \vec{H} = \vec{J} + \frac{\partial \vec{D}}{\partial t} \tag{E.1}$$

In equation E.1, $\vec{H}$: magnetizing field, $\vec{J}$: free current density, $\vec{D}$: electric displacement field, t: time.

When the primary magnetizing field goes through the ground, the magnetic susceptibility(μ) of the ground determines the magnetic field($\vec{B}$) according to the equation: $\vec{B} = \mu\vec{H}$. This is the primary magnetic field and it can be thought of as the total magnetic field from the material. Note that as $\vec{H}$ varies, so does $\vec{B}$ proportionally. As mentioned previously, we control this primary magnetizing field and thus we control the primary magnetic field as well.

At this point the primary magnetic field is varied. The manner in which this is done depends on whether we are using FDEM or TDEM. When this primary magnetic field is varied, a responding electric field($\vec{E}$) is created within the rocks according to Faraday's Law of Induction:

$$\nabla \times \vec{E} = \frac{\partial \vec{B}}{\partial t} \tag{E.2}$$

In equation E.2, $\vec{E}$: electric field, $\vec{B}$: magnetic field, t: time.

As the $\vec{E}$ field goes through the ground, the conductivity (σ) of the ground determines the current density within the ground according to Ohm's Law: $\vec{J} = \sigma\vec{E}$. Additionally the electric field creates an electric displacement according to the equation: $\vec{D} = \epsilon_0\vec{E} + P$, where ϵ_0 is the vacuum permittivity and P is the polarization density. Now we have a varying current and electric displacement field in the ground.

As known from equation E.1, this varying current density and electric displacement field will create a responding magnetizing field. This magnetizing field is known as the secondary magnetizing field. This field has originated from the ground, and its magnitude has been influenced by the grounds magnetic susceptibility and conductivity.

It is this secondary magnetic field that the receiver loop will record. In order to record this field, we once again utilize equation E.2. As the magnetic field varies through the receiver loop, it will create a current in the loop that can be measured to determine the magnitude of the secondary magnetic field. A diagram with these concepts and fields labeled is available in Figure E.1.

There are now known values for the primary magnetic field and the secondary magnetic field throughout time. These values can be used to determine what the ground conductivity and magnetic susceptibility are.

E.1.1 Time Domain EM vs Frequency Domain EM

There are several distinct differences between TDEM and FDEM.

In TDEM the transmitter loop current is a constant until a shut off point(Figure E.2 (a)). The current within the ground varies by diffusing inwards into heat. Therefore the receiver loop will record a decaying electric field(Figure E.2 (b)).

A typical survey geometry for TDEM is to have the receiver loop within the transmitter loop, with the transmitter loop being much larger. The dipole orientation of most TDEM surveys is horizontal(loop axis perpendicular to ground).

In FDEM the transmitter loop current varies sinusoidally throughout the data acquisition (Figure E.4 (a)). Both the primary and secondary magnetic fields are picked up at the receiver loop, because the primary current never shuts off, however this can be corrected later(Figure E.4 (b)).

Because the primary current varies sinusoidally in FDEM, the current within the ground varies

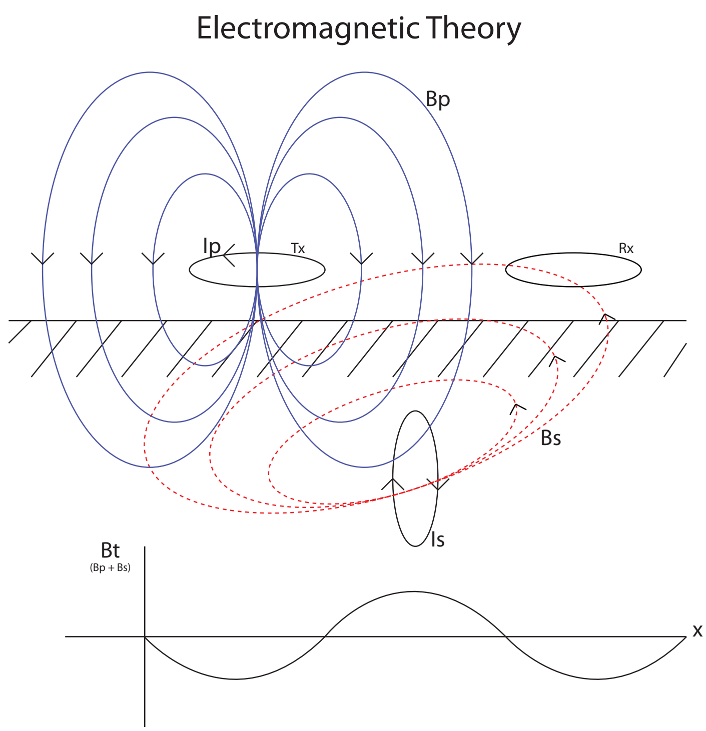

Figure E.1: *Demonstration of how the EM method works. Ip induces Bp, then Bp induces Is, then Is induces Bs, and finally Bs induces a current in the reciever(Rx).*

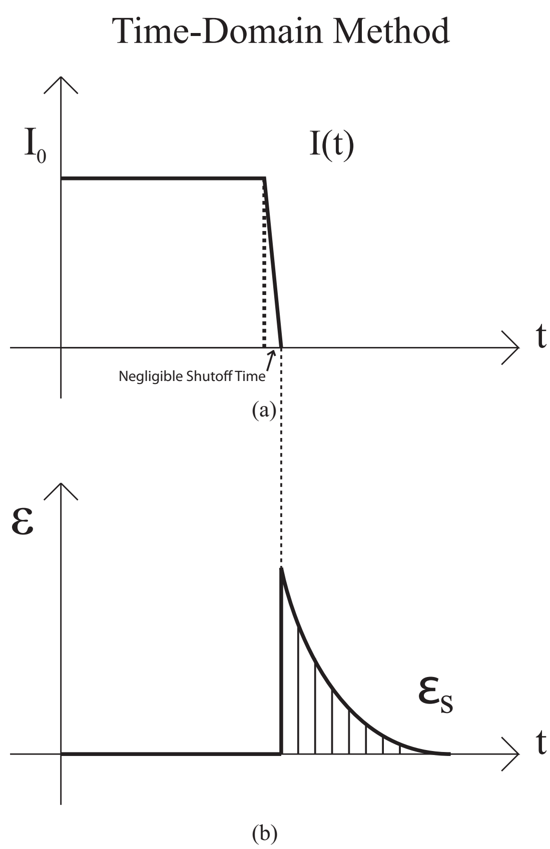

Figure E.2: *(a) Plot demonstrating the current vs time for the transmitter loop in a TDEM survey. (b) Plot demonstrating the voltage vs time for the reciever loop in a TDEM survey.*

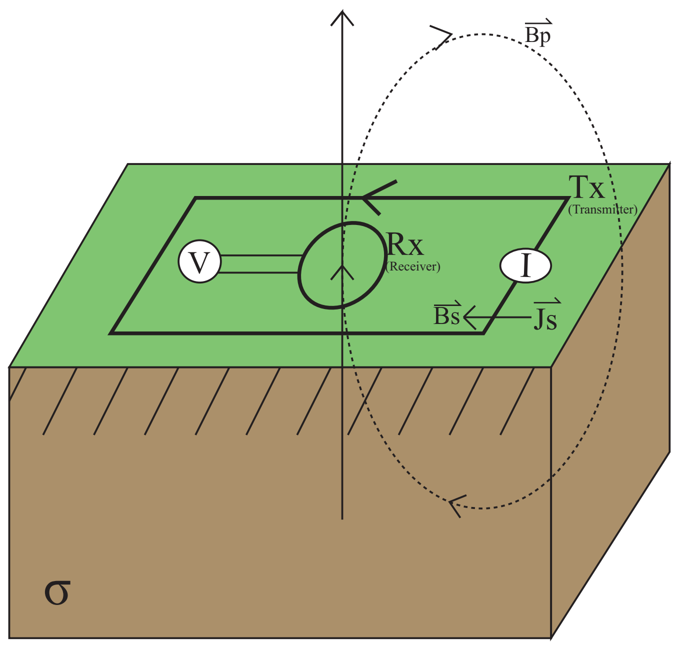

Figure E.3: *A typical setup geometry for a TDEM survey. Note that the receiver is within the transmitter loop. Also note the horizontal dipole configuration. Only the primary magnetic field is shown, because this is before the primary magnetic field is shut off and the secondary magnetic field is created.*

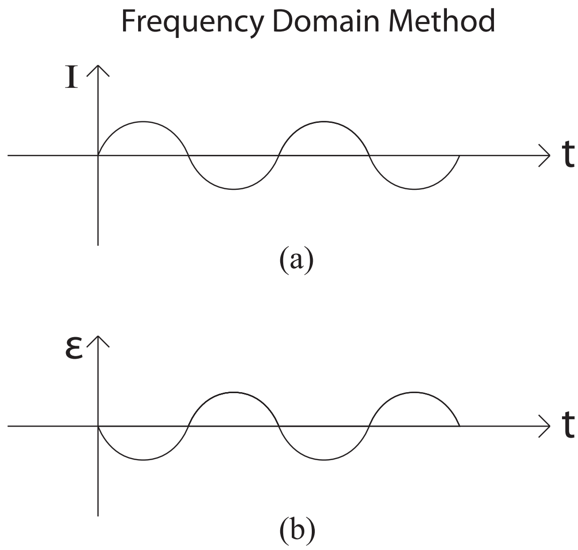

Figure E.4: *(a) Plot demonstrating the current vs time for the transmitter loop in a FDEM survey. (b) Plot demonstrating the voltage vs time for the receiver loop in a FDEM survey.*

in eddy currents. In FDEM there is usually a separation distance between the transmitter and receiver. Additionally the dipole orientation is vertical(loop axis parallel to ground). In FDEM the frequencies can be changed to attenuate certain frequencies of electrical noise.

E.2 Data Analysis

E.2.1 Noise

The EM method is highly susceptible to environmental noise. As EM provides a measure of subsurface conductivity, any anomalous conductive material (e.g. metal objects) on, or near the surface in the vicinity of the EM31 produces a significant response in the measured data. Noise from metallic objects is more identifiable in the in-phase component due to it being an indicator of magnetic susceptibility. Spikes that exist in the in-phase data correlate well with the locations of potential noise sources listed in the observer logs for each survey location. By identifying anomalous high values in the in-phase data allows a more accurate interpretation of the quadrature data.

Noise can also be introduced into the survey from poor operation of the EM31 device. The boom must be kept sufficiently level with the ground which can be a problem on steep terrain or in difficult weather conditions. A rough style of walking will constantly change the

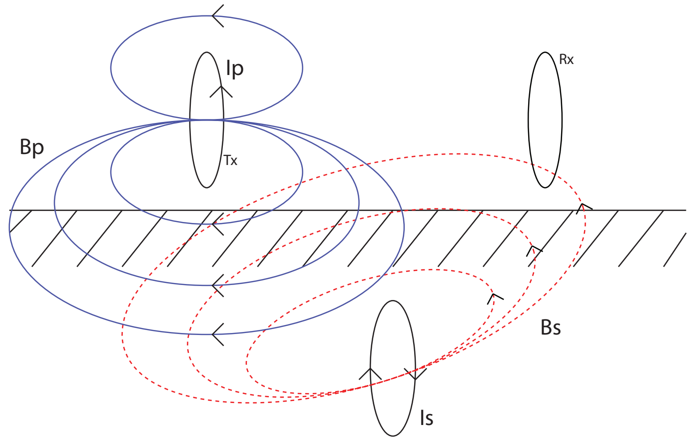

Figure E.5: *A typical setup geometry for a FDEM survey. In an FDEM the loops are typically separated by a distance. Also note the vertical dipole configuration. Both the primary and secondary magnetic fields are shown because in an FDEM survey both fields occur at the same time.*

acquisition height producing an artificial upward and downward continuation of the measured data. The in-phase component is most sensitive to this variation in elevation [10]. The same operator should complete the entire survey area to minimize the uncertainty caused by walking style and conductivity of the clothing they may be wearing.

E.2.2 Uncertainty

At Poncha Springs a forward and reverse survey was completed along line A (Fig. **??**). The existence of a repeat survey along the same line enables a more rigorous analysis of the uncertainty of the EM geophysical survey method. The quantifiable measure of the uncertainty is assumed to be consistent through all collected datasets.

A qualitative analysis of the repeat line shows that generally the trend of the lines is similar. However a finer analysis reveals that there appears to be opposing responses at numerous points along the line. This is not assumed to be an artifact of the opposite orientation of source and receiver coils for the forward and reverse surveys. If this were the case, then the survey methods adopted at Hecla Junction and Dead Horse Lake would be invalid as every neighboring survey line was acquired in the opposite direction.

Table E.1 and Table E.2 summarise the quantitative statistical analysis on line A surveys. Values for correlation and covariance highlight both the similarity between datasets and how they co-depart from their average values respectively:

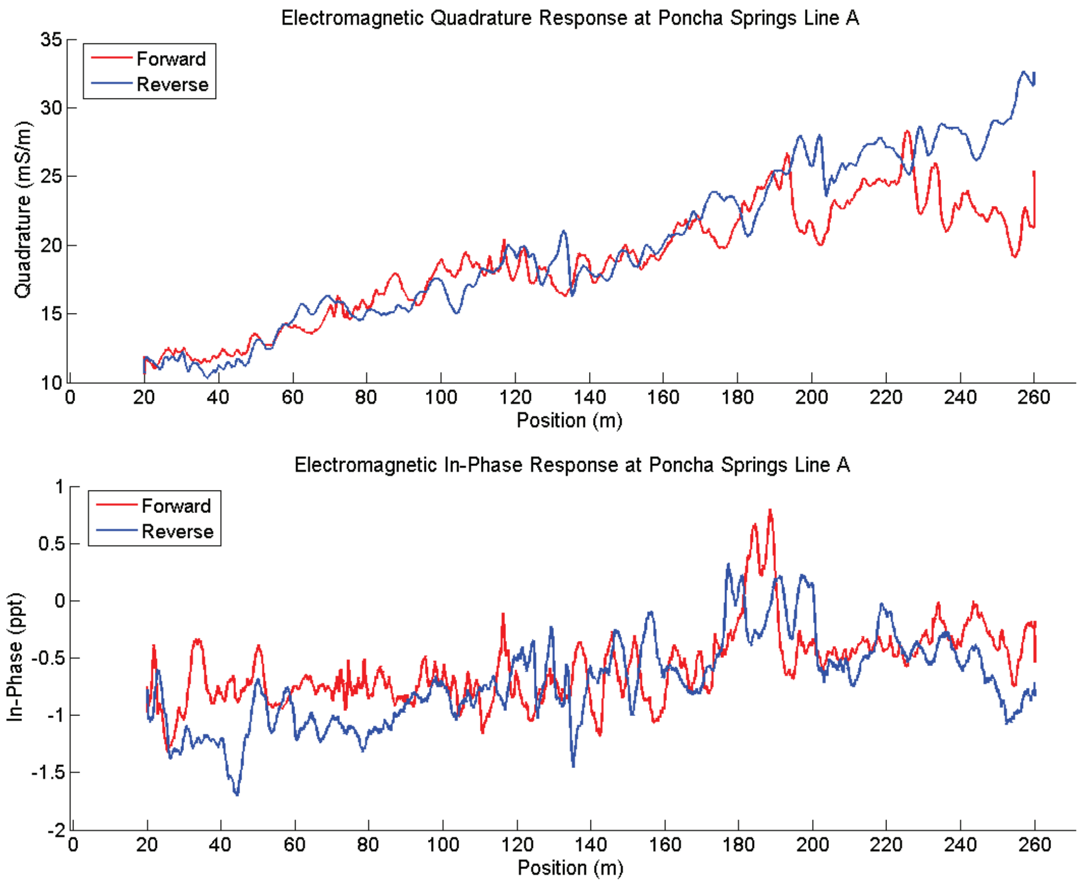

Figure E.6: *EM31 measurements taken along line A at Poncha springs. A forward and reverse profile was conducted allowing anaylsis of the uncertainty of the survey. The EM31 measures both quadrature (top) and in-phase (bottom).*

$$Corr(X, Y) = \frac{E[(X - \mu_x)(Y - \mu_y)]}{\sigma_x \sigma_y} \tag{E.3}$$

$$Cov(X, Y) = E[(X - \mu_x)(Y - \mu_y)] \tag{E.4}$$

where E = expected value, X & Y = random variables, μ = mean, σ = standard deviation.

Ideally, for a repeat survey over the same line the measurements should be identical, assuming the ground is time invariant. For this ideal case the covariance would simply be equal to the variance. In reality this will never be the case due to errors introduced by the operator, environmental noise and intrinsic instrument errors. An assessment therefore of uncertainty in the EM31 data should be determined from the difference between covariance and variance.

	Variance	Mean
Line 1 Quadrature	17.0	18.8
Line 2 Quadrature	33.4	19.9
Line 1 In-Phase	0.103	-0.572
Line2 In-Phase	0.148	-0.716

Table E.1: *Individual Summary of Statistical Analysis*

	Covariance	Correlation Coefficient
Quadrature	21.1	0.89
In-Phase	0.063	0.51

Table E.2: *Summary of Statistical Analysis between forward and reverse surveys along line A, Poncha Springs*

The correlation between quadrature values is high indicating reasonable similarity between the two datasets. The in-phase correlation is relatively low, which is likely due to the fact this measurement is highly sensitive to changes in acquisition height. The terrain along line A is arduous and encounters a series of obstacles which all contribute to uncertainty in acquisition.

Application of this analysis to the two other EM datasets allows an understanding of potential variances in measurement between neighbouring survey lines due to the acquisition method. During minimum curvature gridding much of this subtle variance is suppressed, emphasizing only the major conductivity anomalies.

Appendix F

Gravity Appendix

F.1 Theory

The gravity method is a method of investigating the subsurface which utilizes the gravitational field created by the mass of the Earth. Measuring changes in this field gives information on the density variation in the composition of the Earth. The gravity method can be used to distinguish the presence of density contrasts such as caves, ore bodies, basin bottoms, and faults in the subsurface. The ability to identify subsurface geometry using the gravity method makes it beneficial for the task of exploring a sedimentary basin and characterizing potential geothermal resources.

The application of the principles of gravity to geological problems has a lengthy and diverse history. The establishment of the law of gravitational attraction by Newton in the 17th century led to an understanding of how two bodies influence each other through gravity and the concept of the gravity field [25]. Anomalies in the Earth's predicted gravity field can be caused by latitude, elevation, topography, earth tides, and subsurface density variation [37]. The measurement of the strength of the gravity field at a point is taken using a gravimeter. The targets of geophysical investigation are usually smaller-scale density variations within the crust, which can be overshadowed by the other factors influencing the observed gravity. In order to isolate the target anomalies, a series of corrections to negate the unwanted influences has been established.

Following the corrections, results can be modeled to attempt to explain the subsurface geometries influencing the observed gravity. Due to ambiguities in the interpretation of gravity data, these model solutions are non-unique. Several mathematically valid models can fit a single set of results. Because of this ambiguity, other considerations such as the regional geology and the results of other geophysical investigations must be applied to constrain the model for a realistic and useful interpretation.

F.1.1 Newton's Law of Attraction

Newton's law of attraction is a fundamental basis of the gravity method. This law demonstrates that objects of mass exert a force on each other that is proportional to the amount of mass of the objects and inversely proportional to the square of the distance between the masses. Equation (1) shows this relationship mathematically.

$$F = \frac{Gm_1m_2}{r^2} \tag{F.1}$$

In equation (1), F is the gravitational force between the two bodies, G is the universal gravitational constant (6.6748 x10^{-}11 N), m_1 and m_2 are the masses of the two bodies respectively, and r is the distance between them.

Since the relationship between the gravitational force and the masses of the interacting bodies is established, and it is a known mass within the gravimeter on which the gravitational force is measured, the density of a target anomaly in the subsurface can be modeled [37]. Changes in the density distribution of the ground can also be observed through this established relationship.

F.2 Data

F.2.1 Ambiguity

The ambiguity of the inverse problem in the gravity method is related to the fundamental concept of gravitational attraction. Bodies exert forces on each other that depend upon the masses of the bodies and on the distance between them. A closer, smaller object can exert an observed force equal to that of a larger, farther away object. This applies also to the attraction between a mass in the gravimeter and a buried density contrast in the subsurface. Even if the gravitational field could be measured to exact precision, which is currently impossible, the inversion of the observed gravity would still have ambiguous results [37]. As the measurement of the gravity field is taken at the surface rather than near the source of the anomaly the inverse problem is made more complicated.

F.3 Data Reduction

The processing of gravity data requires a detailed, multi-step correction process in order to isolate target anomalies from other factors that influence the observed gravity of the Earth at a point on the surface. These corrections uncover the geometries and density distributions in the subsurface which make it different from the homogeneous layered earth model. The shape and extent of the anomalies in the gravity curve can distinguish one sort of geometry from another.

F.3.1 Drift Correction

The first correction applied to the raw data set was the drift correction/tide correction. Drift is an affect caused by instability in the instrument taking the readings including temperature changes and wear on the instrument. This drift increases with time, which is why it is important to take a final reading at the base station so that the linear relationship between the drift in the measurement and time. Once the data has been collected, difference between the first and last readings at the same station can be linearly subtracted from the data in between, correcting both for instrument drift and for the approximately linear influence of gravitational tides. Equation (1) is the correction equation.

$$\Delta g_D = g_b + (t - t_b)\frac{g_e - g_b}{t_e - t_b} - g_1 \tag{F.2}$$

In (1), t is the reading of the measurement (hours), g_b and g_e are the gravity readings (mGal) at the beginning and end of survey loop, at times t_b and t_e, respectively, and g_1 is the reading (mGal) at the first recorded instance of the base station.

F.3.2 Latitude Correction

Next in the series of corrections to the data is the latitude correction. The difference in gravitational acceleration over latitude is caused by the Earth's rotation and the equatorial bulge [37]. The equation for taking the influence of latitude out of the gravity is Equation (2).

$$\Delta g_L = \pm 0.001626 sin(\theta) cos(\theta) \Delta y \tag{F.3}$$

Δg_L is the latitude correction to be applied to the data. θ is the latitude of the station in degrees. Δy is the local, or relative, northing in reference to one station.

F.3.3 Free-Air Correction

Free-air correction was applied in order to normalize the effects of elevation on the data. The effect of elevation is due to the varying distances of the survey points from the center of mass of the Earth. The stations must be reduced to a common datum. This correction does not take into account material between the station and the datum [37]. Equation (3) is the free-air correction equation.

$$\Delta g_F A = \pm 0.3086h \tag{F.4}$$

h is the station elevation above sea level (m). The 0.3086 constant takes into account the radius of the Earth and the average acceleration of gravity. $\Delta g_F A$ is the Free-air correction to be applied to the data.

F.3.4 Bouguer Correction

The Bouguer correction was also applied to the data. It takes into account the gravity of materials between gravity stations and the datum plane that was established in the Free-air correction by assuming there is a continuous slab of material with constant density in the space. The density was assumed to be 2.67 g/cm^3, which is the average density of the continental crust. The formula used for the Bouguer correction is seen in equation (4).

$$\Delta g_S = 0.1119h \tag{F.5}$$

In (4), h is the station elevation above sea level (m). The combination of the Free-air and Bouguer corrections is also called the elevation correction.

F.3.5 Static Shifting

Before the final correction could be preformed, there were some "jumps" visible in the data. Because the gravity measurements were relative and therefore were not tied into an absolute gravity marker, instrument errors from day-to-day caused shifts in the data from different days. These shifts were corrected using a technique called static shifting in which the difference between the upper and lower shifted data is added to the lower to bring it all to the same level. Because the readings are relative, it is more important to be able to observe the trend in gravity over the survey line than the actual readings themselves.

F.3.6 Terrain Correction

The final correction applied to the gravity data was the terrain correction. While the Bouguer correction accounts for the mass between the station's elevation and the datum, it does so with an infinite slab of constant height. The variance in elevation between the stations, such as hills and valleys, is accounted for by the terrain correction. The exact elevations of the line were provided by a digital elevation map from the USGS seamless server with a spatial resolution of 10m. A software package called Oasis Montaj from Geosoft was employed to correct the data utilizing the digital elevation model as well as a larger regional model of lower 90m resolution de-sampled to 200m resolution. The lower resolution regional correction terrain grid was created in the Oasis Montaj software's GRREGTER GX option. Using both the local and regional grids, the algorithm extracts the effects of the terrain by breaking it up into sloping triangular sections and calculating the gravity for square prisms comprising the terrain under the stations [16].

Appendix G

Well logging

On site, it was the intention to leg three logs at well MPG1: temperature, induction, and gamma ray. The following is a brief description of the parameters and methods used during each of the three logging processes at well MPG1.Temperature logs are measurements of the subsurface temperature down hole. They have multiple uses: to correct other borehole-measurements that are temperature sensitive, to explore for geothermal resources, to interpret the movement of groundwater, and occasionally to map stratigraphy. In geothermal wells the temperature in the subsurface increases with depth. Accordingly, the temperature gradient measured by the tool in the well is controlled by the formation heat capacity divided by the thermal conductivity of the rock [18].

In general, rocks have three main thermal properties: conductivity, diffusivity, and temperature dependence. The thermal conductivity of a rock is determined by the conductivity of it constituent materials, the rock's porosity, and by the heat transfer coefficients between non similar minerals within the rock. The thermal conductivity of water is much lower than that of most minerals, and the thermal conductivity of fluid is even lower. Thus, if a rock is saturated in water or gas its overall thermal conductivity will be lower than normal that of dry rock. Thermal diffusivity compares a material's ability to conduct heat versus its heat capacity. The higher this ratio is, the faster the thermal transients will dissipate; in other words the rock will be less likely to contain a lot of heat. Temperature dependence refers to the fact that the thermal conductivity of rocks decreases as temperature increases, so the thermal conductivity of most rocks decreases with increasing depth into the subsurface as temperature increases with depth into the earth's crust. Temperature readings from logs are used to find the geothermal gradient. This is the rate at which the temperature increases with depth into the earth's subsurface. It indicates an outward heat flow from the earth's hot interior. The temperature log measurements are a linear function of depth, expressed as $T(z) = T + Gz$, where G is the geothermal gradient, z is depth, and T is the initial temperature at the top of the borehole [18].

The temperature tool is 38in long, and the measuring device is located 6in form the tip of the

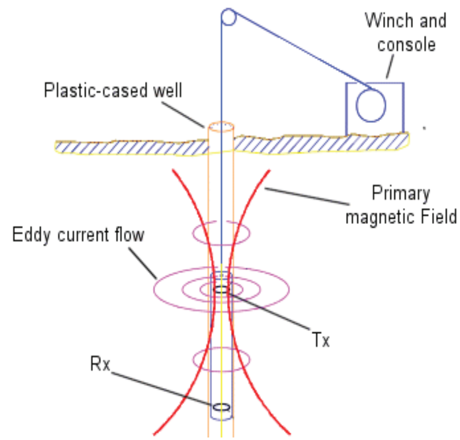

Figure G.1: *The induction method creates an alternating primary field, which in turn induces a secondary current and field in the ground (down-hole in the well) [23]. This field, altered by the formation properties, is received by the receiver coil in the induction tool.*

tool. The computer software was calibrated so that the depth reading on the computer was the depth reading of the tool. The measuring interval was initially set to 0.1ft, however the tool seemed to be malfunctioning. The temperature tool was then pulled out of the hole to begin with induction logging.

The induction method is an electrical geophysical method which uses a transmitter coil that induces a secondary field within the earth. Please refer to Fig. G.2. As illustrated in Fig. 4.44, the transmitter coil creates a secondary field response within the earth, which is picked up by a receiver coil. The properties of this secondary field are controlled by the frequency of the transmitted field and the properties of the rocks (lithology) within the well. Appropriately, the inductive method can be used to map aquifers and is widely used for mineral exploration and resistivity logging.

A few important concepts to regard are wave propagation and skin depth. The electromagnetic wave propagates into the subsurface, but dissipates over time as the current is conducted by the surrounding medium. Consequently, the higher the conductivity of the rocks being surveyed, the larger the current will be and the shorter the distance the wave will propagate into the surrounding formation. The skin depth is defined as the measure of the distance the electromagnetic wave will penetrate into the formation, and is a function of resistivity and frequency. Induction tools are designed to reduce or eliminate the effect of the primary signal measured by the receiver coil, are designed to compensate for the propagation effect and to obtain good vertical resolution in order to achieve a certain depth of investigation [19].

The tool used in the induction survey is a long plastic pipe with a transmitter coil in the and a receiver coil at the other end (similar to an EM-31 induction method). The tool was calibrated before it was sent down-hole into the well to be the same temperature as the ambient air, which is essential as temperature affects the response of the induction tool. The transmitter coil was energized to 12,769 cycles per second, and the sampling rate set to a 0.163ft measuring interval. Normally the induction log would be recorded from the bottom of the well to the top, but in this case the well is too hot for the tool to operate properly at depth. Accordingly, the induction log was recorded from the top of the well downwards until the borehole temperature barely exceeded 50^{o}C, which was around 300ft deep. The tool initially gave erroneous readings and had to be pulled out and recalibrated. The tool got hung up at 25ft and had some odd readings at the top of the hole, but otherwise the readings seemed to be alright at the time log was recorded.

Gamma ray logs are used to measure the naturally occurring gamma radiation that is emitted from the subsurface rocks in a well or borehole. By measuring the gamma ray emission, the logs can be used to characterize the rocks in the well or borehole. A gamma ray is a photon (a quantum of radiant energy). The emission of these rays occurs when the nucleus of an atom absorbs an electron, or changes its energy state. The energies of gamma rays are characteristic of the nuclide that emits them, so they can be used to identify what kind of element emitted the ray. Gamma rays logs have the option of employing one of two types of sources, natural and artificial. Isotopes of elements emit gamma rays as they decay, these can be made artificially or they can occur naturally, thus the two different source types for gamma ray emissions. There are three families of radionuclides that occur naturally in the earth's crust, the uranium chain, the thorium chain, and potassium. There are two artificial radio nuclides that are used commonly for logging purposes, a cobalt isotope and a caesium isotope [20]. In this case, gamma ray tool employed the natural emission source.

Gamma rays interact with matter commonly in 3 ways; the photoelectric effect, the Compton effect and pair production. The photoelectric effect is the dominant interaction at lower energies. In this case the gamma ray gives all its energy to an electron that is orbiting an atom; this energizes the electron which passes on this energy to other atoms in the material and then drops back into its original orbit (equilibrium state). When the electron does this it emits an X-ray, which is characteristic of the medium that is stopping the gamma rays, that interacts with the material again and again until all the energy is absorbed. The Compton effect occurs at intermediate energies; in this case the gamma ray only gives up part of its energy to an electron, and the rest of its energy scatters elsewhere. The electron again affects other atoms in the medium, and then emits an X-ray as it stabilizes. The scattered gamma ray either repeats its process of bouncing around electrons or gets absorbed in a photoelectric interaction. At high energies pair production interaction takes over. In this case the gamma ray is equal to exactly twice the mass of the electron, and the two become an electron-positron pair when near the nucleus. The positron is antimatter, and when it interacts with an electron they annihilate one another and produce two gamma rays. These rays propagate in opposite directions and interact by Compton and photoelectric effect until they are absorbed [20]. Please refer to Fig. G.2.

When attempting to log well MPG1 with the gamma ray tool, the tool was sent to the bottom

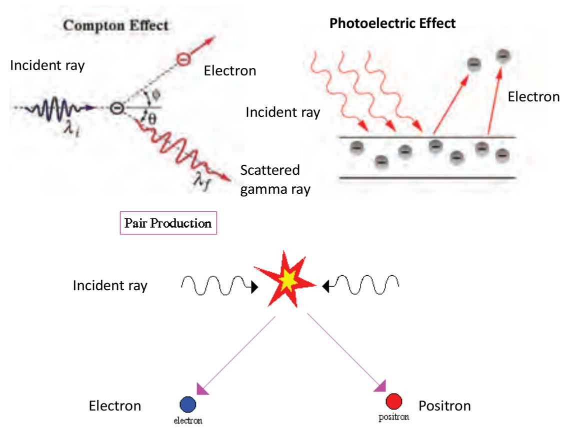

Figure G.2: *This figure shows how the gamma ray interacts with matter as explained above, via the pair production effect (high energy)[30], the Compton effect (intermediate energy) [3], or the Photoelectric effect(low energy) [4].*

of the hole, disregarding the temperature rating for the tool. Unfortunately, the tool was rated to 50?C. The electronics within the tool were fried at the bottom of the hole and the tool was rendered useless.

Appendix H

Magnetic Methods Appendix

H.1 Theory

The Earth's natural magnetic field (Figure H.1) is the result of molten metal circulating around a solid core. This field changes through geologic time, with occasional polar reversals and intensity fluctuations. Generally, the magnetic field is around 50,000 nanotelsa (nT) [28]. However, when a rock or artifact in this total magnetic field exhibits its own unique magnetic properties, it can either amplify or detract from the total field. This change is usually very subtle and may only be on the order of tens of nT, but for naturally-occurring magnetic deposits (such as magnetite) the differences in the total field can be in the hundreds of thousands of nT.

Unfortunately, the Earth's magnetic field is not always constant. Small daily variations, or external effects like solar activity, can result in significant changes in readings. Therefore, it is very important to set up a base station that measures the total magnetic field from one observation point throughout the length of the survey, so that such variations can later be removed from the data. It is also important to take detailed notes when recording survey data that make note of any anomalous objects visible along the survey line, such as exposed metallic objects.

Magnetic data is easily obtained by an instrument called a magnetometer, which requires no ground contact and is highly portable. Magnetic surveys can be completed by only two or three individuals in rougher terrain where it may not be possible to bring vehicles or heavy equipment.

H.1.1 Magnetization

The Earth's magnetic field resembles that of a bar magnet (Figure H.1), with north and south poles and an expansive field lines circumventing the Earth. The cause of this is the molten metal (iron, nickel) irregularly circulating in the core. The uneven flow results in the magnetic field having uneven intensity or orientation. This field is conventionally called the total field.

There are two primary types of magnetization: remnant magnetization and induced magnetization.

H.1.1.1 Remnant Magnetization

When a material reaches or surpasses its Curie temperature, the permanent magnetism of the material is lost and the material is able to realign. This alignment generally mimics that of the total field. The temperatures for materials of geologic interest range between 500-600 degrees C, temperatures that are found in lower portions of continental crust [28]. After cooling, the rock still exudes a magnetic signature similar to that of the total field at time of creation, even without the presence of an external field.

H.1.1.2 Induced Magnetization

In the presence of an external field, a subsurface feature will adopt the properties of the external field it is exposed to. The extent of this adaption depends on the magnetic susceptibility of the feature, which is a result of the mineral composition.

Once a rock becomes magnetized by the total field, it contributes or detracts from the total field measurement and can be detected by a geophysical magnetic survey. The level of field contribution is dependent on anomaly size, orientation and depth. Figure H.2 is a graphical and illustrative example of an arbitrary metal bar buried in the subsurface.

In the case of smaller anomalies, the typical output will be a dipolar structure with a high and low end (which are stronger or weaker depending on geometry). However, in the case of Chaffee County, the primary objective is to measure geologic units, which are far vaster and much weaker magnetically. Therefore, it is unlikely there would be a graphical anomaly like Figure H.2 in any data obtained in Chaffee County that was not attributed to human interference or artifacts.

The magnetic susceptibilities measured from the 2009 Field Camp in the Chaffee County area can be seen in Table H.1. While these measurements may not be precise, they show relative susceptibility changes in different rock structures. The volcanic sediments seem to be more susceptible to magnetic influence, and therefore would appear as magnetic highs in any data collected. This could be useful in determining what sort of geology exists in the subsurface.

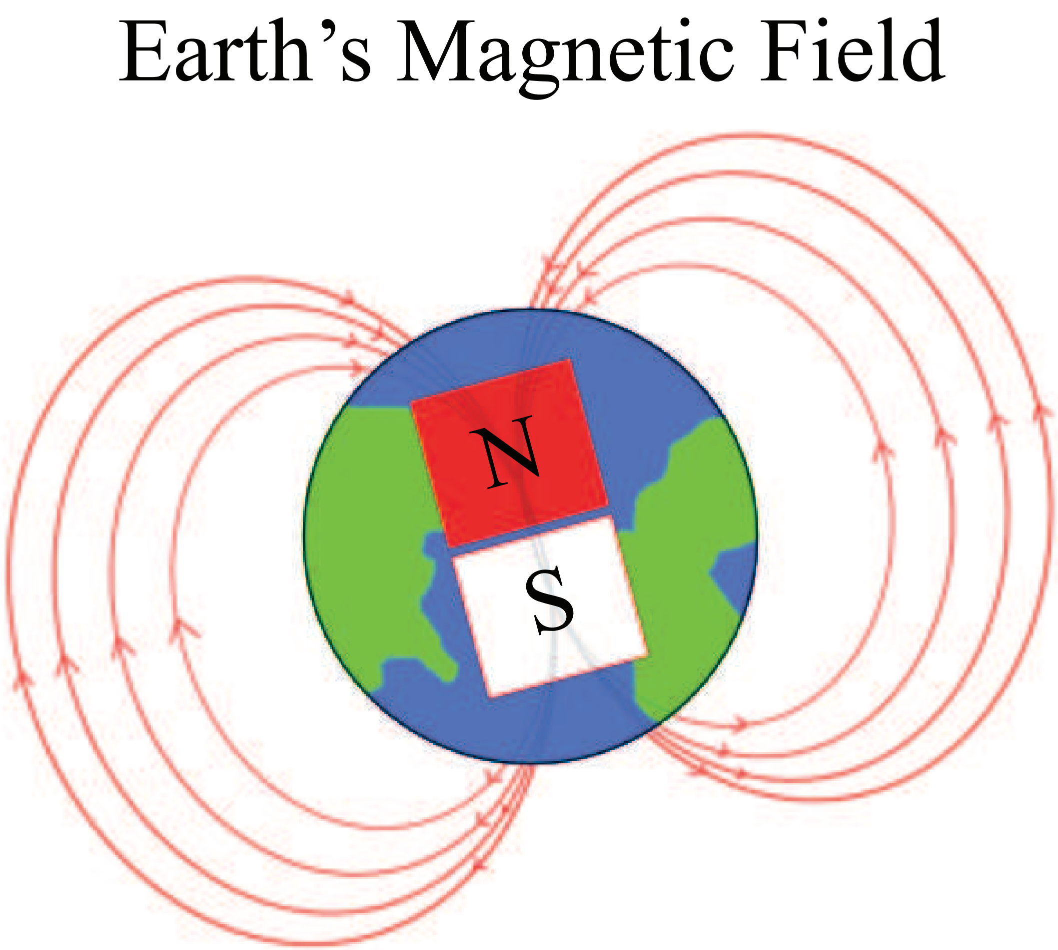

Figure H.1: *Illustration of Earth's natural magnetic field. The magnetic north and south poles are not perfectly aligned with geographic north and south poles. The magnetic poles fluctuate with the field [9].*

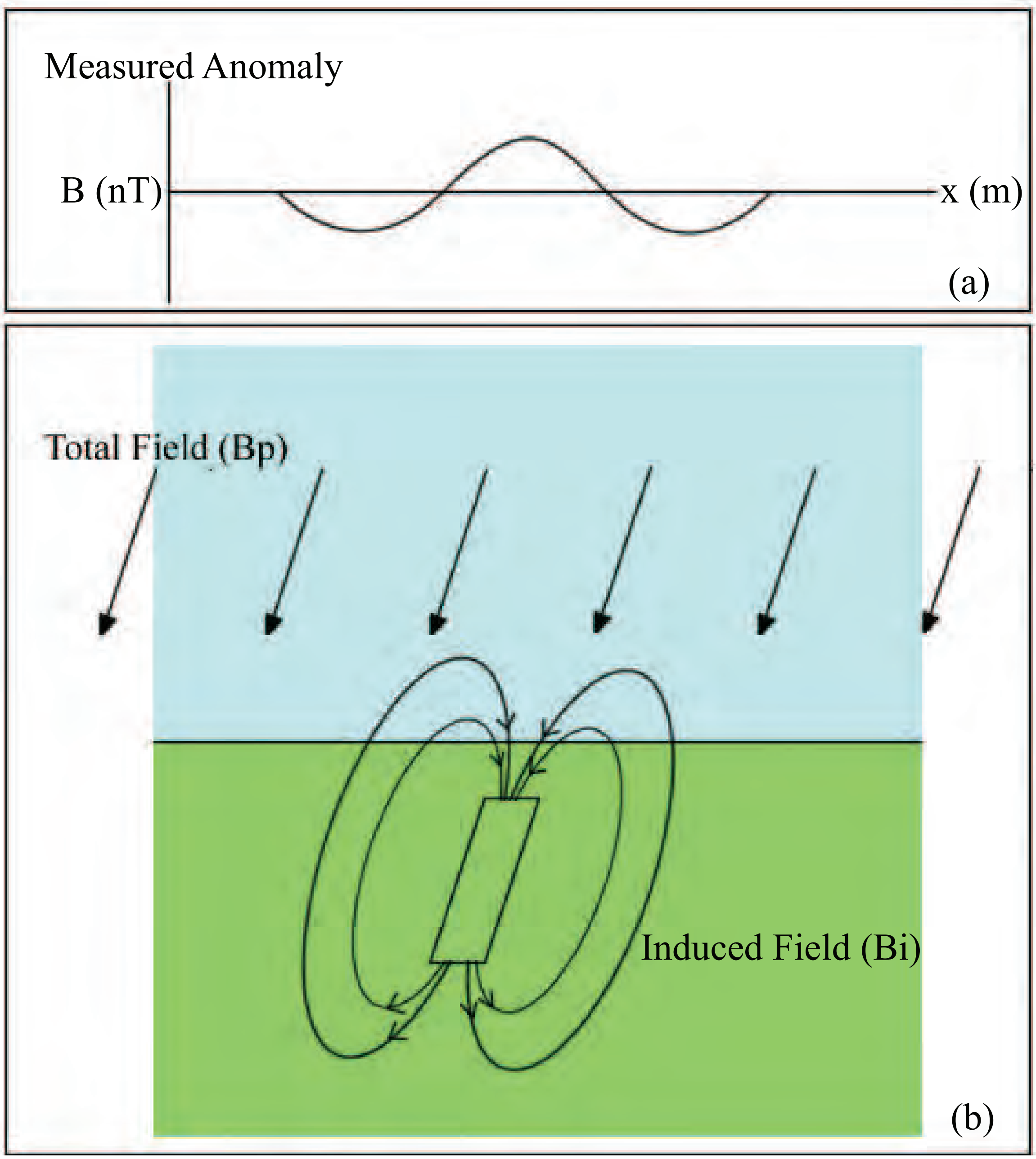

Figure H.2: *Approximate anomaly response from a buried anomalous object (in this case, likely a metal bar) on a graphical plot. (a) Plotted measured response from anomaly. (b) Cross-sectional illustration of the anomaly in the subsurface and the behavior of both the total field (Bp) and induced field (Bi).*

Unit	*Susceptibility [SI]*
Highly magnetic sediments	0.019
Basin fill	0.017
Mt. Princeton Batholith	0.020
Sawatch Front Fault Zone	0.001
Dry Union Formation	0.005
Deep Dry Union Formation	0.010
Volcanics	0.080
Basement Rock	0.022
East side fault zone (basin fill)	0.017
East side fault zone (volcanics)	0.060
East side fault zone (deep)	0.020

Table H.1: *Magnetic susceptibilities of various formations from the Chaffee County area. From the Colorado School of Mines hosted Field Camp of 2009 [2]. Values are not precise, but do reflect relative changes between rock types. (For example, volcanic units are more magnetically susceptible than basin fill.)*

H.2 Equipment

H.2.1 Cesium Magnetometer

The cesium magnetometer, or the G-858, works by sending circularly polarized light through a cesium vapor chamber at a specific wavelength at which the cesium vapor absorbs the photons. This absorption causes specific low-energy electrons to excite to a higher energy level. An AC current is sent through a wire coil that surrounds the cesium chamber, the frequency of which is modified until the Larmor frequency is achieved. When this occurs, the generated magnetic field transfers some electrons back to the lower energy levels. The process is repeated, with less and less intense light intensity measurements until the cesium vapor is saturated. This process is almost instantaneous, giving the cesium magnetometer an accuracy of 0.1 nanotesla (nT) [9]. An illustration of this process can be seen in Figure H.3.

Two such sensors are aligned on the cesium magnetometer, and can be held to mimic either a vertical gradient (with one sensor stacked over the other) or a horizontal gradient (with the sensors side-by-side) along a line. For all surveys conducted in Chaffee County, the vertical gradient was measured, which allows for pinpoint precision along a line.

The depth of investigation for the cesium magnetometer depends largely on the measured anomaly. A stronger anomaly deeper in the subsurface may be measurable, while a weaker anomaly may not. Additionally, depth of investigation depends on magnetometer orientation. If the object is aligned properly with the ambient magnetic field, the anomaly will be stronger than if the axis is skewed.

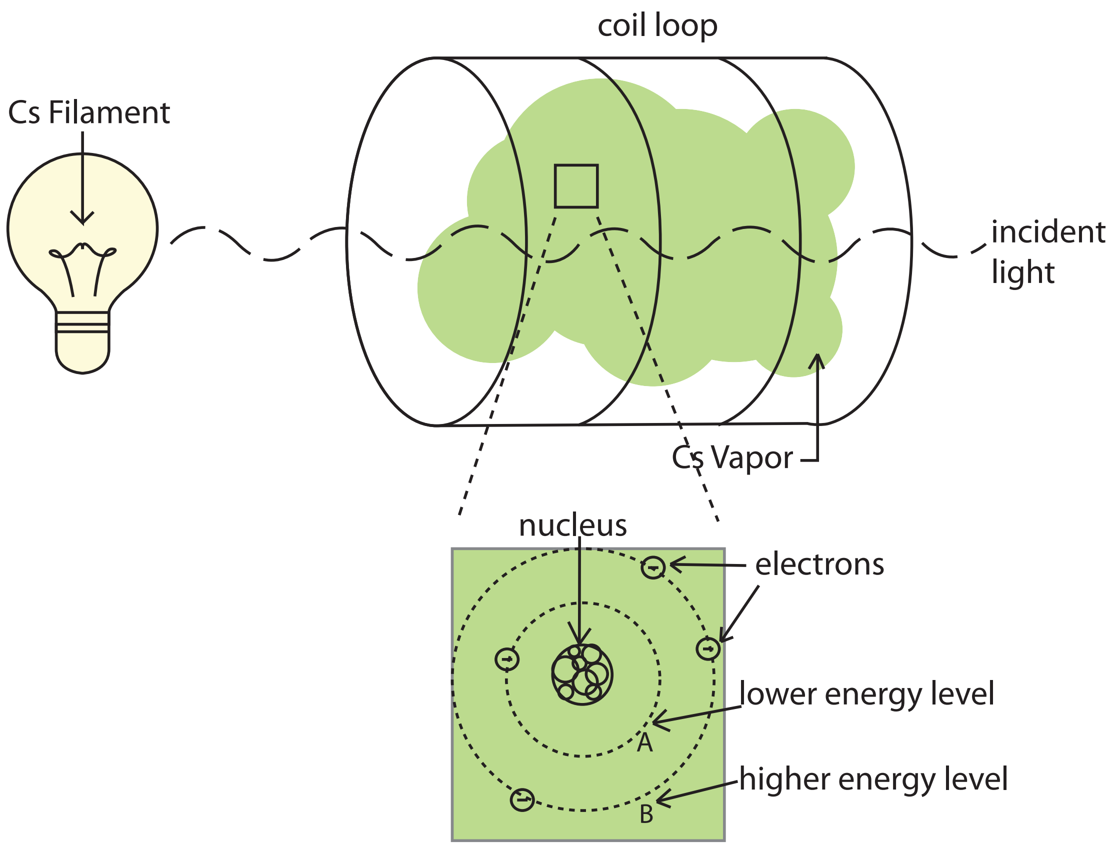

Figure H.3: *Diagram of a cesium magnetometer sensor. From the Colorado School of Mines Field Camp 2009 [2].*

H.2.2 Proton Precession Magnetometer

The proton precession magnetometer, or the G-856AX, which was used only as a base station in the field, has a chamber filled with a protein-rich fluid (kerosene) wrapped in a conductive coil. Initially, the protons of the fluid are aligned with the ambient magnetic field, but when a current is sent through the coil, a secondary field is generated to which the protons align. When the current is shut off, the protons precess back to the ambient field orientation, and the Larmor frequency is measured. The strength of the ambient field affects the precession of the protons [2].

H.3 Magnetic Data Reduction

Once the data sets were downloaded from each individual survey onto a computer, they were viewed in MagMap 2000, a Geometrics program designed to specifically handle G-858 data. The viewing was purely preliminary and offered an opportunity to see the quality of data. To ensure that the geometry of the data was proper, the data files were exported into .dat formats that contained only the mark information, which typically denotes the progression of the survey along a line. Magmap 2000 assigns an equal amount of distance per mark, which means that if an extra mark is pressed, the few data points included there will be stretched to the mark separation. Instead of looking through the entire .dat file to find the mark errors, a histogram of the marks were made. By looking at this histogram which plotted the amount of readings per mark, it became possible to identify erroneous marks that interfered with the geometry. If the column of the histogram was too large, when compared to the average, it means that someone missed a mark along that portion. Alternatively, if the column was too small, it means that an addiction mark was pressed. The notes of the surveys were also taken to help reduce the amount of time required to correct for the geometry.

The geometry corrected files were imported back into MagMap 2000 along with the base station data. The base stations had to be the same date as the standard magnetic data and, if wrong, were corrected in a word editing software. Once the base station became valid, they were used to run a diurnal correction of the magnetic data. This corrected for the changes in the Earth's magnetic field. Once this correction was done the data was exported into three separate files, one diurnally corrected top sensor data, one diurnally corrected bottom sensor data, and one vertical gradient data. The data at this point was broken up into two different groups, line data and grid data. The two data sets were reduced in slightly different ways. The line reduction with be described initially followed by the grid reduction.

The line data at this point had to be despiked due to large sources of noise. Originally, a program created by a previous Colorado School of Mines student, called dnsgui.exe, was used, but the despiking was not working as intended. Many of the data sets were too noisy and thus automated programs took the noise for data and overshadowed the real data and made interpretation impossible. To counter this manual despiking had to be done. Code was

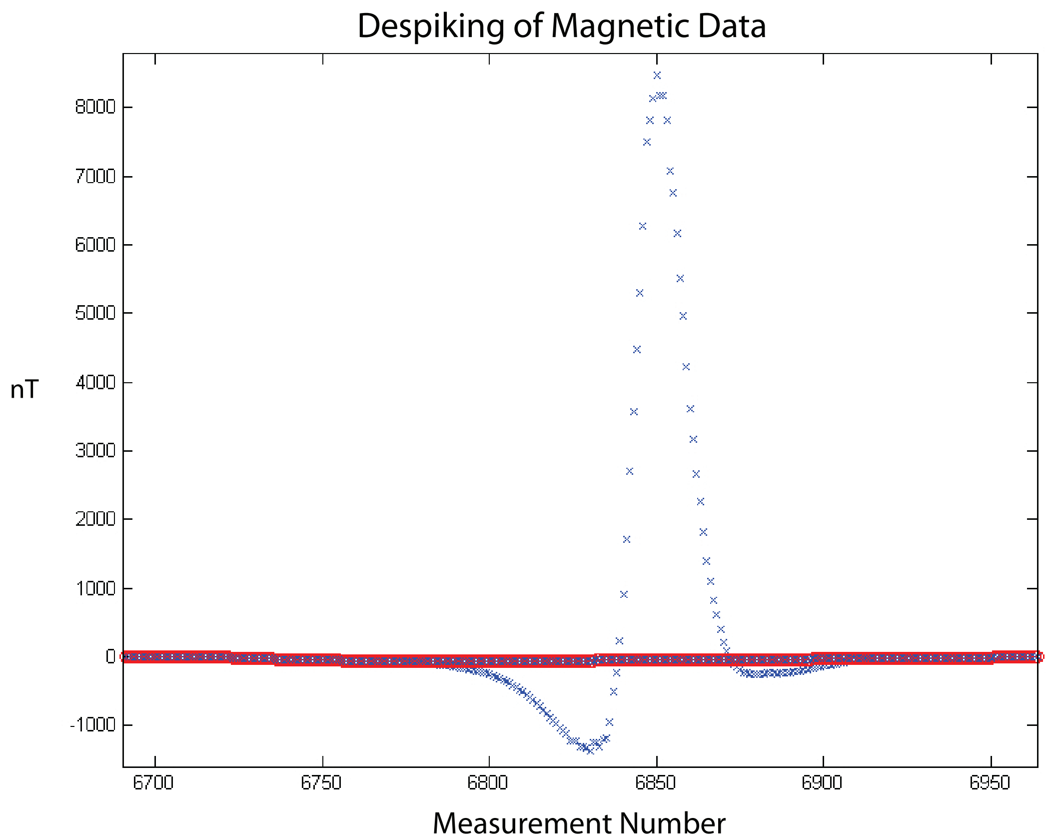

Figure H.4: *Example of the despike program at work. This is along the three thousand line in the green creek area. The blue line represents the original data where as the red line represents the new despiked data. The x-axis is not in meters but in the number or readings, which is around three readings per meter. The y-axis is in nanoTeslas.*

written in Matlab to help with this process. The code, which can be seen in Section H.3.1, took a lower bound and a higher bound and created a linear line between the points while removing the original spike, see Figure H.4. Once the data was despiked, filting was required to take out any excess noise. The program, dnsgui.exe, which was going to be used to despike, was now used to filter the data. The program had an auto filter which was used if it seemed to be a good fit with the data. If not, a symmlet wavelet was used with varying resolutions and coefficients until there was high-quality fit.

Once the line data was despiked and filtered, it was plotted up in matlab and ready for interpretation. There was also a few other filters applied to the data to see if they would help clean up the data. Unfortunately, most of the corrections took too long and did too little to be of much use. The grid data, like the line data, had to be despiked due to large amounts of noise. The same procedure was done for the grids as the lines but the grids had to first be separated into various lines. To do this, a matlab program was written that can be found in Section H.3.1. Once all the various lines of the grids were despiked the lines were reconnected and the data was ready for filtering. The grid data was converted to .xyz files so that it could be easily incorporated into plotgrd which is a program written by the Center for Gravity, Electrical and Magnetic studies. This program takes the data and equalizes it which allows for easier and more accurate filtering. In the program itself, the histogram of the data was equalized so that it would be much easer to see changes in the data. The masking distance was set to five meters to deal with the grids that were not continuous.

At this point the data was filtered a few different ways. The first filtered used was a Fourier transform that was used to attempt to get rid of the higher frequency noise. This was done on a few datasets but the difference between the original data and the transformed data was negligible and due to time constants it was decided that the filter would not be applied to the other datasets. A few addiction filters were attempted including an RTP or reduce to poles filter, which is a phase shift to make finding anomalies easier, but unfortunately they did little to clean up the data so it was decided to use the data which was exported from plotgrd. The data was then loaded back up into plotgrd and was plotted into nice color contours. The grids were now ready for interpretation.

H.3.1 Matlab Codes

H.3.1.1 Despike.m

This code is a background program used by RunDespike.m to despike magnetic data. It takes a lower bound, a higher bound, and linearizes bewteen the two points.

```
function [out] = Despike(x,z,lb,ub)
% DESPIKE Summary of this function goes here
% Detailed explanation goes here
x=sort(x);
nb=ub-lb
out=z;
m=(z(ub)-z(lb))/(x(ub)-x(lb));
c=z(lb);
for ii=1:nb
    dist=x(lb+ii)-x(lb);
    out(lb+ii)=(m*dist)+c;
end
plot(z,'x')
hold on
plot(out,'ro')
```

H.3.1.2 RunDespike.m

This program runs Despike.m N number of times with a specified lower and higher bound.

```
function [FINAL] = Rundespike(x,z,N)
%RUNDESPIKE Summary of this function goes here
    %N is the number of spikes to remove.
out=z;
for ii=1:N
    disp('Spike')
    disp N
    lb=input('Enter lower integer bound   ')
    ub=input('Enter upper integer bound   ')
    [out]=Despike(x,out,lb,ub);
end
FINAL=out;
dataprint=input('Enter write file with quotes and extension    ')
fid=fopen(dataprint,'w');
n=length(x);
for ii=1:n
    fprintf(fid,'%9.5f %9.5f n',x(ii),FINAL(ii));
end
fclose(fid);
end
```

H.3.1.3 Separate.m

Separates a magnetic grid into its respective lines.

```
for ii=1:21
    kk=-500+((ii-1)*25);
    yval=kk/10;
eval(['x' num2str(-kk) '=linecutx(x,y,yval)']);
eval(['y' num2str(-kk) '=linecuty(y,y,yval)']);
eval(['t' num2str(-kk) '=linecutt(top,y,yval)']);
eval(['b' num2str(-kk) '=linecutb(bot,y,yval)']);
eval(['v' num2str(-kk) '=linecutv(vert,y,yval)']);
end
```

Appendix I

S-wave details

I.1 Minivibrator background

A Minivib survey is analogous to a normal vibroseis survey with the theoretical basis behind acquisition and processing remaining the same. A vibroseis survey involves inputting a known signal, called a sweep, into the subsurface using a vibrating pad attached to a truck. The signal inputted has a fixed duration, called the sweep length, and normally involves a linear increase in frequency with time (although a down sweep where the frequency content of the sweep decreases with time is also possible). During the propogation of the sweep function through the subsurface it becomes progressively altered due to changing acoustic properties of the earth at geological boundaries during a process called convolution. At a geological boundary this altered sweep signal is reflected back to the surface where it is recorded by a highly sensitive microphone called a geophone. The acoustic properties of the earth are described by the earth's impulse response and it is this property that is important for an interpreter to understand the subsurface. The typical listening time of a geophone can be 10s of seconds and the recorded signal is a result of the altered sweep reflected back to the surface and a significant amount of external noise.

In order to recover the earth's impulse response from a data set containing repeated copies of the vibrosise sweep and external noise a data processing stage called cross correlation is used. Simplistically the cross correlation procedure removes the vibroseis sweep present in the shot record and replaces it with a spike which is a close approximation to the earth's impulse response.

I.2 S-wave processing parameters

Location of sweep trace	Very first input trace
Start time for sweep	0
Length of sweep	14000
Output trace length	1000

Table I.1: *Correlation parameters: three lines have the same parameters for vibroseis correlation*

Maximum CDP fold	248
Minimum center CDP number	2215
Maximum center CDP number	2466
CDP increment	11
CDPs to combine	11

Table I.2: *Supergathers, line 1*

Maximum CDP fold	227
Minimum center CDP number	2012
Maximum center CDP number	2217
CDP increment	21
CDPs to combine	21

Table I.3: *Supergathers, line 2*

Maximum CDP fold	224
Minimum center CDP number	6013
Maximum center CDP number	6276
CDP increment	21
CDPs to combine	21

Table I.4: *Supergathers, line 3*

Type of filter	Single filter
Type of filter specification	Ormsby band-pass
Phase of filter	zero
Domain for filter application	Frequency
Percent zero padding for FFT's	25
Ormsby filter frequency value	20-30-120-180

Table I.5: *Parameters of band-pass filter: line 1*

Type of filter	Single filter
Type of filter specification	Ormsby band-pass
Phase of filter	zero
Domain for filter application	Frequency
Percent zero padding for FFT's	25
Ormsby filter frequency value	20-30-90-120

Table I.6: *Parameters of band-pass filter: line 2*

Type of filter	Single filter
Type of filter specification	Ormsby band-pass
Phase of filter	zero
Domain for filter application	Frequency
Percent zero padding for FFT's	25
Ormsby filter frequency value	20-30-140-210

Table I.7: *Parameters of band-pass filter: line 3*

Final datum elevation	2517
Replacement velocity	200
Database math method	Surface Source
NMO static method	Elevations
Length of smoother	11
Processing DATUM	NMO DATUM

Table I.8: *Parameters of elevation statics: line 1*

Final datum elevation	2514
Replacement velocity	200
Database math method	Surface Source
NMO static method	Elevations
Length of smoother	11
Processing DATUM	NMO DATUM

Table I.9: *Parameters of elevation statics: line 2*

Final datum elevation	2522.79
Replacement velocity	200
Database math method	Surface Source
NMO static method	Elevations
Length of smoother	11
Processing DATUM	NMO DATUM

Table I.10: *Parameters of elevation statics: line 3*

Minimum CDP to migrate	2189
Maximum CDP to migrate	2473
CDP interval (meters)	0.95895
Minimum frequency to migrate (Hz)	20
Maximum frequency to migrate	120
Interval velocity-time for migration	1:0-200
Percent velocity scale factor	100
Migrate dips	Up to 90 degrees only

Table I.11: *Parameters of migration: line 1*

Minimum CDP to migrate	2002
Maximum CDP to migrate	2227
CDP interval (meters)	0.99516
Minimum frequency to migrate (Hz)	30
Maximum frequency to migrate	120
Interval velocity-time for migration	1:0-200
Percent velocity scale factor	100
Migrate dips	Up to 90 degrees only

Table I.12: *Parameters of migration: line 2*

Minimum CDP to migrate	6002
Maximum CDP to migrate	6287
CDP interval (meters)	0.96738
Minimum frequency to migrate (Hz)	30
Maximum frequency to migrate	120
Interval velocity-time for migration	1:0-200
Percent velocity scale factor	100
Migrate dips	Up to 90 degrees only

Table I.13: *Parameters of migration: line 3*

References

[1] Characterization of the upper Arkansas basin. Technical report, Colorado School of Mines, 2008. Joint report by CSM, ICL and Boise State University. 48

[2] Characterization of the upper Arkansas basin. Technical report, Colorado School of Mines, 2009. Joint report by CSM, ICL and Boise State University. xxi, xxii, 1, 40, 209, 210, 211

[3] Compton effect. http://cph-theory.persiangig.com/1197-6.JPG, June 2010. xxi, 204

[4] Photoelectric effect. http://physweb.bgu.ac.il/COURSES/PHYSICS3_ChemMatr/index_files/Photoelectric_effect.png, June 2010. xxi, 204

[5] ABEM. Terrameter lund imaging system. http://www.abem.se/products/sas4000/sas4000.php, June 2010. xix, 168, 170

[6] AGI. Supersting r8 ip. http://www.agiusa.com/supersting.shtml, June 2010. 169

[7] Michael Batzle, 2010. 9

[8] Thomas L. Blum, 2010. 8

[9] National Resources Canada. Geomagnetism: north magnetic pole. http://gsc.nrcan.gc.ca/geomag/nmp/northpole_e.php, June 2010. xxi, 207, 209

[10] R. Berle Clay. *Conductivity (EM) survey: A survival manual*, 2002. 193

[11] N. Jordan Dimick. The use of statistical multivariate geochannel analysis to determine groundwater mixing in the Upper Arkansas river River Valley, Colorado, USA. Master's thesis, Colorado School of Mines, 2006. 10

[12] Shared Field Measurement Facility. Dc resistivity. http://pangea.stanford.edu/research/groups/sfmf/docs/DCResistivity.pdf, June 2010. 173

[13] Micro g LaCoste. Cg-5 brochure. http://www.scintrexltd.com/documents/CG-5BrochureRev1.pdf, June 2010. 57, 117

[14] National Geographic. Colorado seeks a renewable energy peak, May 2010. 1

[15] Geosoft. *Topics in Gridding Workshop*, 2007. 74

[16] Geosoft. Gravity and terrain correction. http://www.geosoft.com/resources/pinfo/montaj_GravityandTerrain_F.pdf, June 2010. 200

[17] John Gibson, Forest Lin, Alexandre Egreteau, Julien Meunier, and Malcolm Lansley. The case for longer sweeps in vibrator acquisition. *The Leading Edge*, 29(6):648–652, 2010. 43

[18] Joseph R Hearst and Philip H. Nelson. *Well logging for physical properties*. McGraw-Hill, New York :, second edition, 2000. 81, 201

[19] Joseph R Hearst and Philip H. Nelson. *Well logging for physical properties*. McGraw-Hill, New York :, second edition, 2000. 202

[20] Joseph R Hearst and Philip H. Nelson. *Well logging for physical properties*. McGraw-Hill, New York :, second edition, 2000. 203

[21] Klaus Helbig and Leon Thomsen. 75-plus years of anisotropy in exploration and reservoir seismics: A historical review of concepts and methods. *Geophysics*, 70(6):9ND–23ND, 2005. 40

[22] F. Henderson, P. Morgan, and H. Olson. Mt. princeton geothermal 500 foot temperature gradient hole study: State purchase order no. 09-250, 2009. 185

[23] Northwest Geophysical Associates Inc. Geophysical borehole logging. http://www.nga.com/graphics/Geo_ser_Borehole_logging_sketch.gif, June 2010. xx, 202

[24] Reynolds International. *EM31 electro-magnetic ground conductivity mapping*, 2009. 69, 77

[25] Alex A. Kaufman and Richard O. Hansen. *Principles of the Gravitational Method*. Cambridge University Press, second edition, 1990. 153, 196

[26] Harold L. Levin. *The Earth through time*. Wiley, fifth edition, 1996. 7

[27] John Milsom. *Field Geophysics (Geological Field Guide)*. Wiley, London, third edition, 2002. 72

[28] John Milsom. *Field Geophysics*. Wiley, third edition, 2003. 205, 206

[29] Inc. Northwest Geophysical Associates. Self potential technique. http://www.nga.com/Geo_ser_Self_potential_tech.htm, June 2010. xix, 166, 168

[30] James Schombert: University of Oregon. Pair production. `http://abyss.uoregon.edu/~js/images/pair_production.gif`, June 2010. xxi, 204

[31] A. J-M. Pugin, S. E. Pullan, and J. A. Hunter. Sv-wave and p-wave high resolution seismic reflection using vertical impacting and vibrating sources. pages 585–594. SAGEEP. SAGEEP annual meeting. 38

[32] A. J-M. Pugin, S. E. Pullan, and J. A. Hunter. Update on recent observations in multi-component seismic reflection profiling. pages 39–48. SAGEEP. SAGEEP annual meeting. 38, 40

[33] Dr. Raynolds, 2010. 6, 7, 8

[34] G. R. Scott, R. E. van Alstine, and W. N. Sharp. Geologic map of the Poncha Springs quadrangle, Chaffee County, Colorado. U.S. 14

[35] J. L. Simmons and M. M. Backus. Shear-wave splitting: Tutorial, issues and implications for 9-c 3-d seismic reflection data. *SEG Expanded Abstracts*, 1999. 40

[36] Brian R. Spies. Depth of investigation in electromagnetic sounding methods. *Geophysics*, 54(7):872–888, 1989. 95

[37] W. M. Telford. *Applied geophysics*. Elsevier Science, 2007. 196, 197, 198, 199

[38] Leon Thomsen. Weak elastic anisotropy. *Geophysics*, 51(10):1954–1966, 1986. 40

[39] R. E. van Alstine. Geology and mineral deposits of the Poncha Springs NE quadrangle, Chaffee County, Colorado. Technical report, USGS, 1969. USGS professional paper. 7, 8, 12

[40] C. A. Zelt and R. M. Ellis. Practical and efficient ray tracing in two-dimensional media for rapid traveltime and amplitude forward modelling. *Can. J. Expl. Geophys*, 24:16–31, 1988. 153